Process Development Tools for Cross-Flow Filtration in Biopharmaceutical Downstream Processing

Zur Erlangung des akademischen Grades eines
DOKTORS DER INGENIEURWISSENSCHAFTEN (DR.-ING.)

von der KIT-Fakultät für Chemieingenieurwesen und Verfahrenstechnik des
Karlsruher Instituts für Technologie (KIT)
genehmigte

DISSERTATION

von
Nils Hillebrandt, M.Sc.
aus Frankfurt am Main

Tag der mündlichen Prüfung: 29. Juni 2023
Erstgutachter: Prof. Dr. Jürgen Hubbuch
Zweitgutachter: Prof. Dr. Michael Wolff

Danksagung

Im Rahmen dieser Arbeit durfte ich Zeit mit vielen Menschen verbringen, die mich unterstützt, inspiriert, geprägt sowie zum Erfolg der Arbeit beigetragen haben. Deshalb möchte ich mich bei allen bedanken, die mich auf diesem Weg begleitet haben und im Folgenden einige besonders hervorheben.

Zuerst möchte ich mich bei Prof. Jürgen Hubbuch für die Möglichkeit und das Vertrauen bedanken, meine Doktorarbeit an seinem Lehrstuhl durchführen zu können. Vielen Dank für Deine Betreuung über die letzten Jahre, ich habe die Balance aus gutem Rat und gestalterischer Freiheit immer sehr genossen.

Prof. Michael Wolff möchte ich für die Übernahme des zweiten Gutachtens danken sowie für das Interesse an der Arbeit und die Reise zur Prüfung nach Karlsruhe.

Bei Tobias Hahn, Thiemo Huuk und der GoSilico GmbH/Cytiva, Simon Kluters und der Boehringer Ingelheim Pharma GmbH & Co. KG, Thorsten Klamp und der BioNTech SE sowie Prof. Adam Zlotnick und der Indiana University möchte ich mich für die gute Zusammenarbeit und/oder die Bereitstellung von Proteinen bzw. deren Sequenzen für meine Arbeit bedanken. Ich möchte mich außerdem beim Rheometer-Team um apl. Prof. Christian Pylatiuk für die angenehme Zusammenarbeit bedanken.

Vielen Dank an Philipp Vormittag und Till Briskot für die konstruktiven Diskussionen sowie die gute und erfolgreiche Zusammenarbeit an den gemeinsamen Projekten und Manuskripten.

Ein besonderer Dank gilt dem Institut für Molekulare Aufarbeitung von Bioprodukten in seiner aktuellen und ehemaligen Besetzung. Danke für die gute Arbeitsatmosphäre im Labor und im Büro. Danke für die vielen wissenschaftlichen, tiefsinnigen und vor allem auch die unsinnigen Gespräche. Ich habe die einzigartige Professionalität bei der Arbeit und beim Feiern immer sehr genossen. Vielen Dank an

- Marion, Margret, Michael und Iris für Eure Hilfe bei den bürokratischen Hürden des Unialltags,

- Birgit, Kristina, Nico, Susi, Nicola und Jasmin für Eure zahlreichen Bestellungen, Antworten auf Fragen über vergangene Zeiten, und Eure unsichtbare Arbeit im Hintergrund,
- Jan (und seinem Team) für den besten IT-Support, den man sich nur wünschen kann, inklusive einzigartiger Rettungsaktionen, nächtlicher Lötsessions und so viel weiterer Genialität,
- Anna und Marieke für Eure Hilfe während des On-Boardings sowie Dennis und allen anderen Bewohnerinnen und Bewohnern von Büro 207 für unseren guten Austausch auf allen Ebenen,
- Svenja für unvergessliche Zeiten beim Praktikum,
- Angela, Robin und Tina für Euer Feedback zu diversen Präsentationen und Manuskripten, gute Gespräche und den wunderbaren Trip nach Porto,
- Lukas für Deine Hilfe hier und da sowie für lebhafte Diskussionen und Partys,
- Carsten für den Einstieg am MAB und Deine treue Begleitung über viele Jahre,
- Annabelle für Deine Verlässlichkeit und Unterstützung sowie Dein ehrliches Feedback,
- Basti für unsere gemeinsamen Auszeiten am Lago, interessante Gespräche zwischen Flur und Büro auf dem Weg nach Hause, und Deine guten Ratschläge,
- Philipp für Dein Mentoring, die Hilfe in allen Lebenslagen und vor allem den Spaß und die Begeisterung für unsere gemeinsamen Projekte.

Weiterhin möchte ich Thomas, Tina, Robin und Annabelle danken, deren Masterarbeiten ich betreuen durfte. Danke für Eure hervorragende und gewissenhafte Arbeit. Es hat mir viel Freude bereitet, durch und mit Euch mehr als nur Fachliches zu lernen.

Von Herzen danke ich meinen Freunden. Danke, dass Ihr für mich da seid, auch wenn ich öfter mal körperlich oder mit dem Kopf nicht ganz anwesend war und Ihr mir (un-)gewollt gezeigt habt, dass es neben dieser Arbeit auch noch wichtigere Dinge gibt. Außerdem möchte ich den Jungs von der DJK Karlsruhe-Ost danken, dass Ihr mit Sport und Gemeinschaft für unvergessliche Feierabende und Sonntage gesorgt habt, bei denen ich Abschalten und Energie tanken konnte.

Ich möchte meinen Eltern zutiefst danken, dass sie mir mit ihrer Unterstützung ermöglicht haben, meine Ausbildung erfolgreich zu absolvieren. Danke, dass Ihr mir Freiheiten gelassen habt und mich begleitet

habt. Neben meinen Eltern möchte ich auch meinem Opa danken, der mir in meiner Jugend viele Dinge beigebracht und gezeigt hat und damit meine Art zu arbeiten und zu denken maßgeblich geprägt hat.

Besonders möchte ich Franziska danken. Ich bin Dir unendlich dankbar für Deine bedingungslose Unterstützung auf allen Ebenen. Danke, dass Du mir im Laufe dieser Arbeit so viele wundervolle Momente geschenkt hast.

Nils Hillebrandt, im Juli 2023

Abstract

In modern medicine, biopharmaceutical proteins are important substances for the treatment and prevention of diseases such as lymphoma and hepatitis B, respectively. These proteins have a complex structure that requires biological synthesis in cells and their parenteral administration requires subsequent purification. Finally, the protein has to be formulated in a liquid that provides a certain stability and physiological compatibility. Recovery of the protein from the cell broth, purification, and formulation are referred to as downstream processing (DSP). Each processing step in DSP is conducted by a unit operation, one of which is cross-flow filtration (CFF), also known as tangential flow filtration (TFF). In CFF, proteins are separated from impurities or the surrounding liquid phase by size-exclusion, ideally decoupling the separation mechanisms from other protein properties such as charge or hydrophobicity. Size-exclusion is realized by porous membranes. In DSP of biopharmaceutical proteins, CFF can be applied for cell separation, purification, and final formulation. The latter usually consists of a combination of buffer exchange and concentration increase, referred to as ultrafiltration/diafiltration (UF/DF). Compared to conventional normal-flow filtration, the feed stream in CFF is directed parallelly to the membrane surface and the filtrate penetrates the pores of the membrane. Therefore, CFF leads to less accumulation of retained species at the membrane surface and thus faster processes and less concentration-dependent aggregation. Despite these advantages, process development for CFF comes with several challenges, which are time- and material-consuming experiments, limited purification performance, and deviations of ion concentrations from the target at high protein concentrations. In DSP, several tools for process development and optimization are available, for example, process integration, high-throughput screenings (HTS), process analytical technology (PAT), and mechanistic modeling. However, these tools are only rarely applied to CFF when compared to other unit operations such as chromatography. The objective of this thesis was to provide solutions to the mentioned challenges through the implementation of these tools in dedicated case studies. Ultimately, this thesis aimed to gain knowledge from these case

studies to extend the process development toolbox for CFF processes in biopharmaceutical DSP.

In Chapter 1 of this thesis, DSP approaches for the two biopharmaceuticals exemplarily used in this thesis, virus-like particles (VLPs) and monoclonal antibodies (mAbs), are reviewed. VLPs are non-infectious viral particles missing the viral genome. Non-enveloped VLPs are composed of protein subunits that spontaneously assemble into capsids in the producing cell. VLPs are often dis- and reassembled during DSP to improve their homogeneity, stability, and immunogenicity. Biopharmaceutical applications of VLPs are vaccines and potentially therapeutic vaccines or vectors for the delivery of other molecules. MAbs are immunoglobulins consisting of four covalently bound protein chains. Compared to mAbs, most VLPs are more than one order of magnitude larger in size and molecular weight. MAbs are one of the most frequently licensed biopharmaceuticals for human use with a variety of applications, including the treatment of cancers and inflammatory diseases. Furthermore, the principles and applications of CFF are discussed in Chapter 1. Finally, background information and current research on the applied process development tools are reviewed.

Alternative separation techniques to chromatographic purification often show lower purification performance and poor scalability. The main measures for DSP performance are purity and productivity. Both can be improved by process integration, which is realized by combining unit operations in a common space or their seamless connection. Chapter 3 presents the application of process integration to improve the process performance and scalability in the DSP of non-enveloped VLPs. Therefore, VLP precipitation, wash, and re-dissolution were combined with CFF. Permeate flow rate control was implemented and reduced the compaction of precipitate at the membrane surface. Compared to centrifugation-based precipitate separation, this approach led to improved purity and productivity as well as a higher degree of automation. Permeate flow rate control also facilitated additional integration of multimodal size-exclusion chromatography (SEC) into the re-dissolution stream to further improve purity. In-line ultraviolet light (UV) absorbance monitoring and product fractionation were implemented to improve purity based on data-driven in-process decisions. Ultimately, the presented approaches led to an integrated capture and purification step with flexible scalability and great potential for full automation. Purification performance was also comparable to entire DSP approaches in literature. The integration of multiple separation techniques created synergies, overcoming the limitations of the individual techniques. The resulting DSP approach is based only on size-selective separations exploiting the size difference of VLPs and

common impurities. This size difference applies to most VLPs and thus promises a wide applicability of the presented DSP approach.

In biopharmaceutical development, the availability of protein material is often limited whereas CFF requires comparably large amounts for experimental studies. In Chapter 4, these challenges are addressed by presenting a process development approach for protein reactions driven by a change in liquid phase conditions. As a case study, the disassembly of non-enveloped VLPs was investigated. It may be induced by a change in liquid phase conditions, for example by increasing pH and urea concentration. Low-volume HTS were applied to find the optimal liquid phase conditions for VLP disassembly. Therefore, VLP solutions were mixed with stock solutions to match the process conditions and automatically analyzed by SEC under reaction conditions. The resulting high-resolution data allowed for characterization of the VLP disassembly reaction with regard to CFF-based processing. Optimal conditions were then applied in a laboratory-scale cross-flow DF process step. Higher yield and purity observed after DF-based processing were attributed to a controlled change of liquid phase conditions, intensified mixing, and the simultaneous depletion of impurities. Moreover, the disassembly step was embedded in a sequence of filtration-based processing steps which markedly reduced undesired higher molecular weight species. Employing only filtration as a size-selective technique makes the developed process independent of other molecular protein properties and therefore offers the potential for platform processing of non-enveloped VLPs in general. Ultimately, the presented process development approach reduces time and protein material requirements by decoupling the condition screening from CFF development and offers the potential for thorough characterization.

The study presented in Chapter 5 aimed to overcome the challenge of material limitations by maximizing the knowledge gained from CFF experiments. Therefore, a PAT framework was developed for the same VLP disassembly process step that is presented in Chapter 4. An array of PAT sensors was evaluated under varying processing conditions. Filtration performance parameters such as pressures, flow rates, and buffer exchange were monitored in-line. VLP disassembly progress was qualitatively traced by on-line UV absorbance and static light scattering spectroscopy. The second derivative analysis of the UV spectra further revealed changes in the tertiary structure of subunit proteins during disassembly. On-line monitoring of dynamic light scattering showed potential as a qualitative indicator of undesired protein aggregation. Regression models using UV data as input and VLP subunit concentration as output were calibrated and validated using at-

line SEC data as a reference. Using the models, the subunit concentrations and thus the disassembly progress was accurately predicted. Predictions were successfully applied for process endpoint detection. In addition, univariate raw signals of UV and static light scattering were found to successfully detect the process endpoint providing a simple approach for large-scale manufacturing. Overall, the developed PAT framework provided process- and product-related signals in (near) real-time enabling comprehensive monitoring, characterization, and endpoint detection. The presented approach has great potential to characterize the disassembly of other VLPs or reactions involving a change in particle size or tertiary protein structure.

Formulation of biopharmaceutical proteins by UF/DF becomes increasingly challenging with increasing protein concentration. The accumulation of charged proteins leads to an uneven distribution of charged excipients across the membrane, referred to as Gibbs-Donnan effect. This effect leads to deviations in pH and excipient concentrations from target conditions. These deviations may be further enhanced or reduced by the volume exclusion effect or the ionic strength dependency of p*K* values. The complex network of these interdependent phenomena makes simple or generic estimations of the final composition difficult. In Chapter 6, the development and validation of a mechanistic model describing the mentioned phenomena and interactions are presented. The study aimed to provide a better understanding of model variables and predict the composition during high-concentration UF/DF processes. Currently available models describe and validate the high-protein-concentration regime above 100 gL^{-1} only insufficiently or require experimental calibration. A mechanistic model based on Poisson-Boltzmann theory and a basic Stern model was developed to describe the electrostatic interactions of proteins and charged solutes. A particular focus during development was on high protein concentrations. The model was also designed to require only usually known theoretical information on the protein and buffer compositions as input variables. The model was thoroughly validated with comprehensive experimental data of entire UF/DF/UF sequences of mAbs and multiple liquid phase conditions. Model predictions showed better accuracy in the high-concentration regime compared to existing approaches. In conclusion, the developed model and the applied validation strategy provide a deeper understanding of UF/DF models using Poisson-Boltzmann theory. The purely predictive model enables systematic *in silico* design of high-concentration UF/DF steps without requiring any protein material.

In summary, process integration, HTS, PAT, and mechanistic modeling were successfully implemented for CFF process development and applied to

improve process performance, protein material requirements, and development timelines. This thesis thereby provides potential solutions to challenges in biopharmaceutical CFF process development based on dedicated case studies. In addition to these solutions, the developed CFF processes offer new approaches for size-selective purification of non-enveloped VLPs and thus building blocks for platform DSP. For modeling the composition during UF/DF of highly concentrated mAb formulations, a thorough understanding of model variables and the validity of assumptions is provided. This thesis contributes to the expansion of scientific knowledge on CFF process development through advanced development approaches and process designs.

Zusammenfassung

In der modernen Medizin sind biopharmazeutische Proteine wichtige Substanzen für die Behandlung und Vorbeugung von Krankheiten wie Lymphomen bzw. Hepatitis B. Diese Proteine haben eine komplexe Struktur, die eine biologische Synthese in Zellen erfordert, und ihre parenterale Verabreichung bedarf einer anschließenden Reinigung. Abschließend muss das Protein in einer Flüssigkeit formuliert werden, die eine gewisse Haltbarkeit und physiologische Verträglichkeit gewährleistet. Die Gewinnung des Proteins aus der Zellbrühe, die Reinigung und die Formulierung werden als *downstream processing* (DSP) bezeichnet. Jeder Prozessschritt im DSP wird mit einer Grundoperation durchgeführt, eine davon ist die Querstromfiltration (*cross-flow filtration*, CFF), auch bekannt als Tangentialflussfiltration (TFF). Bei der CFF werden die Proteine durch Größenausschluss von Verunreinigungen oder der umgebenden flüssigen Phase getrennt, wobei der Trennmechanismus im Idealfall von anderen Proteineigenschaften wie Ladung oder Hydrophobizität entkoppelt ist. Der Größenausschluss wird durch poröse Membranen realisiert. Im DSP biopharmazeutischer Proteine kann die CFF für die Zellseparation, die Reinigung und die finale Formulierung eingesetzt werden. Letztere besteht in der Regel aus einer Kombination von Pufferaustausch und Konzentrationserhöhung, die als Ultrafiltration/ Diafiltration (UF/DF) bezeichnet wird. Im Vergleich zur herkömmlichen Normalstromfiltration wird der Zulaufstrom bei der CFF parallel zur Membranoberfläche gerichtet und das Filtrat dringt durch die Poren der Membran. Daher führt die CFF zu einer geringeren Anreicherung der zurückgehaltenen Spezies an der Membranoberfläche und somit zu schnelleren Prozessen und weniger konzentrationsabhängiger Aggregation. Trotz dieser Vorteile ist die Prozessentwicklung für die CFF mit einigen Herausforderungen verbunden: Diese sind zeit- und materialaufwändige Experimente, begrenzte Reinigungsleistung und Abweichungen der Ionenkonzentrationen vom Zielwert bei hohen Proteinkonzentrationen. Im DSP stehen mehrere Werkzeuge für die Prozessentwicklung und -optimierung zur Verfügung, zum Beispiel Prozessintegration, Hochdurchsatz-Screenings (*high-throughput screenings*, HTS), prozessanalytische Technologie (*process*

analytical technology, PAT) und mechanistische Modellierung. Im Vergleich zu anderen Grundoperationen, wie zum Beispiel der Chromatographie, werden diese Werkzeuge jedoch nur selten für die CFF eingesetzt. Das Ziel dieser Arbeit war es, Lösungen für die genannten Herausforderungen zu finden, indem diese Werkzeuge in speziellen Fallstudien eingesetzt werden. Zudem war es Ziel dieser Arbeit, Erkenntnisse aus diesen Fallstudien zu gewinnen, um die Auswahl der Werkzeuge zur Entwicklung von CFF-Prozessen im biopharmazeutischen DSP zu erweitern.

In Kapitel 1 dieser Arbeit wird einen Überblick über DSP-Ansätze für die beiden in dieser Arbeit exemplarisch verwendeten Biopharmazeutika, virusähnliche Partikel (*virus-like particles*, VLPs) und monoklonale Antikörper (*monoclonal antibodies*, mAbs), gegeben. VLPs sind nicht-infektiöse virale Partikel, denen das virale Genom fehlt. Nicht-umhüllte VLPs bestehen aus Proteinuntereinheiten, die sich in der produzierenden Zelle spontan zu Kapsiden zusammensetzen. VLPs werden meist während des DSP zerlegt und neu zusammengesetzt, um ihre Homogenität, Stabilität und Immunogenität zu verbessern. Biopharmazeutische Anwendungen von VLPs sind Impfstoffe und potenzielle therapeutische Impfstoffe oder Vektoren für die Einschleusung anderer Moleküle. MAbs sind Immunglobuline, die aus vier kovalent gebundenen Proteinketten bestehen. Im Vergleich zu mAbs sind die meisten VLPs um mehr als eine Größenordnung größer in Durchmesser und Molekulargewicht. MAbs gehören zu den am häufigsten zugelassenen Biopharmazeutika für den menschlichen Gebrauch und finden unter anderem bei der Behandlung von Krebs- und Entzündungskrankheiten Anwendung. Außerdem werden in Kapitel 1 Grundlagen und Anwendungen der CFF erläutert. Abschließend werden Hintergrundwissen und aktuelle Forschung zu den angewandten Werkzeugen der Prozessentwicklung dargestellt.

Alternative Trennverfahren zur chromatographischen Reinigung weisen häufig eine geringere Trennleistung auf und sind schlecht skalierbar. Die wichtigsten Messgrößen für die Prozessleitung im DSP sind Reinheit und Produktivität. Beide können durch Prozessintegration verbessert werden, die durch die Kombination von Grundoperationen in einem gemeinsamen Arbeitsraum oder deren nahtlose Verbindung erreicht wird. In Kapitel 3 wird die Anwendung der Prozessintegration zur Verbesserung der Prozessleistung und der Skalierbarkeit des DSP von nicht-umhüllten VLPs vorgestellt. Dazu wurden die VLP-Fällung, -Wäsche und -Rücklösung mit CFF kombiniert. Es wurde eine Steuerung der Permeatflussrate implementiert, die die Verdichtung des Präzipitats an der Membranoberfläche reduzierte. Im Vergleich zur Abtrennung des Präzipitats mittels Zentrifugation, führte dieser Ansatz zu

einer verbesserten Reinheit und Produktivität sowie zu einem höheren Automatisierungsgrad. Die Steuerung der Permeatflussrate ermöglichte auch die zusätzliche Integration von multimodaler Größenausschlusschromatographie (*size exclusion chromatography*, SEC) in den Rücklösungsstrom und damit eine weitere Verbesserung der Reinheit. Die *in-line*-Überwachung der Absorbanz von ultraviolettem Licht (UV) und die Produktfraktionierung wurden implementiert, um die Reinheit auf der Grundlage von datengesteuerten Entscheidungen während des Prozesses zu verbessern. Die vorgestellten Maßnahmen führten zu einem integrierten Abtrennungs- und Reinigungsschritt mit flexibler Skalierbarkeit und großem Potenzial für eine vollständige Automatisierung. Die Trennleistung war außerdem vergleichbar mit kompletten DSP-Ansätzen in der Literatur. Durch die Integration mehrerer Trenntechniken wurden Synergien geschaffen, die die Leistungsgrenzen der einzelnen Techniken überwinden. Der resultierende DSP-Ansatz basiert ausschließlich auf größenselektiven Trenntechniken, die den Größenunterschied von VLPs zu üblichen Verunreinigungen ausnutzen. Dieser Größenunterschied gilt für die meisten VLPs und verspricht somit eine breite Anwendbarkeit des vorgestellten DSP-Ansatzes.

In der biopharmazeutischen Entwicklung ist die Verfügbarkeit von Proteinmaterial oft begrenzt, während die CFF vergleichsweise große Mengen für experimentelle Studien benötigt. In Kapitel 4 werden diese Herausforderungen adressiert, indem ein Ansatz zur Prozessentwicklung für Proteinreaktionen, die durch eine Änderung der Flüssigphase angetrieben werden, vorgestellt wird. Als Fallstudie wurde die Zerlegung von nichtumhüllten VLPs untersucht. Sie kann durch eine Änderung der Flüssigphase ausgelöst werden, zum Beispiel durch eine Erhöhung des pH-Werts und der Harnstoffkonzentration. Um die optimalen Flüssigphasenbedingungen für die Zerlegung von VLPs zu finden, wurden HTS in kleinen Volumina durchgeführt. Dazu wurden VLP-Lösungen mit Stammlösungen gemischt, um den Prozessbedingungen zu entsprechen, und unter Reaktionsbedingungen automatisch mittels SEC analysiert. Die daraus resultierenden hochauflösenden Daten ermöglichten die Charakterisierung der Zerlegung der VLPs im Hinblick auf die CFF-basierte Prozessierung. Die optimalen Bedingungen wurden dann in einem DF-Prozessschritt im Labormaßstab angewendet. Die nach der DF-basierten Prozessierung beobachtete höhere Ausbeute und Reinheit wurde auf eine kontrollierte Änderung der Flüssigphase, eine intensivere Durchmischung und die gleichzeitige Abreicherung von Verunreinigungen zurückgeführt. Darüber hinaus wurde der VLP-Zerlegungsschritt in eine Sequenz von filtrationsbasierten Prozessschritten eingebettet, wodurch unerwünschte Spezies mit höherem Mole-

kulargewicht deutlich reduziert wurden. Die ausschließliche Verwendung der Filtration als größenselektiver Trenntechnik macht den entwickelten Prozess unabhängig von anderen molekularen Proteineigenschaften und bietet daher das Potenzial für eine Plattformprozessierung von nicht-umhüllten VLPs im Allgemeinen. Der vorgestellte Ansatz zur Prozessentwicklung reduziert den Zeit- und Proteinbedarf durch die Entkopplung des Screenings der Bedingungen von der CFF-Entwicklung und bietet das Potenzial für eine umfassende Charakterisierung.

Die in Kapitel 5 vorgestellte Studie zielte darauf ab, die Herausforderung der Materialbeschränkungen zu überwinden, indem das aus CFF-Experimenten gewonnene Wissen maximiert wird. Dazu wurde ein PAT-Konzept für denselben Prozessschritt der Zerlegung von VLPs entwickelt, der in Kapitel 4 vorgestellt wird. Eine Reihe von PAT-Sensoren wurde unter verschiedenen Prozessbedingungen evaluiert. Parameter der Filtration wie Drücke, Durchflussraten und Pufferaustausch wurden *in-line* überwacht. Der Fortschritt der Zerlegung der VLPs wurde *on-line* mittels UV-Absorbanz und statischer Lichtstreuung qualitativ überwacht. Die Analyse der zweiten Ableitung der UV-Spektren zeigte außerdem Veränderungen in der Tertiärstruktur der Proteinuntereinheiten während der VLP-Zerlegung. Die *on-line* Überwachung der dynamischen Lichtstreuung zeigte Potenzial als qualitativer Indikator für unerwünschte Proteinaggregation. Regressionsmodelle, die UV-Daten als Eingangsgröße und die Konzentration der VLP-Untereinheiten als Ausgangsgröße verwenden, wurden kalibriert und anhand von *at-line* SEC-Daten als Referenz validiert. Mit Hilfe der Modelle wurden die Konzentrationen der Untereinheiten und damit der Fortschritt der VLP-Zerlegung präzise vorausgesagt. Die Vorhersagen wurden erfolgreich zur Erkennung von Prozessendpunkten eingesetzt. Darüber hinaus wurde nachgewiesen, dass unverarbeitete univariate Signale von UV und statischer Lichtstreuung den Prozessendpunkt erfolgreich erkennen, was einen einfachen Ansatz für die großtechnische Herstellung darstellt. Insgesamt liefert das entwickelte PAT-Konzept prozess- und produktbezogene Daten in (nahezu) Echtzeit, was eine umfassende Überwachung, Charakterisierung und Endpunktdetektion ermöglicht. Der vorgestellte Ansatz hat großes Potenzial zur Charakterisierung der Zerlegung anderer VLPs oder von Reaktionen, die eine Veränderung der Partikelgröße oder der tertiären Proteinstruktur mit sich bringen.

Die Formulierung biopharmazeutischer Proteine mittels UF/DF wird mit steigender Proteinkonzentration anspruchsvoller. Die Anreicherung von geladenen Proteinen führt zu einer ungleichmäßigen Verteilung von geladenen Hilfsstoffen durch die Membran, was als Gibbs-Donnan-Effekt bezeichnet wird. Dieser Effekt führt zu Abweichungen des pH-Werts und der

Konzentration der Hilfsstoffe von den Zielbedingungen. Diese Abweichungen können durch den Volumenausschlusseffekt oder die Abhängigkeit der pK-Werte von der Ionenstärke noch verstärkt oder verringert werden. Das komplexe Geflecht dieser voneinander abhängigen Phänomene erschwert einfache oder generische Abschätzungen der endgültigen Zusammensetzung. In Kapitel 6 wird die Entwicklung und Validierung eines mechanistischen Modells vorgestellt, das die genannten Phänomene und Wechselwirkungen beschreibt. Ziel der Studie war es, ein besseres Verständnis der Modellvariablen zu erlangen und die Zusammensetzung während UF/DF-Prozessen mit hohen Konzentrationen vorherzusagen. Derzeit verfügbare Modelle beschreiben und validieren den Bereich hoher Proteinkonzentrationen über 100 gL^{-1} nur unzureichend oder erfordern eine experimentelle Kalibrierung. Es wurde ein mechanistisches Modell entwickelt, das auf der Poisson-Boltzmann-Theorie und einem grundlegenden Stern-Modell basiert, um die elektrostatischen Wechselwirkungen von Proteinen und geladenen gelösten Stoffen zu beschreiben. Ein besonderer Fokus bei der Entwicklung lag auf hohen Proteinkonzentrationen. Das Modell wurde außerdem so konzipiert, dass als Eingangsvariablen lediglich üblicherweise bekannte theoretische Informationen über das Protein und die Pufferzusammensetzung benötigt werden. Das Modell wurde anhand umfassender experimenteller Daten kompletter UF/DF/UF-Sequenzen von mAbs und verschiedenen Flüssigphasenbedingungen sorgfältig validiert. Die Vorhersagen des Modells zeigten im Vergleich zu bestehenden Ansätzen eine bessere Genauigkeit im Bereich hoher Konzentrationen. Zusammenfassend lässt sich sagen, dass das entwickelte Modell und die angewandte Validierungsstrategie ein tieferes Verständnis von UF/DF-Modellen, die auf der Poisson-Boltzmann Theorie basieren, ermöglichen. Das rein prädiktive Modell ermöglicht ein systematisches *in silico* Design von hochkonzentrierten UF/DF-Schritten, ohne dass Proteinmaterial benötigt wird.

Abschließend kann gesagt werden, dass Prozessintegration, HTS, PAT und mechanistische Modellierung erfolgreich für die Entwicklung von CFF-Prozessen implementiert und zur Verbesserung der Prozessleistung, des Proteinbedarfs und der Entwicklungszeiten eingesetzt wurden. Diese Arbeit liefert somit potenzielle Lösungen für die Herausforderungen in der biopharmazeutischen CFF-Prozessentwicklung auf der Grundlage von konkreten Fallstudien. Zusätzlich zu diesen Lösungen bieten die entwickelten CFF-Prozesse neue Ansätze für die größenselektive Aufreinigung von nicht-umhüllten VLPs und damit Bausteine für ein Plattform-DSP. Für die Modellierung der Zusammensetzung während der UF/DF von hochkonzentrierten mAb-Formulierungen wird ein umfassendes Verständnis der

Modellvariablen und der Gültigkeit der Annahmen erarbeitet. Diese Arbeit zur Erweiterung des Forschungsstandes zur CFF-Prozessentwicklung durch fortschrittliche Entwicklungsansätze und Prozessdesigns bei.

Table of contents

1

Introduction

Pharmaceutical substances are an important pillar of modern medicine. A major area of application is the treatment and prevention of diseases. Traditional active pharmaceutical ingredients usually consist of organic substances with molecular weights up to several hundred daltons and can be produced by chemical synthesis. Higher molecular weight pharmaceutical substances, such as the hormone insulin, were initially extracted from animals or other biologically active sources (Walsh, 2013). Modern biotechnology based on recombinant deoxyribonucleic acid (DNA) technology enabled the targeted and efficient production of these complex biological substances (Walsh, 1999). Most of these substances are based on proteins or nucleic acids and are typically referred to as biopharmaceuticals (Nahler, 2017; Rader, 2008; Schellekens, 2002; Walsh, 2002). Since the approval of recombinant human insulin as the first biopharmaceutical in 1982, many other biopharmaceuticals have been developed and licensed for human use (Evens, 2016; Walsh, 2018). The range of substances has been extended to further hormones and other molecules, for example, clotting factors, monoclonal antibodies (mAbs), fusion proteins, nucleic acids, cells, and vaccines that treat or prevent a variety of diseases (Walsh, 2018). This thesis focuses on the major subgroup of protein-based substances and therefore uses the term 'biopharmaceutical' to refer to this subgroup. These proteins consist of L-amino acid subunits with a potential glycosylation, which is the covalent attachment of sugar molecules. Compared to low molecular weight substances, proteins have a complex three-dimensional structure allowing for highly specific functions on a molecular level (Crommelin et al., 2003; Leader et al., 2008). The functions may be a catalytic or regulatory activity, targeted binding to agents, or presentation of epitopes to elicit an immune response (Leader et al., 2008). Biopharmaceuticals allow for the treatment of many diseases, for example, anemia, diabetes mellitus, hemophilia, hepatitis C, rheumatoid arthritis, or numerous cancers as well as the immunization against hepatitis B, human papillomavirus (HPV)-induced cervical cancer or meningococcus B (Walsh, 2018).

The production of biopharmaceuticals is separated into an upstream processing part for synthesis and a downstream processing (DSP) part for recovery, purification, and formulation of the protein. The complex nature of proteins requires biosynthesis in living cells, so-called host cells. *Escherichia coli* (*E. coli*) and Chinese hamster ovary cells are frequently used microbial and mammalian host cells, respectively (Jagschies & Lacki, 2018). Different cell types have different capabilities such as the ability to perform glycosylation or secretion of proteins but also requirements such as the complexity of the growth medium.

DSP aims to achieve high target protein purity and yield in a reasonable process time. The recovery step of secreted proteins mostly aims to separate the liquid phase containing the target protein from cells. In the case of non-secreted proteins, recovery aims for the removal of cell debris after lysis. The subsequent purification can be subdivided into capture, intermediate purification, and polishing. These steps aim to isolate the target protein and remove process-related impurities, such as host cell proteins and nucleic acids, and product-related impurities, such as aggregates and undesired variants. For the DSP of single proteins, such as mAbs, viruses are regarded as process-related impurities. When viral particles are the target species, for example for gene therapy or vaccines, malformed or empty virus particles are prominent product-related impurities (Gagnon, 2009; Wolff & Reichl, 2011). During the formulation step, the protein solution is transferred to storage conditions which requires the addition or removal of small molecules, such as excipients or water. The resulting liquid solution is referred to as the (bulk) drug substance. It is further processed into the drug product which involves sterile filtration, fill, and finish. The scope of this thesis spans from capture to bulk drug substance formulation.

Most DSP steps aim to separate the target protein from impurities or undesired molecules, such as certain solutes or water. This is realized by unit operations which are separation techniques such as centrifugation, filtration, chromatography, precipitation, or extraction. Important properties of unit operations are scalability and productivity. Scalable processes and separation techniques can be used from research and development over (pre-) clinical to commercial manufacturing which enables continuous knowledge generation. Productivity refers to the mass of target protein per utilized goods and time. Utilized goods are for example chromatography resin volume, membrane area, buffer volume, or space. Another consideration is the applicability of the separation techniques to different proteins or classes of proteins to use templated development or production procedures and thus gain efficiency through standardization.

Filtration is used when the separation of differently sized species is required whereas chromatography can separate species according to properties such as charge, hydrophobicity, or size. The latter is realized by size-exclusion chromatography (SEC) which is, however, costly, limited to low productivity due to small injection volumes per resin volume, and time-intensive at a large scale (Aldington & Bonnerjea, 2007; Carvalho et al., 2019). Furthermore, such packed-bed chromatography is scaled up by volume with no economy of scale (Gottschalk, 2008). On the contrary, size-selective separation by filtration is cheaper and more efficient under low fouling conditions (Kurnik et al., 1995; Liderfelt & Royce, 2018), especially at larger scales (Gottschalk, 2008). Another advantage is the simple scale-up by increasing the filter area (van Reis, Goodrich, Yson, Frautschy, Dzengeleski, et al., 1997). Cross-flow filtration (CFF), also known as tangential flow filtration (TFF), is therefore a valuable unit operation when implemented properly. Several new tools emerged in the biopharmaceutical process development and optimization portfolio during the last decades (Kiss et al., 2018). Among these tools, process integration, high-throughput screenings (HTS), process analytical technology (PAT), and mechanistic modeling are investigated in this thesis. In the past, research and development of these tools mainly focused on chromatography. Nevertheless, CFF-based separations have been shown to benefit from the application of these tools or even require them to foster efficient process development.

In this chapter, background information and the state of the art in biopharmaceutical DSP are presented with regards to the abovementioned process development tools and their application to CFF. Section 1.1 elaborates on the biopharmaceuticals exemplarily investigated in this thesis and their associated DSP. Section 1.2 introduces theoretical and practical aspects of CFF in biopharmaceutical DSP. Section 1.3 elaborates on the process development tools investigated in this thesis.

1.1. Biopharmaceuticals and their downstream processing

The biopharmaceutical proteins investigated in this thesis are virus-like particles (VLPs) and mAbs. The latter are the flagship protein of the biopharmaceutical industry (Section 1.1.1) which are usually produced in a standardized template process with only minor adaption for each new molecule which is referred to as a platform process (Section 1.1.2). VLPs were chosen as a complementary biopharmaceutical in terms of properties (Section 1.1.3) and the resulting DSP (Section 1.1.4).

1.1.1. Monoclonal antibodies and their derivatives

Antibodies are glycoproteins of the immunoglobulin (Ig) family. Their function in the body is to bind and neutralize antigens and induce further

immune reactions (Zahavi & Weiner, 2020). MAbs are identical copies of the same antibody which all target one specific epitope of an antigen (Zahavi & Weiner, 2020). In the past, mAbs of the class IgG were the most frequently licensed biopharmaceuticals (Walsh, 2018). An IgG consists of two heavy and two light chains which are connected by disulfide bonds to form a Y-shaped protein with an approximate molecular weight of 150 kDa (Wang et al., 2007). In this thesis, mAb refers to IgG. Each arm of the 'Y' is formed by one light chain and one end of a heavy chain. The two other ends of the heavy chains form the stem of the 'Y'. An arm of a mAb is referred to as fragment antigen binding (Fab). It contains the highly variable region at the tip, which is specific for an antigen. The stem part is referred to as the crystallizable fragment and is responsible for the interaction with effectors of the immune system (Wang et al., 2007). The development of mAbs which specifically bind to receptors and other targets enables the treatment of a variety of diseases including several cancers, autoimmune diseases, and blood disorders. Further details and modes of action can be reviewed elsewhere (Rodgers & Chou, 2016). The capabilities of mAbs were further exploited to develop antibody-drug conjugates that enable the targeted delivery of cytotoxic drugs to cancer cells (Birrer et al., 2019). The molecular derivatives of mAbs are referred to as 'formats' and include fragments, single domains, or various combinations of these (Bates & Power, 2019; Holliger & Hudson, 2005). Fabs reduce or avoid an effector cell binding due to the lack of the crystallizable fragment and were among the first licensed mAb fragments for human use (Bates & Power, 2019; Holliger & Hudson, 2005). The upstream production of mAbs is dominated by mammalian cell culture, such as Chinese hamster ovary cells, due to the ability to perform the glycosylation of the crystallizable fragment (D. C. Andersen & Reilly, 2004; Kelley et al., 2018). Glycosylation is critical for antibody properties such as effector function or the blood half-life (Wright & Morrison, 1997). Fabs but also antibodies can be produced in *E. coli* and other non-mammalian host cells without glycosylation, which is sufficient for some applications (D. C. Andersen & Reilly, 2004).

1.1.2. Monoclonal antibody downstream processing

MAbs developed under a common framework usually have similar physico-chemical properties which enables similar DSP (H. F. Liu et al., 2010). This template structure of unit operations is referred to as a platform process. Advantages of implementing platform processes from early-stage development to commercial manufacturing are time savings in process development, documentation, and supply chain (Y. Li et al., 2017). Platform processes are also highly similar between different manufacturers (Shukla et al., 2017). Clarification by centrifugation or filtration is followed by a capture

step using protein A affinity chromatography, low pH virus inactivation, one or two chromatographic purification steps (anion exchange (AEX), cation exchange, or hydrophobic interaction), virus filtration, and concentration/buffer exchange (Kelley, 2017; H. F. Liu et al., 2010; Shukla et al., 2017). A sequence of concentrating the target protein and exchanging the buffer by CFF using ultrafiltration membranes is commonly referred to as ultrafiltration/diafiltration (UF/DF). The operating conditions for the unit operations, for example, flow rates, salt concentrations, or pH values, are then customized for each mAb candidate individually. The downstream processes of biopharmaceuticals in general have a similar basic structure whereas an exchange or addition of individual unit operations is possible or required (Pfister et al., 2018). In the case of lambda Fabs, Eifler et al. (2014) developed an affinity resin analogous to protein A to enable platform processing. In this thesis, UF/DF for highly concentrated mAb and Fab solutions is investigated, and the next paragraph provides a general introduction to UF/DF.

The final UF/DF operation, the formulation step, is performed to exchange the buffer into the formulation buffer and to concentrate the protein. The formulation conditions aim to provide a well-tolerated and stable drug with a certain storage/shelf life to ensure safety and efficacy (Daugherty & Mrsny, 2006; Frokjaer & Otzen, 2005). Instabilities may be physical such as denaturation, aggregation, and surface adsorption or chemical such as oxidation, deamidation, fragmentation, and cross-linking (Wang et al., 2007). Formulation parameters to achieve the abovementioned quality criteria are protein concentration, pH, buffering agents and concentration, tonicity, and other excipients such as stabilizing sugars or surfactants (Daugherty & Mrsny, 2006; Wang et al., 2007). High protein concentrations of 150 g L^{-1} and above are often required to reduce the dose volume and injection volume (Garidel et al., 2017; Holstein et al., 2020; Shire et al., 2004). For high-concentration formulations, UF/DF is usually performed by CFF in three steps, the protein is concentrated to an intermediate concentration, buffer exchange is performed, and followed by a final concentration step (Liderfelt & Royce, 2018; Y. Li et al., 2017; Rolinger, Rüdt, Diehm, et al., 2020; Wasalathanthri et al., 2020; West et al., 2021). This UF/DF/UF sequence is a simple, yet not always perfect (Paulen et al., 2012) method to minimize the total process time and buffer consumption of the DF step. Splitting up UF into two separate steps enables DF at a desired, intermediate protein concentration. DF at a higher protein concentration leads to a decreased buffer consumption but also a decreased permeate flux due to concentration polarization (Section 1.2.3) and vice versa. At high protein concentrations, the viscosity and osmotic pressure may increase considerably reducing the filtrate flow (Binabaji et al., 2015,

2016), (Section 1.2.3). A potential solution to this challenge is the adaption of the formulation to reduce the viscosity (Hung et al., 2016; J. Liu et al., 2005) or osmotic pressure (Binabaji et al., 2014). Aggregation occurring due to UF/DF can be reduced by optimizing the operating conditions for CFF (Rosenberg et al., 2009) or the ionic strength (Ahrer et al., 2006). Further challenges at high protein concentrations are the Gibbs-Donnan effect and volume exclusion which are introduced in Section 1.3.4.

1.1.3. Virus-like particles[1]

VLPs are multimeric structures that resemble viruses but lack the viral genome which makes them non-infectious (Chackerian, 2007). Non-enveloped VLPs consist of at least one structural protein, several of which assemble into capsids of one or more layers (Roy & Noad, 2009). In the case of enveloped VLPs, an additional lipid membrane layer is formed by budding from the host cell (Fuenmayor et al., 2017). Enveloped VLPs can also consist of a layer of host cell lipid membrane containing viral proteins (Lua et al., 2014). Hepatitis B surface antigen VLPs have a similar structure to enveloped VLPs but are regarded as non-enveloped VLPs (Kushnir et al., 2012). These and other structural properties, such as post-translational modification, influence the choice of the host cell for recombinant production of VLPs. Commonly used hosts are bacteria, yeast, insect, plant, or mammalian cells (Fuenmayor et al., 2017; Kushnir et al., 2012). The size of VLPs approximately ranges from 20 to 200 nm (Grgacic & Anderson, 2006; Mohsen et al., 2020). The dense and repetitive structure of antigens makes VLPs highly immunogenic and in combination with their non-infectivity potent vaccine candidates (Chackerian, 2007). The insertion of antigens or epitopes into the subunit proteins, for example by genetic fusion or chemical conjugation, leads to chimeric VLPs (Grgacic & Anderson, 2006; Roldão et al., 2010). Chimeric VLPs were developed as prophylactic and therapeutic vaccines against several diseases including infectious diseases and cancers (Mohsen et al., 2020; Roldão et al., 2010). Non-enveloped VLP-based vaccines licensed for human use protect against hepatitis B virus, HPV, hepatitis E virus, and one chimeric VLP-based vaccine protects against malaria (Lua et al., 2014; Nooraei et al., 2021). One of the licensed vaccines protecting against the severe acute respiratory syndrome coronavirus 2 has a similar structure to enveloped VLPs with viral proteins embedded in a micellar core of polysorbate 80 (Bangaru et al., 2020; Wise, 2022). Another application of non-enveloped VLPs is their

[1] Section was published in an adapted form as a review article: Hillebrandt, N., & Hubbuch, J. (2023). Size-selective downstream processing of virus particles and non-enveloped virus-like particles. *Frontiers in Bioengineering and Biotechnology 11:1192050*.

utilization as nanocarriers for the delivery of nucleic acids, peptides, or drugs (Garcea & Gissmann, 2004; Le & Müller, 2021).

In this thesis, hepatitis B core antigen (HBcAg) VLPs and chimeric HBcAg VLPs are investigated. HBcAg can serve as a backbone for chimeric VLPs (Karpenko et al., 2000; Pumpens & Grens, 2001; Whitacre et al., 2009) but also as a delivery system (Petrovskis et al., 2021; Shan et al., 2018; Strods et al., 2015; Suffian & Al-Jamal, 2022). The VLPs consist of a single layer, are non-enveloped, and can be produced in *E. coli* as a prokaryotic production system (Wingfield et al., 1995). HBcAg VLPs consist of 180 or 240 copies of the HBcAg protein and form icosahedral particles (Crowther et al., 1994).

1.1.4. Virus-like particle downstream processing[1]

The purification of non-enveloped VLPs can be subdivided into two parts (Pattenden et al., 2005). The first part is the purification of the particles as a whole which is similar to or overlapping with the purification of non-enveloped viruses and to some extent also with enveloped VLPs and viruses. These different virus-based or viral particles are referred to as virus particles (VPs) in this thesis. The second part of purification is more specific to VLPs and is optional depending on the VLP and its application. It includes dis- and reassembly *in vitro*. Another approach is performing DSP of VLP subunits in the disassembled state, followed by *in vitro* assembly (Gerstweiler, Billakanti, et al., 2021; Liew et al., 2012). This approach offers the possibility to use purification techniques applied in conventional protein purification without adaptions due to the particulate structure of VLPs. However, prevention of self-assembly during processing is required, for example by supplementing reducing, chelating, or chaotropic agents. The presence of these substances may impact or limit the unit operations available. Furthermore, VLPs consisting of different subunit proteins would require multiple downstream processes. This processing route also prevents exploiting the size difference between particles and impurities during purification (Morenweiser, 2005). Using size-selective purification techniques offers the possibility to purify different variants of a VP similarly. For example, different virus strains, chimeric VLP candidates, or therapeutic cargo within the particle could be purified using the same platform process. However, compared to mAbs, platform processes for VPs are not well established (Moleirinho et al., 2020).

1.1.4.1. Virus particles

At the end of upstream processing, the location of a VP depends on its properties in terms of the viral life cycle. VPs either remain intracellularly or are released into the extracellular space, for example by budding or cell lysis. The cell viability or the necessity of a lysis step to increase the VP yield dictate

the impurity profile, as they are directly linked to the release of host cell impurities (Moleirinho et al., 2020). Especially non-enveloped VLPs can be produced in microbial cells, such as HBcAg in *E. coli* (Schumacher et al., 2018) or HPV in *Saccharomyces cerevisiae* (Cook et al., 1999), usually requiring cell lysis. Typical process-related impurities resulting from host cells are proteins, nucleic acids, and cell debris. Product-related impurities are aggregated VPs, fragmented VPs, or empty viral vectors (Gagnon, 2009). Co-packaged host cell DNA and non-infectious or empty particles are considered product-related impurities in the case of viral vectors (European Medicines Agency Committee for Advanced Therapies (CAT), 2018). Further considerations for product-related impurities of non-enveloped VLPs are reviewed in Section 1.1.4.2. This section focuses on the removal of process-related impurities which is usually performed early in DSP.

Table 1.1 lists recently published DSP approaches for a variety of VPs. It provides an overview of state-of-the-art strategies with the potential for non-enveloped VLP purification, even though not all listed VPs are non-enveloped VPs or VLPs. A benchmark for host cell DNA of continuous cell lines according to the European Pharmacopoeia is a reduction to a maximum of 10 ng per vaccine dose to minimize tumorigenic potential (Council of Europe, 2017). The reduction of host cell nucleic acids in VP purification is often performed enzymatically by nucleases at the end of upstream processing or early in DSP. Nuclease application is present in almost all processes listed in Table 1.1 and in older purification processes such as for HPV VLPs (Cook et al., 1999). However, nucleases require specific conditions for optimal activity and thus temperature, pH, or ion composition may have to be adapted. Especially for high nucleic acid burden after cell lysis, efficient processing may require a trade-off between incubation time and product loss due to instability at the chosen conditions (Kawka et al., 2021). However, also short processing within 30 min, at room temperature, and without product loss was demonstrated (Lothert, Pagallies, et al., 2020). Nevertheless, even for long incubation times, nucleic acid removal was observed to be incomplete (Kawka et al., 2021; Lothert, Pagallies, et al., 2020; Weigel et al., 2014). At a large production scale, the use of nuclease and required conditioning steps may considerably increase production costs. Nuclease removal during further DSP is another important consideration for patient safety. For gene therapy applications, the removal of nucleases is a crucial step as it prevents the digestion of target nucleic acids.

The capture step, at the beginning of the purification train, aims to remove most of the process-related impurities. For chromatographic separation, highly selective affinity ligands are available, for example, protein A for mAbs.

However, for VPs, the number of commercially available affinity ligands is small or non-existent requiring costly and custom-made solutions. Alternatives for VPs are separations based on size promising universal processing independent of strain, construct, or candidate. Additionally, size-selective separation is beneficial due to the large size differences between VPs and common impurities. This is also reflected in Table 1.1 in which filtration, steric exclusion chromatography (SXC), SEC, multimodal size-exclusion chromatography (mmSEC), and precipitation are frequently used. These techniques are highlighted in the following.

In DSP of VPs, CFF is commonly used in the form of UF/DF and for purification purposes as indicated by Wolff & Reichl (2011) and in Table 1.1. This contrasts with the mAb platform process, where UF/DF is mainly applied for formulation purposes (Section 1.1.2). VPs are either retained by the membrane and smaller impurities (for example host cell proteins and DNA) are depleted or larger particles (for example cell debris or aggregates) are retained and VPs permeate through the membrane (Grzenia et al., 2008; Wickramasinghe et al., 2005). UF is used as an alternative to ultracentrifugation (Peixoto et al., 2007; Reiser, 2000). Ultracentrifugation, both density gradient and continuous, is generally considered to be poorly scalable, costly, time-consuming, and requires an additional buffer exchange in case of density gradients (Ladd Effio & Hubbuch, 2015; Moleirinho et al., 2020; Morenweiser, 2005; Nestola et al., 2015; Vicente, Roldão, et al., 2011; Wolff & Reichl, 2011). Carvalho et al. (2019) showed that DSP purely using filtration techniques is more efficient in terms of process duration and buffer consumption when compared to ion exchange chromatography and SEC, however with the drawback of low DNA removal.

SEC separates molecules according to their ability to penetrate the pores of porous resin beads within a column. Therefore, larger particles are excluded from either all or some of the pores depending on the pore and particle size. With decreasing size, solutes diffuse into an increasing fraction of the pores leading to a longer residence time in the column. SEC thus has a high selectivity for the separation of VPs and host cell impurities, and is mostly independent of the liquid phase conditions (Gagnon, 2009). SEC with pore sizes that exclude VPs enables their elution in the void volume of the column while impurities elute later. This enables higher flow rates, shorter columns, and higher loads, reducing some of the drawbacks in conventional protein SEC (Gagnon, 2009). However, SEC leads to dilution and is limited by restricted loading volumes, especially for separation problems with similar size magnitudes, such as VPs and their aggregates. SEC thus benefits from reduced

Table 1.1. Examples of recently published downstream processes (recovery and purification) for VPs. If the recovery steps do not contain a lysis step, culture supernatants were processed.

VP	Type	Host cell	Recovery	Purification	Reference
Adeno-virus	Non-env.	A549	Lysis Nuclease MF_d MF_d	UF/DF AEX UF/DF SEC	(Moleirinho et al., 2018)
HBcAg VLP	Non-env.	*E. coli*	Lysis Centrifug.	AMS prec. Disassembly Nuclease imAC Reassembly	(Y. Zhang et al., 2021)
Hepatitis C virus	Env.	Huh7.5	MF_d MF_d	UF Inactivation Nuclease SXC_m $psAC_m$	(Lothert, Offersgaard, et al., 2020)
Influenza A virus	Env.	MDCK	MF_m Nuclease Inactivation MF_m	SXC_m $psAC_m$	(Bissinger et al., 2021)
Influenza A VLP	Env.	High five	Nuclease MF_d MF_m	UF/DF UF/DF	(Carvalho et al., 2019)
Lentiviral vector	Env.	HEK293	Nuclease MF_d	UF/DF AEX_m	(Valkama et al., 2020)
Measles virus vector	Env.	Vero	MF_d	Nuclease mmSEC UF/DF	(Steppert et al., 2022)
Orf virus	Env.	Vero	Lysis MF_d MF_d	Nuclease SXC_m mmSEC	(Lothert, Pagallies, et al., 2020)
Adeno-associated virus	Non-env.	HEK293	MF_m	UF Nuclease Heat prec. AMS prec. AEX UF SEC	(Tomono et al., 2018)
Zika/ Yellow fever VLP	Env.	HEK293	MF_m	AEX mmSEC	(Lima et al., 2019)

Abbreviations: AMS, ammonium sulfate; centrifug., centrifugation; env., enveloped; imAC, immobilized metal affinity chromatography; MF, microfiltration; mmSEC, multimodal size-exclusion chromatography; prec., precipitation; psAC, pseudo affinity chromatography; SXC, steric exclusion chromatography. For abbreviations of the host cells, refer to the respective reference. Subscripts: d, depth filtration; m, membrane (filtration).

process volumes toward the end of DSP as shown in Table 1.1 and other studies (Peixoto et al., 2007; T. Rodrigues et al., 2007; Tomono et al., 2016).

Next to SEC as a conventional chromatographic technique for VP purification (Gagnon, 2009), modern mmSEC (commercially available as Capto Core 400/700 by Cytiva) is increasingly applied in recent publications [Table 1.1 and (Reiter et al., 2019; Weigel et al., 2014)]. MmSEC is based on the core-shell bead technology where the core with multimodal ligands is surrounded by an inert size-restricting shell. This technology enables the binding of smaller impurities and recovery VPs in the flow-through. The drawback of mmSEC is that the required capacity is determined by the impurity content, not the target species content. This property makes it more attractive in later process stages with a lower impurity burden, for example during polishing.

Another chromatographic technique that is beneficial for the purification of VPs and larger proteins is SXC (J. Lee et al., 2012). Here, the addition of polyethylene glycol (PEG) to the VP solution increases the free energy of the system. The increase in free energy is attributed to the steric exclusion of PEG molecules from the VP surface and other surfaces leading to an energetically unfavorable discontinuity in PEG concentration. This excluded volume effect is highly correlated to the VP or protein hydrodynamic radius but is also affected by other solute and solvent properties (J. Lee et al., 2012). The association of VPs with each other and hydrophilic surfaces reduces the free energy, which is thermodynamically more favorable. Using monolith columns (J. Lee et al., 2012) or membranes (Marichal-Gallardo et al., 2017) as stationary phases allows for the binding and elution of VPs by increasing and decreasing the PEG concentration in the mobile phase, respectively. In addition to the examples in Table 1.1, it is applied as a capture step for adeno-associated viruses achieving a high recovery (Marichal-Gallardo et al., 2021). The advantages of SXC are binding and elution under native/any conditions only requiring the addition of PEG as well as low costs and good scalability using membranes (Marichal-Gallardo et al., 2017).

Purification of VPs using PEG precipitation underlies similar principles as SXC (J. Lee et al., 2012). As for SXC, larger proteins or particles tend to precipitate earlier than smaller species at identical conditions (Rothstein, 1994). Besides using non-ionic polymers such as PEG, protein precipitation is performed by increasing the salt concentration (salting-out), for example using ammonium sulfate as a precipitant (Wingfield, 1998). Salting-out is dominated by a preferential exclusion of the precipitant from the hydrated protein surface leading to self-association and precipitation (Timasheff & Arakawa, 1988; Wingfield, 1998). Precipitation is usually applied for capturing at the beginning of DSP. Examples are the precipitation of norovirus VLPs using PEG

(Koho et al., 2012) or precipitation of different HBcAg VLP candidates (Schumacher et al., 2018; Y. Zhang et al., 2021) and adeno-associated virus strains using ammonium sulfate (Tomono et al., 2016, 2018).

Apart from size-selective separations, heparin and sulfated cellulose are applied as adsorbers for (pseudo) affinity chromatography. Both have a similar molecular structure and were shown to preferentially bind certain VPs (Opitz et al., 2007, 2009). Heparin ligands were applied for the separation of human immunodeficiency virus-1 gag VLPs and extracellular vesicles (Reiter et al., 2019) as well as HPV VLP purification (Kim et al., 2010). Sulfated cellulose membrane adsorbers were used for pseudo affinity capture of influenza virus (Opitz et al., 2009; Weigel et al., 2016) and VLPs (Carvalho et al., 2018) as well as for polishing of hepatitis C and influenza virus (Table 1.1). Further chromatography types are also used where AEX is often applied for enveloped (Table 1.1) and non-enveloped VPs such as adenovirus (Kawka et al., 2021), norovirus VLPs (Koho et al., 2012), and HPV VLPs (Cook et al., 1999). A potential disadvantage of ion exchange chromatography is the elution at a high ionic strength or a different pH, which might lead to VP aggregation or instability and thus requires optimization for each new strain or candidate. Compared to membranes and monoliths, bead-based bind-elute chromatography of VPs often suffers from low dynamic binding capacities due to size-exclusion and low diffusion coefficients (Gagnon, 2009).

Regarding formulation, an advantage of VLP vaccines is that strategies of conventional protein therapeutics can be applied, and no individual stabilization strategy must be developed as for some live, attenuated, or bacterial vaccines (Jain et al., 2015). In contrast to mAbs, for example, VLP concentrations in vaccine products are usually below 0.1 gL^{-1} and contain additional adjuvants to stimulate the immune response (Lua et al., 2014). Viral vectors for gene therapy applications are formulated similarly to other biopharmaceuticals and in the same concentration range as VLP vaccines (G. A. Rodrigues et al., 2019) but do not contain any adjuvants. In terms of processing, formulation is performed in combination with polishing by SEC (Dormond et al., 2010; Merten et al., 2011; Moleirinho et al., 2018; Peixoto et al., 2007) or UF/DF (Carvalho et al., 2019; Liew et al., 2012; Moreira et al., 2021; Valkama et al., 2020; Wagner et al., 2014) as for mAbs and other biopharmaceuticals.

1.1.4.2. Non-enveloped VLPs

As described above, non-enveloped VLPs can be produced as subunits, purified, and assembled or first purified as a whole, optionally disassembled into subunits, and subsequently reassembled. This thesis and section focus on

the latter processing route as it enables to exploit VP size for purification as mentioned in Section 1.1.4.1. This route is possible due to the spontaneous self-assembly of VLPs in host cells, even in prokaryotic ones such as *E. coli* (Kushnir et al., 2012). However, *in vivo* assembly may lead to malformed VLPs (Roldão et al., 2012), and *in vitro* dis- and reassembly were shown to improve VLP properties such as immunogenicity and stability (Mach et al., 2006; Q. Zhao, Allen, et al., 2012; Q. Zhao, Modis, et al., 2012). Furthermore, this process sequence enables to remove entrapped impurities (Link et al., 2012; Mohsen et al., 2018; Strods et al., 2015; Vicente, Mota, et al., 2011). For gene therapy applications, bound nucleic acids need to be removed to ensure product safety and free binding sites for target nucleic acids (Petrovskis et al., 2021; Strods et al., 2015).

The disassembly of non-enveloped VLPs can be achieved by changing the liquid phase conditions, for example by the addition of dithiothreitol in combination with a pH increase for HPV VLPs (Mach et al., 2006), the addition of urea or guanidine hydrochloride at low ionic strength for HBcAg VLPs (K. W. Lee & Tan, 2008; Singh & Zlotnick, 2003), or a pH increase at low ionic strength for Norwalk VLPs (Ausar et al., 2006). Liquid phase conditions for disassembly at a laboratory scale are achieved by the direct addition of substances (Zlotnick et al., 1996), by the addition of stock solutions (K. W. Lee & Tan, 2008), or by dialysis (Ausar et al., 2006; Holmes et al., 2015; Porterfield et al., 2010; Strods et al., 2015). At a larger scale, these techniques for changing liquid phase conditions have considerable disadvantages. Direct addition and stock solutions of chaotropic agents (urea and guanidine hydrochloride) may lead to local concentration peaks and subsequent unfolding of proteins (Singh & Zlotnick, 2003). On the other hand, stock solutions with a lower concentration result in dilution and large process volumes. Alternatives for buffer exchange at a constant volume are dialysis and DF. Compared to DF, dialysis leads to long processing times (Phillips & Signs, 2004) and high buffer consumption. Another option is pelleting the target protein in form of inclusion bodies (Bin Mohamed Suffian et al., 2017) or by precipitation (Y. Zhang et al., 2021) with subsequent re-solubilization at disassembly conditions. However, pelleting the target protein by centrifugation was shown to entrap impurities and leads to longer re-solubilization times due to floc compaction when compared to DF-based processing (Hammerschmidt et al., 2016).

At a laboratory scale, the purification of the disassembled VLP subunits is often performed by SEC (Schumacher et al., 2018; Strods et al., 2015) or poly-histidine tags with corresponding affinity chromatography (Middelberg et al., 2011; Y. Zhang et al., 2021). However, SEC has limited scalability and affinity

tags may lead to undesired alterations in the protein structure or require subsequent removal of the tag. Other (chromatographic) separations, for example ion exchange, are also conceivable, when compatible with disassembly agents as mentioned above. (Strods et al., 2015) suggested and applied alkaline hydrolysis of nucleic acid impurities which, however, requires sufficient stability of the subunit proteins.

VLP reassembly is usually initiated by reversing the disassembly conditions, hence by increasing ionic strength, decreasing pH to the neutral range, or removing chaotropic or reducing agents (Mach et al., 2006; Porterfield et al., 2010; Ren et al., 2006; Wingfield et al., 1995; Y. Zhang et al., 2021). For gene therapy applications, reassembly can be induced by the addition of nucleic acids which are subsequently encapsulated similarly as in natural virus assembly (Petrovskis et al., 2021; Porterfield et al., 2010; Strods et al., 2015). Compared to disassembly, reassembly was already investigated in the frame of DF providing a scalable process and the opportunity to improve VLP yield by controlled buffer exchange (Liew et al., 2012). Furthermore, a process monitoring approach was developed to monitor product and process properties during DF-based VLP reassembly (Rüdt et al., 2019).

1.2. Cross-flow filtration in biopharmaceutical downstream processing

This section introduces the principles of CFF with regard to biopharmaceutical DSP and demonstrates its capabilities by highlighting relevant applications and considerations for this thesis. The aim of filtration is either solid-liquid separation or the separation of solutes according to their size, hence their ability to permeate the filter. Filtration can be categorized by multiple properties such as filter type, excluded size, flow configuration, or process configuration, which are covered in the following sections.

1.2.1. Filter type

Membranes are commonly utilized as filter media for surface filtration which mainly relies on surface sieving or straining. In depth filter media, straining occurs within the pores over the entire depth in combination with surface interactions between particles and the filter media matrix. The principles of surface and depth filtration are illustrated in Figure 1.1. Details on principles and applications of depth filtration, for example for initial clarification, can be found elsewhere (Nejatishahidein & Zydney, 2021). This thesis focuses on membrane filtration. Commonly used membrane materials are composites based on cellulose or polyethersulfone, which were developed to achieve low protein adsorption (van Reis & Zydney, 2007). Currently available membrane modules are designed to enable a linear scale-up due to the availability of modules with varying membrane area but identical material, fluid dynamics

as well as system and module geometry (van Reis, Goodrich, Yson, Frautschy, Dzengeleski, et al., 1997). An additional option is to increase the number of modules by connection in parallel giving additional flexibility in membrane area.

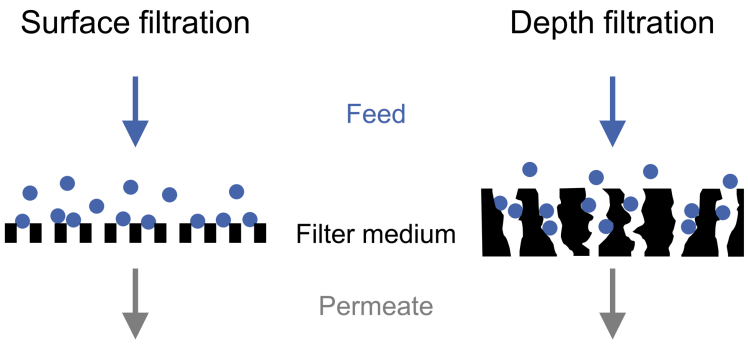

Figure 1.1. Schematic illustration of filter types. Surface (membrane) filtration (left) and depth filtration (right).

1.2.2. Excluded size

The excluded size during a filtration process is determined by the pore size of the membrane. For biopharmaceutical DSP, microfiltration and UF are commonly applied as schematically illustrated in Figure 1.2. Microfiltration refers to filtration using membranes with pore sizes from 0.05 to 10 µm (van Reis & Zydney, 2007). Surface (membrane) microfiltration in cross-flow mode is applied for solid-liquid separation after harvest and after cell lysis to retain cells and cell debris, respectively (Schlaeppi et al., 2006; van Reis et al., 1991). An advantage of clarification using 0.2 µm membrane filtration over centrifugation is that no additional filtration for the removal of submicron particles is required (H. F. Liu et al., 2010). Microfiltration from 0.1 to 0.22 µm in normal-flow mode is the standard technique for sterile filtration (Sundaram et al., 1999). Microfiltration is also used for the separation of viruses from smaller or larger impurities depending on the chosen pore size (Wickramasinghe et al., 2005). Another solid-liquid separation application is the concentration and wash of precipitate (Burgstaller et al., 2019; Devereux & Hoare, 1986; Dutra et al., 2020; Venkiteshwaran et al., 2008). Further examples of integrated aspects of microfiltration, such as alternating TFF and precipitation, are reviewed in Section 1.3.1.

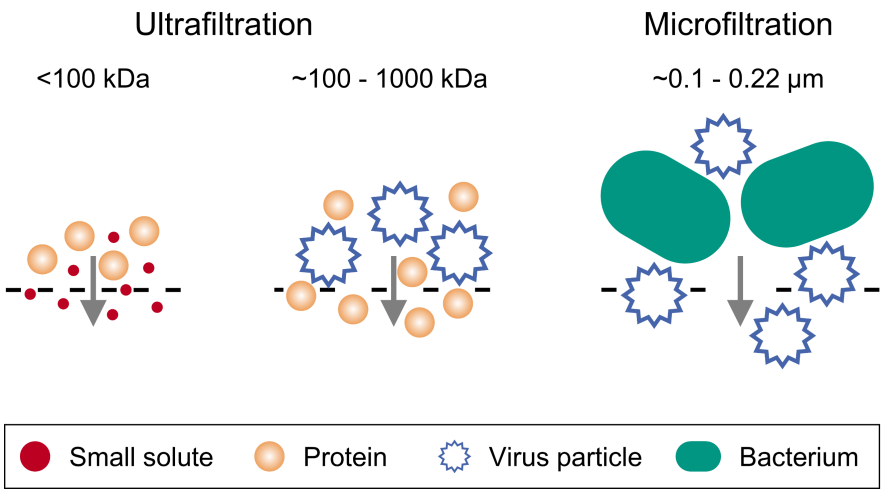

Figure 1.2. Schematic illustration of the excluded size in bioprocess filtration and exemplary retained/permeating solutes. Two molecular weight cut-off ranges are shown for ultrafiltration (left and center) as well as one pore size range for microfiltration (right). Salt and buffer molecules are referred to as small solutes.

Compared to the retention of particles in microfiltration, pore sizes and retention in UF are on a molecular level with pore sizes ranging from 1 to 20 nm. UF membranes are rated by the molecular weight cut-off which is often defined as 90% retention of molecules having the respective molecular weight. Consequently, membranes should be selected with a safety margin or ideally qualified experimentally to find the desired trade-off between permeability and retention characteristics (Mehta & Zydney, 2005). The separation of different proteins by UF is regarded as limited to a more than 10-fold size-difference (Cherkasov & Polotsky, 1996; van Reis, Gadam, et al., 1997). However, cascade configurations and identification of operating conditions by mathematical descriptions, known as the high-performance TFF approach, allow for separations with a higher resolution (Ghosh, 2003; van Reis, Gadam, et al., 1997). The resolution of membrane separations of two proteins, referred to as selectivity, is expressed by the ratio of their sieving coefficients (van Reis & Saksena, 1997). The intrinsic sieving coefficient

$$S = \frac{c_{\mathrm{Perm}}}{c_{\mathrm{Mem}}} \tag{1.1}$$

determines the partitioning of a partially retained solute based on its concentration at the membrane surface c_{Mem} and in the permeate c_{Perm}. Note that the intrinsic retention coefficient is defined as $R = 1 - S$ and apparent coefficients of S or R are calculated using the bulk concentration c_{Bulk} instead of c_{Mem}.

1.2.3. Flow configuration

CFF describes the mode of operation for filtration processes in terms of flow configuration. In normal-flow filtration or dead-end filtration, the feed stream is directed perpendicular to the membrane surface (Figure 1.3). In CFF, the feed stream is directed along the membrane surface while the filtrate (permeate) permeates perpendicularly through the membrane (Figure 1.3). The non-permeating fraction of the feed stream is referred to as retentate. In conventional CFF, the retentate is recycled back into a stirred feed tank. An alternative is single-pass TFF which enables in-line filtration at the cost of a larger membrane area to achieve comparable permeate flux (Dizon-Maspat et al., 2012).

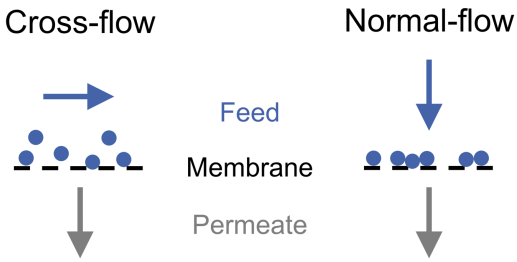

Figure 1.3. Schematic illustration of flow configurations in filtration. Cross-flow filtration (left) and normal-flow filtration (right).

The pressure difference through the membrane, the transmembrane pressure (TMP), is the filtration driving force. A common equation to describe the resulting permeate flux is Darcy's law (Jönsson & Trägårdh, 1990)

$$J = \frac{\Delta p_{\mathrm{Mem}}}{\eta\, R_{\mathrm{h}}} \tag{1.2}$$

where η is the dynamic viscosity of the permeate and R_{h} is the hydraulic resistance of the membrane. The TMP is defined as

$$\Delta p_{\mathrm{Mem}} = \frac{p_{\mathrm{Feed}} + p_{\mathrm{Ret}}}{2} - p_{\mathrm{Perm}}\,, \tag{1.3}$$

where p_{Feed}, p_{Ret}, and p_{Perm} indicate the feed, retentate, and permeate pressure respectively. The volumetric permeate flow rate Q_{Perm} is commonly normalized by the filter area A_{Mem} leading to the permeate flux

$$J = \frac{Q_{\mathrm{Perm}}}{A_{\mathrm{Mem}}}\,. \tag{1.4}$$

A high permeate flux is desirable to achieve high productivity in the filtration process. For protein or particle solutions, Equation 1.2 is usually only applicable up to a certain TMP, depending on the filter and feed characteristics. Convective flow through the membrane and retention of solutes leads to an increasing accumulation toward the membrane surface

which is referred to as concentration polarization and shown in Figure 1.4. The concentration polarization layer is considered a hydraulic resistance reducing the permeate flux (Blatt et al., 1970).

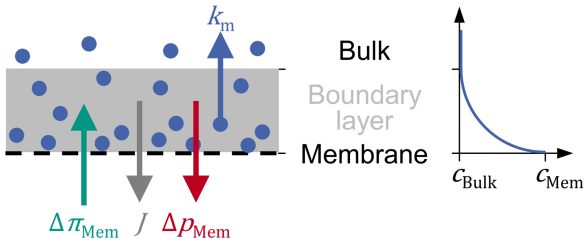

Figure 1.4. Schematic illustration of concentration polarization (left) and corresponding concentration profile perpendicular to the membrane (right).

There are several models to describe the permeate flux during filtration processes, which are reviewed elsewhere (Quezada et al., 2021). Two basic models are briefly introduced here to provide an overview of relevant mechanisms. The first is the concentration polarization model (Blatt et al., 1970) based on a one-dimensional stagnant film model

$$J = k_m \ln\left(\frac{c_{Mem} - c_{Perm}}{c_{Bulk} - c_{Perm}}\right), \tag{1.5}$$

where the mass transfer coefficient k_m is defined as the ratio of the diffusion coefficient and boundary layer thickness (D/δ). Note that Equation 1.5 assumes a steady state. Both k_m and c_{Mem} cannot be easily measured and are thus determined by fitting it to experimental data or theoretical approximations (van Reis & Zydney, 2010). The validity of Equation 1.5 is limited to a low extent of concentration polarization in terms of c_{Mem}/c_{Bulk} (Zydney, 1997). The experimental observation that J has an upper limit and does not further increase with Δp_{Mem} was explained by the formation of a gel layer due to the solubility limit or closest packing of the retained solutes (Blatt et al., 1970). The limiting concentration $c_{Mem} = c_{Gel}$ is referred to as gel concentration in this gel polarization model. An increasing c_{Mem} also leads to a notable osmotic pressure difference across the membrane $\Delta\Pi_{Mem}$, especially for solutes smaller than 100 kDa (Wijmans et al., 1984). The osmotic pressure difference counteracts the TMP (Figure 1.4) and can be described by the osmotic pressure model (Kedem & Katchalsky, 1958) as

$$J = L_p \left(\Delta p_{Mem} - \sigma_O \, \Delta\Pi_{Mem}\right) \tag{1.6}$$

where L_p is the total hydraulic permeability of the membrane and equals $1/(\eta \, R_{Mem})$. Furthermore, σ_O is the osmotic reflection coefficient of the retained solute where $\sigma_O = 1$ is full retention and $\sigma_O = 0$ is no retention. Note that Equation 1.6 in the presented form is only valid for a single type of

retained solute to which $\Delta\Pi_{\mathrm{Mem}}$ and σ_{O} refer. As mentioned above, the effects of osmotic pressure and concentration polarization may be differently pronounced, for example for varying protein concentration during UF (van Reis & Zydney, 2010). To overcome the limitations of the two basic models, many extensions, adaptions, or combinations as well as other modeling approaches have been reported (Quezada et al., 2021). In a recent example (Binabaji et al., 2015), an extended concentration polarization model was combined with the osmotic pressure model to account for back-filtration (negative permeate flux) occurring during protein UF when $\Delta\Pi_{\mathrm{Mem}} > \Delta p_{\mathrm{Mem}}$ at high c_{Mem} (Binabaji et al., 2015). The concentration polarization model was proportional to the gradient in chemical potential and included a concentration dependency of the viscosity as well as a description of the axial pressure drop (along the flow channel in the membrane module).

1.2.3.1. Practical implications

As indicated by the concentration polarization model (Equation 1.5), the convective transport of solutes from the bulk solution towards the membrane surface is counteracted by the back-transport of solutes into the bulk solution. Achieving a high flux requires therefore high mass transfer coefficients which can be achieved by CFF. The cross-flow velocity parallel to the membrane surface results in a shear rate sweeping solutes from the boundary layer out of the membrane module. In addition to shear rate, back-transport depends on particle size whereas Brownian diffusion is dominant for particles in the nanometer range, and shear-induced diffusion as well as inertial lifting are increasingly pronounced for micrometer-sized solutes (Davis, 1992). Spacer nets (screens) in the flow channel additionally disturb the boundary layer leading to an increased mass transfer coefficient and permeate flux (da Costa et al., 1991; da Costa & Fane, 1994; Subramani et al., 2006).

Another reason for flux reduction is membrane fouling which is loss of permeability due to solute/protein adsorption, deposition on the surface, or pore blockage (Belfort et al., 1993; Meireles et al., 1991). Fouling can be reduced by CFF and a high ratio of feed to permeate flux (low conversion rate) which both aim to operate at a low degree of concentration polarization (Marshall et al., 1993). A low conversion rate is also important to consider for retained target species with a low solubility or sensitive to aggregation at higher concentrations.

1.2.4. Process configuration

Regarding the process configuration, filtration can be performed in regular or DF mode as shown in Figure 1.5 for CFF. In regular mode, also referred to as UF or microfiltration depending on the pore size, the concentration of

retained solutes increases due to the removal of solvent through the permeate stream.

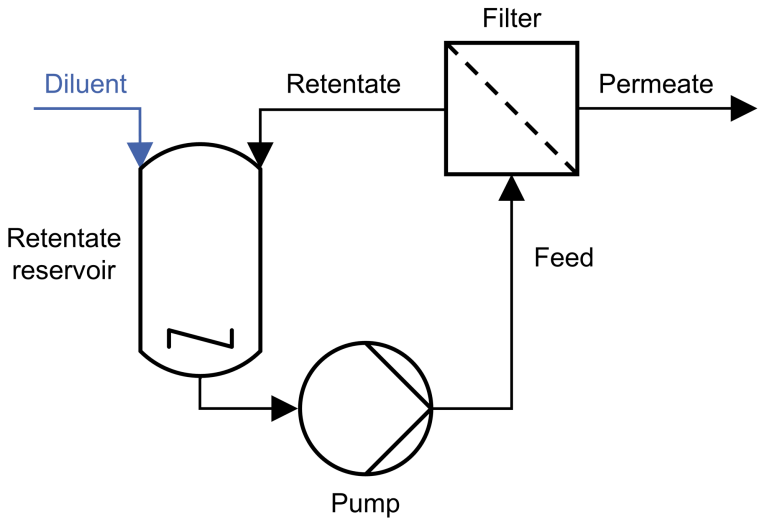

Figure 1.5. Schematic illustration of filtration process configurations. The regular cross-flow filtration setup is shown in black. The extension for the diafiltration (DF) configuration is highlighted in blue, diluent is added to the retentate reservoir.

In DF mode, a new solvent is added to the retentate to replace the volume of the permeate leading to an exchange of the solvent. The new solvent can be added continuously or discontinuously and is often referred to as DF buffer or diluent. In constant-volume DF, the flow rates of the added solvent and the permeate are identical, which keeps the concentration of the retained solutes constant. The concentration of a species in the retentate during DF is defined as

$$c = c_0 \exp(-v_{\mathrm{DV}}\, S_{\mathrm{Mem}}) \tag{1.7}$$

where c_0 is the concentration of the species at the beginning of the DF and v_{DV} is the number of DF volumes which is the added solvent volume divided by the initial volume. Considering a non-retained solute, such as salt ions or buffer molecules during buffer exchange, the assumption of $S_{\mathrm{Mem}} = 1$ is justified (Equation 1.1). Furthermore, Equation 1.7 can be applied to estimate the degree of depletion of impurities that are smaller than the pore size of the membrane.

In the case of filtration-based wash steps of cells or precipitate, countercurrent multi-stage DF is an efficient option for implementation (Z. Li et al., 2019; Nambiar et al., 2018). The retentate is transferred to sequential filtration stages while the permeate of a stage is used as the DF buffer for the preceding state. This approach reduces buffer consumption at the cost of more complex process setups and equipment (Nambiar et al., 2018). Buffer

consumption during DF can also be reduced by operating at lower volumes and thus higher concentrations, for example, achieved by a preceding concentration step as discussed in Section 1.1.2.

1.2.5. Shear stress

A point to consider when increasing the cross-flow rate to increase the permeate flux is shear stress that can damage the target species. Although it was demonstrated, that the exposition of proteins to air-liquid interfaces is the major contributor to the formation of undesired aggregates in CFF (Bee et al., 2009; Callahan et al., 2014), shear stress induced by equipment (Arunkumar et al., 2016) and operating condition (Rosenberg et al., 2009) were shown to be influencing factors. Contrarily, other authors did not observe any impact of shearing on the formation of aggregates (Ahrer et al., 2006). For CFF of soy protein precipitate with high shear rates, a breakup of precipitate was expected to impact the filtration performance (Devereux & Hoare, 1986).

For viruses and VLPs, shear is often mentioned to cause instability of particles. However, actual primary literature is scarce and investigations of shear forces are often not or cannot be decoupled from potentially biasing effects. These effects may be air-liquid interfaces during mixing, micro cavitation during pumping, or changing liquid phase conditions such as osmotic pressure during ultracentrifugation. Enveloped measles virus showed sensitivity in terms of infectivity to shear stress generated in a CFF membrane module while pumping alone had only a minor impact on infectivity (Loewe et al., 2019). In the same study, low shear rates (cross-flow rates) showed low recoveries attributed to adsorption to the membrane. The infectivity of rod-shaped, enveloped baculovirus was not considerably affected by pumping- and stirring-induced shear (Michalsky et al., 2008). Prolonged vortex mixing, on the other hand, led to degradation of measles and mumps viruses (Sviben et al., 2016). Compared to CFF, a reduced particle recovery and infectivity of measles and mumps viruses was attributed to shear forces in ultracentrifugation without sucrose or cesium chloride addition (Sviben et al., 2016). For non-enveloped adenoviruses, moderate shear stress was found to resolve minor aggregation but high shear rates led to viral activity loss (Morgan et al., 2020).

From a process development perspective, the cross-flow rate needs to be optimized to achieve a trade-off between product recovery and permeate flux. Low cross-flow rates reduce the risk of shear-induced product degradation while leading to a higher degree of concentration polarization and vice versa. Concentration polarization, in turn, leads to a higher local concentration at the membrane surface that potentially promotes unintended product

adsorption, aggregation, or precipitation. For products that are sensitive to both, shear stress and high concentrations, the membrane area can be increased for a given batch size and permeate flow rate. In this case, the permeate flux and thus concentration polarization are reduced without increasing shear stress, however, at the cost of a larger membrane.

1.2.6. Applications

CFF is a promising technique to separate species with large size differences, for example, VPs and host cell impurities or proteins and small molecular solutes, such as salt ions, buffer molecules, or other excipients. Interestingly, processes that employ purely filtration-based separations achieve high yields and purity for small proteins (Mayani et al., 2010) and VLPs (Carvalho et al., 2019).

Purification of a variety of viruses and VLPs was successfully achieved by CFF (Carvalho et al., 2019; Grzenia et al., 2008; Peixoto et al., 2007; Wickramasinghe et al., 2005) (Section 1.1.4). Virus filtration for the removal of undesired viruses in smaller protein biopharmaceuticals follows similar principles and is performed with similar equipment and procedures (van Reis & Zydney, 2007) but is out of the scope of this thesis.

CFF with UF membranes is frequently applied for concentration increase and buffer exchange in DF mode (Nestola et al., 2015; Pfister et al., 2018; Zydney, 2020). The purpose is to adjust the protein concentration and the liquid phase conditions, such as pH, ionic strength, excipients, or type of buffer molecule. During DSP, this step either aims for intermediate conditioning of the process solution (Hekmat et al., 2015) or to achieve the desired storage solution conditions (Ambrožič et al., 2021; Ladwig et al., 2020; Peixoto et al., 2008). The latter is also referred to as the formulation step as described in Section 1.1.2. Formulations with high protein concentrations are desirable to reduce dosage volumes. However, producing highly concentrated formulations by UF/DF also comes with challenges which are protein aggregation, high viscosity, as well as concentration and pH non-idealities (Holstein et al., 2020). The latter arise due to the Gibbs-Donnan effect and volume exclusion, these phenomena are further explained in Section 1.3.4.

Another application of CFF is the separation of solvents or residual small and macro molecular impurities from proteins after conjugation reactions (Gates et al., 2020; Molek & Zydney, 2007). Inclusion body refolding by DF enables a controlled buffer exchange into renaturation conditions and processing at higher protein concentrations leading to higher yield, smaller reaction tanks, and higher productivity (Ryś et al., 2015; D. Zhao et al., 2014). Similarly, the *in vitro*-assembly of VLPs was mediated by DF to remove assembly-inhibiting

agents and/or to add assembly-promoting salt ions (Liew et al., 2012; Rüdt et al., 2019).

1.3. Process development tools

In biopharmaceutical DSP, several tools for process development and optimization are available. The tools covered in this thesis are process integration, HTS, PAT, and mechanistic modeling. The following sections introduce the mentioned tools and provide an overview of relevant research and applications with regard to CFF. In accordance with the case studies performed in this thesis, Sections 1.3.1 to 1.3.3 place emphasis on the purification of non-enveloped VLPs and Section 1.3.4 on the formulation process step of mAbs.

1.3.1. Process integration

Process integration refers to the connection or combination of two or more unit operations aiming for process intensification, hence improving yield, productivity, and cost-effectiveness (Schügerl & Hubbuch, 2005). To achieve this goal, the selection of unit operations with regards to the separation problem and interconnectivity is crucial (Nfor et al., 2008). Process integration is often motivated by the development of continuous processes, which require a seamless and end-to-end realization from cultivation to formulation (Konstantinov & Cooney, 2015; Rathore et al., 2015). Nevertheless, it has been shown that even the implementation of partly integrated processes or integrated batch steps already reduces equipment footprint and processing time due to the elimination of hold steps (Warikoo et al., 2012; J. Zhang et al., 2017). For process integration, unit operations can either be I) connected modularly with intermediate conditioning or surge vessels, II) adapted to enable a seamless connection, or III) merged into an overlapping operating space (Rathore et al., 2018). The latter ideally reduces the number of process steps and thus the target protein loss, footprint, and processing time. To synchronize the operating condition of integrated units, for example flow rates, PAT is required for process monitoring and control (Chopda et al., 2021; Pfister et al., 2018; Rathore et al., 2018). PAT is covered in Section 1.3.3.

The size-selective separation of species makes CFF a versatile unit operation, which can be easily integrated with other separation techniques. In the following, a broad range of examples is provided to demonstrate the suitability of CFF for process integration. A prominent example of the integration of CFF is the alternating tangential flow system for integrated cell (debris) retention and clarification during perfusion cultures (Clincke et al., 2013; Coronel et al., 2019; Khanal & Lenhoff, 2021; Warikoo et al., 2012). For the same purpose, classical CFF can be applied as an alternative to the alternating tangential flow

system (Clincke et al., 2013; Coronel et al., 2019; Karst et al., 2016). These systems provide an end-to-end approach for process integration by connecting upstream and DSP (Godawat et al., 2015). Vogel et al. (2002) integrated clarification and adsorption by an affinity membrane using a rotating disk filter. The special design allows for controlled shear rates independent of any operating pressures and therefore high cell viability with the potential for perfusion culture implementation. Furthermore, CFF was utilized for phase separation of an aqueous two-phase system which also integrated the clarification and purification of mAbs (Kruse et al., 2019). Single-pass TFF is employed for in-line concentration increase (Dizon-Maspat et al., 2012) or buffer exchange by DF (Rucker-Pezzini et al., 2018) to connect unit operations and thus enable integrated processing. According to the abovementioned categorization, Gomis-Fons et al. (2019) implemented a hybrid approach by integrating multiple chromatography steps and a filtration step using a single chromatography device. This study showed that an integrated design of the process could reduce the required equipment and processing time considerably. Precipitation and CFF were integrated for the purification of antibodies with the advantage of an efficient precipitate wash and re-dissolution (Burgstaller et al., 2019; Dutra et al., 2020; Hammerschmidt et al., 2016; Kuczewski et al., 2011; Z. Li et al., 2019; Venkiteshwaran et al., 2008).

For VPs, process integration is just on the rise. Mainly integration schemes that were previously applied to other biopharmaceuticals are adapted and provide useful building blocks for future process integration. For example, by implementing perfusion cell culture (Coronel et al., 2019) or by integrating clarification and capture using expanded bed adsorption (Ng et al., 2008; Yap et al., 2010) or aqueous two-phase systems (Benavides et al., 2006; Ladd Effio et al., 2015; Luechau et al., 2011). Integrated optimization of VP-specific processes was performed for a combination of nuclease treatment and membrane chromatography (Kawka et al., 2021) as well as upstream processing and UF as a first DSP step (Cruz et al., 2000). Moreover, the integration of two membrane-based chromatography steps, steric exclusion and pseudo-affinity (Bissinger et al. 2021), or the implementation of continuous SEC (Kröber et al., 2013) provide purification steps that can be easily integrated into a DSP train. Overall, innovative and VP-specific integrated process designs, especially for merged unit operations, are scarce. As mentioned in Section 1.1.4, CFF and precipitation are well-suitable, size-selective, cost-effective, and scalable separation techniques for VP capture. Combining both separation techniques using the merger approach offers the

potential for synergistic effects. Furthermore, the seamless integration of CFF and subsequent separation techniques offers further process intensification.

1.3.2. High-throughput screenings

HTS are automated, parallelized, small-scale experiments which enable faster data generation than conventional experiments (Lacki & Brekkan, 2011; Shukla et al., 2018). The screenings are usually performed in multi-well (microtiter) plates, which are compatible with robotic liquid handling stations and auto samplers of many analytical devices. At an early development stage, small-scale experiments are advantageous due to their low material consumption (Titchener-Hooker et al., 2008). During late-stage development of commercial processes, HTS are often referred to as high-throughput (HT) process development which is applied in process development, validation, and characterization (Shukla et al., 2018). HTS are regarded as an enabler technology for the Quality by Design (QbD) approach initiated by regulatory authorities (Bhambure et al., 2011; Lacki & Brekkan, 2011). QbD aims for a systematic process development away from trial-and-error testing (ICH Expert Working Group, 2009). A design space is defined in which process parameters and materials are known to provide the required quality. Additionally, critical quality attributes (CQAs) need to be defined to ensure that quality is measurable. The (multivariate) relationships between parameters and quality can be determined using prior knowledge, design of experiments methodology, and quality risk management (ICH Expert Working Group, 2009). A combination of HTS with design of experiments and qualified scale-down models provides the required data in a short time and with low material consumption (Chhatre et al., 2011; Shukla et al., 2018).

HTS are particularly beneficial for the development of CFF operations such as UF/DF, which require large amounts of material and are time-consuming at a laboratory scale (Abel et al., 2018; Fernandez-Cerezo et al., 2020; Kazemi & Latulippe, 2014). For CFF, commercial and non-commercial scale-down models are available for screening filtration parameters and their influence on filtration performance. For example, stirred (Kazemi et al., 2016; Kazemi & Latulippe, 2014) and unstirred microtiter filtration plates (Chandler & Zydney, 2004) allow for a determination of basic filtration parameters. Automated, parallel, CFF scale-down models mimic the whole process and enable the screening of protein load, fluxes, and pressures (Fernandez-Cerezo et al., 2020). For DF process steps, the aim is to change the liquid phase composition, for example during the final formulation step in DSP. Here, formulation compositions are commonly screened in advance by mixing the components in small-scale and subsequent analysis, either manually or using HT technology in multi-well plates (Capelle et al., 2007; Chaudhuri et al., 2014;

Ying et al., 2016). For this initial condition screening, filtration parameters or the impact of the filtration process on the product quality are not considered. CFF process development is then performed separately once the formulation composition is known, as it usually requires larger volumes for processing, even at a small scale. This segregation of condition screening and filtration process development enables efficient utilization of resources, especially when only small material quantities are available. Similarly, HTS of liquid phase conditions were implemented for other DSP unit operations, for example, inclusion body refolding (Berg et al., 2012; Vincentelli et al., 2009), crystallization (Klijn & Hubbuch, 2018), and precipitation (Großhans et al., 2019).

Analytical techniques that enable rapid measurements of quality attributes are a prerequisite for HTS. During the last decades, standard analytical techniques for conventional biopharmaceutical proteins were transformed into HT-compatible techniques (Lacki & Brekkan, 2011; Shukla et al., 2018). For VLPs, standard HT protein concentration measurements are also applicable and specific immunoassays can be implemented as HTS (Wenger et al., 2007). Microtiter plate-based dynamic light scattering measurements are used to pre-screen for formulation conditions with low aggregate formation (Mohr et al., 2013). Analytical SEC applying interlaced injections and a dedicated column selection was used for HT VLP aggregate determination (Ladd Effio, Oelmeier, et al., 2016). Overall and with respect to CFF-based VLP processing steps, HTS offer a potential pre-screening tool for liquid phase conditions in multi-well plates before performing more complex CFF experiments at a laboratory scale. Here, the implementation of suitable analytical techniques is crucial to obtain results efficiently.

1.3.3. Process analytical technology

PAT is a regulatory framework initiated by the U.S. Food and Drug Administration (2004) to foster innovative development and manufacturing in the pharmaceutical industry. The framework defines PAT as a tool to design, analyze, and control processes through timely analysis of CQAs. It aims for the development of well-understood processes that result in consistently high product quality. PAT was also integrated into guidelines of international regulatory agencies (ICH Q8(R2) and Q11) as a tool for QbD implementation (Chhatre et al., 2011; ICH Expert Working Group, 2009, 2012). An essential part of PAT is real-time process monitoring and control where comprehensive monitoring includes critical process parameters (CPPs) and CQAs (Rathore et al., 2010). This requires timely measurements, either by in-line, on-line, or at-line sensors with minimal and non-destructive sample preparation (U.S. Food and Drug Administration, 2004). Apart from standard univariate sensors, such

as pH, conductivity, pressure, or temperature, (multivariate) spectroscopic sensors have been applied to extract complex information on the target protein or impurities (Rolinger, Rüdt, & Hubbuch, 2020a; Rüdt, Briskot, et al., 2017). The implementation of PAT offers increased efficiency by reducing release time, product rejections, human errors, cycle times, and energy demands (U.S. Food and Drug Administration, 2004). Along with industrial interest, PAT has been an extensive research topic in the biopharmaceutical field throughout the last two decades (Rathore et al., 2010; Rathore & Kapoor, 2015; Rolinger, Rüdt, & Hubbuch, 2020a; Rüdt, Briskot, et al., 2017).

In biopharmaceutical processes, ultraviolet light (UV) spectroscopy is commonly employed to monitor the protein concentration utilizing the UV absorption of aromatic amino acids (Hansen et al., 2013; Rüdt, Briskot, et al., 2017). Concentrations of pure substances are determined by measuring the absorbance at a single wavelength and applying the Beer-Lambert 'law' (Swinehart, 1962), which is referred to as Beer's law hereafter. For process solutions containing the target protein and impurities with similar absorption properties, UV spectroscopy combined with multivariate data analysis enables the determination of component concentrations (Brestich et al., 2018; Brestrich et al., 2015; Hansen et al., 2013; Rüdt, Brestrich, et al., 2017). The mentioned studies utilized partial least squares (PLS) regression for this purpose. The PLS regression model

$$\mathbf{Y} = \mathbf{XB} + \mathbf{E}\,, \tag{1.8}$$

which is a matrix equation, that correlates UV spectra $\mathbf{X}$ with component concentrations $\mathbf{Y}$ through the regression coefficients $\mathbf{B}$. The matrix $\mathbf{E}$ contains residuals. In the UV spectra $\mathbf{X}$, absorbance values of the i wavelengths are referred to as predictor variables $\mathbf{x}_i$ (column vectors). Concentrations of each component j are response variables $\mathbf{y}_j$ (column vectors) in $\mathbf{Y}$. The rows in $\mathbf{X}$ and $\mathbf{Y}$ represent the number of observations, for example, time points. In the case of spectra, the use of PLS regression is beneficial as it can handle multiple and strongly collinear predictor variables (Wold, Sjöström, et al., 2001). Centering spectral variables to their average often eases the interpretation of the resulting PLS model, however, without scaling to prevent amplification of noise (Kessler, 2006). The PLS model approximates the latent variables, named X-scores $\mathbf{T}$, as linear combinations of $\mathbf{X}$ (Wold, Sjöström, et al., 2001). Therefore, $\mathbf{X}$ is decomposed into

$$\mathbf{T} = \mathbf{XW} \tag{1.9}$$

and $\mathbf{Y}$ into

$$\mathbf{Y} = \mathbf{UC}^{\mathsf{T}} + \mathbf{F} \tag{1.10}$$

where **U** contains the Y-scores, **C** the Y-loadings, and **F** the Y-residuals. The decomposition of **X** and **Y** is performed simultaneously while maximizing their covariance through the weight vectors in **W** (Wold, Trygg, et al., 2001). The according operations are performed by established algorithms and are described in detail elsewhere (de Jong, 1993). The X-loadings (not shown here) relate **X** to **T** analogously to Equation 1.10, which has the same form as for principal component analysis. The regression coefficients of the model are calculated as

$$\mathbf{B} = \mathbf{W}\mathbf{C}^{\top} . \tag{1.11}$$

Before applying the abovementioned equations for model calibration, it is necessary to ensure a high predictive power by determining the right model complexity. Therefore, the number of latent variables (PLS components) needs to be high enough to fit the data sufficiently but low enough to prevent over-fitting, for example of noise. The number of latent variables determines the number of variables (columns) in **C**, **T**, **U**, and **W**. A procedure to evaluate a good number of latent variables is cross validation (CV) using the cross-validated coefficient of determination

$$Q^2_{\mathrm{CV}} = 1 - \frac{PRESS}{SS} = 1 - \frac{\sum_{n=1}^{N}\sum_{m=1}^{M}(y_{n,m} - \hat{y}_{n,m})^2}{\sum_{n=1}^{N}\sum_{m=1}^{M}(y_{n,m} - \bar{y})^2} \tag{1.12}$$

as a metric (Wold, Sjöström, et al., 2001). $PRESS$ is the predictive residual sum of squares and SS is the sum of squares. For CV, each $\mathbf{y}_i$ is split into N validation groups with M data points each. For each group, the model is calibrated with the remaining data. In the validation group, $y_{n,m}$ (elements of $\mathbf{y}_i$) are measured data points, $\hat{y}_{n,m}$ are corresponding model predictions, and $\bar{y}$ is the average of all $y_{n,m}$. The coefficient of determination R^2 is calculated according to Equation 1.12 using predictions of the calibrated model after CV. High and similar Q^2_{CV} as R^2 indicate a high predictive power of the model (Wold, Sjöström, et al., 2001). The root mean square error of CV (RMSECV) is calculated as

$$RMSECV = \sqrt{\frac{PRESS}{MN}} . \tag{1.13}$$

Model validation apart from CV during calibration is performed using external data sets. Comparing Q^2 and the root mean square error of prediction of an external data set with the ones of CV allows for further validation of the model. Once the model is calibrated and validated, new spectra $\widehat{\mathbf{X}}$ can be used to predict component concentrations $\widehat{\mathbf{Y}}$ using **B** without additional off-line measurements, which are usually more complicated and/or time-consuming.

Besides concentrations of products or impurities, the (quality) characteristics of the target protein can be retrieved from UV spectra. Therefore, the derivative(s) of each spectrum (row vector in **X**) with respect to the wavelength is calculated (Ausar et al., 2006). Changes in the derived UV spectrum of proteins were shown to correlate to the solvent exposure of aromatic amino acid residues and provide information about the tertiary protein structure (Mach & Middaugh, 1994; Ragone et al., 1984).

Furthermore, light scattering sensors allow for the monitoring of protein size (Rüdt, Briskot, et al., 2017). Static light scattering refers to averaging the detected scattered-light intensity over time. Static light scattering of particles can be described by the Rayleigh ratio

$$R(\theta) = f_g\left(I_p - I_s\right) \approx K_o c \left(\frac{1}{M_w P(\theta)} + 2A_2 c\right)^{-1} \tag{1.14}$$

where f_g is a device-specific factor, I is the light scattering intensity, K_o is a physical constant dependent on refractive indices and laser wavelength λ, M_w is the particle weight-average molar mass (molecular weight), $P(\theta)$ describes scattering intensity dependent on the scattering angle θ, c is the particle mass concentration, and A_2 is the second virial coefficient (Wyatt, 1993). The subscripts p and s denote particle (solute) and solvent, respectively. At dilute conditions, ideal solute behavior is assumed and A_2 vanishes. Then, Equation 1.14 simplifies and measuring I_p (and I_s before) with a light scattering spectrometer allows for the determination of M_w when the c is known or measured by another technique (Schärtl, 2007). For particles smaller than approximately $\lambda/20$, $R(\theta)$ is independent of θ leading to $P(\theta) = 1$ (Schärtl, 2007). For larger particles, utilizing multi-angle light scattering enables the determination of the radius of gyration (root mean square radius) only based on the angular dependence without further knowledge of M_w and c (Wyatt, 1993).

In dynamic light scattering, also known as quasi-elastic light scattering, fluctuations of the light scattering intensity are measured over a time scale of ns to µs. Intensity fluctuations arise from the Brownian motion depending on the size of particles and can be analyzed using an autocorrelation function (Stetefeld et al., 2016). A mean diffusion coefficient D assuming a monomodal size distribution is retrieved from the autocorrelation function using the method of cumulants (Koppel, 1972). The particle hydrodynamic radius r_H is then calculated using the Stokes-Einstein equation

$$D = \frac{k_b T}{6\pi\eta r_H} \tag{1.15}$$

where k_b is the Boltzmann constant, T is the absolute temperature, and η is the solvent viscosity. According to the applied principles above, r_H is a light scattering intensity-weighted harmonic mean of the particle radius and is referred to as the z-average radius. The z-average radius is comparable to other size analytical techniques for monodisperse particles and biased towards larger particle sizes for polydisperse systems (Hassan et al., 2015). Considering $P(\theta) = 1$ and $A_2 = 0$, hence $R(\theta) = K_O c M_w$, the conversion of c into a particle number density ρ_n yields $I_p \sim \rho_n m_p^2$ and therefore $I_p \sim \rho_n d^6$ (Schärtl, 2007). Here, m_p is the single particle mass and d is the particle diameter.

Several monitoring approaches were recently applied to CFF as PAT tools. Rüdt et al. (2019) implemented on-line UV spectroscopy, static light scattering, and dynamic light scattering to monitor the reassembly of chimeric VLPs. Light scattering sensors enabled monitoring of the VLP assembly progress and aggregation throughout the process. UV spectroscopy was used to trace the protein concentration, the solvatization of aromatic amino acids by second derivative spectroscopy, and to calibrate a PLS model. In a similar setup, Rolinger, Rüdt, Diehm, et al. (2020) implemented in-line variable pathlength UV spectroscopy to measure high protein concentrations during UF/DF of a mAb solution. A preceding off-line determination of the A_2 (Equation 1.14) along with on-line concentration measurements enabled on-line M_w determination during high-concentration UF/DF (Rolinger, Rüdt, Diehm, et al., 2020). West et al. (2021) implemented on-line analytical SEC in a UF/DF step for mAbs to monitor the formation of high molecular weight species (aggregates) as well as excipient shifts due to the Gibbs-Donnan effect. For the same process step, Wasalathanthri et al. (2020) implemented in-line Fourier-transform infrared spectroscopy in combination with a PLS model to monitor protein and excipient concentrations. A similar approach was suggested by Ramasubramanyan et al. (2011) using Raman spectroscopy and PLS models to trace excipient concentrations. As mentioned above, spectroscopic PAT tools have already provided considerable insights into the dynamics of the reassembly step during VLP processing. Additionally, analytical SEC is a powerful size-selective analytical tool for VLP solutions and can be utilized close to the process as on- or at-line sensor.

1.3.4. Mechanistic modeling

Mechanistic models are considered parametric, white box models in contrast to empirical black box models, such as PLS regression models (von Stosch et al., 2014). Therefore, mechanistic models require a fundamental understanding of the phenomena and mechanisms they describe

mathematically. These descriptions are based on continuum equations along with conservation equations and balance conditions (Smiatek et al., 2020). Depending on the nature of the mechanistic model, parameters are determined based on theoretical knowledge, properties, and calculations or need to be calibrated experimentally using process data or dedicated analytical measurements.

Within the QbD framework, mechanistic models are another valuable tool for process development, especially to increase process understanding by linking material attributes and CPPs to CQAs (ICH Expert Working Group, 2009). During development, optimization, and validation, it may reduce laborious experiments and material consumption while it can be used for troubleshooting and model-based control during commercial manufacturing (Narayanan et al., 2020; Staby et al., 2017). Representative models of a process step or a whole process (digital twin) are hence beneficial throughout the whole lifecycle of a process. These process models combined with hardware sensors are applied as soft sensors to estimate and control variables that are otherwise more difficult to determine (Luttmann et al., 2012). PAT approaches using spectroscopic sensors with PLS models as described in Section 1.3.3 are regarded as data-driven soft sensors while model-driven soft sensors are based on mechanistic models (Luttmann et al., 2012).

In DSP, mechanistic models are applied to predict chromatographic separations (Kumar & Lenhoff, 2020), dead-end viral filtration (Rathore et al., 2014), or conjugation reactions (Andris et al., 2019). For CFF, available mechanistic models describe filtration performance and flux decline (Section 1.2.3) as well as non-idealities of pH and excipient concentrations during UF/DF operations (Ambrožič et al., 2021; Ladwig et al., 2020). In this thesis, the latter case is investigated and non-idealities refer to the three phenomena Gibbs-Donnan effect, volume exclusion, and the ionic strength dependency of pK values (Baek et al., 2017; Stoner et al., 2004). The Gibbs-Donnan effect describes the partitioning of charged solutes which can permeate through a semi-permeable membrane in the presence of retained charged solutes. The retention and accumulation of macromolecules (proteins) leads to an accumulation of charges in the retentate. Consequently, like-charged small solutes are repelled leading to an enhanced depletion into the permeate to preserve electroneutrality and an equal electrochemical potential on each side of the membrane (Bolton et al., 2011; Stoner et al., 2004). At the same time, oppositely charged solutes are attracted and not depleted as expected during DF (Equation 1.7). The Gibbs-Donnan effect is illustrated in Figure 1.6.

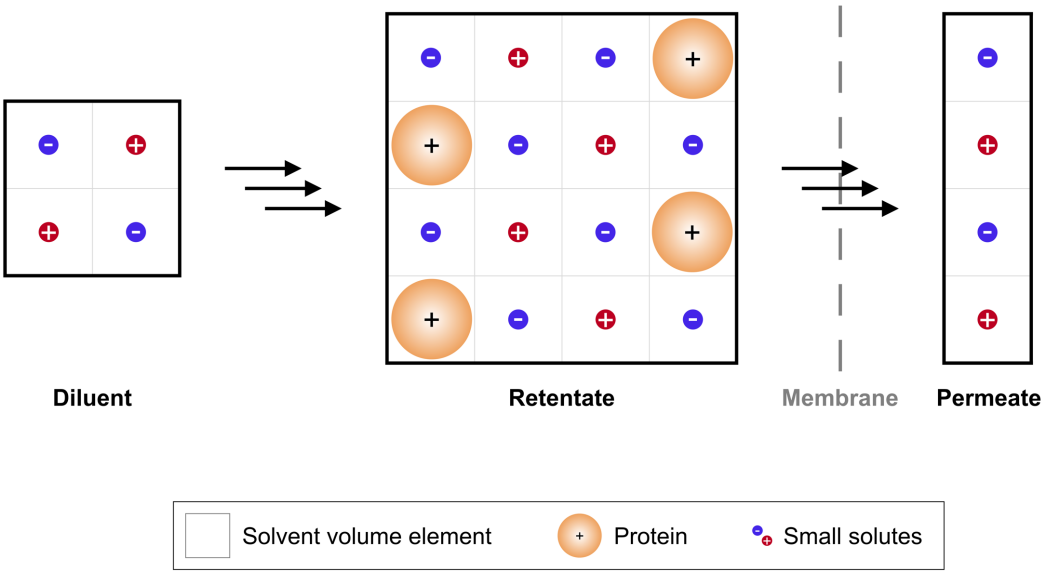

Figure 1.6. Schematic illustration of the Gibbs-Donnan effect during diafiltration (DF). The equilibrium state of a diafiltration process is shown. Further addition of diluent (diafiltration buffer) does not lead to the same composition of small solutes in the retentate even though it is the same in the permeate. Note that the spatial distribution of small solutes in the center of the solvent volume elements does not represent their actual distribution but was chosen to facilitate illustration of concentration differences.

Volume exclusion is independent of the charge of molecules and solely depends on the concentration and partial specific volume of the retained proteins, hence their volume (in the solution) per weight (Bolton et al., 2011; Stoner et al., 2004). When the protein concentration in the retentate increases during UF, the retained proteins occupy an increasing fraction of the retentate volume while the solvent and small solutes are removed (Figure 1.7). The concentration of small solutes per solvent mass (molality) is constant but decreases in relation to the total retentate volume (molarity).

Buffer substances and other excipients are often weak acids or bases with one or more dissociation sites. The non-ideal behavior of their pK values at varying ionic strength (C. W. Davies, 1938) may lead to unintended changes in the solution pH during DF (Baek et al., 2017). Changes in the retentate composition during UF due to the Gibbs-Donnan effect may lead to changes in the ionic strength influencing the pH indirectly (Ladwig et al., 2020). The Gibbs-Donnan effect applies not only to buffer molecules or excipients but also to hydronium and hydroxide ions and thus leading to direct pH shifts. The protein charge again depends on solution pH as some amino acid residues and the protein termini also have (ionic strength dependent) dissociation sites. Consequently, the protein charge directly influences the Gibbs-Donnan effect but also indirectly due to the self-buffering property of proteins, especially at

high protein concentrations (Karow et al., 2013). This interdependence of the multiple phenomena and molecules makes predictions of the solution composition and pH a complex problem. Other effects influencing the distribution of small solutes across the membrane are non-electrostatic, for example, hydrophobic interaction with proteins or protein-protein interactions (Baek, Emami, et al., 2019; Baek & Zydney, 2018; Stoner et al., 2004).

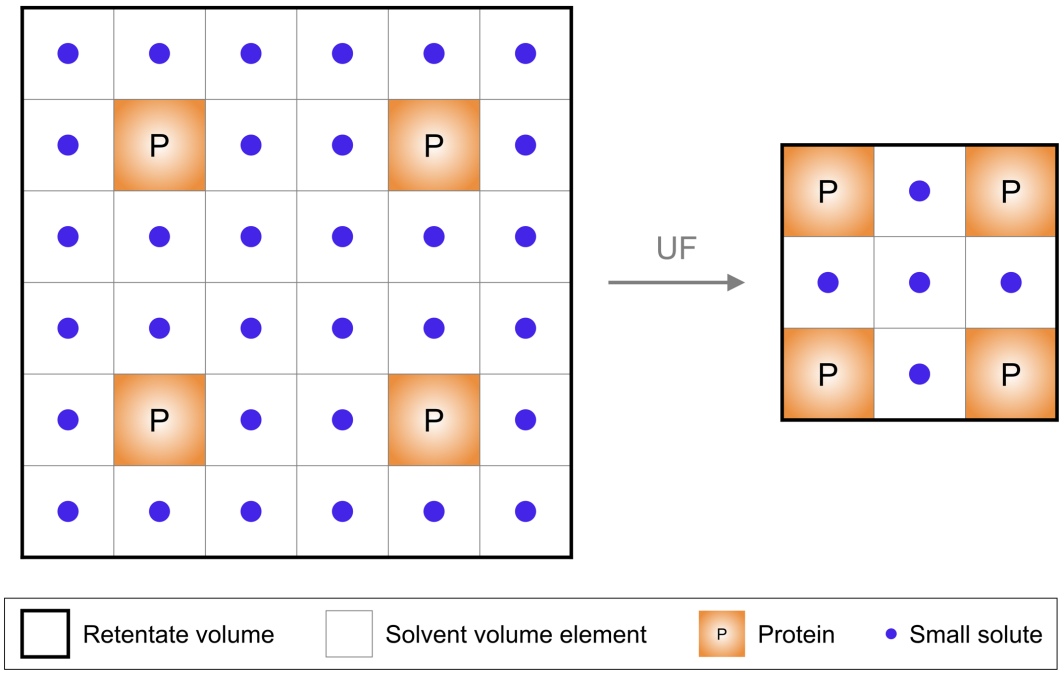

Figure 1.7. Schematic illustration of the volume exclusion effect during ultrafiltration (UF). The two bold squares represent the retentate volume which is reduced during UF. While solvent and solutes smaller than the membrane cut-off (small solutes) are removed, proteins are retained. The concentration of small solutes per solvent volume is constant but decreases with respect to the retentate volume.

During UF/DF of proteins at high concentrations, the abovementioned non-idealities thus lead to deviations of small solute concentrations from the target, which is usually the concentration in the DF buffer. Deviations of the pH or excipient concentrations are undesired because they may lead a product out of specifications with a potential impact on stability or safety (Section 1.1.2). Volume exclusion cannot be mitigated but can be well predicted (Stoner et al., 2004). Mitigation of the Gibbs-Donnan effect is possible by advanced processing routes but its prediction is more difficult due to the complex interdependence of the abovementioned phenomena. Mitigation strategies include the use of DF buffers with high ionic strength (Baek, Singh, et al., 2019) or at a certain pH that results in a low protein charge (Bolton et al., 2011). Holstein et al. (2020) suggested a trial-and-error approach in which the DF

buffer is adapted to account for the deviation from the target. However, high ionic strength might interfere with protein stability and experimental (trial-and-error) work is time and material-consuming. As a compromise, faster depletion of attracted ions might be achieved by DF into an intermediate high-salt buffer. However, developing such complex processing routes experimentally is again time and material-consuming. Alternatively, representative mechanistic process models are particularly beneficial to simulate and evaluate potential processing options. Thereby (buffers for) UF/DF steps can be designed and optimized *in silico* to achieve the desired drug substance solution without any deviations. For example, Ladwig et al. (2020) observed incomplete citric acid depletion due to the Gibbs-Donnan effect. A processing route was identified using simulations, resulting in a two-phase DF into high- and then low-concentrated acetate buffer. Currently available models (Ambrožič et al., 2021; Ladwig et al., 2020) are based on multiple components known from previous works. Mass balances account for solutes entering and leaving the retentate (Baek, Singh, et al., 2019) and are coupled with the Poisson-Boltzmann equation to account for the interaction of retained proteins with charged solutes (Miao et al., 2009). Different approaches are known to model protein charge, for example, the dissociation of amino acid residues depending on pH (Stoner et al., 2004) and ionic strength (Jabra et al., 2020) or titration curves (Bolton et al., 2011). While the earlier can be determined theoretically based on the primary structure of the protein, the latter requires physical protein material and experimental work. Furthermore, the dissociation of buffer substances and other excipients is important to consider where the electroneutrality of the solutions is an important constraint (Stoner et al., 2004). Finally, a volumetric description of the protein in the solution accounts for volume exclusion (Stoner et al., 2004).

The demand for highly concentrated mAb formulations (Section 1.1.2) is concomitant with a more pronounced Gibbs-Donnan effect and volume exclusion. Therefore, a well-working model in the high-concentration regime is crucial to simulate UF/DF steps. Simulations may then be used to develop DF buffers while taking the non-idealities into account and thus reaching target conditions at the end of the process. Additionally, a calibration-free model enables the evaluation of multiple and/or sophisticated processing routes with zero material consumption. This is especially desirable since even small-scale CFF experiments usually require a considerable amount of protein material to reach high concentrations. The hold-up volume of the CFF system dictates the minimal volume of the concentrated solution and thus the amount of protein required. In light of the above, currently available UF/DF process models are limited by the requirement of calibration and the use of empirical

parameters. Furthermore, only limited validation strategies are available in the high-protein-concentration regime around 150 gL^{-1}.

2

Thesis outline

2.1. Research proposal

Cross-flow filtration (CFF) is a size-selective separation technique in which the feed stream is directed parallel to the membrane surface while the filtrate permeates through its pores. Compared to normal-flow filtration, this flow configuration leads to less accumulation of retained species at the membrane surface enabling higher permeate flux and lower concentration-dependent aggregation. Efficient and gentle processing along with good scalability and cost-effectiveness make CFF a ubiquitous unit operation in biopharmaceutical downstream processing (DSP) and beyond. During purification, CFF is used to separate the target protein from other macromolecular impurities such as host cell proteins and nucleic acids. Another major field of application is concentration and buffer exchange during the final formulation step, often referred to as ultrafiltration/diafiltration (UF/DF). In UF/DF, the target protein is separated from the surrounding liquid phase containing low molecular weight solutes.

Time pressure, cost constraints, and the demand for high product quality are key challenges in biopharmaceutical process development. Specific challenges in CFF process development are limited purification performance, laborious experimental work with high protein material requirements, and non-idealities during UF/DF at high protein concentrations. Product quality requirements can be met by applying Quality by Design (QbD) principles, which aim for systematic and knowledge-based process development, rather than testing quality into products. Efficient solutions to the other challenges require advanced process development approaches. In biopharmaceutical process development, several tools are available which may help to overcome these challenges. Potential process development tools are (I) integration of unit operations to intensify processes, (II) high-throughput screenings (HTS) to reduce development effort and time, (III) process analytical technology (PAT) to increase knowledge gained per experiment, and (IV) mechanistic modeling to increase process understanding and enable *in silico* process design. Despite the challenges in CFF process development, the

abovementioned tools are only rarely applied to CFF operations. The objective of this thesis is therefore to apply these tools to CFF and ultimately provide solutions to current challenges in CFF process development. The tools will be developed for and applied in dedicated case studies processing two exemplary biopharmaceutical modalities. These modalities are virus-like particles (VLPs) as multi-protein assemblies for the first three studies and monoclonal antibodies (mAbs) as standard biopharmaceutical proteins for the fourth study.

Process integration is a powerful tool for the intensification of unit operations in DSP of biopharmaceuticals. Applying the 'merger approach' of process integration, intensification is achieved by combining two or more separation techniques into one unit operation. The physical combination into one unit ideally reduces equipment and residence time while the combination of separation techniques may lead to improved process performance such as purity, yield, and productivity. On an inter-unit operation level, process integration is implemented by seamless connections without intermediate hold tanks or conditioning steps. Both process integration approaches require a holistic process design with alignment between the integrated components, for example flow rates. The purification of VLPs in research and development is often performed by selective precipitation/re-dissolution. However, the separation of precipitated VLPs by centrifugation negatively affects their re-suspension and re-dissolution behavior and thus reduces process performance and scalability. The application of CFF may tackle these challenges while providing size-selective separation of precipitated VLPs from smaller impurities. Separation based on size offers to process multiple VLP variants similarly with only minimal changes in processing conditions. The first study of this thesis will investigate the integration of CFF and selective precipitation/re-dissolution by the merger approach for the capture of VLPs. A flow rate monitoring and control strategy will be developed to enable a seamless connection to subsequent size-selective chromatographic purification. Ultraviolet light (UV) monitoring will be employed to trace intermediate wash and re-dissolution steps and to identify stop criteria. The objective of this study is the multi-level integration of CFF with other separation techniques to overcome their individual performance limitations and ultimately increase the overall process performance.

HTS are automated and parallel small-scale experiments that enable process characterization and identification of a design space, hence aiding in QbD implementation. A prerequisite for HTS are suitable analytical techniques to evaluate screened conditions. For certain biopharmaceuticals, DSP involves improving the protein's structural conformation, for example, VLP dis-

/reassembly or inclusion body dissolution/refolding. These reactions are initiated and driven by a change in liquid phase conditions, for which cross-flow DF offers rapid and controlled processing. Moreover, impurities and undesired solutes can be depleted using DF. However, the development of CFF operations is time- and material-consuming. Tight timelines and low availability of protein material at early development stages thus pose a challenge for CFF process development. Decoupling the condition screening from the filtration process offers to overcome this challenge. For this purpose, HTS in multi-well plates are a valuable tool as results are generated fast and with low protein material requirements. The second study of this thesis will investigate the disassembly reaction of VLPs and a subsequent transfer of the optimal conditions to a CFF process. A workflow based on multi-well plates will be developed to screen VLP disassembly conditions and to characterize the reaction with regard to DF-based processing. Therefore, an analytical size-exclusion chromatography (SEC) method will be developed to provide fast and representative data on the disassembly state. In the second part of this study, a filtration-based DSP sequence will be designed, in which the screening results will be used to develop a DF-based VLP disassembly process step. The HTS tool and subsequent transfer to the filtration-based process will be evaluated using two different VLP candidate molecules. This study aims to develop a DF-based VLP disassembly step using a representative HTS and embed this step in a filtration-based DSP sequence.

PAT is a tool suggested by regulatory authorities for monitoring and control of critical quality attributes (CQAs). A key objective of PAT is the knowledge-based development of processes to achieve and maintain high product quality. Especially spectroscopic measurements are valuable to thoroughly characterize proteins. In combination with data analytical methods, such as regression modeling, they allow for structure determination or quantification of proteins in complex mixtures. For this purpose, in-line and on-line measurements are desirable as they can provide a non-destructive, unbiased, and rapid analysis. As mentioned above, time and material constraints are common challenges in CFF process development. PAT can compensate for these constraints by increasing the amount and quality of knowledge obtained per experiment. For the DF-based VLP disassembly step described above, no PAT tool is yet available. In addition, off-line analysis provides an incomplete picture of the disassembly reaction throughout the process. Therefore, the third study of this thesis will apply a PAT framework to the developed DF-based VLP disassembly step. An existing PAT setup will be advanced to monitor process parameters and multiple attributes of the target protein. The latter will be achieved by on-line UV and light scattering spectroscopy as well

as at-line analytical SEC. Process parameters will be varied to evaluate the capabilities of the developed framework. The resulting data will be used to establish and compare endpoint detection approaches with varying levels of complexity. The objective of this study is to thoroughly monitor and characterize DF-based VLP disassembly by implementing a PAT framework.

Mechanistic models enable *in silico* design and optimization of process steps and entire biopharmaceutical DSP. They increase process understanding in various stages of the process life cycle, for example by determining the influence of critical process parameters on CQAs as part of the QbD approach. Model parameters can be determined theoretically or calibrated experimentally. The latter, especially for CFF experiments, requires a considerable amount of protein material which might not be present during development stages. Therefore, purely predictive mechanistic models based on theoretical product and process properties are desirable. A major challenge in CFF process development is the prediction of the liquid phase composition during UF/DF of mAbs and other proteins which require high concentrations of 150 gL^{-1} and above. At high protein concentrations, deviations of the retentate composition from the target conditions in the DF buffer occur. The deviations result from multiple interdependent phenomena, such as the Gibbs-Donnan effect, volume exclusion, and p*K* drifts. Available models require calibration, empirical parameters, or lack validation of assumptions by entire UF/DF/UF sequences. In the fourth study of this thesis, a mechanistic model will be developed to describe pH and excipient concentrations during UF/DF process steps. The model will be based on Poisson-Boltzmann theory and will advance existing models through the implementation of new approaches. Predictions will only require structural information on the protein and process parameters as inputs. Validation experiments will be designed at a laboratory scale to reduce mAb material requirements and provide representative experimental data. This study aims to develop a model that describes pH and excipient concentrations during UF/DF steps. Another goal is to demonstrate the applicability of the model by thorough validation using multiple buffer systems and entire UF/DF/UF sequences reaching the high-protein-concentration regime.

2.2. Outline and author statement

This section provides an overview of the manuscripts written within the scope of this thesis. Sections 1.1.3 and 1.1.4 were published in an adapted form as a review article as outlined below. Chapters 3 to 6 were published as outlined below. In the manuscripts of Chapters 3 and 6, the first authorship was shared (contributed equally) among colleagues and me. This was undertaken to elevate the quality of our common publication. A list of the author contributions signed by the respective authors is attached to the examination copy of this thesis.

Sections 1.1.3 and 1.1.4: Size-selective downstream processing of virus particles and non-enveloped virus-like particles.

Nils Hillebrandt, Jürgen Hubbuch

published in *Frontiers in Bioengineering and Biotechnology* (2023), volume 11, article 1192050, doi 10.3389/fbioe.2023.1192050 in an adapted form.

In Sections 1.1.3 and 1.1.4, VLPs and concepts for their DSP are reviewed. A challenge in DSP of VLPs is the low availability of platform approaches. Size-selective separation techniques, such as filtration, precipitation, and size-exclusion chromatography, offer a solution to this challenge. Separation by size is beneficial for VLP purification due to the large size difference between VLPs and impurities. Furthermore, size-selective separations are mostly independent of other molecular properties such as charge or hydrophobicity, promising wide applicability. Therefore, essential principles of common size-selective techniques are reviewed along with literature applying the same for the DSP of VLPs. The advantage of size-selective separations is underlined by providing a detailed listing of recently published downstream processes for viral particles in which size-selective separations play an important role.

Author contributions: **Nils Hillebrandt**: conceptualization (initial idea, manuscript structure), investigation (literature review and selection), supervision (experiments), visualization (figures and tables), writing (original draft, review, and editing); **Jürgen Hubbuch:** conceptualization (consultation), supervision, writing (review).

Chapter 3: Integrated process for capture and purification of virus-like particles: Enhancing process performance by cross-flow filtration

Nils Hillebrandt, Philipp Vormittag*, Nicolai Bluthardt, Annabelle Dietrich, Jürgen Hubbuch*

* Contributed equally

published in *Frontiers in Bioengineering and Biotechnology* (2020), volume 8, article 489, doi 10.3389/fbioe.2020.00489.

In Chapter 3, process integration for CFF is demonstrated. The study addresses the challenge of limited purification performance of standard filtration operations. An integrated process sequence for the capture and purification of VLPs is developed. Process integration is realized by combining VLP precipitation, wash, and re-dissolution with cross-flow DF. Furthermore, a seamless connection to a chromatography system is established through a custom-made flow controller. This allows for the integration of multimodal size-exclusion chromatography, making in-process decisions based on UV monitoring, and fractionation of the product stream. The integrated process sequence is compared with centrifugation-based precipitation/re-dissolution and other process variants based on process performance.

Author contributions: **Nils Hillebrandt**: conceptualization (initial idea, study design), methodology (experimental design and methods), investigation (literature review, experiments and analysis), supervision (experiments), data curation (data preparation), formal analysis and validation (analysis and interpretation of data), visualization (figures and tables), writing (original draft, review, and editing); **Philipp Vormittag:** conceptualization (initial idea, study design), methodology (experimental design and methods), investigation (literature review, experiments and analysis), supervision (experiments), data curation (data preparation), formal analysis and validation (analysis and interpretation of data), visualization (figures and tables), writing (original draft, review, and editing); **Nicolai Bluthardt:** investigation (experiments and analysis), writing (review); **Annabelle Dietrich:** investigation (experiments and analysis), writing (review); **Jürgen Hubbuch:** conceptualization (consultation), supervision, writing (review).

As mentioned above, the study was designed and conducted in collaboration with Philipp Vormittag. The study focus with regards to this thesis was, among others, on the integrated design of the setup including the selection and

assembly of devices, the flow rate monitoring and control, the UV monitoring, the product fractionation, and the automated time-alignment of on-line and off-line measurement data.

Chapter 4: Process development for cross-flow diafiltration-based VLP disassembly: A novel high-throughput screening approach

Nils Hillebrandt, Philipp Vormittag, Annabelle Dietrich, Christina H. Wegner, Jürgen Hubbuch

published in *Biotechnology and Bioengineering* (2021), volume 118, issue 10, pages 3926-3940, doi 10.1002/bit.27868.

In Chapter 4, the application of HTS for the development of a CFF-based purification step is presented. The study addresses the challenges of limited protein material availability, time pressure, and the requirement for knowledge-based CFF process development. As a case study, VLP disassembly is investigated as part of DSP of non-enveloped VLPs. In the developed process step, VLP disassembly is achieved by DF into a buffer with higher urea concentration and higher pH. Disassembly conditions are identified beforehand using an HTS approach with low VLP material requirements. Therefore, a workflow based on multi-well plates and analytical SEC is developed. The results are used to transfer VLP disassembly to a laboratory-scale CFF unit and to embed it into a filtration-based DSP sequence. The HTS approach and transfer to the filtration-based process are evaluated using two VLP candidates with different properties.

Author contributions: **Nils Hillebrandt:** conceptualization (initial idea, study design), methodology (experimental design and methods), investigation (literature review, experiments and analysis), supervision (experiments), data curation (data preparation), formal analysis and validation (analysis and interpretation of data), visualization (figures and tables), writing (original draft, review, and editing); **Philipp Vormittag**: conceptualization (initial idea, study design), methodology (experimental design and methods), investigation (literature review, experiments and analysis), supervision (experiments), data curation (data preparation), formal analysis and validation (initial analysis and interpretation of data), visualization (figure concepts), writing (review); **Annabelle Dietrich:** investigation (experiments and analysis), data curation (experimental data preparation), writing (review); **Christina H. Wegner:** investigation (experiments and analysis), writing (review); **Jürgen Hubbuch:** conceptualization (consultation), supervision, writing (review).

Chapter 5: Process monitoring framework for cross-flow diafiltration-based virus-like particle disassembly: Tracing product properties and filtration performance

Nils Hillebrandt, Philipp Vormittag, Annabelle Dietrich, Jürgen Hubbuch

published in *Biotechnology and Bioengineering* (2022), volume 119, issue 6, pages 1522-1538, doi 10.1002/bit.28063.

In Chapter 5, the application of PAT for the characterization of a CFF-based purification step is demonstrated. The study addresses the demand for knowledge-based process development with a limited number of experiments. Following up Chapter 4, the developed VLP disassembly step is investigated using a comprehensive monitoring framework. Varying processing conditions are applied to evaluate and validate the capabilities of the monitoring approach. In-line monitoring of DF process parameters and buffer exchange as well as product-related monitoring by on-line spectroscopy and at-line SEC are implemented. Static and dynamic light scattering are monitored as an indicator for changes in particle size. Regression models based on recorded UV spectra are used to predict the disassembly progress. Ultimately, multiple approaches for endpoint determination are evaluated to enable process control.

Author contributions: **Nils Hillebrandt:** conceptualization (initial idea, study design), methodology (model development, experimental design and methods), investigation (literature review, experiments and analysis), software (model application), supervision (experiments), data curation (data preparation), formal analysis and validation (analysis and interpretation of data), visualization (figures and tables), writing (original draft, review, and editing); **Philipp Vormittag:** conceptualization (consultation), supervision (experiments), writing (review); **Annabelle Dietrich:** investigation (experiments and analysis), data curation (experimental data preparation), writing (review); **Jürgen Hubbuch:** conceptualization (consultation), supervision, writing (review).

Chapter 6: Modeling the Gibbs-Donnan effect during ultrafiltration and diafiltration processes using the Poisson-Boltzmann theory in combination with a basic Stern model

Till Briskot, Nils Hillebrandt*, Simon Kluters, Gang Wang, Joey Studts, Tobias Hahn, Thiemo Huuk, Jürgen Hubbuch*

* Contributed equally

published in *Journal of Membrane Science* (2022), volume 648, article 120333, doi 10.1016/j.memsci.2022.120333.

In Chapter 6, the development and thorough validation of a mechanistic model for cross-flow UF/DF processes of proteins are presented. The study addresses the challenge of non-idealities occurring during UF/DF at high protein concentrations. Model components are selected from literature together with new approaches to describe the Gibbs-Donnan effect, volume exclusion, and p*K* shifts in the high-concentration regime. Electrostatic interactions of the protein and microions are described by Poisson-Boltzmann theory and a basic Stern model. The model is designed to require only basic structural information on the protein and initial buffer compositions as input. It is applied to predict the liquid phase composition throughout combined UF/DF/UF sequences. Predictions are validated using multiple buffer systems and a representative sampling strategy, especially during high-concentration UF.

Author contributions: **Till Briskot:** conceptualization (initial idea, study design), methodology (model development, experimental design and methods), software (programming for model solving), data curation (simulation data preparation), investigation (literature review, simulations), formal analysis and validation (analysis and interpretation of data), visualization (figures and tables), writing (original draft, review, and editing); **Nils Hillebrandt:** conceptualization (initial idea, study design), methodology (model development, experimental design and methods), investigation (literature review, experiments and analysis), data curation (experimental data preparation), formal analysis and validation (analysis and interpretation of data), visualization (figures and tables), writing (original draft, review, and editing); **Simon Kluters:** conceptualization (consultation), methodology (experimental methods), investigation (historical experimental data), data curation (historical data preparation), resources, supervision, writing (review); **Gang Wang:** conceptualization (consultation), resources, writing

(review); **Joey Studts:** conceptualization (consultation), resources, writing (review); **Tobias Hahn:** conceptualization (initial idea, consultation), supervision, funding acquisition, writing (review); **Thiemo Huuk:** conceptualization (consultation), supervision, writing (review); **Jürgen Hubbuch:** conceptualization (consultation), supervision, writing (review).

As mentioned above, the study was designed and conducted in collaboration with Till Briskot. The study focus with regards to this thesis was, among others, on the identification of gaps in existing models and potentials for new models, the design of laboratory-scale experiments with a particular focus on generating comprehensive high-quality data with low protein material requirements, the implementation of suitable analytical techniques for given samples, and the practical considerations for model development and validation.

3

Integrated process for capture and purification of virus-like particles: Enhancing process performance by cross-flow filtration

Nils Hillebrandt[*,a], *Philipp Vormittag*[*,a], *Nicolai Bluthardt*[a], *Annabelle Dietrich*[a], *Jürgen Hubbuch*[a]

* Contributed equally

[a] Institute of Engineering in Life Sciences - Section IV: Biomolecular Separation Engineering, Karlsruhe Institute of Technology (KIT), Karlsruhe, Germany

Abstract

Virus-like particles (VLPs) are emerging nanoscale protein assemblies applied as prophylactic vaccines and in development as therapeutic vaccines or cargo delivery systems. Downstream processing (DSP) of VLPs comes both with challenges and opportunities, depending on the complexity and size of the structures. Filtration, precipitation/re-dissolution and size-exclusion chromatography (SEC) are potent technologies exploiting the size difference between product and impurities. In this study, we therefore investigated the integration of these technologies within a single unit operation, resulting in three different processes, one of which integrates all three technologies. VLPs, contained in clarified lysate from *Escherichia coli*, were precipitated by ammonium sulfate, washed, and re-dissolved in a commercial cross-flow filtration (CFF) unit. Processes were analyzed for yield, purity, as well as productivity and were found to be largely superior to a reference centrifugation process. Productivity was increased 2.6-fold by transfer of the wash and re-dissolution process to the CFF unit. Installation of a multimodal SEC column in the permeate line increased purity to 96% while maintaining a high productivity and high yield of 86%. In addition to these advantages, CFF-based capture and purification allows for scalable and disposable DSP. In summary, the developed set-up resulted in high yields and purities, bearing

the potential to be applied as an integrated process step for capture and purification of *in vivo*-assembled VLPs and other protein nanoparticles.

3.1. Introduction

Vaccination has reduced morbidity and mortality world-wide, especially since the introduction of the World Health Organization's Expanded Programme on Immunization (Greenwood, 2014). Expansion of the vaccine portfolio by virus-like particles (VLP) has opened up new opportunities, such as the prevention or treatment of cancer (Bolli et al., 2018; Bryan et al., 2016; F.-X. Ding et al., 2009; Goldinger et al., 2012; Klamp et al., 2011; Lizotte et al., 2016; Mohsen, Heath, et al., 2019; Mohsen, Vogel, et al., 2019; Palladini et al., 2018). However, especially VLP downstream processing (DSP) faces major challenges, such as low yields and the lack of platform processes or rapid analytical techniques. This is due to the complexity of the product and the associated processes, resulting in high development and production costs (Ladd Effio & Hubbuch, 2015). The structural properties of VLPs are similar or identical to the corresponding virus structure they are derived from (Zeltins, 2013). Composed of at least one type of viral structural protein, they are in a size range of approximately 25 nm to 200 nm (Chung et al., 2010; Reiter et al., 2019). Incorporation of foreign epitopes into VLP-forming viral structural proteins results in so-called chimeric VLPs (Pumpens & Grens, 2001). In a previous study, we observed that upon insertion of smaller peptides, the size of chimeric Hepatitis B core antigen (HBcAg) VLPs remained comparable to native HBcAg VLPs with a diameter of 31±2-33±3 nm (Rüdt et al., 2019; Selzer & Zlotnick, 2017). During production, the size difference between VLPs and host cell proteins (HCPs) as well as other smaller contaminants can be exploited for DSP of VLPs (Ladd Effio & Hubbuch, 2015).

A typical VLP production process is shown in Figure 3.1 including unit operations such as centrifugation, filtration, and chromatography. Bind and elute chromatography, the work horse in biopharmaceutical manufacturing for capture, purification, and polishing, suffers from low dynamic binding capacities (Ladd Effio & Hubbuch, 2015), diffusion limitations (Kramberger et al., 2015), and often too small pore sizes (Kattur Venkatachalam et al., 2014) for the purification of VLPs. Size differences between VLPs and the bulk of host cell contaminants can be exploited by size-sensitive techniques such as size-exclusion chromatography (SEC) – especially for analytical purposes (Ladd Effio, Hahn, et al., 2016) –, precipitation, filtration, and ultra-centrifugation (Ladd Effio & Hubbuch, 2015). While ultracentrifugation is applied to lab-scale processes (Ausar et al., 2006; Jiang et al., 1992; Mason et al., 1996), scalability and variability issues, among others, hamper its

application to industrial-scale processes (Kleiner et al., 2015; Koho et al., 2012).

Originally developed for the fractionation of blood by Edward Cohn and coworkers in the 1940s (Cohn, 1941; Cohn et al., 1946), precipitation of contaminants or native precipitation of the product are promising alternatives for protein separation and purification (Martinez et al., 2019). In this context, native precipitation has been reported as highly selective for VLPs (Kim et al., 2010; Koho et al., 2012; Tsoka et al., 2000; Zahin et al., 2016), since larger proteins or protein assemblies are more susceptible to precipitation (Rothstein, 1994). The steric exclusion effect associated with the frequently applied precipitant polyethylene glycol (PEG) generally leads to steeper slopes in the precipitation curves for larger proteins (Iverius & Laurent, 1967; Sim et al., 2012). For precipitation with kosmotropic salts, surface charge is however thought to have a greater effect than size (Curtis et al., 1998). Separation of product-containing precipitate and supernatant can be achieved by centrifugation or filtration. While PEG has been successfully applied to VLP precipitation (Koho et al., 2012; Tsoka et al., 2000), its application is limited when filtration is used as solid-liquid separation technique, as filtration

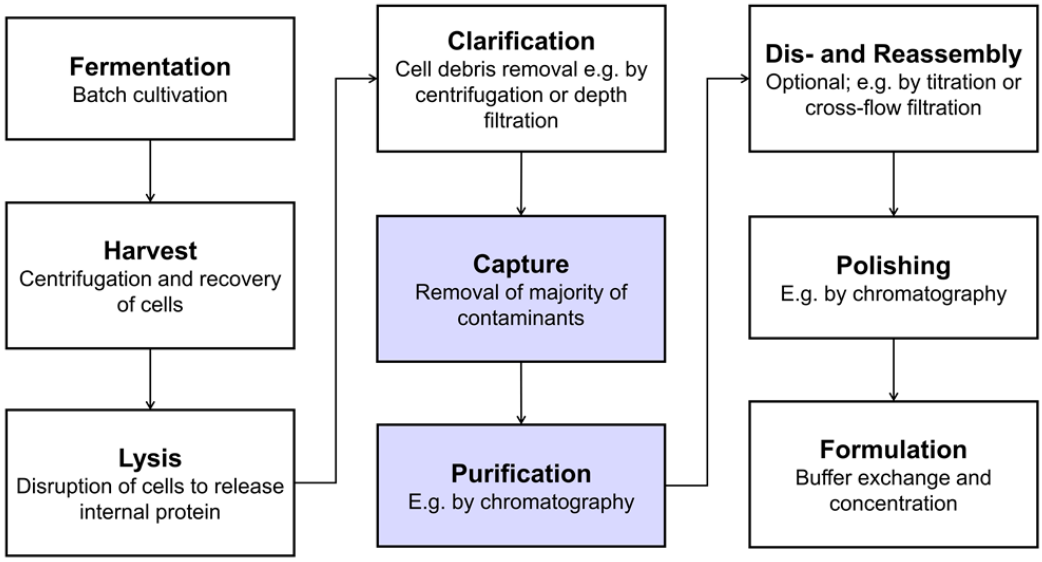

Figure 3.1. Typical production process for intracellularly produced, *in vivo*-assembled virus-like particles (VLPs). Virus structural proteins can be expressed in a variety of host systems, such as *E. coli*, yeast or plant cells (Ladd Effio & Hubbuch, 2015). After harvest and lysis, cell debris are removed by solid-liquid separation and the VLPs remain in solution. VLPs are then captured and purified, followed by an optional dis- and reassembly step, which has shown to increase VLP stability, homogeneity and immunogenicity (Klamp et al., 2011; Mach et al., 2006; Q. Zhao, Allen, et al., 2012). Finally, the product is polished and formulated. The process steps that were investigated as integrated unit operations in this study are highlighted in blue.

performance is impaired by a PEG-induced viscosity increase (Z. Li & Zydney, 2017; Plisko et al., 2016). Next to PEG of various molecular weights, the kosmotropic salt ammonium sulfate ($(NH_4)_2SO_4$) is a commonly applied precipitant (Kazaks et al., 2017; Kim et al., 2010; Zahin et al., 2016). In a study on adenovirus (Schagen et al., 2000), dead-end filtration has been applied to retain $(NH_4)_2SO_4$-precipitated virus but exhibited only 46-61% recovery from the filter. As an alternative to dead-end filtration, cross-flow filtration (CFF) in diafiltration (DF) mode has been applied to recover precipitated monoclonal antibodies (mAbs) (Hammerschmidt et al., 2016; Kuczewski et al., 2011; Venkiteshwaran et al., 2008). Precipitate was retained by a microfilter, allowing for a wash in DF mode. In CFF, turbulent flow along the membrane surface ensures better recovery from the filter (J. L. Davies & Smith, 2010), also reducing concentration polarization and fouling (van Reis & Zydney, 2007). A main advantage of precipitate recovery by CFF over centrifugation lies in avoiding the compaction of precipitate that occurs during centrifugation, which allows for shorter precipitate re-dissolution times using CFF (Hammerschmidt et al., 2016). Additionally, in the above-mentioned studies, precipitation and wash were conducted as integrated CFF-based process steps that showed a higher wash efficiency as compared to centrifugation (Hammerschmidt et al., 2016; Kuczewski et al., 2011). In these studies, the precipitate was re-dissolved by dilution.

This said, it seems promising to dissolve precipitated product by DF into a re-dissolution buffer. Product could subsequently be recovered in the permeate stream as it passes the microfilter. Implementing this approach, the permeate can be separated into fractions allowing for purity increase and concentration adjustment by strategic pooling while undissolved contaminants are retained by the microfilter.

In our experience with DSP of *Escherichia coli* (*E. coli*)-derived VLPs, HCP reduction poses a minor challenge as compared to nucleic acid depletion, demanding for a purification method to reduce the nucleic acid burden. One commonly applied strategy is the supplementation of lysate with Benzonase, a nucleic acid digestion enzyme (Molin et al., 1992). In recent years, a novel multimodal SEC (mmSEC) medium Capto Core 400/700 has been developed that found successful application in the purification of VLPs, decreasing impurity levels significantly (Lagoutte et al., 2016; Somasundaram et al., 2016; D. Zhao et al., 2015). Integration of a precipitation, wash, and re-dissolution step on a CFF system together with this novel mmSEC medium seems therefore promising.

In the light of the above, the objective of our study was to develop an integrated membrane-aided precipitation, wash, and re-dissolution process

for capture and purification of VLPs. The set-up was realized on a commercial CFF unit coupled to a basic preparative chromatography system for monitoring of ultraviolet (UV) absorbance at 280 nm and fractionation. Three process variants were developed, the simplest of which comprised precipitation, wash, and re-dissolution within an integrated CFF-based set-up (Figure 3.2, Process *Basic*). To improve product purity, this method was further either extended by installation of a Capto Core 400 column in the CFF permeate line (Process *mmSEC*) or by pretreatment of the lysate with Benzonase prior to the precipitation step (Process *Nuclease*). As a model VLP, a C-terminally truncated chimeric HBcAg VLP was investigated. The three process variants were compared to a centrifugation-based precipitation, wash and re-dissolution process (Process *Reference*).

3.2. Materials and methods

3.2.1. Materials, buffers, and VLPs

All chemicals were purchased from Merck Millipore (Darmstadt, DE), unless otherwise stated. Solutions and buffers were prepared with ultrapure water (PURELAB Ultra, ELGA LabWater, Lane End, UK). A buffer consisting of 50 mM Tris, 100 mM NaCl, 1 mM EDTA (AppliChem GmbH, Darmstadt, DE), pH 8 was used as lysis buffer. The wash buffer was created from lysis buffer that was adjusted to 0.25% (v/v) polysorbate 20 (AppliChem GmbH, Darmstadt, DE) with a 10% (v/v) polysorbate 20 stock solution and to 150 mM $(NH_4)_2SO_4$ (AppliChem GmbH, Darmstadt, DE) with a 1 M $(NH_4)_2SO_4$ stock solution. In the *Nuclease* process and respective experiments, the digestion and nuclease wash buffers were both 50 mM Tris at pH 8, containing 20 mM NaCl, 0.2 mM EDTA, and 2 mM $MgCl_2$. The re-dissolution buffer was 50 mM Tris at pH 8 for all experiments. All buffers were pH-adjusted with 32% HCl. BioNTech Protein Therapeutics generously provided the chimeric HBcAg VLP plasmid. HBcAg was expressed in *E. coli* and liberated by lysis as described in Appendix A, Section S3.1. Its extinction coefficient at 280 nm of 1.558 L g^{-1} cm^{-1} was derived from the web-tool ProtParam (Gasteiger et al., 2005) and used for all methods. *E. coli* lysate was diluted to ensure a consistent HBcAg content, resulting in HBcAg concentrations between 2.60 g L^{-1} and 2.66 g L^{-1}, used as lysate for all processes and experiments.

3.2.2. Precipitation and re-dissolution screening

For processes *Reference*, *Basic*, *mmSEC*, and *Nuclease*, optimal parameters for the precipitation were determined in screening experiments. Screening experiments for precipitant concentration were performed at a small scale in reaction tubes. Lysate was used either untreated or pretreated. Pretreatment comprised overnight dialysis with Slide-A-Lyzer G2 cassettes (10 kDa, 3 mL,

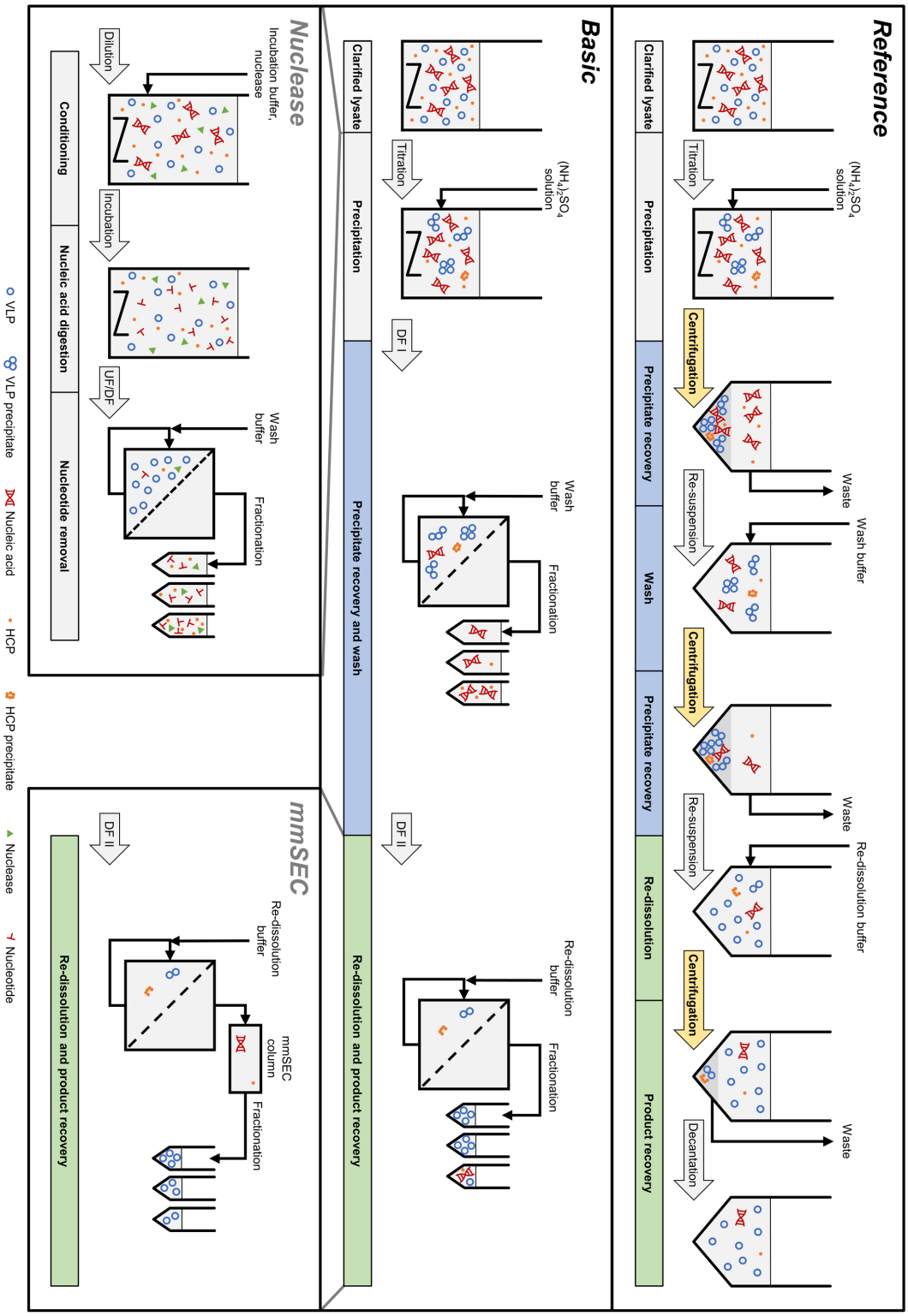

Figure 3.2. *Rotated 90° clockwise*. Schematic overview of the processes investigated in this study. The *Reference* process is shown at the top, consisting of centrifugation-based precipitation, wash, and re-dissolution. Process transfer to a cross-flow filtration (CFF) unit resulted in the *Basic* process. Transferred process steps are wash and re-dissolution, highlighted in blue and green, respectively. Wash and re-dissolution are multiple process steps consisting of repeated centrifugation

(highlighted in yellow) in the *Reference* process. In the *Basic* process, these are reduced to two consecutive diafiltration (DF) steps by simply switching between diafiltration buffers (Figure 3.3). Alternative CFF process variants, either *Nuclease* or *mmSEC*, are modifications from the *Basic* process. The *Nuclease* process adds a nucleic acid digestion and a 300 kDa wash step preceding precipitation and continues like the *Basic* process. The *mmSEC* process sequence is identical to the *Basic* process sequence but has a modified re-dissolution step (DF II) including a multimodal size-exclusion chromatography (mmSEC) column in the permeate line. Abbreviations: $(NH_4)_2SO_4$, ammonium sulfate; HCP, host cell protein; UF/DF, ultrafiltration/diafiltration; VLP, virus-like particle.

Thermo Scientific, Rockford, US-IL) into the digestion buffer with or without addition of >114 U mL^{-1} of Benzonase (Sigma Aldrich, Saint Louis, US-MO) to the lysate. In 1.5 mL reaction tubes, 170 µL or 200 µL of these solutions, adjusted to 0.25% (v/v) polysorbate 20, were mixed with different volumes of $(NH_4)_2SO_4$ stock solution and incubated for 30 min at room temperature (RT), which was between 22 °C and 23 °C for all experiments. The solution was spun down at 17000 rcf for 2 min in a tabletop centrifuge and the supernatant was recovered. For screening of the incubation time during precipitation, untreated lysate was precipitated in a 20 mL batch, sampled at 10 min intervals, and treated as described above.

Small-scale re-dissolution experiments were conducted to test the influence of solution components on re-dissolution efficiency. Pooled fractions F3-F11 of the *mmSEC* process were concentrated to 7.74 g L^{-1} using 50 mL VivaSpins with 100 kDa MWCO (Sartorius Stedim Biotech GmbH, Göttingen, DE). In 1.5 mL tubes, 0.5 mL of concentrated HBcAg solution was mixed with 0.5 mL of five different solutions. Solutions were a) 200 mM NaCl, 50 mM Tris, 2 mM EDTA, pH 8.0, b) 40 mM NaCl, 50 mM Tris, 2 mM EDTA, pH 8.0, c) 200 mM NaCl, 50 mM Tris, 0.4 mM EDTA, 4 mM $MgCl_2$, pH 8.0, d) supernatant of the precipitation step during the *Reference* (Section 3.2.5) process, and e) supernatant of the wash step during the *Reference* process. Solutions were adjusted to 0.25% (v/v) polysorbate 20 and then to 150 mM $(NH_4)_2SO_4$ for precipitation. Samples were incubated for 30 min at 300 rpm and 23 °C in a thermo-shaker Thermomixer comfort (Eppendorf, Hamburg, DE) and subsequently centrifuged at 15294 rcf in an Eppendorf 5810R centrifuge for 20 min at 20 °C. Supernatant was removed by pipetting. A volume of 1 mL re-dissolution buffer was added and the pellet was resuspended. The reaction tubes were incubated at 10 rpm at RT in an overhead shaker LD-79 (Labinco, Breda, NL) for 60 min, centrifuged with identical settings, and the supernatant was recovered.

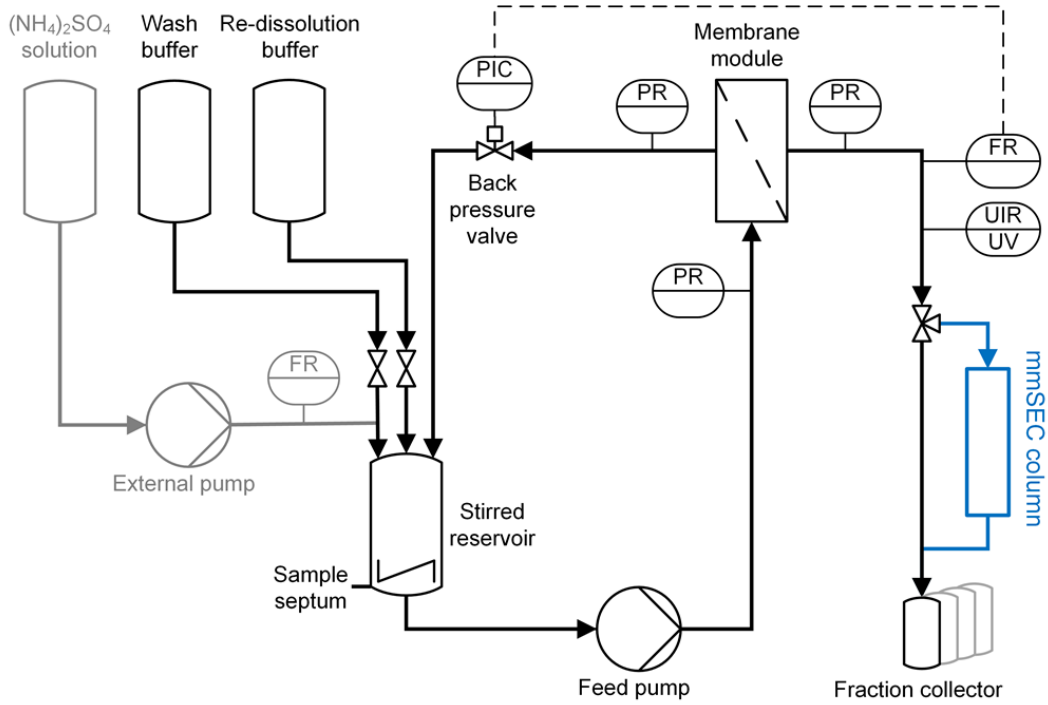

Figure 3.3. Piping and instrumentation diagram (P&ID) of the precipitation and cross-flow filtration (CFF) setup. The set-up used for wash and re-dissolution of the CFF processes *Basic* and *Nuclease* is shown. For process *Nuclease*, the depicted set-up was used with different membranes (300 kDa and 0.2 µm) for the respective wash steps. The *mmSEC* process included an additional multimodal size-exclusion chromatography column (mmSEC) in the permeate stream, highlighted in blue. The precipitation set-up consists of the components highlighted in gray on the left and the stirred reservoir. Precipitant was ammonium sulfate ($(NH_4)_2SO_4$). Gray highlighted components were removed after completion of precipitation. Abbreviations: C, control; F, flow rate; I, indicate; P, pressure; R, record; U, multivariable; UV, ultraviolet.

3.2.3. CFF instrumentation and set-up

The CFF precipitation, wash, and re-dissolution set-up (Figure 3.3) was based on a KrosFlo Research KRIIi CFF system with automatic backpressure valve (Spectrum Labs, Rancho-Dominguez, US-CA) with a stirred cell (Sartorius Stedim Biotech GmbH, Göttingen, DE) as reservoir, and 0.2 µm 200 cm^2 Hydrosart or 300 kDa MWCO 200 cm^2 polyether sulfone (PESU) membranes (both Sartocon Slice 200) with corresponding membrane holders (all Sartorius Stedim Biotech GmbH, Göttingen, DE). The three stirred cell inlet ports were connected to retentate, wash buffer, and re-dissolution buffer lines. A Sensirion Liquid Flow Meter SLS-1500 (Sensirion AG, Stäfa, CH) was installed at the permeate outlet of the membrane holder and connected with a 1/16” PEEK capillary with 0.75 mm inner diameter to the wash valve of an ÄKTA Start (GE Healthcare, Uppsala, Sweden). On-line ÄKTA Start UV sensor data were converted to on-line concentration data applying Beer’s law using

the HBcAg extinction coefficient. The permeate was fractionated in either 15 mL (wash) or 5 mL (re-dissolution) fractions in 15 mL tubes (Corning, Reynosa, MX-TAM). In all presented filtration processes, a constant permeate flow rate of 2 mL min^{-1} was set and maintained using the automatic backpressure valve either by manual valve control (Process *Basic*) or automatic control (Processes *mmSEC* and *Nuclease*). Therefore, the backpressure valve controller was fed with flow rate data of the flow meter (at >1 Hz) instead of transmembrane pressure data as in normal operation mode using a custom-written communication MATLAB 2018b script (The Mathworks, Natick, US-MA). Flow rate, path, and control were optimized in pre-experiments, and data were temporally aligned considering delay volumes (for more detail see Appendix A, Section S3.2).

3.2.4. Precipitation, wash, and re-dissolution process by CFF

Diluted lysate, adjusted to 0.25% (v/v) polysorbate 20, was filled into the aforementioned stirred cell with three inlets and two outlets. One outlet was capped with an injection plug (Fresenius Kabi, Bad Homburg, DE) for sampling, the other outlet either closed or connected to the suction port of the CFF feed pump. A Minipuls 3 peristaltic pump (Gilson, Villiers le Bel, FR) was used to pump 1 M $(NH_4)_2SO_4$ solution at 1 mL min^{-1} through one of the inlet ports of the cell up to a final concentration of 150 mM $(NH_4)_2SO_4$ (Figure 3.3). The flow rate was monitored using a Sensirion Liquid Flow Meter SLS-1500. The stirred cell was set to minimal stirring speed. The solution was incubated for 30 min at RT. During incubation, 250 µL samples were taken every 10 min.

Three wash and re-dissolution process variants were examined, referred to as *Basic*, *mmSEC,* and *Nuclease* (Figure 3.2). The *Basic* process consisted of wash and re-dissolution of precipitate suspension by constant volume DF against wash and re-dissolution buffer, respectively, and fractionation of the permeate. CFF feed flow rate in all filtration steps was 30 mL min^{-1}. Compared to the *Basic* process, the *mmSEC* process included a Capto Core 400 HiScreen column (GE Healthcare, Uppsala, SE) with a nominal column volume of 4.7 mL in the permeate line downstream of the fractionation valve of the ÄKTA Start (Figure 3.3). The *Nuclease* process was conducted like the *Basic* process with additional pretreatment of the lysate prior to precipitation. The lysate was diluted 1:5 with a buffer containing 50 mM Tris and 2.5 mM $MgCl_2$ at pH 8 to optimize the conditions for the digestion of nucleic acids by Benzonase, resulting in the composition of the digestion buffer. Benzonase was added to a concentration of ≥114 Units mL^{-1} and incubated overnight for 16 h at 80 rpm and 23 °C in a 225 mL tube in a MaxQ 6000 Shaker (Thermo Scientific, Marietta, US-OH). The solution was concentrated fivefold by ultrafiltration (UF) in the CFF unit with the 300 kDa membrane. The solution was diafiltered for five

diafiltration volumes (DV) using nuclease wash buffer. The permeate of UF and DF was fractionated into 15 mL fractions. The retentate was processed analogous to the lysate in the other processes.

3.2.5. Centrifugation-based wash and re-dissolution

In a centrifugation-based process (Figure 3.2, process *Reference*), precipitation was performed identically to the experimental procedure for the CFF runs, whereas wash and re-dissolution were performed as a centrifugation protocol. The suspension of 20 mL was centrifuged at 17387 rcf at 20 °C for 20 min. Supernatant was removed and the pellet was resuspended. The procedure including centrifugation and resuspension was repeated with re-dissolution buffer. The suspension was transferred into a stirred cell and stirred at minimal speed. After 1 h, 2 h, and 3 h, a sample was taken, spun down at 17000 rcf for 2 min in a table top centrifuge Heraeus Pico 17 (Thermo Electron LED GmbH, Osterode am Harz, DE), and the supernatant was recovered.

3.2.6. Analytical characterization

Size-exclusion chromatography (SEC) was coupled with a diode array detector (DAD), multi-angle light scattering (MALS), and quasi-elastic light scattering (QELS) to quantify and specify differently sized species. An Agilent BioSEC-5 4.6 × 300 mm, 5 µm, 1000 Å column (Agilent, Santa Clara, US-CA) was used at a Dionex Ultimate 3000 RS UHPLC system controlled by Chromeleon version 6.8 SR15 (Thermo Fisher Scientific, Waltham, US-MA). The method was isocratic for 14 min at a flow rate of 0.4 mL min^{-1} with 50 mM potassium phosphate buffer at pH 7.4. The injection volume was 20 µL. The outlet of the DAD was connected to a Dawn Heleos 8 MALS/QELS system (Wyatt Technology Corporation, Santa Barbara, US-CA). MALS and QELS data were analyzed with the ASTRA V software (Version 5.3.4.15, Wyatt Technology Corporation, Santa Barbara, US-CA) and resulted in root mean square radius (rms) and molecular weight (both assessed by MALS) and hydrodynamic radius (assessed by QELS). For protein separation and quantitation, a Caliper LabChip GX II (PerkinElmer, Waltham, US-MA) high-throughput capillary gel electrophoresis (HT-CGE) device was employed. An HT Protein Express LabChip and the corresponding HT Protein Express Reagent Kit were used and results analyzed with LabChip GX software (Version 4.2.1745.0, PerkinElmer, Waltham, US-MA). Analyses were performed using the HT Protein Express 200 assay in reduced mode using dithiothreitol (DTT, Amresco, Solon, US-OH) according to the assay standard operation procedure provided by the manufacturer. For data analysis, all peaks of 21.5 ± 1 kDa were regarded as HBcAg monomers, which is the form in which HBcAg is present after sample preparation. The range derived from experiments with pure HBcAg. For SDS

PAGE, LDS sample buffer, MES running buffer, and NuPage 4-12% BisTris Protein Gels were used and run on a PowerEase 500 Power Supply (all Invitrogen, Carlsbad, US-CA) in reduced mode with 50 mM DTT in the sample solution according to the manufacturer's manual with minor adaptations. The gel was stained with a Coomassie blue solution. CFF re-dissolution samples of fractions with maximum concentration were analyzed by transmission electron microscopy (TEM) on a Fecnei Titan^3 80 – 300 microscope (FEI company, Hillsboro, US-OR). Samples were adjusted to 0.5-1 g L^{-1} with ultrapure water and filtered with a 0.2 µm syringe filter. Sample preparation and image analysis were conducted similarly to previous studies with chimeric HBcAg VLPs (Rüdt et al., 2019). Hydrophilization and staining solutions were 1% (w/v) alcian blue 8GX (Alfa Aesar, Ward Hill, US-MA) in 1% acetic acid solution and 2% ammonium molybdate(VI) (Acros Organics, Geel, BE) solution (pH 6.25, adjusted with NaOH), respectively.

3.2.7. Calculation of yield, purity, and productivity measures

The yield Y of a process was calculated by

$$Y = \frac{\sum_{i=\text{start}}^{\text{end}} m_{\text{F}_i}}{m_{\text{lysate}}}, \tag{3.1}$$

where m_{lysate} is the mass of HBcAg, calculated from the processed lysate volume and HBcAg concentration as determined by HT-CGE, and m_{F_i} is the mass of HBcAg in re-dissolution fraction F as determined by SEC, where fractions were considered from fraction F_{start} to F_{end}. HT-CGE purity was determined by the ratio of HBcAg concentration to total protein concentration in HT-CGE samples. SEC purity was calculated by the ratio of HBcAg peaks to total peak area at 280 nm (for details on peak identification, the reader is referred to Appendix A, Section S3.3). A260/A280 was calculated by dividing the cumulated peak areas at 260 nm by the cumulated peak areas at 280 nm. Absolute spatial productivity P was calculated by

$$P = \frac{m_{\text{HBcAg,recovered}}}{t_{\text{process}}}, \tag{3.2}$$

where $m_{\text{HBcAg,recovered}}$ is the accumulated mass of pooled fractions and t_{process} the time to complete the process starting with precipitated material through to recovery of the product. Relative spatial productivity was derived by the ratio of absolute productivities to the absolute productivity of the *Reference* process.

3.3. Results

3.3.1. Precipitation

In pre-experiments, 150 mM $(NH_4)_2SO_4$ was determined as optimal concentration for all process variants, where most of the product is found in the precipitate. Figure 3.4 shows HT-CGE and SDS PAGE data of the clarified supernatant of small-scale precipitation experiments from I) lysate, II) lysate with added Benzonase dialyzed against digestion buffer overnight, and III) lysate dialyzed against digestion buffer over night without addition of

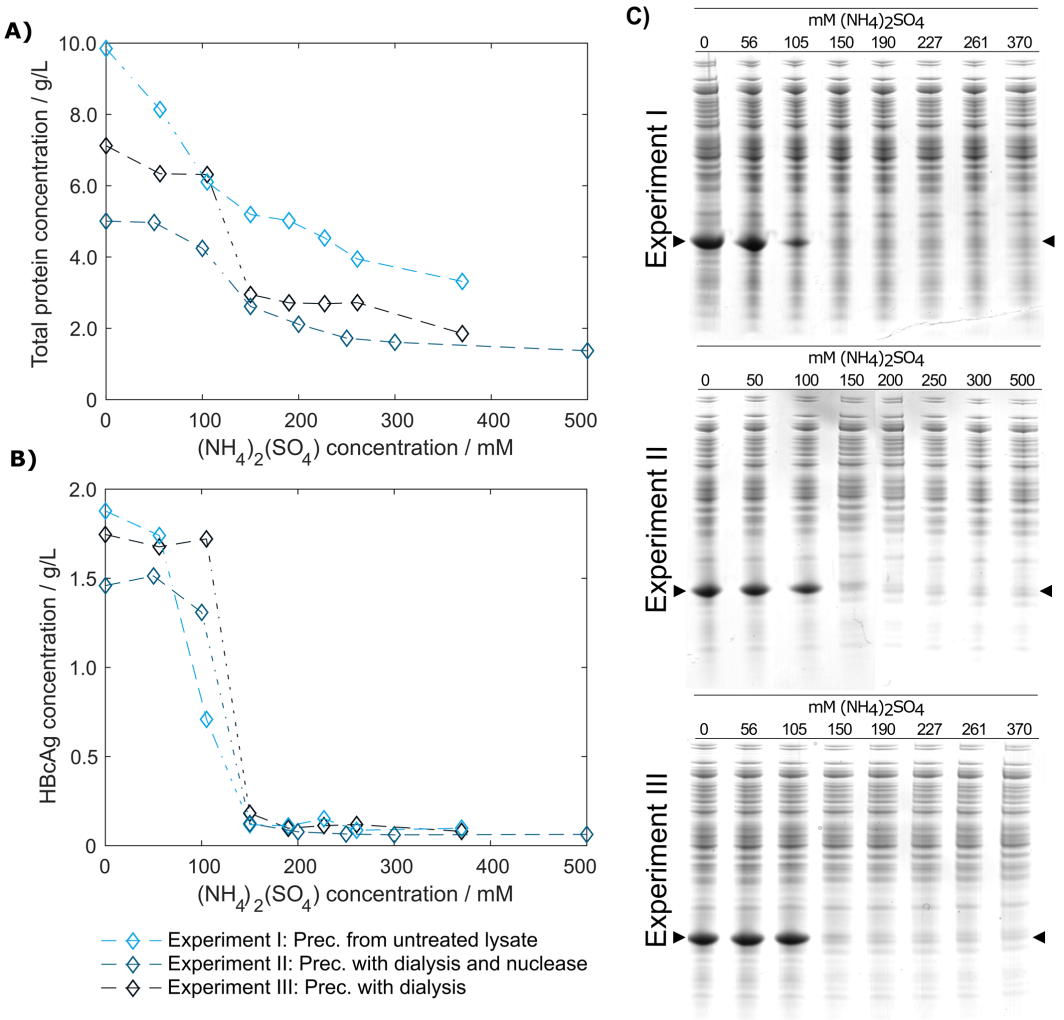

Figure 3.4. Total protein and hepatitis B virus core antigen (HBcAg) concentration in the supernatant after precipitation depending on ammonium sulfate ($(NH_4)_2SO_4$) concentration. Total protein concentration by reducing high-throughput capillary gel electrophoresis (HT-CGE) is shown in **(A)**, HBcAg concentration by HT-CGE in **(B)**. Experiments I-III represent precipitation (Prec.) from I) lysate (-◊-), II) lysate with added Benzonase dialyzed against digestion buffer overnight (-◊-), and III) lysate dialyzed against digestion buffer overnight without addition of Benzonase (-◊-). Experiments I-III are also shown as reducing SDS PAGE scans **(C)**, where lanes 1-8 show $(NH_4)_2SO_4$ concentrations. The HBcAg band is indicated by arrows.

Benzonase. The total protein concentration in the supernatant (Figure 3.4A) was higher for almost all $(NH_4)_2SO_4$ concentrations for precipitation from untreated lysate than for dialyzed samples, as had been expected due to depletion of molecules during dialysis. HBcAg concentrations in all three experiments (Figure 3.4B) were comparable, except for the region between 100 mM and 150 mM $(NH_4)_2SO_4$, where supernatant HBcAg concentrations during precipitation from non-dialyzed lysate dropped significantly at 100 mM $(NH_4)_2SO_4$, while the dialyzed samples remained at comparably constant HBcAg concentrations from 0 mM to 100 mM $(NH_4)_2SO_4$. SDS PAGE analysis (Figure 3.4C) showed similar results based on band intensities.

To validate that precipitation incubation time is sufficient at larger scale, HBcAg concentration in the supernatant was investigated in 10 min intervals at the previously determined 150 mM $(NH_4)_2SO_4$. Precipitation of HBcAg was already completed directly after addition of $(NH_4)_2SO_4$, judging visually based on SDS PAGE scans (Figure 3.5). It has to be noted that to the first sampling time 2-3 min have to be added, accounting for drawing of samples, transferring the samples into reaction tubes, and centrifugation of the samples. Interestingly, during titration of the untreated lysate with $(NH_4)_2SO_4$, we observed a rapid increase in turbidity when a concentration of 100 mM $(NH_4)_2SO_4$ was exceeded. Nevertheless, 150 mM $(NH_4)_2SO_4$ and a precipitation duration of 30 min were chosen to include a safety margin, which was successful in all processes.

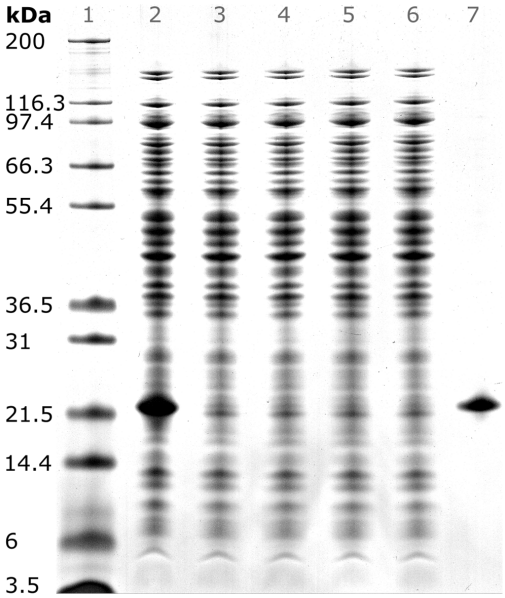

Figure 3.5. SDS PAGE scan of 1) Invitrogen Mark 12 Unstained Standard, 2) hepatitis B virus core antigen (HBcAg)-containing *E. coli* lysate, 3-6) supernatant of precipitation experiments with 150 mM ammonium sulfate directly, 10, 20, and 30 min after ammonium sulfate addition, and 7) pure chimeric HBcAg sample. Molecular weights of the proteins contained in the standard are shown on the left.

3.3.2. Centrifugation-based *Reference* process

After precipitation, solid-liquid separation aims at separating the contaminant solutes and precipitation buffer from the precipitated product. A wash step increases the efficiency of contaminant removal. The *Reference* process was based on centrifugal solid-liquid-separation for precipitate recovery, wash, and re-dissolution. HBcAg concentration of re-dissolution supernatant increased over the first 3 h and was 1.67 g L^{-1}, 1.80 g L^{-1}, and 1.85 g L^{-1}, respectively (Figure 3.6A). Table 3.1 shows the re-dissolution concentration and purity measures after 3 h, where SEC purity was 76%, HT-CGE purity was 83%, and A260/280 was 0.87. After precipitation, which was conducted identically for all CFF processes and the *Reference* process, the *Reference* process was completed in 4.5 h. Time-specific productivities of all processes were calculated based on mg HBcAg per hour relative to the *Reference* process productivity. Therefore, the relative productivity of the *Reference* process is 100%, as shown in Table 3.1. Assuming a similar area foot print of the unit operations, a spatial component of the productivity was neglected.

3.3.3. CFF-based wash and re-dissolution processes

While in the centrifugation-based *Reference* process, wash, re-dissolution, and product recovery steps have to be performed individually (Figure 3.2, *Reference*), the CFF set-up allows for process step integration. Diafiltration with a wash buffer retains the product while depleting solutes continuously. Diafiltration into a re-dissolution buffer replaces the wash/precipitation buffer and re-dissolves the product, which is then able to pass the 0.2 µm membrane. This additionally ensures that larger particles, such as insoluble precipitate, are removed by retention. The developed set-up facilitates fractionation of the permeate stream enabling individual analysis of the fractions (Figure 3.3).

In the presented CFF processes, the wash step was stopped when the initially saturated on-line UV absorbance in the permeate fell below 4 mAU (for visualization of this process see Appendix A, Section S3.4). Product loss during the wash step was determined by HT-CGE. HBcAg concentrations in wash fractions were 0.02-0.03 g L^{-1}. The additional wash step prior to precipitation of the *Nuclease* process resulted in less than 0.1 mg HBcAg loss (analyzed by SEC). After precipitation and wash, re-dissolution of the product was initiated by switching DF buffer lines from wash buffer to re-dissolution buffer. Figure 3.6B depicts on-line and off-line process data over time for the re-dissolution step in the three CFF process variants. Upon DF into re-dissolution buffer, on-line permeate concentrations for all process variants increased to

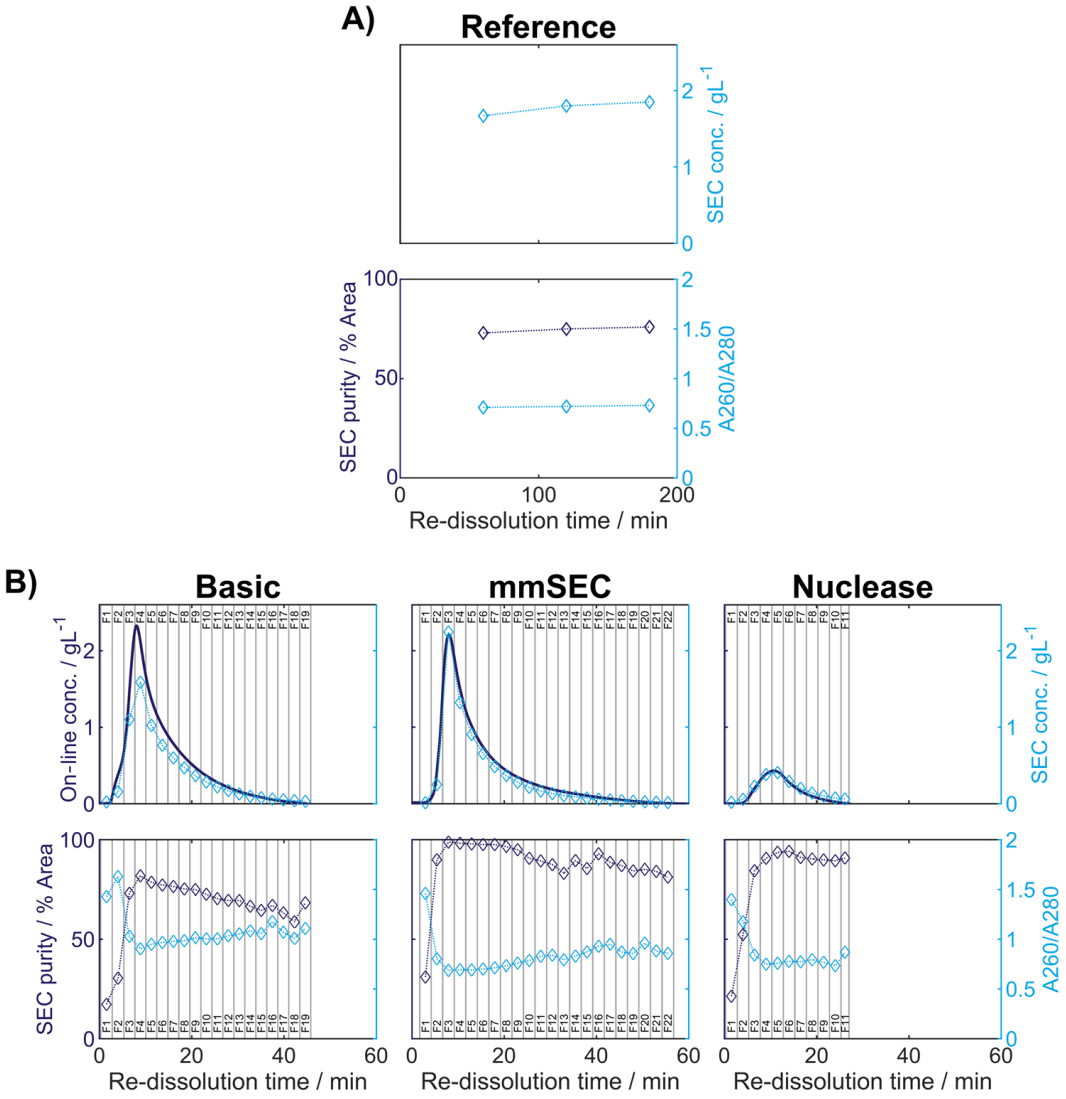

Figure 3.6. Re-dissolution protein concentration (conc.) and purity. Each figure column represents a re-dissolution process variant: (A) *Reference* and (B) *Basic*, *mmSEC* and *Nuclease*. In subfigure (A), the *Reference* process concentration and purity data is shown based on off-line analysis of the supernatant after centrifugation. Top row: Off-line concentrations (◊) were derived from size-exclusion chromatography (SEC) peak areas of hepatitis B virus core antigen (HBcAg) species (Appendix A, Section S3.3). Bottom row: SEC purity (◊) is defined as percentage of HBcAg peak area at 280 nm with respect to the area of all SEC peaks at 280 nm. A260/A280 (◊) is defined as quotient of the cumulated SEC peak areas at 260 and 280 nm, respectively. Dotted lines are added to guide the eye. In subfigure (B), on-line monitoring of the permeate concentration and off-line analysis of the corresponding permeate fractions (F, indicated by vertical lines) during CFF are shown. The metrics of subfigure (A) are shown in subfigure (B) using the same symbols. Additional to these metrics, protein concentrations (—) are shown. Protein concentrations are based on absorbance at 280 nm assuming the chimeric HBcAg extinction coefficient.

a maximum after a lag phase of nearly 2 min and subsequently decreased exponentially. The process was stopped as soon as the on-line absorbance dropped below 4 mAU (on-line concentration of 0.01 g L^{-1}). The final retentate was analyzed for unrecovered product by HT-CGE. It showed a negligible HBcAg mass of <0.5 mg for processes *Basic* and *mmSEC,* as opposed to 22.4 mg in the *Nuclease* process. The maximum on-line concentrations were 2.3 g L^{-1}, 2.2 g L^{-1}, and 0.4 g L^{-1} for processes *Basic, mmSEC* and *Nuclease*, respectively. The curve shapes of the off-line HBcAg concentration are in good agreement with the on-line data. In all three CFF processes, SEC purities were the lowest in fraction F1 and constantly increased to the purity maximum which coincided with the concentration maximum. Maximum purities were 82%, 99%, and 94% for processes *Basic, mmSEC,* and *Nuclease*, respectively. The SEC A260/A280 coefficient showed a nearly inverse progression compared to SEC purity data.

Table 3.1. Summary of re-dissolution process data for centrifugation (*Reference*) and cross-flow filtration (*Basic*, *mmSEC*, *Nuclease*) processes. Process data above the thin horizontal border are calculated based on a pool of all fractions. Results below this border are based on a fraction pool that aimed for a product concentration of at least 1 g L^{-1} and a maximum yield. This was not possible for the *Nuclease* process. Values are calculated using total hepatitis B virus core antigen concentrations except A260/A280, which is based on all species in the size-exclusion chromatography (SEC) chromatogram (Appendix A, Figure S3.1). Best results of each table column are printed in bold.

	Mass[†]	**Yield**[‡]	**Conc.**[†]	**SEC purity**[†]	**A260/ A280**[†]	**HT-CGE purity**	**Relative productivity**[†]
	mg	%	g L^{-1}	% Area	-	%	%
Reference	30.73	72	**1.85**	76	0.87	83	100
Basic [CFF,§]	36.26	82	0.38	73	1.02	96	264
mmSEC [CFF,§]	**37.82**	**86**	0.34	96	0.73	96	239
Nuclease [CFF,§]	9.72	22	0.18	86	0.82	**98**	8
Basic [CFF,¶]	25.19	57	1.01	78	0.96	95	248
mmSEC [CFF,‖]	30.01	68	1.00	**98**	**0.70**	96	**269**

[CFF] cross-flow filtration process, [†] assessed by SEC, [‡] for definition see Material and Methods Equation 3.1, [§] Pool of all fractions, [¶] Pool of fractions F3-F7, [‖] Pool of fractions F3-F8. Process data for pools were calculated by accumulating fraction process data. Abbreviations: A260/A280, absorbance ratio of the sample at 260 nm to 280 nm; Conc., concentration; HT-CGE, high-throughput capillary gel electrophoresis; SEC, size-exclusion chromatography.

3.3.4. Comparison of process data

As seen from summarized process data (Table 3.1), processes *Basic* and *mmSEC* showed higher HT-CGE purities and VLP yields compared to the *Reference* process. SEC purity was comparable between the *Reference* and the *Basic* process, while it was highest for the *mmSEC* process. The *mmSEC* process also showed lowest A260/A280 with 0.73. The relative productivities of processes *Basic* and *mmSEC* were higher than the *Reference* and the *Nuclease* process with >239%. While processes *Basic* and *mmSEC* were superior with regard to aforementioned process data, their concentrations were lower with 0.34-0.38 g L^{-1} as compared to 1.85 g L^{-1} for the *Reference* process. To increase pool concentrations, higher concentrated fractions can be selected for pooling. Strategic pooling increased concentrations for processes *Basic* and *mmSEC* to 1 g L^{-1} while maintaining purity and productivity. However, the yield decreased to 57-68%. Overall, the *mmSEC* process showed highest recovered mass, yield, SEC purity, and lowest A260/A280, along with high productivity and HT-CGE purity, both for strategic pooling and pooling of all fractions.

The *Nuclease* process showed great product loss during re-dissolution, as mentioned above. It exhibited the lowest yield and relative productivity of 22% and 8%, respectively. Due to low concentrations, purity is not comparable to the other processes. For completeness, these values are plotted in Figure 3.6B and shown in Table 3.1. Compared to the other processes, the precipitation process following nuclease treatment started with altered solution conditions regarding NaCl, $MgCl_2$, EDTA, and impurity concentrations. Five screening experiments were designed to investigate the influence of solution conditions during precipitation on re-dissolution efficiency. The recovery of HBcAg in the re-dissolution experiments was 82±1%, indicating no significant difference in HBcAg recovery between the investigated experimental conditions.

3.3.5. VLP size analysis

SEC, coupled to DAD, MALS, and QELS, detected three peaks attributed to HBcAg (compare Appendix A, Section S3.3 for peak identification). A main peak was identified with 15.3-15.5 nm rms radius and 16.4-17.7 nm hydrodynamic radius, corresponding to 79-84% of the HBcAg peak area in the CFF processes. In the *Reference* process, it was 65%. The two earlier-eluting peaks showed 24.4-25.2 nm and 30.4-32.0 nm radius, respectively. The molecular weights were 3.8-4.1 MDa, 7.5-7.8 MDa, and 12.2-12.7 MDa for the three peaks in ascending order by radius. Figure 3.7 shows TEM micrographs of the processes *Basic*, *mmSEC*, *Nuclease*, and the *Reference* process. Graphical

analysis resulted in average radii of 13.4±1.2 nm, 14.6±1.5 nm, 13.6±1.2 nm, and 15.3±1.8 nm, respectively, not showing distinct species as observed in SEC. While samples from processes *mmSEC* and *Reference* showed a spatially equal distribution of VLPs, *Basic* and *Nuclease* samples appeared clustered.

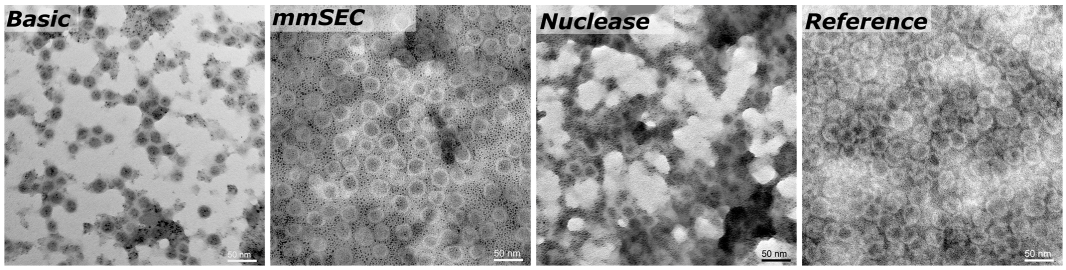

Figure 3.7. Transmission electron microscopy micrographs of re-dissolution peak samples of four processes: *Basic*, *mmSEC*, *Nuclease*, and the *Reference* centrifugation process. The magnification was 27,000-fold.

3.4. Discussion

3.4.1. Interpretation of analytical methods

In this study, SEC and HT-CGE have been applied to determine concentrations and to identify the quantified species. It is therefore important to discuss the meaning of the analytical data as determined for the presented processes. HT-CGE has been employed as, compared to SDS PAGE, a high-throughput compatible and quantitative size-dependent concentration analytical technique. HT-CGE purity informs about the relative HBcAg fraction of the total protein content, i.e. HBcAg protein purity. SEC is applied to assess particle size and molecular weight, HBcAg and contaminant concentrations, and additionally provides spectral data of the sample.

The ratio of the absorbance at 260 nm to the absorbance at 280 nm (A260/A280) is characteristic for the ratio of nucleic acid to protein concentration, whereby higher A260/A280 values indicate a larger fraction of nucleic acids (Wilfinger et al., 1997). SEC purity describes purity based on all species absorbing at 280 nm, such as proteins and nucleic acids.

The combination of these two purity measures together with the A260/A280 are thus seen to be powerful to describe a sample. Figure 3.8 illustrates the connection between these measures. For example, samples with high HT-CGE purity but lower SEC purity therefore probably also show increased A260/A280 values, indicating nucleic acid contamination. It is important to note that SEC measurements are more accurate than HT-CGE measurements for concentration determination. This being said, SEC could only be applied to rather clean, non-turbid samples (see also Appendix A, Section S3.5). Therefore, SEC rather was applied to assess concentrations during re-

dissolution while lysate and precipitation/wash samples were assessed by HT-CGE. Yields were calculated based on lysate HBcAg concentrations and re-dissolution sample concentrations and are therefore based on both HT-CGE and SEC measurements. Discussion on comparability of yields can be found in Appendix A, Section S3.5.

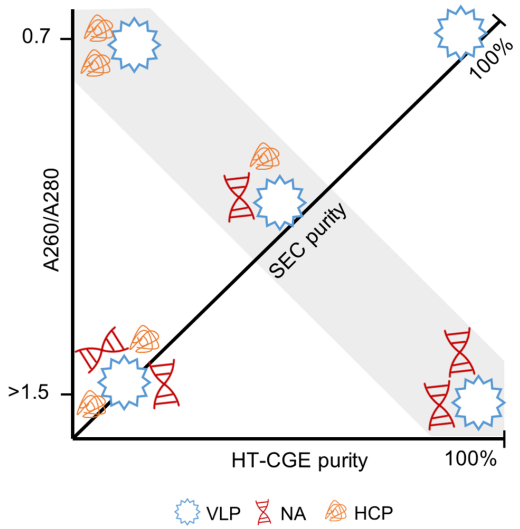

Figure 3.8. Illustration of the interdependence of derived purity measures. Virus-like particles (VLPs) with different degree of contamination by host cell proteins (HCPs) and nucleic acids (NAs) are shown. Size-exclusion chromatography (SEC) provides the A260/A280 (ordinate) and SEC purity (diagonal axis). A high-throughput capillary gel electrophoresis (HT-CGE) protein assay provides the HT-CGE purity (abscissa). The gray highlighted area is characterized by identical SEC purity, while HT-CGE purity and/or A260/A280 describe the composition of the contaminants. A pure hepatitis B virus core antigen VLP sample is characterized by 100% SEC purity, 100% HT-CGE purity and an A260/A280 of ~0.7.

Off-line SEC and HT-CGE analysis indicated that mainly HBcAg species pass through the membrane upon re-dissolution. It was therefore reasonable to convert the on-line UV absorbance into an on-line HBcAg concentration value, applying the HBcAg coefficient. The good agreement between on-line and off-line concentration profiles underlines the usefulness of this approach. However, the *mmSEC* process set-up included an additional purification step between the UV flow cell and the fraction collector, making off-line samples purer than the on-line measured permeate stream.

The MALS detector coupled to the SEC system provides an estimate of molecular weight. HBcAg capsids naturally occur as 180-mer with icosahedral symmetry T=3 and as 240-mer with symmetry T=4 (Wynne et al., 1999). As SEC is incapable of separating different capsid symmetries, the molecular weight measured is the average weight of T=3 and T=4 capsid species. The theoretical molecular weight for a chimeric T=4 capsid is 4.8 MDa and a T=3 capsid is

3.6 MDa. The SEC-MALS-derived molecular weights of the latest-eluting HBcAg peak were between 3.8 and 4.1 MDa, representing 18%/82% and 43%/57% mixture of T=3/T=4 capsids, respectively. *In vitro,* HBcAg VLPs are predominantly T=4, but can shift towards higher percentage of T=3 symmetry capsids upon VLP modification (Böttcher et al., 1997; Rybka et al., 2019; Zlotnick et al., 1996). As an orthogonal method, TEM imaging confirmed the presence of approximately 30 nm sized nearly spherical particles. TEM image-based size measurements did not result in significant differences between the VLP sizes in samples of the different processes. Due to graphical sizing inaccuracies, TEM was unable to resolve different HBcAg species as observed with SEC. These three differently sized HBcAg species, of which the smallest corresponds to the typical size of an HBcAg VLP, were observed in all CFF processes and the *Reference* process. Interestingly, the VLP fraction of these three peaks was similar in all the CFF processes but higher than in the reference process. It would be interesting to analyze these species separately in the following process steps, such as disassembly, which is, however, out of the scope of this study.

3.4.2. Precipitation of chimeric HBcAg VLPs

Precipitation of complex mixtures involves interactions that are only partly understood (Przybycien, 1998). This has also recently been pointed out in a study on PEG-induced precipitation of mAbs (Großhans et al., 2019). Although differences were small in our study, variations of HBcAg concentrations were observed especially at 100 mM $(NH_4)_2SO_4$, where supernatant concentrations after precipitation from untreated lysate were lowest. This is in accordance with previously reported results on mAb precipitation from complex mixtures in the study mentioned above, where precipitation from a complex mixture led to higher precipitation propensity of product molecules (Großhans et al., 2019). This rapid decrease in HBcAg solubility at 100 mM concurs with the observed rapid turbidity increase at 100 mM $(NH_4)_2SO_4$ at a larger scale during the CFF and centrifugation processes. Experiments on precipitation incubation time revealed that the investigated HBcAg VLPs precipitate almost immediately, which is fast compared to incubation times of 15 min – 4 h for different VLPs and precipitants stated in literature (Koho et al., 2012; Schagen et al., 2000; Tsoka et al., 2000).

3.4.3. Product loss in the *Nuclease* process

The *Nuclease* process showed significantly lower concentrations of recovered HBcAg, making it difficult to compare this process variant to the other processes. Due to its low relative productivity and comparably complicated process route, it is not competitive with the *Reference* process and the other

CFF processes *Basic* and *mmSEC*. The low yield observed in this process is mainly due to incomplete re-dissolution, with 22.4 mg of HBcAg in the final retentate. In order to reveal the effect of different solution conditions during the precipitation step, this was investigated in small-scale re-dissolution experiments. However, no significant differences could be identified when investigating the influence of NaCl, EDTA, $MgCl_2$, and contaminants with regard to this problem. Further reasons could be the additional wash step by DF on a membrane of different material or overnight incubation at RT, resulting in irreversible precipitation. Apart from low yields, its low relative productivity derives from the 16 h Benzonase incubation, yet only increases to 42% if an incubation time of 1 h at optimized digestion conditions would be considered. From a scientific standpoint, it would be interesting to identify which factors contributed to the low re-dissolution yields, whereas from a technical standpoint this process route cannot be justified.

3.4.4. Benefits of process transfer to a CFF unit

The main advantage in implementing CFF for precipitation/re-dissolution lies in the combination of product recovery by membrane retention with the capability of exchanging the product-containing buffer in a single process step. During CFF wash steps, impurities smaller than 0.2 µm are expected to be washed out with the permeate. Impurity depletion was observed in all processes indicated by the decrease of on-line UV absorbance. HBcAg VLPs are expected to be retained by the membrane due to the size of their precipitate, as was seen for mAb precipitate in previous studies (Hammerschmidt et al., 2016; Kuczewski et al., 2011). Although HT-CGE results point at minor product loss during wash, it is important to note, that all proteins of 19.5-21.5 kDa were assigned to HBcAg in our analysis due to sizing inaccuracies. Therefore, product loss is expected to be lower than reported. The wash process step was comparable for processes *Basic* and *mmSEC*. Higher protein purities in the CFF processes are probably due to a more efficient wash as compared to the centrifugation-based *Reference* process, whereby interstitial pellet liquid cannot be removed. However, in the *Basic* process, SEC purity was slightly lower and A260/A280 higher than in the *Reference* process. This indicates that the main impurity in the *Basic* process are nucleic acids. This is in accordance with previous unpublished results of CFF-based processes from our group. It may be suggested that DNA interacts with the VLPs in the kosmotropic environment during precipitation and wash which hampers its depletion during the wash step.

As opposed to re-dissolution of the compact pellet in the *Reference* process, re-dissolution from a turbid solution in CFF-based processes was expected to improve process performance. This was for example observed by the

increased yields of processes *Basic* and *mmSEC* compared to the *Reference* process. Product loss in the *Reference* process can be attributed to unrecoverable interstitial pellet liquid and high precipitate compaction (Hammerschmidt et al., 2016), which leads to slower and incomplete re-dissolution. This is in agreement with comparably slow re-dissolution in the *Reference* process. As a result, CFF processes *Basic* and *mmSEC* showed strongly enhanced relative productivities. Additionally, CFF process durations are reduced by minimizing manual handling compared to the *Reference* process. The *mmSEC* process showed superior SEC purity compared to all other processes. As discussed above, the main contaminant in the *Basic* process are nucleic acids. These were efficiently depleted in the *mmSEC* process, leading to excellent purity, while maintaining the increased yield of the *Basic* compared to the *Reference* process, underpinning the usefulness of the mmSEC column in the permeate line (Figure 3.3).

In summary, process transfer to the CFF set-up led to improved yields, accelerated re-dissolution kinetics, and process intensification by integrating multiple process steps into one unit operation. Compared to literature VLP processes showing a 31-76% recovery (Carvalho et al., 2019; D. Zhao et al., 2015), up to 95% protein purity (Wetzel et al., 2018), and a 78% nucleic acid reduction (Carvalho et al., 2019), the process data of the *mmSEC* process are comparable or superior while applying only a single unit operation after lysate clarification. The main drawback of the CFF-based processes were lower product concentrations as compared to the *Reference* process. The exponential permeate concentration decrease observed for all re-dissolution processes, as expected for non-retained species in DF (Kurnik et al., 1995), results in decreased concentrations when aiming for a maximized process step yield. Although the re-dissolution concentration profile cannot be improved from a technical point of view, this effect can be ameliorated by strategic pooling. This was exemplified by creating 1 g L^{-1} pools, which resulted in improved purity and 18-25% yield decrease. Alternatively, collection of all fractions followed by a concentration process via UF could maximize both yield and concentration. Another interesting option would be loading the permeate onto an anion exchange column or membrane as a polishing step to bind VLPs, deplete $(NH_4)_2SO_4$, and achieve further purification from other contaminants while obtaining concentrated VLPs in the elution step. While it seems reasonable to dissolve the precipitated product by dilution to avoid DF-associated concentration decrease, DF shows several advantages. Considering 0% retention, 40% of $(NH_4)_2SO_4$ is theoretically found in fractions 1-2, which could be discarded due to low VLP concentrations. On the contrary, all $(NH_4)_2SO_4$ remains in the product solution for re-dissolution by dilution as

used in several concepts for mAb capture processes (Hammerschmidt et al., 2016; Kuczewski et al., 2011; Z. Li et al., 2019). This drawback may be circumvented by employing dead-end filtration to drain precipitate before re-dissolution (Chen et al., 2016; W. Liu et al., 2019; Lohmann & Strube, 2020). This approach was not considered in this study to avoid unknown effects of draining, precipitate compaction on the membrane, and uncontrolled concentration increase on product stability and yield. DF allows for highly efficient $(NH_4)_2SO_4$ removal in the retentate enabling maximum re-dissolution and therefore yield. Conversely, comparable levels of $(NH_4)_2SO_4$ can only be reached by dilution to very large volumes. Especially if a UF step is established after re-dissolution, a simple DF step after concentration can remove residual $(NH_4)_2SO_4$ efficiently.

To the best of our knowledge, this is the first study to present a fully integrated CFF system-based precipitation, wash and re-dissolution set-up for VLP capture and purification that includes DF-based re-dissolution. The presented approach showed exceptionally good performance with regard to yield, purity, and productivity while being based on a simple lab-scale set-up with basic commercial devices. As a filtration-based process, it exhibits good scalability and the possibility of disposable manufacturing (van Reis & Zydney, 2007). For vaccines, especially cancer vaccines, which are envisaged to be produced as personalized medicine (Buonaguro et al., 2013; Castiblanco & Anaya, 2015; Rammensee & Singh-Jasuja, 2013), this highly efficient, easy-to-control, and scalable process could enable distributed manufacturing of personalized protein nanoparticle-based therapeutics.

3.4.5. Considerations for method transfer

From a technical point of view, CFF process control of the presented method can be achieved by maintaining a constant transmembrane pressure (TMP) or permeate flow rate. In case of TMP-based control, low TMP values are required to obtain the target permeate flow rate due to the large membrane pore size of 0.2 µm. During wash and re-dissolution in processes *Basic* and *mmSEC*, the TMP was in the range of 0.01 bar to 0.02 bar. Therefore, a careful adjustment of the TMP is recommended to avoid exceeding the maximum flow rate of the mmSEC column. Nevertheless, a constant flow rate is advantageous for fractionation and mmSEC separation.

The prerequisites for the successful application of this process to the purification of other VLPs are the ability I) to precipitate the target product, II) to retain the majority of impurities in solution, III) to re-dissolve the product, and IV) to avoid electrostatic or hydrophobic interaction between product and impurities or matrices, such as the membrane material. These

prerequisites are probably fulfilled – to varying degrees – for most non-enveloped VLPs.

Precipitation of the target product might require adaption of the precipitant concentration or agent for different VLPs. From unpublished results of our group, we learned that the precipitation of other chimeric HBcAg VLPs required ammonium sulfate concentrations of 0.1 M to 1 M. Their large size compared to the typical contaminants facilitates the precipitation of VLPs while retaining most impurities in solution. The application of this process to smaller product molecules (such as capsomers) could also be feasible, if a suitable precipitation method is developed, which retains impurities in solution. Product re-dissolution and hydrophobic or electrostatic interactions are influenced by the solution conditions, which might need to be optimized, presumably with a focus on the optimum solution pH.

Compared to the here investigated non-enveloped VLPs, enveloped VLPs might pose a challenge due to their lower stability (Dai et al., 2018). VLPs derived from other hosts such as yeast or plants require changes in the lysis procedure and bring along a different impurity profile than *E. coli.* This said, the separation in the presented process is largely based on the size difference between product and impurities, which should be comparable for other hosts. Extracellularly produced VLPs could benefit from the higher purity of the starting material and therefore potentially result in yet higher purities using this process. Conclusively, the transfer of this method to the purification of other VLPs probably requires few adaptations, mainly regarding the development of optimal solution conditions for VLP precipitation and re-dissolution in small scale.

3.5. Conclusion and outlook

In this study, we have developed a set-up for integrated capture and purification of VLPs within a CFF unit. Clarified lysate was precipitated, washed, and re-dissolved. Three CFF process variants were investigated and characterized for yield, purity, and relative productivity and were compared to a centrifugation-based *Reference* process. Process transfer of the *Reference* process to the CFF unit led to increased purities, probably attributed to a more efficient wash step. The *mmSEC* process, integrating an additional purification step by an mmSEC column in the permeate line, was superior to all tested variants and the *Reference* process resulting in the highest purity and productivity. As one single unit operation, it compares favorably to entire DSP processes found in the literature and shows great potential for disposable and scalable manufacturing. Another key advantage of CFF processes is the possibility to fractionate the VLP-containing permeate, allowing for efficient

pooling with regard to the desired target process data and product analytical profile. In the future, this mainly size-based DSP step could be applied to other VLPs or similarly sized therapeutics with only minor adaptations, laying the foundation for a platform process for protein nanoparticles.

Acknowledgments

The authors would like to thank Matthias Rüdt and Thorsten Klamp for proofreading as well as Steffen Großhans and Sebastian Andris for inspiring discussions. The authors express their gratitude to Reinhard Schneider for technical and scientific support in performing TEM imaging. The authors would also like to thank BioNTech Protein Therapeutics, especially Thorsten Klamp and Anja Wilming, for the provision with VLP sequence data and production plasmids, without which this work would not have been possible.

Supplementary material

Appendix A contains the supplementary material associated with this chapter:

- S3.1 Chimeric HBcAg expression and cell lysis
- S3.2 CFF set-up and temporal alignment
- S3.3 SEC-MALS analysis
- S3.4 CFF wash and re-dissolution process data
- S3.5 Analytical considerations

4

Process development for cross-flow diafiltration-based VLP disassembly: A novel high-throughput screening approach

Nils Hillebrandt[a], *Philipp Vormittag*[a], *Annabelle Dietrich*[a], *Christina H. Wegner*[a], *Jürgen Hubbuch*[a]

[a] Institute of Engineering in Life Sciences - Section IV: Biomolecular Separation Engineering, Karlsruhe Institute of Technology (KIT), Karlsruhe, Germany

Abstract

Virus-like particles (VLPs) are particulate structures, which are applied as vaccines or delivery vehicles. VLPs assemble from subunits, i.e. capsomeres, composed of recombinantly expressed viral structural proteins. During downstream processing, *in vivo*-assembled VLPs are typically dis- and reassembled to remove encapsulated impurities and to improve particle morphology. Disassembly is achieved in a high-pH solution and by addition of a denaturant or reducing agent. The optimal disassembly conditions depend on the VLP amino acid sequence and structure, thus requiring material-consuming disassembly experiments. To this end, we developed a low-volume and high-resolution disassembly screening that provides time-resolved insight into the VLP disassembly progress. In this study, two variants of C-terminally truncated hepatitis B core antigen were investigated showing different disassembly behaviors. For both VLPs, the best capsomere yield was achieved at moderately high urea concentration and pH. Nonetheless, their disassembly behaviors differed particularly with respect to disassembly rate and aggregation. Based on the high-throughput screening results, a diafiltration-based disassembly process step was developed. Compared to mixing-based disassembly, it resulted in higher yields of up to 0.84 and allowed for integrated purification. This process step was embedded in a

filtration-based process sequence of disassembly, capsomere separation, and reassembly, considerably reducing high-molecular-weight species.

4.1. Introduction

Virus-like particles (VLPs) are multi-molecule structures that resemble the native virus they were derived from, but lack infectious nucleic acids (Chackerian, 2007). Their particulate and repetitive structure makes them highly immunogenic, which has been harnessed by several licensed vaccines, such as VLPs against hepatitis B virus and human papillomavirus infection (Bryan et al., 2016; McAleer et al., 1984). Chimeric VLPs are VLPs which incorporate a foreign antigenic epitope against which an immune reaction is intended. This has been evaluated in several pre-clinical and clinical trials, and recently, a vaccine against the circumsporozoite protein of the malaria pathogen has been locally approved (European Medicines Agency, 2015). Recent efforts to develop VLP-based severe acute respiratory syndrome coronavirus 2 (SARS-CoV-2) vaccines underline the flexibility and simplicity of chimeric VLPs (Ghorbani et al., 2020; Yang et al., 2021). However, the versatile platform of chimeric VLPs not only comes with promises, but also with fundamental challenges, such as the ability to form stable capsids (Borisova et al., 1999; Böttcher et al., 2006; Nassal et al., 2005; Pumpens & Grens, 2001). Challenges related to the production process include the limited solubility of candidate molecules (Jegerlehner, 2002; Karpenko et al., 2000; Vormittag et al., 2020a) and the dependence of process parameters on molecular properties, which are both influenced by the amino acid sequence of the inserted foreign antigenic epitope (Rüdt et al., 2019). A typical production process is shown in Figure 4.1A. Process steps that are influenced by the epitope insertion are, for example, precipitation, where a varying amount of ammonium sulfate is required for VLP precipitation (Hillebrandt et al., 2020; Vormittag et al., 2020b), and VLP reassembly, which has been proposed to depend on VLP zeta potential (Rüdt et al., 2019). VLPs are disassembled (dissociated into capsomeres) and reassembled (capsomeres triggered to form capsids) to improve structural homogeneity, stability, and immunogenicity (Q. Zhao, Allen, et al., 2012; Q. Zhao, Modis, et al., 2012). Disassembly is realized by a high pH and low ionic strength, often adding denaturants or reducing agents (Bin Mohamed Suffian et al., 2017; Mach et al., 2006; McCarthy et al., 1998; Singh & Zlotnick, 2003; Strods et al., 2015; Y. Zhang et al., 2021), while reassembly is achieved at neutral pH and high ionic strength (Mach et al., 2006; Zlotnick et al., 1996). Since disassembly releases capsid-internal impurities and typically leads to incomplete disassembly or aggregate formation, a capsomere separation step is added between dis- and reassembly (Zlotnick et al., 1996). As a denaturant, urea has been investigated

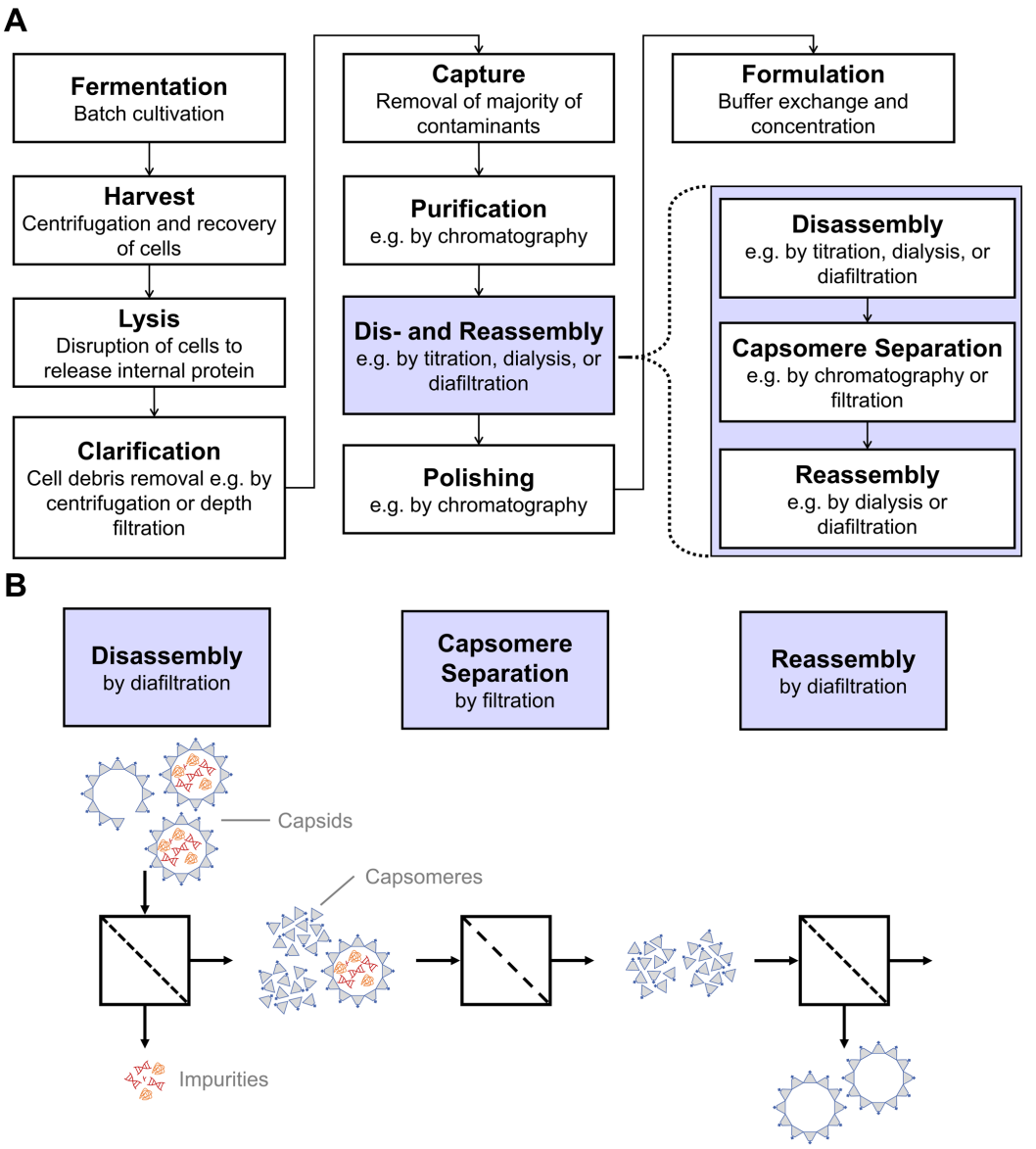

Figure 4.1. (A) Process of intracellularly produced, *in vivo*-assembled capsids, highlighting unique VLP process steps. Compared to other biotechnological products, upstream processing and primary purification are followed by a sequence of disassembly, capsomere separation, and reassembly. This sequence allows for improvement of particle homogeneity and removal of encapsulated impurities. (B) Concept of a filtration-based VLP purification cascade. Capsids are disassembled by cross-flow diafiltration (DF) into a disassembly buffer while the capsomeres are retained by the membrane. Encapsulated impurities are released during disassembly and washed out if smaller than the membrane molecular weight cut-off. Non-disassembled capsids and potential aggregates are separated by a dead-end ultrafiltration step. The capsids are then reassembled in a second cross-flow DF step into a DF buffer that favors the assembled state. Abbreviations: DF, diafiltration; VLP, virus-like particle.

at several concentrations for hepatitis B core antigen (HBcAg) VLP disassembly into HBcAg dimers (capsomeres) (Singh & Zlotnick, 2003; Y. Zhang et al., 2021), further referred to as dimers. These publications show that an increasing urea concentration leads to a more complete and rapid disassembly, while urea concentrations of $\geq 4\,M$ resulted in protein denaturation, which in turn can lead to aggregation or the inability to reassemble. It therefore seems reasonable to use urea concentrations for disassembly which are high enough to maximize the dimer yield but do not result in protein denaturation. For chimeric VLPs, it is conceivable that the inserted epitope influences the optimal disassembly solution conditions. Unpublished results on chimeric HBcAg disassembly by our laboratory confirm these assumptions.

VLP disassembly is typically achieved by addition of disassembly agents (Mach et al., 2006; McCarthy et al., 1998; Singh & Zlotnick, 2003; Zlotnick et al., 1996), mixing VLP product with a disassembly buffer (Bin Mohamed Suffian et al., 2017; K. W. Lee & Tan, 2008; Liew et al., 2012; Y. Zhang et al., 2021), or by dialysis (Holmes et al., 2015; Strods et al., 2015). While mixing is fast, it leads to dilution. Dialysis does not significantly change the original concentration and has the capability to remove some of the (encapsulated) impurities through the dialysis membrane (Mach et al., 2006) but is a slow process (Phillips & Signs, 2004). In recent publications, we have demonstrated the utility of transferring VLP process steps, namely capture and VLP reassembly, to a cross-flow filtration (CFF) unit (Hillebrandt et al., 2020; Rüdt et al., 2019). Figure 4.1A shows that these two process steps frame the disassembly step, which is one of the reasons why it was presumed to be useful to transfer this process step to cross-flow diafiltration (DF). As CFF process development is time and material consuming, it can be accelerated if the optimal DF buffer composition is known before.

In this study, we developed a time-resolved high-throughput disassembly screening for (chimeric) VLP candidates. This approach aims to reduce the experimental effort to identify optimal disassembly conditions for different VLPs and for CFF process development. Since candidate VLP material is scarce at an early stage of process development, it is highly desirable to develop a screening method which requires a small amount of VLPs. To this end, we developed a low-volume, fast, and accurate screening method that allows for assessment of VLP dimer yield and kinetic data based on a high-performance liquid chromatography (HPLC) system. Disassembly of a C-terminally truncated HBcAg and a chimeric C-terminally truncated HBcAg VLP with a polyhistidine tag was investigated (referred to as Cp149 and VLP A, respectively). Optimal disassembly conditions were selected for DF process

development. This integrated DF process step allows for disassembly and depletion of impurities simultaneously. Additionally, we show that the developed disassembly process step can be integrated into a filtration-based sequence of disassembly, dimer separation, and reassembly (Figure 4.1B). The results presented in this paper underline the influence of inserted peptides on the optimal conditions for disassembly and demonstrate the usefulness of the developed high-throughput screening method and its transferability to a filtration-based process.

4.2. Materials and methods

4.2.1. Materials, buffers, and VLPs

All chemicals were purchased from Merck KGaA (Darmstadt, DE), unless otherwise stated. Solutions and buffers were prepared with ultrapure water (PURELAB Ultra, ELGA LabWater, Lane End, UK). All buffers were pH-adjusted with 32% HCl or 4 M NaOH using a SenTix62 pH electrode (WTW, Weilheim, DE) at a HI 3220 pH meter (Hanna Instruments, Woonsocket, US-RI). Solutions were filtered before use and analysis through 0.2 µm cellulose acetate (VWR, Radnor, US-PA) or Millex-GV 0.22 µm polyvinylidene fluoride filters (Merck Millipore), often with glass fiber pre-filtration (Minisart GF, Sartorius Stedim Biotech GmbH, Göttingen, DE). The plasmid for Cp149, a C-terminally truncated HBcAg protein (amino acids 1 to 149 (Zlotnick et al., 1996)), was generously provided by Prof. Adam Zlotnick (Indiana University, Bloomington, US-IN). BioNTech Protein Therapeutics GmbH (Mainz, DE) generously provided the chimeric HBcAg VLP A plasmid. VLP A was C-terminally truncated, contained an inserted epitope, and incorporated a C-terminal polyhistidine tag, similar as in (Schumacher et al., 2018). The Cp149 and VLP A protein dimers had a molecular weight of approximately 34 kDa and 40 kDa, respectively. The 280 nm extinction coefficients were derived from the web-tool ProtParam (Gasteiger et al., 2005) and were 1.764 L g^{-1} cm^{-1} for Cp149 and 1.558 L g^{-1} cm^{-1} for VLP A. Concentrations were calculated using Beer's law and the 280 nm absorbance peak area derived from size-exclusion chromatography (SEC) HPLC. The HBcAg concentration of the VLP feedstock was determined analogously using the total 280 nm absorbance and a NanoDrop 2000c spectrometer (Thermo Fisher Scientific, Waltham, US-MA). HBcAg was expressed in *Escherichia coli,* liberated by lysis, precipitated and re-dissolved applying a centrifugation protocol similarly as described in a recent article (Hillebrandt et al., 2020). Additionally, the re-dissolved and sterile-filtered VLP solution was purified by DF and multimodal SEC as described in the Appendix B, Section S4.1.

4.2.2. Disassembly buffer compositions

The disassembly time series (DisA-TS) is a two-step procedure and described in detail in Section 4.2.3. Briefly, a batch disassembly reaction is followed by SEC-HPLC analysis under the same liquid phase conditions as in the batch reaction. This batch reaction is initiated by mixing equal volumes of HBcAg VLP solution and disassembly buffer in order to reach the target disassembly conditions after mixing. For all conditions, the common target concentrations were 50 mM Tris and 1 g L^{-1} HBcAg. Urea concentrations (c_{urea}) and pH were screened in the ranges from 0 M to 4 M and pH 7.2 to pH 9.0, respectively. The selection of the condition ranges was based on unpublished pre-experiments and other publications investigating HBcAg VLPs (Schumacher et al., 2018; Singh & Zlotnick, 2003). Each target condition required a distinct composition of the added disassembly buffer which was composed of Tris, urea, and titrant. Therefore, the required titrant concentration (c_{titrant}) of each disassembly buffer was determined to eventually reach the target pH after mixing with VLP solution. The procedure of this disassembly buffer composition determination is explained in Figure 4.2A. It was assumed that the protein buffer capacity of HBcAg at a concentration of 1 g L^{-1} is negligible. Under this assumption, 50 mM Tris at pH 7.2 was used to mimic the VLP solution and thereby minimize the VLP (product) consumption. The experiments were performed in duplicates and at a 200 mL scale to minimize pipetting errors. The results were exemplarily confirmed by mixing VLP solution and disassembly buffer at a 200 µL scale and measuring the resulting pH using an Orion PerpHecT ROSS combination micro electrode (Thermo Fisher Scientific).

4.2.3. Disassembly time series and disassembly on column

The DisA-TS is a hybrid disassembly screening in nature. It consists of a batch disassembly reaction followed by SEC-HPLC analyses. During the latter, the disassembly reaction continues until detection, similarly to the on-column disassembly reaction described below. The time series was started at time t_0 by adding 250 µL disassembly buffer to 250 µL VLP solution in a 2.2 mL deep-well plate (VWR) in intervals of 7.5 min between each well. The mixtures were incubated at 23 °C and repeatedly analyzed by SEC-HPLC over a period of 24 h at times t_i (Figure 4.2B). Analytical SEC was performed with 20 µL injections on an AdvanceBio SEC 300 Å, 4.6 × 150 mm, 2.7 µm column (Agilent Technologies, Santa Clara, US-CA) at a Dionex Ultimate 3000 RS UHPLC system with a diode array detector controlled by Chromeleon version 6.8 SR15 (Thermo Fisher Scientific). The mobile phase was adapted to the sample's target disassembly condition, and a flow rate of 0.35 mL min^{-1} was applied. Samples at pH 9.0 were analyzed at pH 8.0 due to the limited pH compatibility

of the column. The efficiency of a disassembly condition was described by the (total) dimer yield

$$Y_{\mathrm{dimer,tot}} = \frac{c_{\mathrm{dimer,tot}}(t)}{\bar{c}_{\mathrm{VLP}}(t_0) + \bar{c}_{\mathrm{dimer}}(t_0)}, \tag{4.1}$$

where $c_{\mathrm{dimer,tot}}(t)$ is the total dimer concentration at the time t after start of the disassembly at t_0. Further, $\bar{c}_{\mathrm{VLP}}(t_0)$ and $\bar{c}_{\mathrm{dimer}}(t_0)$ are the mean initial concentrations of HBcAg VLPs and dimers, respectively, which are present in the VLP feedstock prior to the disassembly reaction. Mean concentrations from 28 samples of the VLP solution at 1 g L^{-1} HBcAg were determined by SEC-HPLC as described above but with 50 mM Tris at pH 7.2 as mobile phase. During the 24 h DisA-TS, evaporation was observed. To estimate an average volumetric evaporation rate, the total HBcAg concentration of a VLP solution was analyzed twice with an interval of 20 h. The mean evaporation rate was then converted into evaporation correction factors $f_{\mathrm{v}}(t)$ that enabled the calculation of an evaporation-corrected concentration

$$c_{\mathrm{dimer,tot}}(t) = \frac{\tilde{c}_{\mathrm{dimer,tot}}(t)}{f_{\mathrm{v}}(t)}, \tag{4.2}$$

where $\tilde{c}_{\mathrm{dimer,tot}}(t)$ is the measured concentration during the DisA-TS. A derivation of $f_{\mathrm{v}}(t)$ and Equation 4.2 can be found in Appendix B, Section S4.4.

In order to investigate the disassembly reaction with a shorter time interval and without prior mixing or batch disassembly, the abovementioned SEC-HPLC method was used as an additional screening tool. This approach is in the following referred to as disassembly on column (DisA-OC) and shown in Figure 4.2C. To this end, a VLP solution with 1 g L^{-1} HBcAg (50 mM Tris, pH 7.2) was analyzed by SEC-HPLC applying the same flow rate and mobile phases at target disassembly conditions as described above. For our SEC-HPLC set-up, we determined the observed time interval $\Delta\bar{t}_{\mathrm{ret}} = \bar{t}_{\mathrm{ret}} - t_{\mathrm{inj}} = 3.36$ min, where $\bar{t}_{\mathrm{ret}}$ is the average retention time of the dimer peak over all experiments and t_{inj} is the injection time. For DisA-OC, the start of the disassembly was defined as $t_0 = t_{\mathrm{inj}}$.

The disassembly rate k_0 was calculated by

$$k_0 = \frac{c_{\mathrm{dimer,tot}}(t) - \bar{c}_{\mathrm{dimer}}(t_0)}{t - t_0}. \tag{4.3}$$

In the following, we define $k_{0,\mathrm{DisA\text{-}TS}}$ as the rate obtained by DisA-TS at $t = t_1 + \Delta\bar{t}_{\mathrm{ret}}$ and $k_{0,\mathrm{DisA\text{-}OC}}$ as the rate obtained by DisA-OC at $t = t_0 + \Delta\bar{t}_{\mathrm{ret}}$, where t_1 is the time of the first sampling after approximately 30 min.

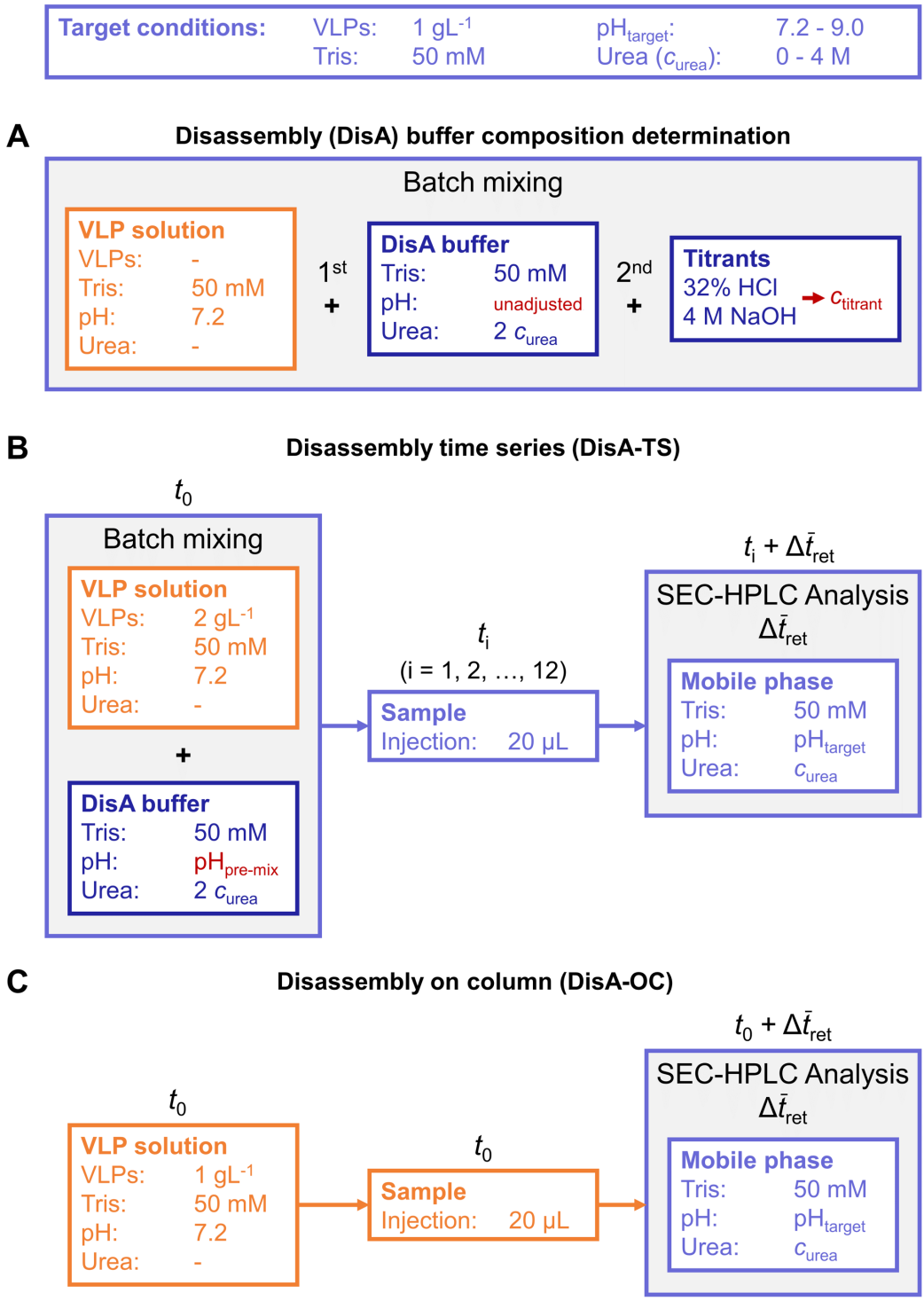

Figure 4.2. Schematic of the developed screening procedures. The large gray boxes represent mixtures of solutions represented by smaller boxes. (A) A separate experiment is required to determine each disassembly buffer composition by titration. First, VLP solution† is mixed with pH-unadjusted (non-titrated) disassembly buffer. Second, the mixture is titrated to the target pH (pH_{target}) and the required amount of titrant (either NaOH or HCl) is used to determine the titrant concentration of the final disassembly buffer $c_{titrant}$. (B) The DisA-TS is started at time t_0 by mixing VLP solution with an equal volume of disassembly buffer to

achieve the target disassembly condition. Samples are repeatedly drawn at times t_i ($i = 1, 2, \ldots, 12$) and analyzed by SEC-HPLC. The obtained results are assigned to $t = t_i + \Delta\bar{t}_{ret}$, where $\bar{t}_{ret}$ is the average SEC-HPLC retention time of the dimer peak. (C) The DisA-OC is started by injecting VLP solution onto the SEC-HPLC column under disassembly conditions at time t_0 without prior mixing or pre-experiments. The obtained SEC-HPLC results are assigned to $t = t_0 + \Delta\bar{t}_{ret}$. Abbreviations: c, concentration; DisA-OC, disassembly on column; DisA-TS, disassembly time series; HBcAg, hepatitis B core antigen; HPLC, high-performance liquid chromatography; SEC, size-exclusion chromatography; VLP, virus-like particle; t, point in time.
† Note: At low target HBcAg concentrations of up to approximately 1 g L^{-1}, the protein buffer capacity is negligible. Therefore, the determination of the disassembly buffer composition (A) can be performed with VLP solution with zero HBcAg concentration, i.e. 50 mM Tris, pH 7.2 buffer.

4.2.4. Filtration-based disassembly, dimer separation, reassembly

The sequential process of disassembly, dimer separation, and reassembly was realized in three steps as shown in Figure 4.1B. Step (I) was DF-based disassembly into a disassembly buffer using a 10 kDa molecular weight cut-off (MWCO), 88 cm^2 Ultracel Pellicon 3 membrane (Merck Millipore) followed by an 18 h overnight hold at 5 °C and subsequently by filtration through a 0.2 µm pore size cellulose acetate syringe filter (VWR). Note, that urea concentration and pH of the DF disassembly buffer were at target disassembly conditions. Step (II) consisted of dimer separation by dead-end ultrafiltration using Vivaspin Turbo 15 RC centrifugal filters with 100 kDa MWCO regenerated cellulose membranes (Sartorius Stedim Biotech GmbH). The disassembly solution was split in six centrifugal filters, which were operated at a relative centrifugal force of 1000 for 15 min, and the product was collected in the filtrate/permeate. The remaining retentate was equally reprocessed with a new filter. Step (III) was DF-based reassembly into 50 mM Tris buffer at pH 7.2 with 650 mM NaCl using a 10 kDa MWCO, 200 cm^2 Sartocon Slice 200 (Sartorius Stedim Biotech GmbH) where the product was collected from the retentate. Both DF process steps were realized on a KrosFlo Research KRIIi CFF system (Spectrum Labs, Rancho Dominguez, US-CA) at a constant volume of 30 mL, a feed flow rate of 30 mL min^{-1}, and permeate flow rate control at 2 mL min^{-1} as implemented previously (Hillebrandt et al., 2020). The corresponding permeate flux setpoints were 13.6 L m^{-2} h^{-1} and 6.0 L m^{-2} h^{-1} for disassembly and reassembly, respectively. The whole process was performed at room temperature (22.5±0.5 °C), unless otherwise stated.

At-line analysis of DF-based disassembly was performed analogously to the HPLC method in the DisA-TS. The mobile phase composition was adapted to the current theoretical buffer composition in the retentate. This was realized by mixing (A) 50 mM Tris at pH 7.2 with (B) the DF disassembly buffer.

Assuming ideal mixing and unrestricted permeability of urea during DF, the fraction of (B) equals $1 - e^{-\mathrm{DV}}$, where DV represents exchanged DF volumes (Kurnik et al., 1995). Feed and reassembly samples were analyzed with a Bio SEC-5 1000 Å, 4.6 × 300 mm, 5 µm column (Agilent Technologies), at a flow rate of 0.4 mL $\mathrm{min^{-1}}$, and in 50 mM Tris at pH 7.2 as mobile phase. Dimer separation samples were analyzed using the same column with the DF disassembly buffer as mobile phase. The resulting dimer concentrations before and after dimer separation were used to calculate the apparent retention coefficient of dimers under process conditions as

$$R_{\mathrm{dimer}} = 1 - \frac{c_{\mathrm{dimer,Sep}}}{c_{\mathrm{dimer,DisA}}}. \tag{4.4}$$

The dimer concentrations after disassembly/hold ($c_{\mathrm{dimer,DisA}}$) and after dimer separation ($c_{\mathrm{dimer,Sep}}$) represent the bulk (feed) and permeate concentrations, respectively.

4.3. Results and discussion

DisA-TS

The long-term development of the disassembly reaction was monitored using an initial batch disassembly reaction followed by twelve SEC-HPLC analyses over a time period of 24 h. The time series was initiated by mixing equal volumes of VLP solution and disassembly buffer (Figure 4.2B). The ionic strength of this mixture is different from the ones of the individual solutions before mixing. The ionic strength of a solution influences the $\mathrm{pK_a}$ of weak acids/bases, such as Tris, and ultimately the solution pH (Beynon & Easterby, 1996). Therefore, the pH does not change linearly with the volume shares upon mixing of VLP solution and disassembly buffer. This nonlinear behavior is not expected for non-dissociating species, such as urea in this screening. Next to the ionic strength, the urea concentration influences the pH of aqueous solutions (Bull et al., 1964). Instead of correcting the pH of the mixture by titration, the exact amount of titrant was determined beforehand in a separate experiment (Figure 4.2A). The disassembly buffer for the DisA-TS was then prepared according to the results of this experiment. Reaction analysis was carried out by a SEC-HPLC method, where the mobile phase composition was the same as the examined disassembly reaction conditions. Compared to using a standard analysis mobile phase, the disassembly reaction is less influenced using the mobile phase at disassembly conditions. The selected 300 Å pore size SEC-HPLC column led to separation of VLPs, dimers (capsomeres), and lower-molecular-weight species (LMWS) such as buffer substances, host cell proteins, and nucleic acids while ensuring a short total analysis time of 7.5 min. For a particular disassembly condition, this enabled

the analysis of four batches, here two different VLPs in duplicates, with a time interval of 30 min between each sampling.

DisA-OC

For determining initial disassembly rates, the abovementioned SEC-HPLC method was directly used as a screening tool (Figure 4.2C). Here, one needs to keep in mind that the reaction conditions are slightly different to the SEC-HPLC analysis in the DisA-TS, due to the unprocessed nature of the sample (pH = 7.2, no urea) and the immediate fractionation of the sample composition based on size and structure of the molecules.

4.3.1. Disassembly rate

Regarding the DisA-TS results, the slope of the dimer yield between the first measured sample ($t_1 + \Delta\bar{t}_{\mathrm{ret}} \approx 33.36$ min) and the starting VLP solution (t_0) can be converted into an approximate initial disassembly rate $k_{0,\mathrm{DisA\text{-}TS}}$ (Equation 4.3). For a better temporal resolution of the initial disassembly rate, the described SEC-HPLC method was used as a screening tool (DisA-OC) reducing the investigated reaction interval to the mean dimer retention time $\Delta\bar{t}_{\mathrm{ret}} = 3.36$ min. Here, VLPs in neutral buffer were directly injected into the mobile phase at disassembly conditions, resulting in an on-column disassembly reaction. Figure 4.3 shows a comparison of the two experimentally determined disassembly rates. While $k_{0,\mathrm{DisA\text{-}OC}}$ increased to 4.7 g L^{-1} h^{-1} for Cp149 and to 7.3 g L^{-1} h^{-1} for VLP A, $k_{0,\mathrm{DisA\text{-}TS}}$ was 1.1 g L^{-1} h^{-1} at most, confirming that $k_{0,\mathrm{DisA\text{-}OC}}$ is a more accurate representation of the initial disassembly rate. Comparing the two screening methods for Cp149, $k_{0,\mathrm{DisA\text{-}OC}}$ below 1.0 g L^{-1} h^{-1} resulted in a similar corresponding $k_{0,\mathrm{DisA\text{-}TS}}$. This behavior is expected if $k_{0,\mathrm{DisA\text{-}TS}}$ is a good representation of the actual initial disassembly rate in the first approximately 33 min. In this study, this is the case if the initial disassembly rate is smaller than 2 g L^{-1} h^{-1} and approximately constant during the observed interval, as the DisA-TS results for Cp149 in Figure 4.4A suggest. In contrast to Cp149, VLP A showed a steeply increasing dimer yield at the beginning which rapidly flattened out afterwards approaching equilibrium (Figure 4.4), resulting in larger $k_{0,\mathrm{DisA\text{-}OC}}$ (Figure 4.3). For fast disassembly reactions such as for VLP A, $k_{0,\mathrm{DisA\text{-}OC}}$ and especially $k_{0,\mathrm{DisA\text{-}TS}}$ are determined by dimer concentrations close to the equilibrium. This is why both could potentially serve as a predictive tool to find disassembly-competent VLP candidates or suggest a promising condition range for screening. Here, the experimental effort, resources, and time for a DisA-OC experiment would be significantly lower than for the DisA-TS. For example, the disassembly rates of 96 VLP candidates can be screened for one disassembly condition within 24 h.

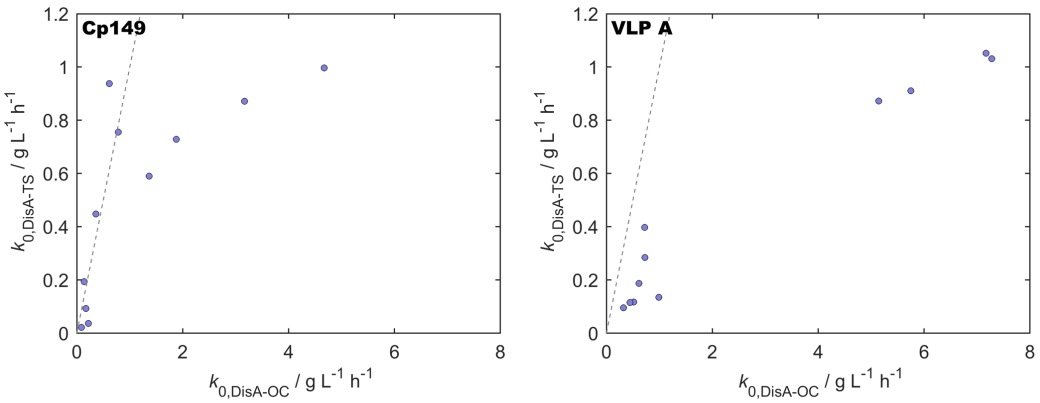

Figure 4.3. Comparison of the disassembly rates from disassembly time series ($k_{0,\text{DisA-TS}}$) and from disassembly on column ($k_{0,\text{DisA-OC}}$) at varying pH and urea concentration. The dashed line indicates equal values of $k_{0,\text{DisA-TS}}$ and $k_{0,\text{DisA-OC}}$. Standard deviations of duplicate measurements are not shown to enhance readability. They were below 0.02 g L^{-1} h^{-1} for $k_{0,\text{DisA-TS}}$ and below 0.18 g L^{-1} h^{-1} for $k_{0,\text{DisA-OC}}$.

4.3.2. Disassembly time series

The developed DisA-TS was applied to investigate the effect of varying c_{urea}, pH, and the combination of both on HBcAg VLP disassembly. From a process development perspective, a high yield obtained in reasonable process time, including knowledge about a potential operating window, is desirable. It is therefore interesting to observe the dimer yield in a time frame of 24 h.

4.3.2.1. Urea screening

Figure 4.4A shows the dimer yield of Cp149 and VLP A at pH 7.2 and varying c_{urea} over time. It has to be noted that the pre-disassembly VLP stock solution also was at pH 7.2 but contained no urea. For Cp149, this condition already resulted in the presence of HBcAg dimers, indicated by an initial dimer yield of 0.07, as similarly observed previously (Singh & Zlotnick, 2003). At the beginning of the reaction ($t \leq 6$ h), the dimer yield increased for all experiments, where a larger c_{urea} led to a stronger increase. After this initial period, the dimer yield still increased for $c_{\text{urea}} \leq 3$ M, stagnated for $c_{\text{urea}} = 3.5$ M, and decreased for $c_{\text{urea}} = 4$ M from a maximum of 0.65 to 0.63. Interestingly, $c_{\text{urea}} \geq 3$ M led to a faster yield increase but resulted in a similar final dimer yield of 0.62 at 24 h. VLP A disassembly was at a generally lower level for these conditions. The highest dimer yield after 24 h was observed for $c_{\text{urea}} = 3$ M. Similarly to Cp149, the dimer yields for a higher c_{urea} increased to a maximum before they declined. This effect was more pronounced for VLP A than for Cp149 and was strongest for $c_{\text{urea}} = 4$ M, where the maximum dimer yield of 0.27 was reached after 1.5 h, after which it decreased to 0.11

after 24 h. When dimer aggregation occurs, aggregate species are expected to have a higher molecular weight and therefore elute earlier than dimers in SEC-HPLC. Considering SEC-HPLC chromatograms of these samples (Appendix B, Figure S4.1), the decline in dimer yield was accompanied by a concentration increase of high-molecular-weight species (HMWS), pointing towards

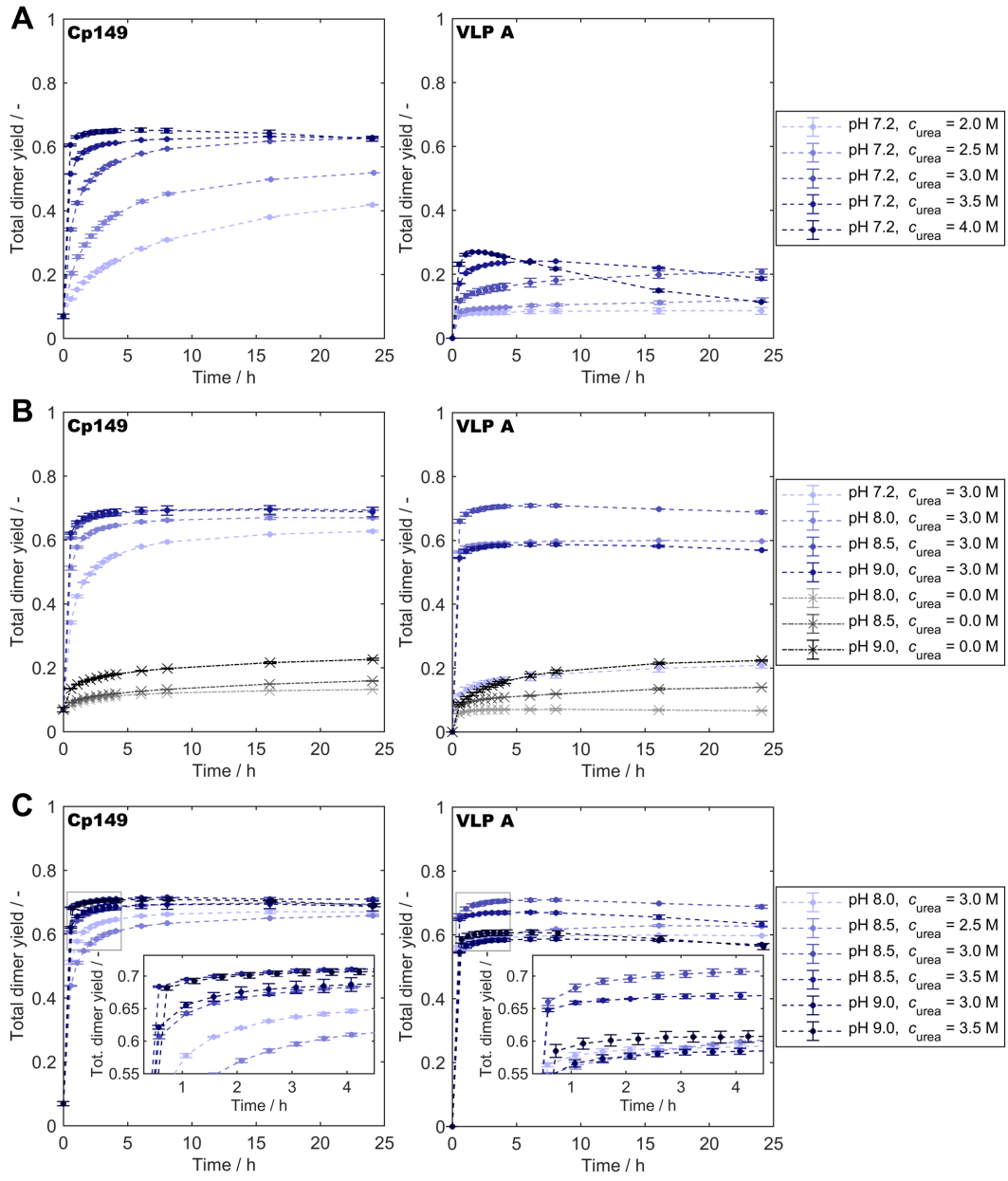

Figure 4.4. Screening of c_{urea} and pH by DisA-TS. Error bars represent the standard deviation of duplicate measurements, and dashed lines were added to guide the eye. (A) DisA-TS of c_{urea} at the same pH as the VLP solution before disassembly, pH 7.2. (B) DisA-TS of pH at a c_{urea} of 3 M (shades of blue) and without urea (shades of black). (C) Combined screening of c_{urea} and pH by DisA-TS. The gray box indicates the position of the magnification shown in the inserted plot. Abbreviations: c_{urea}, urea concentration; DisA-TS, disassembly time series; VLP, virus-like particle.

aggregation. This suggests that VLP A is more susceptible to urea-based degradation. VLP A differs from Cp149 by inclusion of a C-terminal His-tag and the integration of an epitope into the spike tip of the protein. The spike tip insertion could have an impact on dimer stability and thus influence its susceptibility towards urea degradation. The generally higher dimer yield at equal solution conditions for Cp149 as compared to VLP A might also be influenced by the inserted epitope, as an influence of insertions on VLP assembly and stability has been shown (Billaud et al., 2005; Karpenko et al., 2000). Interestingly, it has been reported that addition of a C-terminal polyhistidine tag leads to stabilized VLP structures that are more resilient towards mechanical and chemical stress (Schumacher et al., 2018). As a chemical stress, disassembly may be hampered by addition of a C-terminal polyhistidine tag, which could explain the lower dimer yields for VLP A as compared to Cp149 as observed at pH 7.2.

4.3.2.2. pH screening

Figure 4.4B presents data of pH screenings at $c_{\mathrm{urea}} = 0$ M and $c_{\mathrm{urea}} = 3$ M for Cp149 and VLP A. For both VLPs and c_{urea}, the dimer yield increased until 6 to 8 h. For most experiments, the dimer yield subsequently remained approximately constant. Experiments without urea and a pH ≥ 8.5 as well as $c_{\mathrm{urea}} = 3$ M, pH 7.2 showed a dimer yield increase from 8 h to 24 h. For high pH and c_{urea}, a slight decrease in dimer yield was observed. However, this decrease was less pronounced than for the experiments at $c_{\mathrm{urea}} = 4$ M, as described above. An interesting observation is that for $c_{\mathrm{urea}} = 3$ M, the experiment at pH 9.0, compared to the experiment at pH 8.5, showed slightly lower dimer yields for Cp149 and significantly lower dimer yields for VLP A. This decrease was probably caused by aggregation. This is supported by chromatograms of the pH 9 experiment, showing increased peak areas for HMWS (data not shown). In both experimental series, VLP A dimer yield increased faster relative to its respective maximum dimer yield. As explained above, Cp149 is substantially more inclined to disassemble at pH 7.2 while the experiments at pH > 7.2 did not result in a comparable trend, showing a more similar disassembly progress for VLP A and Cp149. Except for mild and aggregate-promoting conditions, dimer yields showed a plateau towards the end of the DisA-TS (24 h), as observed previously (Singh & Zlotnick, 2003).

4.3.2.3. Synergistic effects

The combination of increasing pH and c_{urea} generally led to higher dimer yields as compared to pH or c_{urea} increase alone. Figure 4.4C shows Cp149 and VLP A dimer yield over time for various combinations of high pH (pH 8 to pH 9) and c_{urea} (2.5 M to 3.5 M). A magnification of the figure reveals that

for Cp149, high c_{urea} and pH led to a steeper yield increase, which, however, resulted in similar final dimer yields of 0.66 to 0.71 after 24 h. For VLP A, this general trend is not applicable. VLP A showed yield decreases over the time course of the experiments at pH ≥ 8.5, indicating aggregation. Final dimer yields ranged from 0.56 to 0.69, where the highest final yield was observed for pH 8.5 and $c_{\mathrm{urea}} = 3$ M. Generally, it has to be noted that dimer yields below 1 are commonly observed for disassembly of *in vivo*-assembled VLPs, e.g. 0.58 to 0.89 in a recent publication (Y. Zhang et al., 2021). This behavior is expected for *in vivo*-assembled VLPs, where dis- and reassembly aim to remove inactive protein (Zlotnick et al., 2002).

A comprehensive overview of the impact of reaction conditions on maximum dimer yield and $k_{0,\mathrm{DisA\text{-}OC}}$ is given in Figure 4.5. While $k_{0,\mathrm{DisA\text{-}OC}}$ was similar for Cp149 and VLP A at pH 7.2, the maximum dimer yield was significantly higher for Cp149. At higher pH and c_{urea}, dimer yields were comparable between Cp149 and VLP A, while $k_{0,\mathrm{DisA\text{-}OC}}$ was generally higher for VLP A. This illustrates that not only the dimer yield but also $k_{0,\mathrm{DisA\text{-}OC}}$ is influenced by the molecular structure of the VLP, in this case the insertion of a foreign epitope and addition of a C-terminal polyhistidine tag for VLP A. In essence, the screening experiments showed that higher pH and c_{urea} lead to higher dimer yields, which is, however, limited by aggregation, especially for VLP A and at pH 9. The highest dimer yields after 24 h were 0.71 for Cp149 and 0.69 for VLP A, achieved at pH 8.5, $c_{\mathrm{urea}} = 3.5$ M and pH 8.5, $c_{\mathrm{urea}} = 3$ M, respectively.

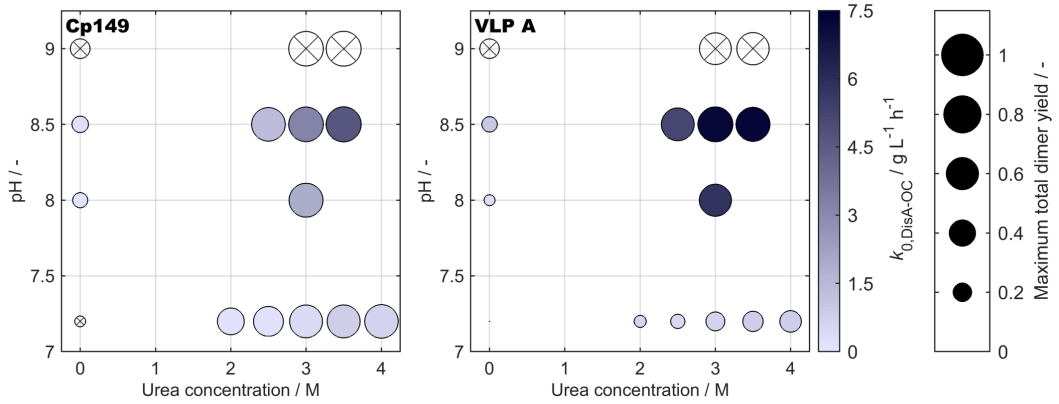

Figure 4.5. Effect of screening conditions on $k_{0,\mathrm{DisA\text{-}OC}}$ and total dimer yield of Cp149 and VLP A. The center of each bubble determines the screening conditions, urea concentration and pH. Color intensity and area of a bubble represent $k_{0,\mathrm{DisA\text{-}OC}}$ and the maximum of the total dimer yield, respectively. Note, the DisA-OC approach was not performed for conditions at pH 9 due to the pH limit of the SEC-HPLC column. Bubbles of conditions which did not allow for $k_{0,\mathrm{DisA\text{-}OC}}$ determination are transparent and marked with a black 'X'. Abbreviations: DisA-OC, disassembly on column; HPLC, high-performance liquid chromatography; $k_{0,\mathrm{DisA\text{-}OC}}$, disassembly rate from disassembly on column; SEC, size-exclusion chromatography.

4.3.3. Filtration-based dis- and reassembly

At a 30 mL scale, DF-based disassembly of Cp149 and VLP A was performed, followed by an 18 h overnight hold, a dimer separation step by dead-end filtration, and DF-based VLP reassembly (Figure 4.1B). In this study, disassembly is achieved by buffer exchange of 6 diafiltration volumes (DV) into the DF disassembly buffer, which is completed after approximately 90 min considering a permeate flow rate of 2 mL min^{-1}. An advantage of DF over other disassembly methods is the simultaneous increase in disassembly buffer component concentration and depletion of undesired LMWS (10 kDa MWCO), such as impurities or VLP stability-enhancing salts from previous process steps. This has implications on the design of the DisA-TS and the interested reader is referred to the Appendix B, Section S4.2. The MWCO selection was based on previous work (Rüdt et al., 2019) and provided full retention of dimers under the conditions used in this study. The conditions for DF-based disassembly were chosen based on the highest dimer yield in the DisA-TS, regardless of disassembly rate $k_{0,\text{DisA-OC}}$ (Section 4.3.1). Considering the expected DF process times and the implementation of an overnight hold, faster disassembly, i.e. larger $k_{0,\text{DisA-OC}}$, does not result in a significant advantage. Therefore, the disassembly process step was conducted at a target HBcAg concentration of 1 g L^{-1}, pH 8.5, and $c_{\text{urea}} = 3.5$ M for Cp149, or $c_{\text{urea}} = 3$ M for VLP A. Another, more differentiated consideration could be the preference of lower pH and urea concentration but a similar dimer yield to prevent 'alkaline stress' and to save resources. The results of the DisA-TS revealed that the dimer yield typically continues to increase after 90 min, which is the process time of DF-based disassembly. Therefore, a hold step was implemented after this process step. Another finding of the DisA-TS was that the highest dimer yields are often concomitant with a yield decrease towards the end of the observed 24 h period, especially for VLP A. In pre-experiments for VLP A, the overnight hold at room temperature resulted in a turbid solution that clogged a 0.2 µm pore size filter, indicating aggregation (data not shown). The turbidity of the process solution was avoided by cooling to 5 °C during the hold step and was implemented in all presented processes. Another potential measure to prevent aggregation is the supplementation of the disassembly buffer with additives such as NaCl (Singh & Zlotnick, 2003), glycerol (Schumacher et al., 2018), or surfactants (Shi et al., 2005). A screening for additives and their optimal concentration could easily be performed using the developed DisA-TS method, which is, however, out of the scope of this study. As observed in the DisA-TS, the highest dimer yield was 0.71. The remainder of the protein is regarded as inactive protein and is therefore removed in a separation step (Zlotnick et al., 1996, 2002). Here, dead-end

filtration with a 0.2 µm syringe filter and a 100 kDa MWCO membrane aimed for removal of undesired species with higher molecular weight than dimers. The MWCO of 100 kDa was selected as it successfully retained VLPs during the preceding purification (Appendix B, Section S4.1). The permeation of dimers through the centrifugal filter membrane was confirmed by SEC-HPLC in a preliminary test (data not shown). For the subsequent VLP reassembly, DF has proven to be a valuable tool (Liew et al., 2012; Rüdt et al., 2019) and was therefore applied for 3 DV in this study.

4.3.4. At-line monitoring of diafiltration-based disassembly

Figure 4.6 shows the DF-based dimer yield over process time determined by at-line SEC-HPLC. The mobile phase conditions were adapted to the current theoretical buffer composition in the retentate of the CFF unit (Section 4.2.4) aiming for a minimal bias of the analysis procedure with regards to the measured dimer yield. The same theoretical 280 nm extinction coefficient was used for all mobile phases in this study. It has to be noted that the absorption of proteins at 280 nm increases with increasing urea concentration (Pace et al., 1995) and thereby leads to a relative overestimation of the protein concentration for samples with higher urea concentration, which was considered negligible for this study. Compared to the DisA-TS, Figure 4.6 shows a 19%-increased initial (feed) dimer yield for Cp149. The feed solutions were frozen at larger scale than for the DisA-TS, most probably leading to a more pronounced freeze/thaw instability of Cp149 VLPs (Schumacher et al., 2018). The dimer yields at the end of the DF (1.4 h) were 0.73 for Cp149 and 0.77 for VLP A, which are higher compared to the DisA-TS results after 1.6 h with 0.70 and 0.69, respectively. The increased dimer yields for DF-based disassembly may result from the slower change of solution conditions avoiding urea concentration peaks or are due to intensified mixing by CFF.

4.3.5. Process data of the filtration-based process sequence

In addition to at-line analysis for dimer quantification during disassembly, all process steps were analyzed by off-line SEC-HPLC using a 1000 Å pore size column. This column allowed for a better separation and quantification of differently sized species as compared to the column used in the disassembly screening. Besides VLPs and dimers, a peak with HMWS larger than VLPs was detected. As already shown in a previous study (Hillebrandt et al., 2020), these HMWS are expected to be forms of HBcAg, such as partially reversible aggregates of VLPs or dimers (Newman et al., 2009; Schumacher et al., 2018), as mainly dimers are detected after disassembly. The recovered mass of each species after each process step is listed in Table 4.1. Besides the aforementioned species, a shoulder of the dimer peak and LMWS were

detected in the 280 nm chromatogram. According to their ultraviolet light spectra, the dimer shoulder is a protein species, which could constitute aggregated or partially unfolded forms (Samandoulgou et al., 2015) of the HBcAg dimers. According to their ultraviolet light spectra, the LMWS are a mixture of nucleic acids, buffer species, and/or proteins (data not shown). The content (by peak area) of LMWS after reassembly was 1.8% for Cp149 and 6.4% for VLP A while the dimer shoulder content was 4.0% and 0%, respectively. As no clear trend was observed, both species were not further investigated.

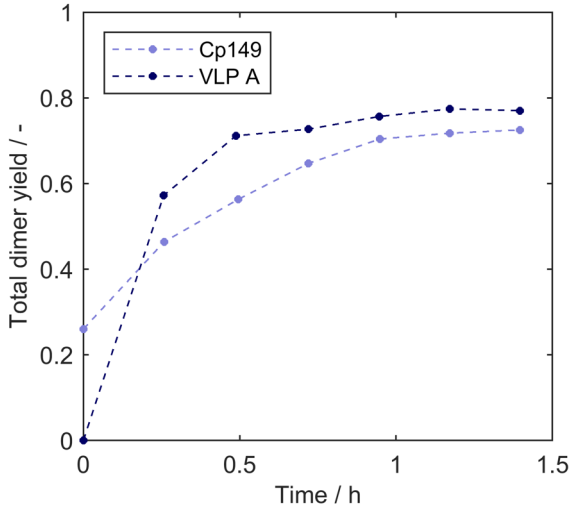

Figure 4.6. Total dimer yield determined by at-line SEC-HPLC during DF-based disassembly. The samples were taken at every DV, and the analysis was completed after a median duration of 13 min. Dashed lines were added to guide the eye. Abbreviations: DF, diafiltration; DV, diavolume; HPLC, high-performance liquid chromatography; SEC, size-exclusion chromatography.

During the 5 °C overnight hold, the Cp149 dimer yield further increased from 0.73 (Figure 4.6) to 0.84 (Table 4.1) showing no HMWS or VLPs. A potential reason for the higher dimer yield is the temperature-related pH increase. The strong temperature dependence of the Tris pK_a (Beynon & Easterby, 1996) resulted in a measured increase of ~0.3 pH units for the used DF disassembly buffer. Further, decreasing the temperature might increase the extent of disassembly as the opposite reaction, i.e. VLP assembly, is favored at higher temperature (Ceres & Zlotnick, 2002). Due to the cooling costs and the long down time, the overnight hold seems not profitable at a larger scale and an immediate continuation of the process is suggested in this case. Note, that a potential yield loss due to the 0.2 µm filtration is included in the aforementioned yields and was not separately investigated. For the dimer separation step, the apparent retention coefficient of dimers R_{dimer} was determined under process conditions. Based on the results in Table 4.1, R_{dimer} was 0.10 for Cp149 and 0.18 for VLP A. The higher retention of VLP A dimers

probably results from the higher level of HMWS. The retained HMWS can build up a fouling layer that has been shown to influence the overall selectivity of a fouled membrane in the case of albumins (Meireles et al., 1991). Another possible explanation could be interaction phenomena resulting from different molecular properties of VLP A compared to Cp149, e.g. size, shape, charge, or hydrophobicity. Overall, R_{dimer} describes the real dimer retention under process conditions not solely the ideal dimer retention of the selected membrane. The dimer separation MWCO was not optimized but membranes with a higher MWCO are expected to increase the dimer yield (decrease R_{dimer}) while a lower MWCO might improve the HMWS removal (and vice versa).

Table 4.1. Summary of process data for the filtration-based downstream process. The product species differ between process steps. HMWS, VLPs, and dimers are regarded as product species of the feed, while dimers are regarded as product species of disassembly & hold and dimer separation. For reassembly, VLPs are regarded as product species. The recovered product species mass of each step is printed in bold. Step yield, concentration, and A260/A280 refer to the product species of each step. Abbreviations: A260/A280, 260 nm to 280 nm absorbance peak area ratio; conc., concentration; HMWS, high-molecular-weight species; VLP, virus-like particle.

	Process step	HMWS mass	VLP mass	Dimer mass	Step yield†	Conc.†	A260/A280†
		mg	mg	mg	-	gL^{-1}	-
Cp149	Feed	**1.17**	**15.89**	**6.93**		0.82	0.61
	Disassembly & hold	0	0	**20.04**	0.84	0.67	0.55
	Dimer separation	0	0	**16.33**	0.82	0.60	0.55
	Reassembly	0.22	**14.19**	1.59	0.87	0.46	0.61
VLP A	Feed	**10.65**	**13.71**	**0.08**		0.84	0.67
	Disassembly & hold	0.20	1.06	**17.76**	0.73	0.62	0.56
	Dimer separation	0.11	0.21	**13.91**	0.78	0.51	0.56
	Reassembly	0.31	**7.90**	0.87	0.57	0.26	0.63

† Refers to the step product species (see caption).

The filtration-based process sequence resulted in 14.19 mg of reassembled Cp149 VLPs and 7.90 mg of VLP A, reducing the HMWS content by 0.95 mg (81%) and 10.34 mg (97%), respectively. An interesting observation was that the process with VLP A produced more dimer than VLP was present in the feed solution, indicating that HMWS are, at least partially, disassembly-competent. Product loss during DF-based disassembly, dimer separation, and reassembly was presumably caused by adsorption to the membrane, hold-up volumes,

and aggregation. As already observed in the DisA-TS, VLP A showed a greater tendency to aggregate. Next to the disassembly process, aggregation challenges have also been reported for reassembly (Y. Ding et al., 2010; Rüdt et al., 2019). For the interested reader, a detailed interpretation of the VLP A product loss can be found in the Appendix B, Section S4.3.

The disassembly experiments showed an initial increase of the transmembrane pressure (Appendix B, Figure S4.2). As this pressure increase is concomitant with the degree of buffer exchange and comparably constant towards the end, it can most probably be attributed to the viscosity increase (van Reis & Zydney, 2010) due to the increasing urea concentration (Kawahara & Tanford, 1966). Reassembly experiments showed slightly decreasing transmembrane pressures over time (Appendix B, Figure S4.2). Overall, DF-based dis- and reassembly resulted in low mean transmembrane pressures of 0.15 bar and 0.10 bar, respectively, with mean absolute deviations of 0.01 bar for each run. For both membranes, cleaning according to the manufacturer's instructions recovered the water permeabilities compared to the ones before the experiment (note, that new membranes were conditioned during pre-experiments to avoid yield or permeability loss due to adsorptive effects). To this end, membrane fouling had no noticeable effect on the filtration performance and was not irreversible. Nevertheless, the permeate flux and membrane loading (amount of retained solutes per membrane area) were comparably low (Liew et al., 2012; Rosenberg et al., 2009; Rüdt et al., 2019; van Reis, Goodrich, Yson, Frautschy, Whiteley, et al., 1997) and not optimized in this study. Hence, membrane fouling and product quality should be carefully investigated when these parameters are increased for economic reasons.

The 260 nm to 280 nm absorbance ratio (A260/A280) is an indicator for the nucleic acid content in a protein solution (Layne, 1957; Porterfield & Zlotnick, 2010) but is also influenced by the solution conditions, such as the urea concentration (Donovan, 1969; Pace et al., 1995). Therefore, only samples analyzed under the same solution conditions can be compared, which are feed and reassembly as well as disassembly/hold and dimer separation. For Cp149, the A260/A280 was equal for these pairs (Table 4.1). It was 0.61 for the feed and after VLP reassembly, where 0.60 was previously regarded as pure non-truncated HBcAg monomer in water, based on theoretical considerations (Porterfield & Zlotnick, 2010). The A260/A280 of dimers after disassembly was 0.55 for Cp149 and 0.56 for VLP A and remained constant after dimer separation. The Cp149 A260/A280 is comparable to 0.57 obtained by affinity chromatography at a urea concentration of 4 M (Y. Zhang et al., 2021). The A260/A280 of the VLP A feed was 0.67 and was decreased to 0.63 after reassembly, indicating the removal of nucleic acids. It is important to mention

that the feed A260/A280 in Table 4.1 is calculated based on the peak areas of HMWS, VLPs, and dimers while it was 0.64 for the VLP peak, suggesting that the depleted nucleic acids were mainly associated with (or bound to) the HMWS. This was also observed in a recent study with murine polyomavirus VLPs (Gerstweiler, Bi, et al., 2021). Both VLPs used in this study lack of the C-terminal protamine-like region of the wild-type HBcAg, which reduces packaging of nucleic acids (Crowther et al., 1994; Zlotnick et al., 1997). Considering VLPs with a higher nucleic acid burden, the developed process sequence could demonstrate even better separation capacities. For further improvement of the purification performance, strongly bound nucleic acids could be digested by a nuclease after disassembly (Y. Zhang et al., 2021) and nucleotides washed out as described previously (Hillebrandt et al., 2020). Another reason for dis- and reassembly lies in the improvement of particle structure and homogeneity (Mach et al., 2006; Q. Zhao, Allen, et al., 2012). This could be shown, especially for VLP A, by the reduction of the HMWS content, suggesting improved VLP homogeneity.

In summary, the filtration-based process sequence has proven efficient in the realization of dis- and reassembly, depleting impurities, and decreasing the HMWS content. An observation during DF-based reassembly was the presence of a small fraction of unassembled protein at the end of the process. A polishing step by flow-through multimodal SEC (Hillebrandt et al., 2020) or an integrated formulation step by DF are conceivable. The integrated formulation step could simultaneously deplete residual unassembled protein and LMWS by appropriate choice of the MWCO, e.g. 300 kDa.

4.4. Conclusions

In this study, we developed a low-volume and high-resolution screening for VLP disassembly conditions. Regarding time and material consumption, this method allows for an efficient determination of the dimer yield and kinetic data of VLPs and is thereby a powerful tool to accelerate VLP downstream process development. Two method variants were developed, one with minimal impact on the disassembly conditions and therefore resulting in an accurate description of the disassembly reaction. Another variant, DisA-OC, allows for higher throughput serving as an indicator for VLP disassembly efficiency of the tested solutions. A synergistic effect of pH and urea on the dimer yield was shown for both investigated *in vivo*-assembled HBcAg VLPs, whereas differences in disassembly rate and aggregation tendency were observed. In the second part of this work, a filtration-based downstream process for VLPs was developed focusing on DF-based disassembly. Here, the optimized disassembly conditions derived from the high-throughput screening were applied and achieved even higher dimer yields of up to 0.84

and a simultaneous reduction of nucleic acids. In the following process steps, capsomeres (HBcAg dimers) were separated from larger species and successfully reassembled to VLPs proving the feasibility of a solely filtration-based VLP downstream processing. The predominantly size-based separations in this approach promise a simple transfer to other chimeric VLP candidates or VLPs.

Acknowledgments

This project received funding from Deutsche Forschungsgemeinschaft (DFG) in the frame of SPP 1934, project number 273937032. The authors would like to thank BioNTech Protein Therapeutics (Thorsten Klamp and Anja Wilming) as well as Adam Zlotnick and Kim Young for the provision with VLP production plasmids. The authors express their gratitude to Heidemarie Knierim for proofreading.

Supplementary material

Appendix B contains the supplementary material associated with this chapter:

- S4.1 Purification of virus-like particles
- S4.2 Implications of diafiltration-based depletion of solution components on disassembly time series
- S4.3 Extended discussion of the filtration-based process for VLP A
- S4.4 Derivation of the evaporation correction factors (Equation 4.2)
- S4.5 Supplementary figures

5

Process monitoring framework for cross-flow diafiltration-based virus-like particle disassembly: Tracing product properties and filtration performance

Nils Hillebrandt[a], *Philipp Vormittag*[a], *Annabelle Dietrich*[a], *Jürgen Hubbuch*[a]

[a] Institute of Engineering in Life Sciences - Section IV: Biomolecular Separation Engineering, Karlsruhe Institute of Technology (KIT), Karlsruhe, Germany

Abstract

Virus-like particles (VLPs) are an emerging biopharmaceutical modality with great potential as a platform technology. VLPs can be applied as gene therapy vectors and prophylactic or therapeutic vaccines. For non-enveloped VLPs, recombinant production of the protein subunits leads to intracellular self-assembly. The subsequent purification process includes VLP dis- and reassembly which aim at removing encapsulated impurities and improving particle properties. Filtration-based separation and processing has proven successful for VLPs but requires large product quantities and laborious experiments in early development stages. Both challenges can be tackled by implementation of process analytical technology (PAT) to efficiently obtain extensive process information. In this study, an existing PAT setup was extended to comprehensively monitor the diafiltration-based disassembly of hepatitis B core antigen (HBcAg) VLPs. Process-related signals were monitored in-line, while product-related signals such as ultraviolet light (UV) spectra, static and dynamic light scattering (SLS and DLS) were monitored on-line. The applicability of the sensors for disassembly monitoring was evaluated under varying processing conditions. HBcAg VLP subunit concentrations were accurately predicted based on UV data using ordinary and partial least squares regression models (Q^2 from 0.909 to 0.976). DLS data

were used for aggregation monitoring while the SLS intensity qualitatively reflected the disassembly progress.

5.1. Introduction

Virus-like particles (VLPs) are particulate assemblies of viral subunit proteins that lack the viral genome. This makes VLPs non-infectious and thus versatile biopharmaceuticals. VLPs usually resemble their originating virus and can therefore be applied as vaccines against the native virus. Among these, vaccines against hepatitis B (for instance Recombivax HB by Merck & Co, Inc or Engerix-B by GlaxoSmithKline Biologicals), human papillomavirus (for instance Gardasil by Merck & Co, Inc or Cervarix by GlaxoSmithKline Biologicals), or hepatitis E (Hecolin by Xiamen Innovax Biotech) are approved for human use. So-called chimeric VLPs contain a foreign peptide or epitope which is inserted into or fused to the protein subunit. Multiple chimeric VLP vaccine candidates were developed against infectious diseases such as malaria (Kingston et al., 2019; Rutgers et al., 1988), influenza A (Neirynck et al., 1999), coronavirus disease 2019 (COVID-19) (Chu et al., 2021; Tan et al., 2021; Yang et al., 2021; Zha et al., 2021), or choriomeningitis (Sedlik et al., 1997). The malaria vaccine RTS,S/AS01 (Chandramohan et al., 2021) is approved as Mosquirix by GlaxoSmithKline Biologicals and was recently recommended by the WHO (World Health Organization, 2021) for children living in countries with a certain malaria transmission. Furthermore, chimeric VLPs are potential prophylactic or therapeutic vaccines against various cancers (Kaufmann et al., 2007; Klamp et al., 2011; Palladini et al., 2018; Y. Zhang et al., 2007). VLPs and chimeric VLPs are also applied as nanocarrier for therapeutic cargo such as nucleic acids, proteins, or chemical drugs (Ashley et al., 2011; Cerqueira et al., 2017; Hartzell et al., 2020; Petrovskis et al., 2021; Shan et al., 2018).

The spontaneous self-assembly of subunits into VLPs in the host cell (*in vivo*) may lead to malformed VLPs (Roldão et al., 2012) or encapsulated impurities (Mohsen et al., 2018; Strods et al., 2015; Vicente, Mota, et al., 2011). The disassembly of these *in vivo*-assembled VLPs into subunits and the following reassembly has been shown to improve their homogeneity, stability, and immunogenicity (Q. Zhao, Allen, et al., 2012; Q. Zhao, Modis, et al., 2012). While dis- and reassembly are beneficial regarding the purity and structure of the VLPs, it also enables packaging of therapeutic cargo (Ashley et al., 2011; Cerqueira et al., 2017; Petrovskis et al., 2021; Shan et al., 2018). VLP disassembly is usually performed by changing the liquid phase conditions, namely pH, ionic strength, and the concentration of chaotropic or reducing agents (Ashley et al., 2011; Carreira et al., 2004; Hillebrandt et al., 2021; McCarthy et al., 1998). The change of the liquid phase conditions can be

performed by dialysis at laboratory scale (Holmes et al., 2015; Strods et al., 2015) but at a larger scale more efficient processing by diafiltration (Phillips & Signs, 2004) is desirable. Cross-flow filtration (CFF) or tangential flow filtration (TFF) has proven as suitable downstream processing operation for virus and VLP processing (Carvalho et al., 2019; Grzenia et al., 2008; Hillebrandt et al., 2020; Kalbfuss et al., 2007; Liew et al., 2012; Lin et al., 2015; Moleirinho et al., 2018; Negrete et al., 2014; Peixoto et al., 2007; Wickramasinghe et al., 2005). Therefore, we recently implemented a diafiltration-based VLP disassembly process step which showed additional purification capabilities (Hillebrandt et al., 2021).

The efficiency and duration of the disassembly reaction mainly depends on the liquid phase conditions (Ausar et al., 2006; Hillebrandt et al., 2021; Mach et al., 2006; Mellado et al., 2009). Changes in the amino acid sequence, such as for chimeric variants, have also been shown to influence the VLP disassembly (Carreira et al., 2004; Hillebrandt et al., 2021; Schumacher et al., 2018). Furthermore, it is presumed that the encapsulation of nucleic acids impacts the stability of certain VLPs (Porterfield et al., 2010; van Rosmalen et al., 2018; Yuan & Parrish, 2001). Variations in the impurity profile, namely the nucleic acid content, can therefore affect the disassembly performance.

In the development and manufacturing stage of (bio-) pharmaceuticals, process analytical technology (PAT) is a valuable tool to obtain process knowledge or facilitate process control through monitoring to ultimately ensure a high product quality (U.S. Food and Drug Administration, 2004). Recently, PAT was implemented to monitor critical quality attributes during CFF processes of biopharmaceutical proteins (Rolinger, Rüdt, Diehm, et al., 2020; Wasalathanthri et al., 2020; West et al., 2021). In the case of VLP disassembly, PAT could reveal the effect of changing liquid phase conditions or impurity levels on diafiltration-based disassembly and provide a solution for a data-based endpoint detection. A previously developed monitoring setup for diafiltration-based VLP reassembly showed high accuracy and revealed detailed insights into the reassembly process (Rüdt et al., 2019). The implementation of a PAT setup for VLP disassembly could complement the knowledge gained with insights into the preceding process step and enable a combination of both technologies, potentially creating synergies.

This study thus implements a monitoring framework as a PAT tool for the VLP disassembly using on-line ultraviolet light (UV) and light scattering sensors. An existing setup was advanced by on-line display of static light scattering (SLS) and by diafiltration progress monitoring using conductivity and pH. Hepatitis B core antigen (HBcAg) VLPs were used as non-enveloped model VLPs which disassemble into homodimeric HBcAg subunits. They are widely

used, especially as a platform for chimeric VLPs (Karpenko et al., 2000; Kingston et al., 2019; Klamp et al., 2011; Y. Zhang et al., 2007) and as a nanocarrier (Petrovskis et al., 2021; Shan et al., 2018; Strods et al., 2015). The capabilities of the PAT tool concerning the disassembly of *in vivo*-assembled VLPs were evaluated by variation of the process duration and liquid phase conditions such as impurity level or salt concentration. The data were further used to compare simple and more complex control strategies based on univariate and multivariate data. Multivariate data analysis was based on ordinary least squares (OLS) and partial least squares (PLS) regression models.

5.2. Materials and methods

5.2.1. Chemicals, buffers, and VLPs

The chemicals used in this study were obtained from Merck KGaA (Darmstadt, DE), unless otherwise stated. All buffers and solutions were prepared with ultrapure water (PURELAB Ultra, ELGA LabWater, Lane End, UK), their pH adjusted with 32% HCl or 4 M NaOH (SenTix62 pH electrode (WTW, Weilheim, DE) and HI 3220 pH meter (Hanna Instruments, Woonsocket, US-RI)), and filtered with 0.2 µm-pore size cellulose acetate filters (VWR, Radnor, US-PA). The HBcAg protein used in this study, Cp149, was truncated at its C-terminus and thereby contained only the first 149 amino acids (Zlotnick et al., 1996). Cp149 was heterologously produced in *Escherichia coli* as previously described (Hillebrandt et al., 2020). The plasmid containing the Cp149 genes was kindly provided by Prof. Adam Zlotnick (Indiana University, Bloomington, US-IN). The downstream process consisted of lysis by sonication, capture by precipitation/re-dissolution, and purification by diafiltration and multimodal size-exclusion chromatography (SEC) as previously described (Hillebrandt et al., 2021). The final VLP feedstock for this study was stored at -20 °C and contained 3.7 g L^{-1} Cp149 in feed buffer (50 mM Tris at pH 7.2). The Cp149 dimer (further referred to as 'dimer') molecular weight and extinction coefficient at 280 nm were determined to be 34 kDa and 1.764 L g^{-1} cm^{-1}, respectively, both based on the amino acids sequence (Gasteiger et al., 2005). A disassembly buffer consisting of 50 mM Tris and 3 M urea at pH 8.5 was used as diafiltration buffer. The feedstock NaCl concentration was adjusted with a 50 mM Tris, 505 mM NaCl high-salt buffer at pH 7.2.

5.2.2. Filtration and monitoring setup

Diafiltration experiments were performed using a KrosFlo Research KRIIi CFF unit with backpressure valve (Spectrum Labs, Rancho Dominguez, US-CA). The CFF system was equipped with a stirred retentate reservoir (Sartorius Stedim Biotech GmbH, Göttingen, DE) and a 10 kDa molecular weight cut-off, 88 cm^2 Ultracel Pellicon 3 membrane (Merck Millipore). Permeate flow rate

control was implemented using a SLS-1500 liquid flow meter (Sensirion AG, Stäfa, CH; note that SLS does not stand for static light scattering in this case) with feedback to the backpressure valve as previously described (Hillebrandt et al., 2020). The feed line contained a T-piece with a septum for at-line sampling (injection plug, Fresenius Kabi, Bad Homburg, DE). A piping and instrumentation diagram of the monitoring setup is shown in Figure 5.1. It was based on a previously established setup (Rüdt et al., 2019) which was extended by several components. Besides the standard in-line pressure sensors, in-line pH and in-line conductivity sensors were implemented. In detail, a pH electrode including flow cell (product number: 18-1134-84, GE Healthcare, Uppsala, SE) was connected to a HI 3220 pH meter (Hanna Instruments) and a conductivity flow cell (product number: 18-1111-05) including a pH/C-900 monitoring unit (GE Healthcare) which was connected to a NI USB-6008 data acquisition device (National Instruments, Austin, US-TX). On-line monitoring was performed with a sample loop which was supplied with a constant flow rate setpoint of 1 mL min^{-1} using a Minipuls 3 peristaltic pump (Gilson, Villiers le Bel, FR). The flow rate measurement from a second SLS-1500 flow meter

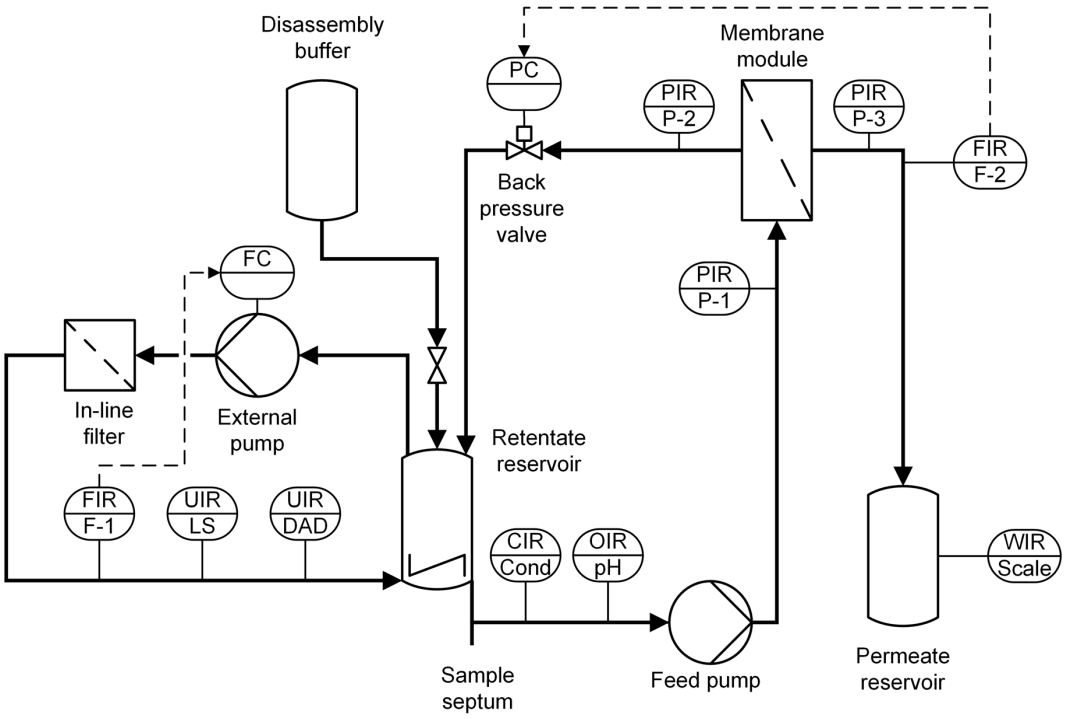

Figure 5.1. Piping and instrumentation diagram of the monitoring setup. All devices are connected to a personal computer (not shown to preserve clarity) with a graphical user interface that allows for the management of digital connections and settings. It further performs data management which includes recording and storage, supply of actuator controllers with sensor data, and real-time visualization of sensor data. Abbreviations: C (first letter) and Cond, conductivity; C (second letter), control; DAD, diode array detector; F, flow; I, indication; LS, light scattering; O, pH; P, pressure; R, recording; U, multivariable (spectrometry); W, weight.

(Sensirion) was the input for an integral controller that controlled the pump speed via the data acquisition device to maintain the desired flow rate. A Minisart GF glass fiber filter (Sartorius Stedim Biotech GmbH) with 0.7 μm^2 pore size was used as a bubble and particle trap to enhance measurement performance. A Zetasizer Nano ZSP light scattering spectrometer (Malvern Instruments, Malvern, UK) with a 10 mm path length cuvette (Hellma Analytics, Müllheim, DE) and a DAD-3000 RS diode array detector with a 0.4 mm path length flow cell (both Thermo Fisher Scientific, Waltham, US) were implemented as sensors in the on-line loop. The elements of the on-line loop were connected by PEEK capillaries with an inner diameter of 0.75 mm whereas the last one in flow direction had an inner diameter of 0.25 mm to increase the backpressure and improve measurement quality.

5.2.3. Diafiltration experiments

The disassembly was performed by constant volume diafiltration of 30 mL feed solution into disassembly buffer. The CFF feed and on-line loop flow rates were 30 mL min^{-1} and 1 mL min^{-1}, respectively. The feed conditions and further process parameters of the disassembly experiments are listed in Table 5.1. The Cp149 concentration was adjusted by dilution with feed buffer based on the 280 nm absorbance (NanoDrop 2000c, Thermo Fisher Scientific) and the Cp149 extinction coefficient. NaCl concentration and 260 nm to 280 nm absorbance ratio (A260/A280) were adjusted by dilution with high-salt buffer or less purified feed solution (post capture) instead of feed buffer. The feed solution was filtered by a 0.2 µm pore size cellulose acetate syringe filter (VWR, Radnor, US-PA). The CFF unit and the on-line loop were flushed with feed buffer prior to the experiment. A detailed description of the startup procedure can be found elsewhere (Rüdt et al., 2019). The membrane was cleaned according to the manufacturer's instructions between experiments. During diafiltration, 0.4 mL samples were taken at each diafiltration volume (DV), filtered by 0.22 µm pore size polyvinylidene fluoride Millex-GV filters (Merck Millipore), and analyzed by at-line SEC high-performance liquid chromatography (HPLC) as previously described (Hillebrandt et al., 2021). Briefly, the mobile phase was adapted to the composition of the analyzed sample, i.e. the retentate buffer composition at the time of sampling, using mixtures of feed and disassembly buffer. SEC-HPLC concentrations were calculated from the peak areas using Beer's law.

5.2.4. Data acquisition, processing, and analysis

All sensors and actuators of the experimental setup were connected to a computer running a custom-made MATLAB application with a graphical user interface (version R2019b, The Mathworks Inc., Natick, US-MA) that enabled

Table 5.1. Feed conditions and processing parameters of the monitored diafiltration-based disassembly experiments. The classification into calibration set and external validation set for regression modeling is specified in the last column. Abbreviations: A260/A280, absorbance ratio 260 nm to 280 nm; cal., calibration; conc., concentration; DV, diafiltration volumes; val., validation.

Experiment	Cp149 conc.	Permeate flux	NaCl conc.	A260/A280	Duration	Set
	g L^{-1}	L m^{-2} h^{-1}	mM	-	DV	-
Run 1	0.50	14	0	0.65	6	Cal.
Run 2	1.04	14	0	0.65	6	Val.
Run 3	2.06	14	0	0.65	6	Val.
Run 4	1.01	14	300	0.65	10 (6†)	Cal.
Run 5	1.83	14	0	0.74	6	Cal.
Run 6	2.02	24	0	0.65	6	Cal.

† Regression model calibration was performed with data of the first 6 DV.

central data collection, live visualization, and device control. The latter included the setting of a common time base, start/stop of acquisitions or actuations, integral control of the on-line loop pump, and data supply for the backpressure valve. The time alignment of the sensor data was performed by subtracting its delay time with respect to the retentate reservoir. DV were calculated from the permeate mass assuming a constant density of 1.045 g cm^{-3} and retentate volume of 30 mL. The dimer yield was calculated from the initial Cp149 and final dimer masses which were defined as the product of at-line SEC-HPLC concentrations and the process volume.

Light scattering data were acquired at 23 °C and 173° backscatter in the Zetasizer's chromatography mode with a measurement duration (interval) of 10 s. Viscosities and refractive indices were assumed to be constant and set in the Zetasizer Software (version 7.12, Malvern Instruments) based on stored values for protein (sample) and the disassembly buffer composition (dispersant). The laser attenuation was adapted to aim for a SLS intensity in the range between $0.2 \cdot 10^6$ s^{-1} and $1.5 \cdot 10^6$ s^{-1} and corrected by attenuation factors according to the manufacturer's instructions. Smoothing of the recorded z-average hydrodynamic particle diameter (z-average) was performed by a moving median with a window of six data points (~1 min).

UV spectra were recorded in the wavelength range between 240 nm and 340 nm at a resolution of 1 nm and a frequency setpoint of 1 Hz. The on-line measured protein concentration was calculated from the 280 nm absorbance using Beer's law. The a/b ratio (Ragone et al., 1984) and the location of the

minimum near 293 nm (tryptophan shift (Mach & Middaugh, 1994)) were determined by second derivative spectroscopy of the recorded spectra. A detailed description of the procedure can be found elsewhere (Ausar et al., 2006; Rüdt et al., 2019).

5.2.5. Regression modeling

Regression models were calibrated for the prediction of dimer concentrations from on-line UV data. PLS modeling was performed in MATLAB (version R2019b, The Mathworks Inc.) similarly as described by (Großhans et al., 2018) but without any preprocessing. Briefly, the data of the first 6 DV of runs 1 and 4 to 6 (Table 5.1) were used for calibration by cross validation (CV) where each run represented one CV group. Repeatedly, one CV group was excluded and a PLS-1 regression (SIMPLS algorithm (de Jong, 1993), function *plsregress*) was performed with the remaining data until each group was excluded once. The predictive residual sum of squares (PRESS) was summed up over all iterations and scaled by the number of samples and number of latent variables (nLV) (Wold, Sjöström, et al., 2001). The coefficient of determination R^2, the cross-validated coefficient of determination Q^2_{CV}, and the root mean square error of cross validation (RMSECV) were calculated according to (Wold, Sjöström, et al., 2001). Note that Q^2_{CV} and RMSECV were derived from the accumulated PRESS. The data of the remaining two runs 2 and 3 (Table 5.1) were used as external validation set. Details on the calculation of the coefficient of determination using the external validation dataset Q^2_{Ext}, and the root mean square error of prediction (RMSEP) can be found in (Nilsson et al., 1997) and (Kessler, 2006), respectively. The workflow for the OLS model was performed identically using two input variables resulting in a multiple linear model.

Before the calibration of the final PLS model, the nLV of the model was determined based on the Q^2_{CV}. Therefore, PLS models were calibrated for $1 \leq nLV \leq 9$. With increasing nLV, the first model which resulted in a local Q^2_{CV} maximum above 0.9 was selected. To further improve the PLS model, an additional variable selection was performed. Variable selection was optimized using a genetic algorithm (function *ga* for mixed integer optimization (Deep et al., 2009)) with a population size of 500, similarly as suggested by (C. M. Andersen & Bro, 2010). The objective was to find a combination of wavelengths (input or X-variable of the PLS regression) that results in a minimal scaled PRESS after calibration by CV, as described above. During the optimization, the absorbance of each wavelength could either be included or omitted resulting in varying combinations of wavelengths generated by the genetic algorithm. For each combination, a PLS model was calibrated and the scaled PRESS calculated. Note that an additional UV data set of run 1 was

recorded under identical conditions for regression model calibration as the initial set showed disturbances which negatively affected the RMSECV.

5.3. Results and discussion

A monitoring setup was implemented for the diafiltration-based disassembly of Cp149 VLPs which was performed under varying conditions as listed in Table 5.1. Briefly, runs 1 to 3 were performed at low, medium, and high protein concentration. The feed solution of run 4 had an elevated salt concentration while run 5 had an elevated impurity level and protein concentration. Run 6 was performed at a high protein concentration with a high permeate flux to expose Cp149 to elevated concentrations at the membrane surface and to reduce the processing time. Pressures, conductivity, and pH were monitored in-line while light scattering and UV spectroscopy were monitored on-line. Light scattering spectroscopy allowed for determination of the SLS intensity and the dynamic light scattering (DLS) z-average. UV spectroscopy (240 nm to 340 nm) allowed for determination of an on-line measured protein concentration and A260/A280 as well as for performing second derivative spectroscopy and regression modeling. As a reference, at-line SEC-HPLC was used to determine the concentrations of Cp149 dimers and high-molecular weight species such as Cp149 VLPs and potential aggregates. A detailed investigation of the influence of the conditions on the dimer yield was out of scope of this study. Yields were approximately between 0.7 and 0.8 (no scatter correction applied).

5.3.1. At-line monitoring

At-line SEC-HPLC analysis was performed as the disassembly reaction was expected to be time-dependent (Hillebrandt et al., 2021) and the bias due to continuation of the disassembly reaction after sampling should be minimized. The results are shown in Figure 5.2 (top row). Generally, the dimer concentration increases over time and flattens out toward the end indicating the progress and final stage of the disassembly reaction, respectively. At the beginning of each run, higher dimer concentrations were detected for higher total Cp149 concentrations showing that a fraction of the VLPs was already partly disassembled under the given feed conditions. An exception is run 4 with a feed NaCl concentration of 300 mM, which resulted in the lowest initial dimer concentration followed by a lag phase before its increase. This lag phase can be attributed to the presence of NaCl which is mostly depleted during the first few DV. This matter is further discussed in detail in Section 5.3.3. All runs reached a dimer concentration plateau which was arbitrarily defined by a slope ≤ 0.0013 $gL^{-1}min^{-1}$. The beginning of each plateau is also highlighted in Figure 5.2. Except for run 1, the plateau was reached after 4 to 5 DV (5^{th} to 6^{th}

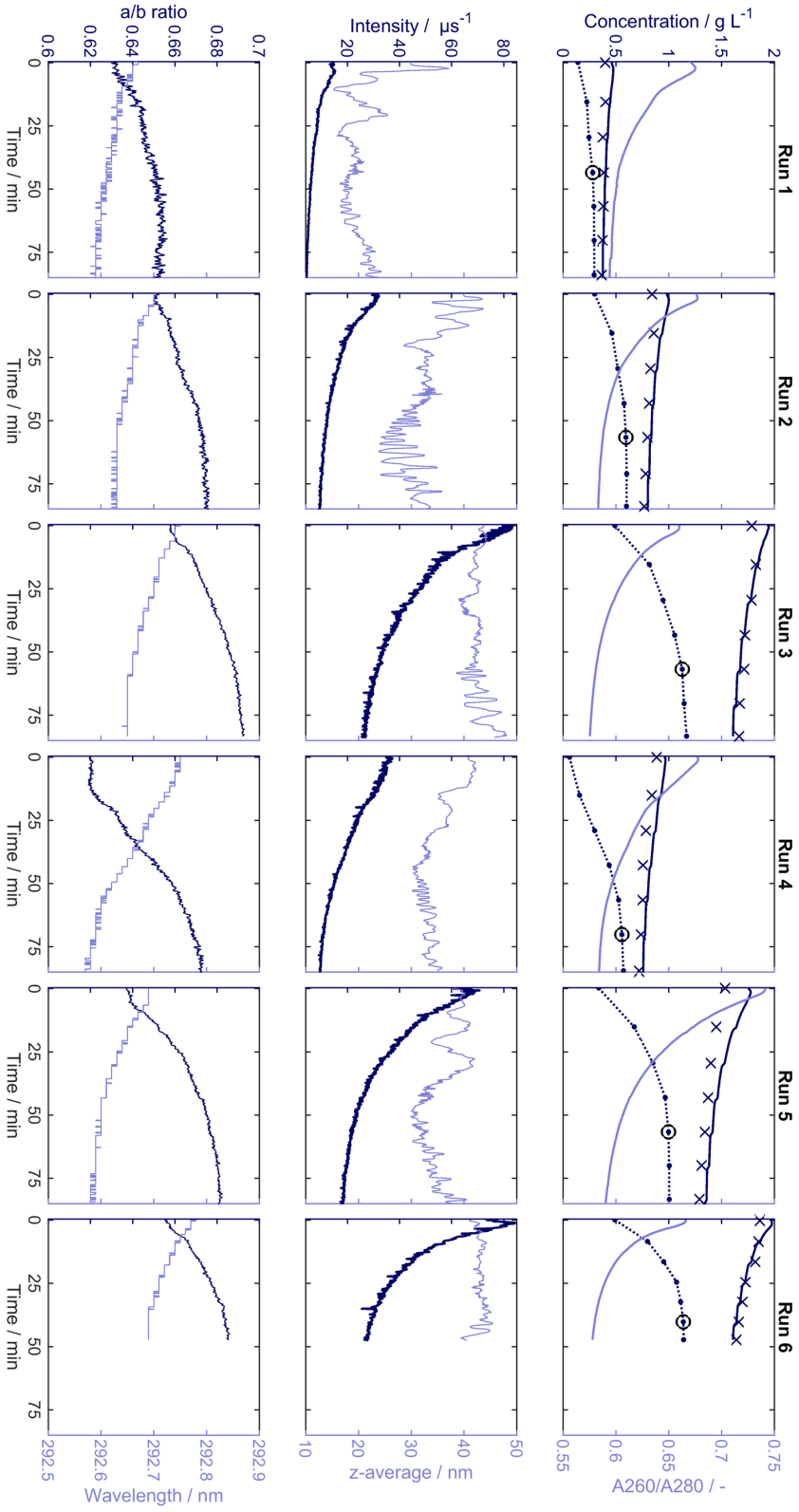

Figure 5.2. *Rotated 90° clockwise*. Process data from on-line monitoring. Each column represents the data of one experiment (compare Table 5.1). Top row: dimer concentration (dark blue dots with dotted lines to guide the eye and the beginning of the concentration plateau indicated by a black circle) and total Cp149 concentration (dark blue crosses) determined by at-line SEC-HPLC, on-line protein

concentration (dark blue lines), and on-line A260/A280 (light blue lines). Center row: on-line SLS intensity (dark blue) and on-line z-average diameter from DLS measurements (light blue). The earlier was corrected by the laser attenuation factor according to the manufacturer's instructions and the latter was smoothed by a moving median with a window of six data points (~ 1 min). Bottom row: a/b ratio (dark blue) and wavelength minimum around 293 nm (light blue), both derived from second derivative spectroscopy. Axis limits were kept constant for all runs to enhance comparability. Another representation can be found in the Appendix C, Figure S5.1. Abbreviations: A260/A280, absorbance ratio 260 nm to 280 nm; DLS, dynamic light scattering; HPLC, high-performance liquid chromatography; SEC, size-exclusion chromatography; SLS, static light scattering.

data point, samples were taken at each DV from 0 to 6). For run 1, the lower feed concentration was most probably the reason for an earlier decrease of the slope below the threshold.

As an example, run 4 was continued until 10 DV (Appendix C, Figure S5.1) and the dimer concentration decreased slightly during the additional 4 DV. An explanation for this decrease is the sampling for at-line analysis and the resulting replacement of the sample volume by diafiltration buffer which leads to a minimal dilution of the dimers. During the disassembly reaction, this concentration reduction is superimposed by the formation of dimers.

Run 6 was performed under the same conditions as run 3 but with a higher permeate flux leading to a 36 min processing time reduction. Nevertheless, both processes show a similar progression of the dimer concentration on a DV basis (cf. Appendix C, Figure S5.1). In the investigated time frame and under the given conditions, the disassembly progress seems to depend mainly on the degree of buffer exchange rather than on process time. This observation was also made during the reassembly process (Rüdt et al., 2019) but is in contrast to the observed time-dependence of small-scale batch disassembly reactions (Hillebrandt et al., 2021). An explanation for this observation could be that intensified mixing and shear stress during the filtration process accelerate the disassembly reaction. However, these observations and assumptions should be verified in further studies. Overall, the variation of processing parameters as well as the variability in the resulting dimer concentration trajectories and levels enable an evaluation of the monitoring and PAT approaches in a broad design space.

The median analysis delay is the median duration from sampling until SEC-HPLC injection and listed in Table 5.2. Samples from run 6 were analyzed with the largest median delay of 22.2 min. The higher permeate flux led to a shorter interval between samplings, which were conducted at each DV. Due to the fixed analysis duration of the SEC-HPLC method queueing of samples was

required and resulted in a larger delay than for other runs. The continuation of the disassembly reaction until analysis theoretically results in an increase of measured dimer concentration compared to an analysis without any delay. This effect was considered negligible for this study as the analysis delay increased and the change in dimer concentration decreased with increasing DV. The samples of all other runs were analyzed with median delays below 14 min. Nevertheless, this analysis delay can be reduced considerably applying on-line monitoring. This example emphasizes the value of the on-line monitoring approach proposed in this study. On-line monitoring is particularly of interest when processes with high permeate fluxes need to be characterized as the abovementioned time limitation causes larger deviations.

Table 5.2. Median at-line analysis delay and its median absolute deviation in parentheses.

Experiment	Median analysis delay min
Run 1	5.6 (0.2)
Run 2	5.8 (0.4)
Run 3	13.9 (0.2)
Run 4	5.7 (0.2)
Run 5	5.5 (0.2)
Run 6	22.2 (5.3)

5.3.2. In-line monitoring

The in-line monitoring results are depicted in Appendix C, Figure S5.2 and discussed in the Appendix C, Section S5.2. Briefly, the signals of all runs showed a similar progression and final values. As expected, a higher permeate flux resulted in a higher transmembrane pressure and higher NaCl or nucleic acid (impurity) levels resulted in a higher conductivity. In summary, the signals allow for a supervision of the diafiltration progress and performance. This monitoring approach enables an identification of deviations of the diafiltration buffer or feed. The buffer exchange is monitored directly by measuring actual retentate properties and is not estimated indirectly through DV which are usually based on influent (diafiltration buffer) and/or effluent (permeate) quantification.

5.3.3. On-line monitoring

Figure 5.2 also shows the on-line monitoring results of the CFF processes. The on-line measured protein concentration and the at-line measured total Cp149

concentration were in good agreement and decreased over time. Both concentrations were determined using the respective 280 nm absorbance. Besides Cp149 dimers and VLPs, host cell nucleic acids and proteins contribute to the measured absorbance. The depletion of these impurities throughout the process leads to a decrease of the measured absorbance and thereby concentration. Using the absorbance for concentration determination of VLP-containing solutions furthermore leads to an overestimation due to the light scattering of VLPs. The decreasing VLP concentration (increasing dimer concentration) due to the disassembly leads to a reduced light scattering contribution to the absorbance over time. In this study, no scatter-correction was applied to the on-line or at-line absorbances but this is recommended if absolute concentration values are desired (for an example, see (Porterfield & Zlotnick, 2010)). For the at-line dimer concentration as the target variable, an overestimation due to light scattering was considered to be negligible because of the low molecular weight of the dimers. The stepwise decrease of the on-line measured protein concentration results from the abovementioned replacement of sample volume by diafiltration buffer. Other potential factors that could contribute to the decreasing total protein concentration are adsorption to the membrane, aggregation and removal by the measurement loop in-line filter, or undesired dilution due to higher diafiltration buffer inflow than permeate outflow. These factors were considered to play only a minor role under the investigated experimental conditions but the presented setup could enable the investigation of their influence in process optimization or characterization studies. It has to be noted that a change of the protein's UV absorption behavior due to the increasing urea concentration is expected but was not considered in this study.

As for the nature of the at-line Cp149 concentration and on-line protein concentration measurements, both are biased by UV-active impurities encapsulated in or bound to the VLPs. However, compared to the on-line measurement, the at-line SEC-HPLC measurement excludes impurities in solution which are smaller than dimers and are not bound to the dimers. The depletion of these small impurities throughout the diafiltration process explains the decreasing differences of on-line and at-line measured concentrations over time. The initially higher on-line measured protein concentration might also be enhanced by a lag of the diafiltration buffer inflow during the CFF startup leading to a concentration increase (feed sample was taken before the CFF start). Regarding the samples taken at 6 DV, the maximum observed deviation between the two measurements was 0.07 g L^{-1} in run 5. The on-line measured protein concentration is therefore an accurate

representation of the total Cp149 concentration by at-line SEC-HPLC during the final phase of the investigated experiments.

The A260/A280 is an indicator for the nucleic acid content, in this case the impurity level, of a protein solution but is also expected to be influenced by light scattering of VLPs (Porterfield & Zlotnick, 2010) and the urea concentration (Hillebrandt et al., 2021). For run 5, the feed solution was spiked with less purified VLP solution and the highest initial A260/A280 of 0.74 was observed (Figure 5.2). For all experiments, the A260/A280 decreased to final values between 0.58 and 0.59, independently of the dimer concentration, initial impurity level, or NaCl concentration. Therefore, the A260/A280 could serve as a simple lumped quality indicator for the nucleic acid removal and disassembly progress or for the nucleic acid removal only if a scatter correction is applied. While the former approach only requires a bivariate UV signal, the latter requires at least three wavelengths (Porterfield & Zlotnick, 2010; Rolinger, Rüdt, Diehm, et al., 2020).

The SLS intensity of all experiments decreased with proceeding disassembly (Figure 5.2). When VLPs disassemble, this behavior is expected as the light scattering intensity decreases linearly with the particle concentration and with the 6^{th} power of the particle diameter (Bohren & Huffman, 2004). For human papillomavirus VLPs, this behavior was previously observed in small scale batch experiments (Mach et al., 2006). Cp149 VLPs are spherical particles with a diameter of approximately 30 nm and mainly consist of 240 dimers (Newman et al., 2003; Wynne et al., 1999). The absolute values of the SLS intensity show the same trend as the Cp149 total concentration reflecting the concentration-dependence.

The z-average describes the intensity-weighted harmonic mean of the particle size determined by DLS (Thomas, 1987). Compared to the SLS intensity, the recorded z-average is rather constant with more noise or oscillation (Figure 5.2). Runs 1, 2, 4, and 5 show a decrease of the z-average during the initial 50 min. As the z-average determination by DLS relies on the Stokes-Einstein Equation, it is sensitive to changes of the solvent viscosity (Thomas, 1987). The viscosity for the DLS measurements was set to the theoretical value of the urea-containing diafiltration buffer which had a higher viscosity than the feed buffer. Therefore, the initial z-average is overestimated and a decrease with increasing buffer exchange is expected. After 4 DV of diafiltration, corresponding to 33 min for run 6 and 57 min for runs 1 to 5, ideal buffer exchange leads to a composition with 98 % diafiltration buffer (Kurnik et al., 1995). Therefore, only a minor viscosity change is expected toward the end of the process. Run 1 resulted in a final z-average of 24 nm, all other runs show final z-averages larger than 30 nm. In a previous work, HBcAg VLPs similar to

Cp149 VLPs were disassembled using urea and resulted in subunits with 6 nm diameter (K. W. Lee & Tan, 2008). According to the abovementioned definitions of the z-average and light scattering intensity, even a small number of large particles in a polydisperse solution lead to a higher z-average than the size of the dominating species (Hassan et al., 2015; Stetefeld et al., 2016). In the case of VLP disassembly, the presence of aggregates or VLPs at the end of the disassembly leads to a higher z-average than the hydrodynamic diameter of the subunits, such as Cp149 dimers. The generally higher level of the z-average at higher protein concentrations might indicate a concentration-dependent aggregation tendency of Cp149 VLPs. Runs 1 to 5 show a z-average increase toward the end which could indicate aggregation. This increase was not observed for run 6, which was performed in less time. An increased aggregation tendency for longer processing time was similarly observed for the diafiltration-based reassembly using a similar monitoring setup (Rüdt et al., 2019). Another observation from that study was a z-average decrease for even longer processing times due to the retention of large aggregates by the measurement loop in-line filter. This behavior was also observed during the extended diafiltration of run 4 as shown in Appendix C, Figure S5.1. The underestimation of the z-average by DLS due to convective flow (Leung et al., 2006) was considered negligible for Cp149 VLPs and dimers due to the low flow rate. For a more detailed discussion see (Rüdt et al., 2019). In summary, the z-average showed to be not suitable for monitoring of the disassembly reaction but for monitoring of aggregation toward the end of the diafiltration-based disassembly process.

Second derivative UV spectroscopy was used to monitor changes in the microenvironment of tyrosine and tryptophan residues of Cp149 by determining the a/b ratio and the location of the minimum near 293 nm, respectively. An increasing a/b ratio indicates an increasing polarity of the microenvironment of tyrosine residues (Ragone et al., 1984) while a blue shift of the tryptophan band correlates to increasing polarity surrounding tryptophan residues (Mach & Middaugh, 1994). The microenvironment of amino acid residues buried within the protein (core) is regarded as non-polar compared to solvent-exposed residues. In previous works, second derivative UV spectroscopy was employed to monitor the disassembly of Norwalk VLPs (Ausar et al., 2006) and the reassembly of chimeric variants of Cp149 (Rüdt et al., 2019). In the latter, the increased surrounding polarity of certain tyrosine and tryptophan residues of HBcAg in the assembled state was attributed to their involvement in the VLP formation and the slope of the a/b ratio was identified as indicator for the assembly rate. Compared to those results, the disassembly experiments in this study showed inversed trends of the a/b ratio

and the tryptophan band shift which is expected as the disassembly is the opposite reaction. The a/b ratio increased during all experiments and showed a similar curve shape over time as the dimer concentration (Figure 5.2) while the progression of the second derivative minimum around 293 nm (tryptophan band) was inversed. This indicates that the UV data contains information about the (dis-) assembly state of the VLPs. For run 4 and 5, both values were approximately constant for the first 13 min and 7 min, respectively. The initial conductivity in both runs, which is assumed to reflect the ionic strength to some extent, was higher due to the presence of NaCl in run 4 and nucleic acids in run 5. A higher ionic strength is known to stabilize the assembled state of Cp149 VLPs (Ceres & Zlotnick, 2002; Singh & Zlotnick, 2003). The higher VLP stability is supported by slower dimer concentration increase (slower disassembly) for run 4 compared to run 2 which was performed with the same initial protein concentration. Comparing run 5 with run 3 which were performed at a similar initial protein concentration but different impurity levels, both resulted in similar dimer concentration trajectories. The reason for that is most probably the low temporal resolution of the at-line analysis leading to the inability of detecting short term changes. Interestingly, when comparing the initial and final dimer concentrations with the corresponding absolute a/b ratios, both quantities show a similar trend supporting their causal relationship. The similar a/b ratios of the runs 3 and 6 support the observation of similar dimer concentration profiles elaborated in Section 5.3.1. The capability to identify the dis- and reassembly state on-line with a high temporal resolution and without any prior calibration makes second derivative UV spectroscopy a valuable monitoring tool.

5.3.4. Endpoint detection (process control)

The diafiltration-based VLP disassembly process requires a timely termination to avoid process-related product damage, for example due to extended exposure to shear forces or to elevated concentrations at the membrane surface. From an economic perspective, a timely termination is also desirable, for example to reduce buffer consumption or processing time. Especially since the disassembly reaction was observed to depend on liquid phase conditions rather than on time, a product-based monitoring is preferred over a simple time- or DV-based process termination decision. Two different methods were applied to detect the endpoint of the diafiltration-based disassembly process. The first was based on the results from second derivative UV spectroscopy (Section 5.3.3) which clearly indicated that the spectral data contain information on the disassembly reaction. Therefore, regression models were calibrated to directly correlate (latent) information in the on-line UV data to the dimer concentration. Once the models are calibrated, the dimer

concentration can be traced without any additional at-line or off-line analysis. One can then simply decide for a termination of the process based on the predicted concentration, for example when the slope falls below a predefined threshold. The second method was implemented to eliminate the need for previous at-line or off-line analyses. It simply uses univariate UV or SLS data to detect threshold values that correspond to the beginning of the plateau dimer concentration.

5.3.4.1. Regression models

Regression models were calibrated by CV as described in Section 5.2.5. The runs for the calibration data set were selected manually as listed in Table 5.1. The selection was based on principal component analysis score plots aiming for a representative distribution of all occurring score values (data not shown).

Variable selection

Two PLS models (models A and B) and one OLS model (model C) were calibrated. Input data for the calibration were absorbances of either full recorded spectra (240 to 340 nm, model A), a wavelength selection based on a genetic algorithm (model B), or two individual wavelengths (model C). After the optimal nLV was determined to be 3 using full spectra (cf. model A), variable selection was carried out using the described genetic algorithm approach. It aimed to improve the model by selecting a set of wavelengths that achieves the best CV results. As the genetic algorithm is based on random number generation, the optimization was performed ten times and the selections of each wavelength were accumulated. The number of genetic algorithm selections for each recorded wavelength are shown in Figure 5.3. For the sake of interpretation, the regression coefficients of model A (nLV = 3) are also shown in Figure 5.3. Here, a high absolute value of a coefficient indicates a high relevance of the corresponding wavelength to the model. The extreme points (highest absolute values) of the regression coefficients are close to the most selected wavelengths by the genetic algorithm. This indicates that the PLS calibration algorithm optimized the model by considering similar wavelength regions important. However, the genetic algorithm approach allows to remove wavelengths that may contain irrelevant or unreliable information before the final PLS model B is calibrated to achieve a better prediction (C. M. Andersen & Bro, 2010). The most selected regions (genetic algorithm) coincide to some extent with characteristic absorption peaks of the aromatic amino acids phenylalanine, tyrosine, and tryptophan (Hansen et al., 2013). This supports the found qualitative correlation of a/b ratio and second derivative minimum near 293 nm with the disassembly (Section 5.3.3). As neighboring variables in spectral data are usually highly correlated (C. M.

Andersen & Bro, 2010), groups of wavelengths around the most selected regions (genetic algorithm) were manually selected to calibrate model B and are highlighted in Figure 5.3. In contrast to the genetic algorithm results, omitting the wavelengths 240 and 241 nm improved the RMSECV and the RMSEP (data not shown). At these lower wavelengths in the mid UV range, the peptide bond and cysteine residues contribute considerably to the absorption of proteins (Hansen et al., 2013). Therefore, the absorbance in this region might rather represent the overall protein concentration than the disassembly state.

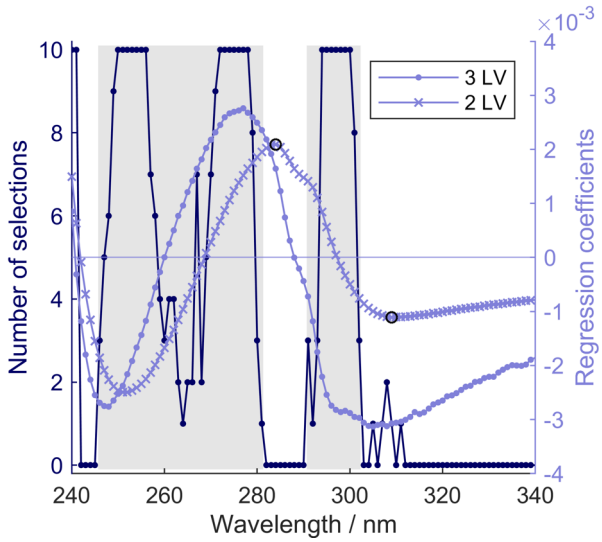

Figure 5.3. Variable selection by genetic algorithm and PLS regression coefficients. Both methods were performed with the full recorded wavelength range from 240 nm to 340 nm. Left axis (dark blue): Number of selections for a nLV = 3 PLS model by the genetic algorithm after ten evaluations. Right axis (light blue): PLS regression coefficients for model A (nLV = 3) and the preliminary model with a nLV = 2. The two wavelength ranges which were selected for model B are highlighted in gray. The two wavelengths which were selected for model C are indicated by black circles. Abbreviations: (n)LV, (number of) latent variables; PLS, partial least squares.

Diode array detectors for acquisition of UV spectra are not commonly available or implemented in current manufacturing facilities of biopharmaceuticals. Inspired by the results of a recent study (Rolinger, Rüdt, & Hubbuch, 2020b), the feasibility of a simple regression model based on only two individual wavelengths was evaluated. Therefore, an OLS regression model was calibrated using the calibration procedure as described in Section 5.2.5. The selection of the two wavelengths was achieved by calibrating a preliminary PLS model using full spectra and a nLV = 2. The resulting regression coefficients are shown in Figure 5.3. Interestingly, the regression coefficients are similar to ones using a nLV = 3 but shifted to higher

wavelengths. The two wavelengths required to calibrate model C were then chosen from the local extreme values of these regression coefficients of the preliminary nLV = 2 model. As mentioned above, wavelengths with higher absolute regression coefficients show a stronger contribution to the model, and neighboring UV wavelengths are usually highly correlated due to the nature of UV light absorption. Therefore, it was assumed that the data at wavelengths with extreme points in the regression coefficients are sufficient for an adequate prediction. Among the three extreme values, the best combination of two wavelengths was 284 and 309 nm (data not shown) and is marked in Figure 5.3.

Calibration and prediction

Figure 5.4 shows the predictions of the dimer concentration using the three regression models (A, B, and C). The results for each model are divided into the runs used for calibration and external runs as independent validation set. Table 5.3 lists the characteristics of the model calibration and validation. In general, all models were calibrated successfully resulting in R^2 values above 0.980 and Q^2_{CV} values from 0.905 to 0.976. For the external validation set, Q^2_{Ext} values were in the range of the calibration values, indicating a strong predictive power of the model.

Table 5.3. Results of the calibration by cross validation (CV) and external validation (Ext) of the three regression models A, B, and C. The models were calibrated with absorbance data of different wavelengths regions as listed. Abbreviations: nLV, number of latent variables; RMSECV, root mean square error of cross validation.

Model	**Wavelengths** nm	**nLV** -	R^2 -	**RMSECV** g L^{-1}	Q^2_{CV} -	Q^2_{Ext} -
A	240-340	3	0.985	0.106	0.909	0.955
B	246-281, 291-302	3	0.990	0.055	0.976	0.963
C	284, 309	2	0.981	0.067	0.964	0.948

Regarding model A, the progressions of the dimer concentration were well predicted by the model as shown in Figure 5.4. This also applies to the external validation set in which the maximum RMSEP occurred in run 3 with 0.064 g L^{-1} (Appendix C, Table S5.1). Most of the feed samples (0 min) were predicted less accurately than samples during the later stages. This can be expected as the feed samples vary most in their composition, for example in salt concentration or impurity profile. Throughout the diafiltration process, buffer exchange leads to a higher similarity of the samples, which are then mainly differing in dimer concentration. Additionally, the larger fraction of

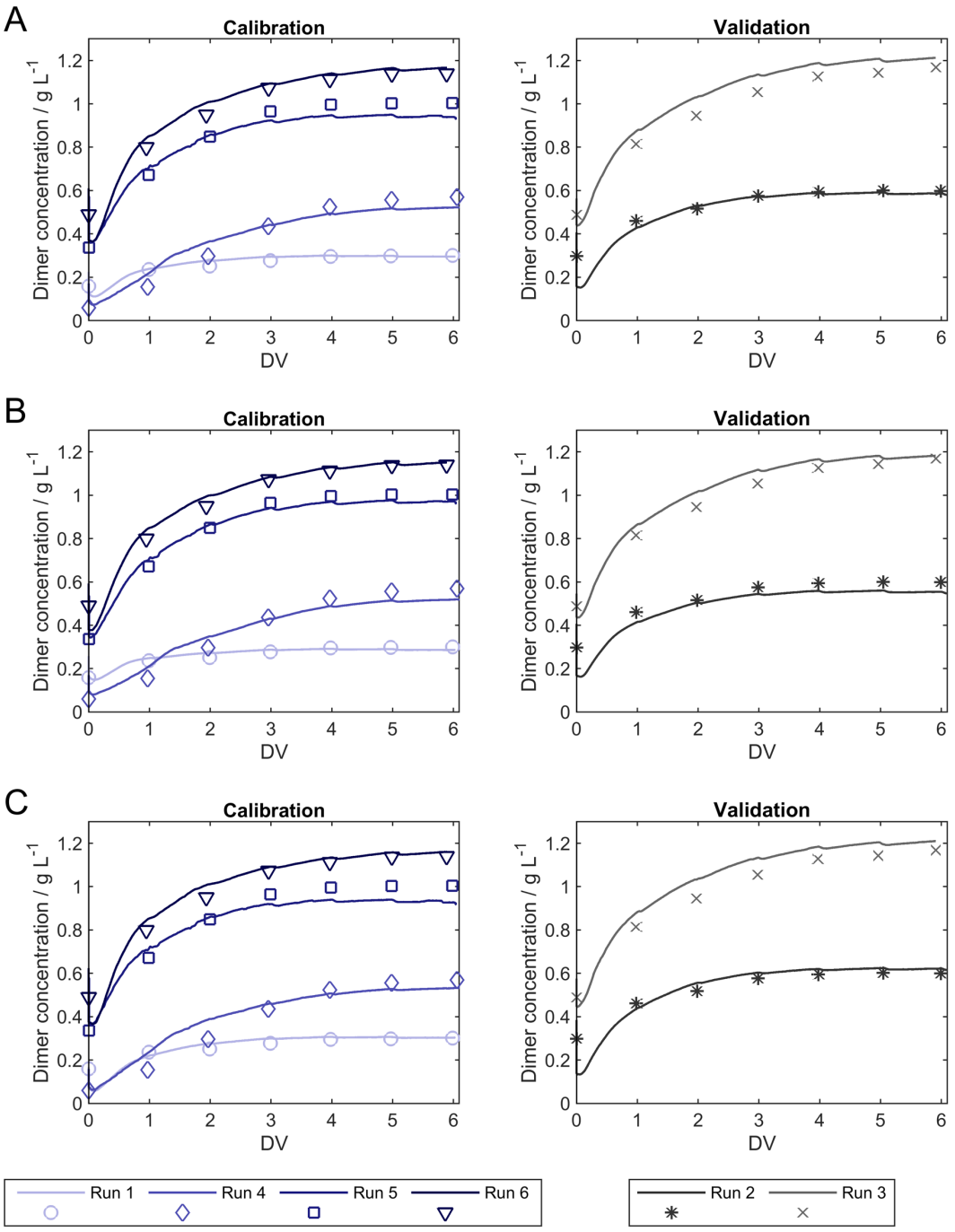

Figure 5.4. Calibration and external validation of regression models. Symbols represent reference measurements of the dimer concentration by at-line SEC-HPLC and continuous lines represent the model predictions based on the on-line UV absorbance measurements. (A), (B), and (C) represent the predictions of the models A, B, and C, respectively. Abbreviations: DV, diafiltration volume; HPLC, high-performance liquid chromatography; SEC, size-exclusion chromatography; UV, ultraviolet light.

samples with rather constant conditions at the end of the process inherently leads to a stronger weighting of theses samples during calibration.

Nevertheless, this behavior is desirable as an accurate prediction of these samples is required for a process termination decision.

Compared to model A, the variable selection applied before the calibration of model B improved the RMSECV by 0.051 g L^{-1} (48 %). This was, along with R^2, Q^2_{CV}, and Q^2_{Ext}, the best of the three models. In comparison to model B, other recent UV-based PLS models (Rolinger, Rüdt, & Hubbuch, 2020b; Rüdt et al., 2019; Zobel-Roos et al., 2017) achieved comparable R^2 and Q^2_{CV} with 0.995 to 0.999 and 0.984 to 0.999, respectively. In accordance with the lower RMSECV, the calibration set was predicted more accurately. This improvement was most pronounced toward the end of run 5, which had a higher impurity level of the feed solution. A potential explanation is that some impurities were not depleted throughout the diafiltration and led to a less accurate prediction by model A. The variable selection applied for model B then leads to a focus on spectral regions that allow for a prediction less biased by the impurities. The predictions of the external validation set were in average improved whereas the RMSEP decreased by 0.016 g L^{-1} for run 3 and increased by 0.005 g L^{-1} for run 2 (Appendix C, Table S5.1).

Model C was calibrated and applied using only two wavelengths. Regardless of the strong reduction of input data the predictions were comparable to or only slightly less accurate than model A. These remarkable results are assumed to arise from the combination of the selected wavelengths. The first, 284 nm, is close to 280 nm, which is considered as the peak of the lumped absorption of aromatic amino acids and therefore commonly used for protein concentration determination. At the second wavelength of 309 nm, the UV absorption of proteins is considerably lower and light scattering contributes increasingly to the overall absorbance. This is supported by similar curve shapes of the on-line 309 nm absorbance (cf. Section 5.3.4.2) and the SLS intensity. The latter coincides with the disassembly progress as shown in Section 5.3.3. Therefore, it is assumed that model C combines the information on concentration and degree of disassembly from the input data to predict the dimer concentration.

Overall, the results indicate that regression models are capable of predicting the dimer concentration at varying protein concentrations and liquid phase conditions, namely salt concentration and impurity level. The accurate prediction of the dimer concentration progress, especially toward the of the process, enables an accurate endpoint detection. As quenching the VLP disassembly reaction is not easily possible, on-line UV monitoring in conjunction with PLS models is furthermore a valuable tool to characterize diafiltration-based disassembly in process development.

Application for detection

Data of model B were used to demonstrate a potential endpoint detection approach as a stagnating dimer concentration indicates the endpoint of the disassembly reaction. Therefore, first derivatives of the predicted dimer concentrations were approximated by calculating the difference using a backward-oriented moving window of ~1 min corresponding to 50 data points. A larger window usually leads to lower noise but also to a larger detection delay. The results are shown in Figure 5.5 together with the at-line measured dimer concentration for comparison. The ideal process endpoint was defined as the beginning of the at-line dimer concentration plateau which was defined by a slope ≤ 0.0013 g L^{-1} min^{-1}. This slope was also used as a threshold for the endpoint detection based on the predicted dimer concentration. To avoid unintended triggering during the startup phase, the detection was activated only after 10 min. For a technical process implementation, this activation is suggested to be based on the conductivity and/or pH signal. The detected endpoints are also shown in Figure 5.5. In all runs, the derivative increased to a global maximum and then decreased non-monotonically. Besides high frequency noise, the derivative showed distinct valleys which resulted from the abovementioned concentration decrease caused by sampling for at-line analysis. These small but rapid concentration changes lead to more pronounced disturbances in the first derivative signals. To enable an automated endpoint detection without additional data processing, the endpoint detection was disabled for 4 min after each sampling to avoid unintended triggering. In an industrial setting, the sample volume would be much smaller in relation to the retentate volume and the disturbance of the UV signal by sampling is expected to be negligible.

Except for run 6, deviations of the detected endpoint from the beginning of the dimer concentration plateau were 12 min at most with a root mean square error (RMSE) of 9 min and within ±1 DV. No endpoint was detected in run 6 as the lowest derivative was just above ($0.5 \cdot 10^{-3}$ g L^{-1} min^{-1}) the threshold value. The threshold would be reached using a lower window for the approximate derivative which led, however, to unsatisfying noise reduction for other runs (data not shown). Based on this single example, using universal data processing parameters is not suggested for varying permeate fluxes. It has to be noted that the plateau onset itself was identified based on the discrete samples with an interval of ~14 min (~7 min for run 6) and should be regarded as an approximation. The discretization by sampling (at each DV) mathematically leads to an underestimation of the dimer concentration slope while the use of a threshold value potentially detects the plateau onset too late. This also demonstrates the advantage of an automated endpoint detection

based on continuously acquired on-line data: decisions can be made faster and are not limited to the sampling interval. The limited accuracy of the plateau onset has to be considered when evaluating the reliability of the endpoint detection approaches, so that an endpoint detection within ±1 DV of the plateau onset was considered as reliable in this study. In this regard, the process endpoint was successfully detected for runs 1 to 5 while the signal was only close to the threshold value in run 6. However, the run-to-run variability in a fully developed and established process should be much lower than the conditions screened in this study. Together with a fine tuning of the detection parameters, an even improved performance of the detection approaches can be expected.

5.3.4.2. Univariate approaches

Besides the regression models, two calibration-free approaches were theoretically investigated for their ability to detect the process endpoint. The first approach was chosen based on the observed visual correlation between the SLS intensity and the dimer concentration. The second approach was chosen based on the expected light scattering contribution to the 309 nm absorbance and its good performance as input parameter for model C. As the SLS intensity decreases due to the disassembly of VLP, a derivative approximating zero indicates the end of the disassembly reaction. Therefore, first derivatives of SLS intensity and 309 nm absorbance were approximated as described in Section 5.3.4.1 using a moving difference with a window of 19 data points (~3 min) and 50 data points (~1 min), respectively. The results are also shown in Figure 5.5. For both approaches and all runs, the derivative decreased to a global minimum and then increased non-monotonically. Compared to the SLS measurements at 633 nm, the 309 nm absorbance is more sensitive to changes in the protein concentration due absorption and a higher SLS intensity according to the Rayleigh approximation. Consequently, the distinct disturbances (valleys) after sampling were more pronounced for the 309 nm absorbance. As the direction of these disturbances did not interfere with the automated endpoint detection, a deactivation after sampling is not required in this case.

For each of the two derivatives, a common threshold value for all runs was required to trigger the endpoint detection. Thus, a grid search was performed to minimize the distances between the detected times and the corresponding beginning of the dimer concentration plateau. Briefly, 1000 evenly spaced threshold values were generated between the lowest derivative value at a plateau onset and the highest derivative value of run 6. The latter was required to enable a detection in all runs as the maximum derivative values of run 6

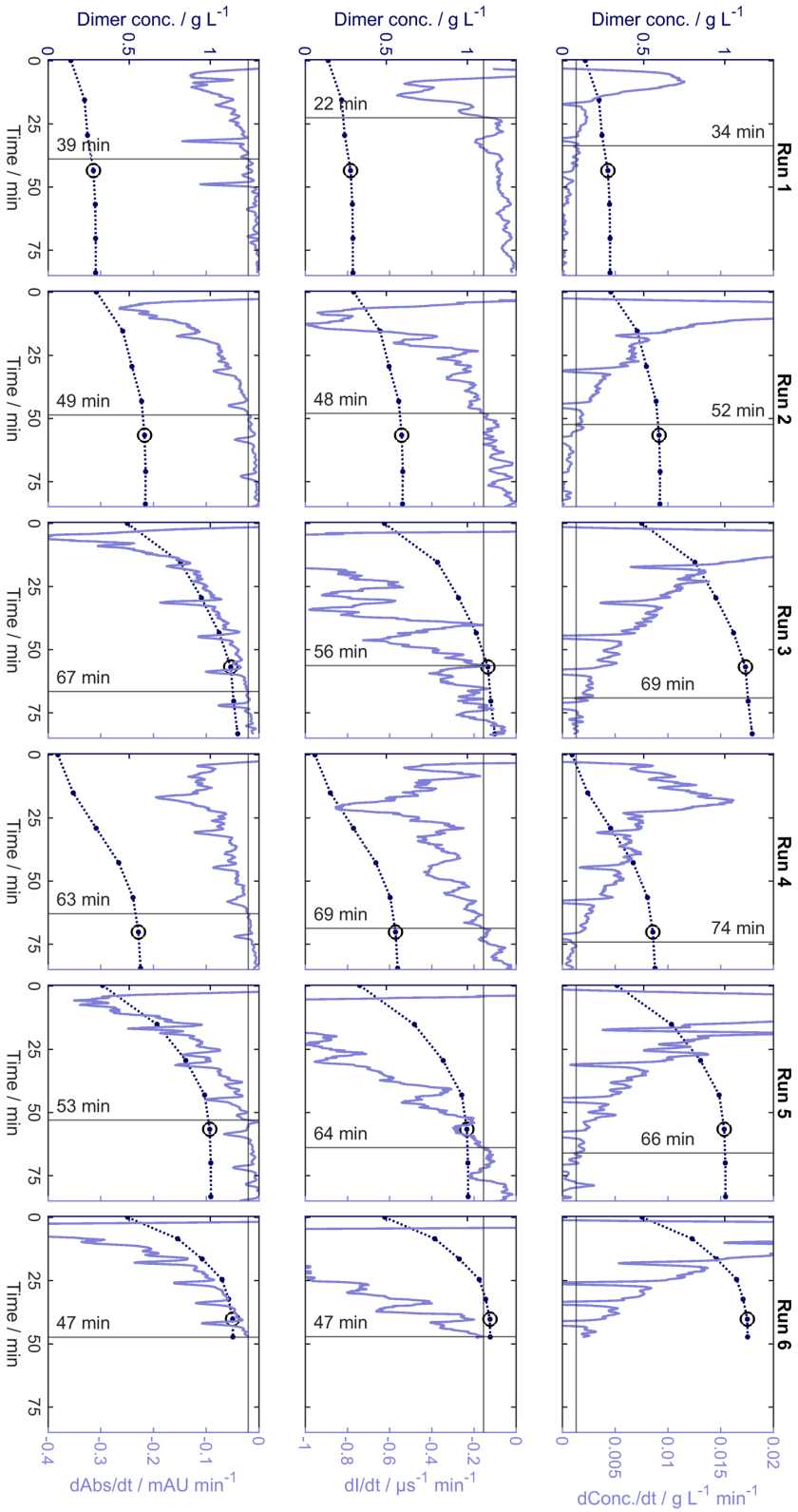

Figure 5.5. *Rotated 90° clockwise*. Endpoint detection. Left axis (dark blue): dimer concentration by at-line SEC-HPLC with dotted lines to guide the eye and the beginning of the concentration plateau indicated by a black circle. Right axis (light blue): approximate first derivative of the predicted dimer concentration by model B (top), the SLS intensity (middle), and the absorbance at 309 nm (bottom) calculated

by a moving difference with a window of ~1 min, ~3 min, and ~1 min, respectively. Horizontal lines indicate the threshold value for endpoint detection. For exceptions to triggering at the threshold value, see Section 5.3.4. Vertical lines indicate the detected endpoint according to the sensor signals predicted dimer concentration, SLS intensity, and 309 nm absorbance. Abbreviations: Abs, absorbance; conc., concentration; HPLC, high-performance liquid chromatography; I, SLS intensity; SEC, size-exclusion chromatography; SLS, static light scattering; t, time.

were lower than for the other runs. The threshold values which achieved the lowest RMSE between the detected times and the plateau onset were -0.1544 $\mu s^{-1} min^{-1}$ with an RMSE of 10 min for SLS intensity and -0.02 $mAU\ min^{-1}$ with an RMSE of 7 min for 309 nm absorbance. Both RMSEs were comparable to the detection based on the predicted dimer concentrations (RMSE of 9 min) and resulted in predominantly similar detections (Figure 5.5). Except for run 1, the detected SLS-based endpoints deviate maximum 9 min and ±1 DV from the beginning of the plateau. For run 1, the early detection resulted from a local maximum of the derivative. Due to the generally lower concentration in run 1, concentration changes due to sampling have a greater impact on the SLS intensity potentially leading to the local maximum. Using the 309 nm absorbance resulted in an improved endpoint detection for run 1 and similar or slightly less accurate detections for the other runs. All deviations were below 10 min and within ±1 DV of the plateau onset. The assumed combination of UV absorption and scattering seems less sensitive to disturbances which is also reflected in less noise apart from the sampling-related disturbances. This is particularly beneficial as it enables rapid and simple process control with a standard UV sensor. The latest/least detection for run 6 is in accordance with the results based on the predicted dimer concentrations (Section 5.3.4.1). This raises the question if this trend originates from an underlying minor time dependence of the disassembly reaction which cannot be resolved by at-line analysis or from a non-optimized data processing and detection algorithm for higher permeate fluxes. As stated in Section 5.3.1, this would be interesting to investigate in further studies. Similarly to the regression model, the univariate approaches reliably detected the end of the disassembly for a range of product concentrations and liquid phase conditions demonstrating its applicability. When changing the permeate flux, an additional detection parameter adjustment might be beneficial.

5.3.4.3. Industrial considerations and potential

From an industrial perspective, the implementation would include model/control robustness testing with regards to run-to-run variability and hardware implementation at a larger scale. Robustness testing for the range

of manufacturing specifications in terms of protein concentration, buffer pH and concentration, and other process parameters would be performed to assess the performance of the implemented model/control at the edge of the design space. The present study already demonstrates the capabilities of the developed framework under a range of conditions and provides the groundwork for this robustness testing. As shown above, a considerable monitoring and control is enabled by the UV absorbance measurement at one or two wavelengths, thus a standard UV sensor would be sufficient hardware for implementation. Currently commercially available pilot and process scale CFF units usually contain an UV sensor in the permeate line (for example ÄKTA UniFlux/readyflux (XL) by Cytiva, Cogent by Merck Millipore, KrosFlo KMPi/KTF by Repligen, and Sartoflow 1000/4500 by Sartorius Stedim Biotech). In-line variable pathlength UV absorbance measurements have been shown to perform well in the CFF retentate (Rolinger, Rüdt, Diehm, et al., 2020) for processes with high protein concentrations. Since VLPs are usually processed at much lower concentrations, in-line UV monitoring in the retentate should be possible with standard equipment and a low degree of customization. In-line measurements further provide continuous data over process time without any additional delays often caused by off-line measurements.

The developed framework aligns well with the demands for the Quality by Design approach suggested regulatory authorities, which aims for a knowledge-based development of processes, cf. Q11 and Q8(R2) guidelines (ICH Expert Working Group, 2009, 2012). The implementation of multiple sensors enables tracing of disassembly trajectories under varying liquid phase and processing conditions. Furthermore, meaningful and reliable sensors to control critical quality attributes can be identified during the development phase. This knowledge can aid in decision-making during manufacturing process development and operation. Overall, the presented approach would enable a larger design space of processes and thereby enhanced manufacturing flexibility (ICH Expert Working Group, 2012).

5.4. Conclusions

In this work, a process monitoring framework consisting of in-line, on-line, and at-line analysis was implemented to investigate the diafiltration-based disassembly of HBcAg VLPs. The framework provides data on multiple characteristics simultaneously such as filtration performance, liquid phase conditions (diafiltration progress), and product properties. For the latter, regression models in combination with on-line UV spectra accurately predicted the dimer (VLP subunit) concentration in the CFF unit. Univariate UV and SLS signals were also identified as qualitative indicators of disassembly progress. Here, the 309 nm absorbance and simple mathematical

operations were utilized to successfully detect the endpoint of the diafiltration-based disassembly. It was concluded that the 309 nm absorbance combines UV absorption and light scattering and therefore indicates a combination of protein properties such as concentration and particle size. Another interesting process-related observation was that a reduction in processing time did not result in a slower disassembly, although this should be confirmed by further research.

The presented framework closes the gap in process monitoring between capture/purification and reassembly for VLP processes that are based on dis- and reassembly. It therefore forms the basis for an end-to-end PAT approach for VLP downstream processing. In future, the developed monitoring framework could be applied to other non-enveloped VLPs, for example derived from papillomaviruses or Norwalk viruses. Changes in SLS intensity and UV spectra due to disassembly are also known for these VLPs, which makes a successful transfer likely. The presented combination of diafiltration and on-line monitoring of product properties might also be beneficial for other biochemical reactions such as inclusion body solubilization and refolding. Overall, the varying complexity of the developed PAT approaches enables potential applications in various fields, ranging from reaction analysis over process development to manufacturing. Regarding current regulatory initiatives such as Quality by Design, this broad complexity scale is particularly beneficial. Complex experimental setups, equipment, and models facilitate a thorough process characterization and the identification of viable signals for process control. This prior knowledge enables the implementation of simple and efficient monitoring and control at manufacturing scale.

Acknowledgments

This project received funding from Deutsche Forschungsgemeinschaft (DFG) in the frame of SPP 1934, project number 273937032. The authors express their gratitude to Adam Zlotnick and Kim Young for the provision with VLP production plasmids. The authors would like to thank Robin Schiemer for thoroughly reviewing the manuscript and providing valuable suggestions.

Supplementary material

Appendix C contains the supplementary material associated with this chapter:

- S5.1 Supplementary process data
- S5.2 Extended discussion of in-line monitoring
- S5.3 Supplementary regression modeling data

6

Modeling the Gibbs-Donnan effect during ultrafiltration and diafiltration processes using the Poisson-Boltzmann theory in combination with a basic Stern model

Till Briskot[*,a,b], *Nils Hillebrandt*[*,a], *Simon Kluters*[c], *Gang Wang*[c], *Joey Studts*[c], *Tobias Hahn*[b], *Thiemo Huuk*[b], *Jürgen Hubbuch*[a]

* Contributed equally

[a] Institute of Engineering in Life Sciences - Section IV: Biomolecular Separation Engineering, Karlsruhe Institute of Technology (KIT), Karlsruhe, Germany

[b] GoSilico GmbH, Karlsruhe, Germany

[c] Late Stage DSP Development, Boehringer Ingelheim Pharma GmbH & Co. KG, Biberach an der Riß, Germany

Abstract

The Gibbs-Donnan effect is a well-known phenomenon causing ions to be distributed unevenly across semi-permeable membranes that are permeable to ions but not to larger macromolecules such as proteins. In protein ultrafiltration and diafiltration (UF/DF) processes, this effect often leads to discrepancies between the pH and excipient concentrations in the final drug substance and in the DF buffer.

In this work, a model describing the retentate and permeate composition throughout combined UF/DF processes is introduced. The model accounts for volume exclusion effects and electrostatic interactions between ions and the protein based on the Poisson-Boltzmann theory in combination with a basic Stern model. Advantages and limitations of the proposed model were analyzed using UF/DF experiments with multiple diafiltration buffers and proteins. A comparison between simulated and experimental permeate data showed good

agreement for low to moderate Donnan potentials but model limitations for high Donnan potentials at protein concentration larger 100 g L^{-1}. In contrast, simulated retentate data showed good agreement for both low and high Donnan potentials and for protein concentrations up to 190 g L^{-1}. It was demonstrated that in this high protein concentration regime, the applied basic Stern model provides more accurate predictions compared to previous theories based on the Poisson-Boltzmann theory alone. This makes the model a valuable tool to describe discrepancies between pH and excipient concentrations in the final drug substance and DF buffer for highly concentrated protein formulations. As model predictions are based solely on structural information on the protein and the composition of the DF buffer, the model is particularly beneficial at an early stage in process development to streamline process development and improve process understanding.

6.1. Introduction

Recombinant proteins, such as monoclonal antibodies (mAbs), are an important class of biopharmaceuticals (Walsh, 2010, 2018). To enable a patient-friendly administration of the therapeutic protein, high protein concentrations, often exceeding 100 g L^{-1}, are required in the final product (Garidel et al., 2017; Hung et al., 2016; Shire et al., 2004). With such high protein concentrations, it is critical that the drug product meets specifications for the solution pH and excipient content to ensure long-term shelf life stability and to maintain drug efficacy (Shire, 2009; Shire et al., 2004).

To control the pH and excipient content of the drug substance, cross-flow ultrafiltration (UF) and diafiltration (DF) steps are ubiquitous unit operations during the manufacturing of pharmaceutical proteins (Liderfelt & Royce, 2018; Lutz & Raghunath, 2006; Rathore & Shirke, 2011; van Reis & Zydney, 2001; Zydney, 2020). Using a semi-permeable membrane that can be passed by smaller solutes but not by the active pharmaceutical ingredient (API) itself, UF and DF are used to concentrate the API and transfer it to the final formulation condition, respectively (Liderfelt & Royce, 2018; Lutz & Raghunath, 2006). Usually, both steps are performed in a combined UF/DF process, where the API is concentrated to an intermediate concentration, diafiltrated against a diafiltration buffer, and subsequently concentrated to its final concentration (Liderfelt & Royce, 2018). Despite the widespread use of UF/DF processes in biopharmaceutical manufacturing, the development of these processes is not straightforward for many reasons. Due to volume exclusion effects and the Gibbs-Donnan effect (Donnan, 1911), deviations between the pH and excipient concentrations in the final drug substance and the actual diafiltration buffer are commonly observed (Abel et al., 2018; Ambrožič et al., 2021; Baek, Singh, et al., 2019; Bolton et al., 2011; Jabra et al., 2020; Ladwig et al., 2020; Miao et

al., 2009; Stoner et al., 2004; Teeters et al., 2011). These discrepancies complicate the definition of a diafiltration buffer that meets desired specifications in the drug substance. Thus, to control and maintain drug substance quality, a profound scientific understanding of volume exclusion effects and the Gibbs-Donnan effect are essential.

To provide a scientific understanding of both effects, a number of theoretical approaches have been proposed over the past two decades (Ambrožič et al., 2021; Baek, Singh, et al., 2019; Bolton et al., 2011; Jabra et al., 2020; Ladwig et al., 2020; Miao et al., 2009; Stoner et al., 2004; Teeters et al., 2011). Depending on the model, the Gibbs-Donnan effect is described either macroscopically using a Donnan model (Baek, Singh, et al., 2019; Bolton et al., 2011; Jabra et al., 2020; Stoner et al., 2004) or microscopically based on the Gouy-Chapman and Poisson-Boltzmann (PB) theory (Baek, Singh, et al., 2019; Bolton et al., 2011; Jabra et al., 2020; Stoner et al., 2004). Both approaches account for an asymmetric distribution of smaller charged solutes across the membrane resulting from the charged nature of the protein and the semi-permeable property of the membrane. As most of the previous work focused only on the DF step (Baek, Singh, et al., 2019; Bolton et al., 2011; Jabra et al., 2020; Stoner et al., 2004), most proposed models are not suited for a holistic description of a combined UF/DF process. Only those models based on the PB theory have been developed explicitly to account for the Gibbs-Donnan effect during both the UF and DF step (Ambrožič et al., 2021; Ladwig et al., 2020; Miao et al., 2009; Teeters et al., 2011). While some of these models require an experimental determination of model parameters before they can be used for prediction (Ambrožič et al., 2021; Ladwig et al., 2020), other models are based solely on structural information of the protein and do not require any experimental calibration (Ambrožič et al., 2021; Ladwig et al., 2020). However, since the latter showed considerable deviations to experimental data and were only applied for histidine-based diafiltration buffers, the validity of these models is not clear. Independent of the calibration effort, all models based on the PB equation use a cell model approximation initially applied by Miao et al. (2009). The theoretical description of the retentate is thereby reduced to a single spherical and electroneutral Wigner-Seitz (WS) cell confining a single charged protein at its center, surrounded by smaller solutes. Within the framework of the cell model, the PB equation is commonly solved using one of two limiting cases defined by boundary condition for the electrostatic potential at the boundary of the WS cell (Denton, 2010; Deserno & Holm, 2001). With the exception of Ladwig et al. (2020), previous works considered the limiting case of Donnan equilibrium, where the retentate and permeate are in thermodynamic equilibrium at all times. A clear validation of this and other

model assumptions requires that model predictions are compared with measurements in both retentate and permeate. However, in previous works, model validation was performed using measurements in the retentate alone. Only in the case of Ambrožič et al. (2021), additional permeate measurements were considered for model validation. However, as these data were limited to the DF step, limitations of the PB theory and other model simplifications are still insufficiently analyzed and discussed.

The aim of this work was to introduce an alternative model that describes the permeate and retentate composition throughout combined UF/DF processes including the high concentration regime. Predictions should be based purely on structural information of the protein and buffer compositions; hence the model should not require any experimental calibration. Therefore, basic concepts of previously published models were considered, advanced, and extended with new components. The developed model accounts for volume exclusion and the Donnan effect using mass balances coupled to PB theory and electroneutrality constraints similarly as the approach of Ambrožič et al. (2021). In contrast, the cell model approximation used in this work ensures coverage of the entire retentate volume by the WS cells, thereby ensuring conservation of mass and greatly simplifying mass balance equations. Furthermore, the effect of charge regulation based on the amino acid sequence is used similarly as in Jabra et al. (2020) to enable a description of the protein charge over a wide range of pH and ionic strength, and to avoid the need for an experimentally determined titration curve. A novel approach among UF/DF models is the description of the electrostatic potential inside the WS cell using a basic Stern model (Westall & Hohl, 1980) to ensure a more accurate prediction in the high concentration regime during the second UF step. The applicability of the model in supporting UF/DF process development is demonstrated by predicting the Gibbs-Donnan effect on retentate pH and excipient concentrations using multiple diafiltration buffer systems and proteins. Limitations of the proposed model are examined by critically discussing model assumptions and simplifications and comparing computed and measured retentate and permeate compositions throughout combined UF/DF processes.

6.2. Theory

In this section a refined mean-field approach is derived that allows for a description of the temporal change in pH and excipient concentrations during combined UF/DF processes. First, general mass balances are defined that describe the temporal change in the target variables. In the following sections, an expression for the Gibbs-Donnan coefficient is derived, which describes the concentration ratio of permeating ions between retentate and permeate.

6.2.1. System description

We consider a system at constant temperature $T = 298.15\,K$ where all solutions are assumed to be electrolyte solutions with a constant relative permittivity of water $\varepsilon = 78.3$. Proteins immersed in the retentate are idealized as perfect hard spheres with radius a_M and homogeneous surface charge density σ_M or net charge $Z_M = 4\pi a_{M^2} e^{-1} \sigma_M$, where e is the elementary charge. The permeate leaving the system is separated from the retentate by a semi-permeable membrane that is permeable to small solutes but not to the protein. The solutions, including the retentate, diafiltration buffer, and permeate may contain multiple smaller solutes. These include, for instance, salt ions, sugars, or buffer substances. Depending on the pH of the solution, some of these solutes may be present in different ionization states. Acetate, for instance, possesses one protonation site and can thus be present in two ionization states. Therefore, the total concentration c_i of the i-th solute can in general be decomposed according to

$$c_i = \sum_j c_{i,j}(\mathrm{pH})\,, \tag{6.1}$$

whereby the concentration of the j-th ionization state $c_{i,j}$ depends on the pH. Given the pH, the concentrations $c_{i,j}$ can be derived from c_i following the dissociation equilibrium of solute i, as described in detail by Ladwig et al. (2020). The non-ideal behavior of electrolyte solutions at higher ionic strength was thereby considered using the Davies equation

$$\log_{10}(\gamma_{i,j}) = -A_H z_{i,j}^2 \left(\frac{\sqrt{I_m}}{1+\sqrt{I_m}} - bI_m \right), \tag{6.2}$$

where $\gamma_{i,j}$ denotes the activity coefficient of the j-th ionization state with charge $z_{i,j}$, $A_H = 0.5\ \mathrm{L}^{0.5}\ \mathrm{mol}^{-0.5}$ is the Debye Hueckel constant, I_m represents the ionic strength, and $b = 0.2$ is a constant (C. W. Davies, 1938). Based on the Davies equation, the shift between the k-th apparent pK of a solute i $\mathrm{p}K_{i,k}^*(I_m)$ and the thermodynamic ideal value $\mathrm{p}K_{i,k}$ is given by

$$\mathrm{p}K_{i,k}^*(I_m) = \mathrm{p}K_{i,k} + A_H(2(\zeta_i - k) + 1)\left(\frac{\sqrt{I_m}}{1+\sqrt{I_m}} - bI_m \right) \tag{6.3}$$

with ζ_i representing the charge of the fully protonated state. It is important to note, that Equation 6.3 is only valid for the condition $I_m \lesssim 0.3\ \mathrm{mol\,L^{-1}}$ considered in this work.

6.2.2. Mass balances

Due to the Gibbs-Donnan effect and volume exclusion effects induced by the protein, the total solute concentration in the retentate $c_{\mathrm{Ret},i}$ and permeate $c_{\mathrm{Perm},i}$ can often deviate from each other. Introducing the Gibbs-Donnan coefficient as

$$r_{\mathrm{D},i,j} = \frac{c_{\mathrm{Ret},i,j}}{c_{\mathrm{Perm},i,j}}, \tag{6.4}$$

the mass balance for a solute i is given by

$$\frac{\mathrm{d}c_{\mathrm{Ret},i}}{\mathrm{d}c_{\mathrm{M}}} = \sum_j \frac{c_{\mathrm{Ret},i,j}}{c_{\mathrm{M}}}\left(1 - r_{\mathrm{D},i,j}^{-1}\right) \tag{6.5}$$

for UF steps and

$$\frac{\mathrm{d}c_{\mathrm{Ret},i}}{\mathrm{d}v_{\mathrm{DV}}} = \sum_j \left(c_{\mathrm{DF},i,j} - r_{\mathrm{D},i,j}^{-1} c_{\mathrm{Ret},i,j}\right) \tag{6.6}$$

for DF steps, where $c_{\mathrm{DF},i,j}$ represents the concentration in the diafiltration buffer and v_{DV} indicates the number of diafiltration volumes. The concentration $c_{\mathrm{DF},i,j}$ is commonly known. Thus, having an expression for $r_{\mathrm{D},i,j}$ and starting conditions for $c_{\mathrm{Ret},i}$, Equations 6.5 and 6.6 can be used to describe the temporal change in $c_{\mathrm{Ret},i}$. For a more detailed derivation of Equations 6.5 and 6.6, we refer to the Appendix D, Section S6.1.

6.2.3. Cell model

To derive a mathematical expression for $r_{\mathrm{D},i,j}$, we consider the approximation of the system shown in Figure 6.1. Following the cell model approximation (Denton, 2010; Deserno & Holm, 2001; Marcus, 1955; Wennerström et al., 1982), the retentate is divided into multiple identical WS cells. Each WS cell contains one protein in its center. Considering a spherical cell geometry, the radius of the WS cell R_{WS} is thus directly related to c_{M} in the retentate according to

$$R_{\mathrm{WS}} = \left(\frac{3}{4\pi N_{\mathrm{A}} c_{\mathrm{M}}}\right)^{\frac{1}{3}}, \tag{6.7}$$

where N_{A} denotes the Avogadro number. The advantage of the cell model is that each cell is representative for the whole retentate. As a consequence, the theoretical description of $r_{\mathrm{D},i,j}$ is reduced to one cell only (Deserno & Holm, 2001).

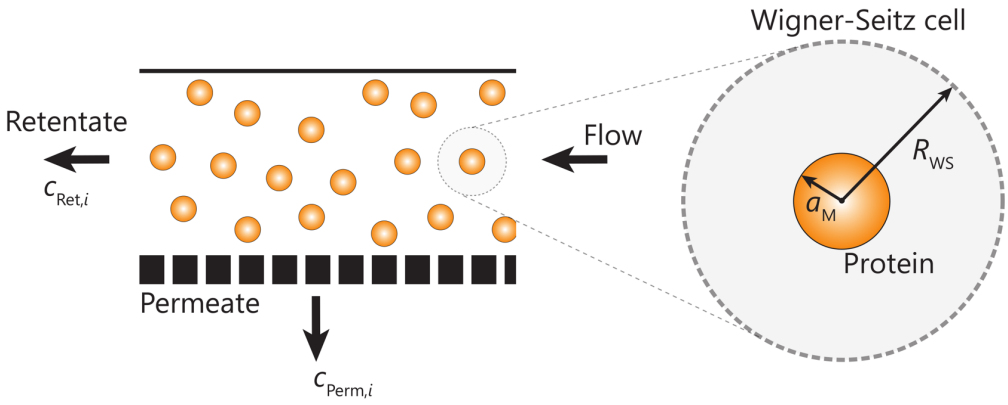

Figure 6.1. Cell model approximation of the retentate. The total retentate volume is divided into multiple identical Wigner-Seitz cells. Each cell contains one protein in its center, indicated in orange. The theoretical description of the retentate is reduced to one cell only.

Given the spherical cell geometry, the solute concentration inside the cell $c_{i,j}(r)$ is also only a function of the radial position $r \in [a_{\mathrm{M}}, R_{\mathrm{WS}}]$. The same applies to other variables like the pH or the electrostatic potential ψ that is formed due to the charged protein. As the protein in the center of the cell is considered to be a hard sphere and impermeable for smaller solutes, the average concentration of a solute in the void volume of the cell $\bar{c}_{i,j}$ is related to $c_{\mathrm{Ret},i,j}$ according to

$$\begin{aligned} \bar{c}_{i,j} &= c_{\mathrm{Ret},i,j}(1-\Theta)^{-1} \\ &= \frac{3}{(R_{WS}^3 - a_M^3)} \int_{a_{\mathrm{M}}}^{R_{\mathrm{WS}}} c_{i,j}(r) r^2 \, dr, \end{aligned} \tag{6.8}$$

where $\Theta = 4\pi a_M^3 c_{\mathrm{M}} N_{\mathrm{A}} 3^{-1}$ denotes the fraction of the cell volume or retentate excluded by the protein. It is important to note that the definition of R_{WS} according to Equation 6.7 differs from previous models based on the PB equation (Ambrožič et al., 2021; Ladwig et al., 2020; Miao et al., 2009). While these previous works defined R_{WS} by half the distance between two adjacent proteins, Equation 6.7 is more common in physics, as it ensures that the integral in Equation 6.8 covers the entire retentate volume (Denton, 2010; Deserno & Holm, 2001). Thus, this approach also ensures conservation of mass. Applying Equation 6.8 to the proton concentration gives the average pH in the cell $\overline{\mathrm{pH}}$. In the following, $\overline{\mathrm{pH}}$ is also referred to as retentate pH and can be determined experimentally using a pH electrode.

6.2.4. Gibbs-Donnan coefficient

Due to interactions between small solutes and the protein, $c_{i,j}(r)$ can deviate significantly from $\bar{c}_{i,j}$. Neglecting the size of a small solute, its electrochemical potential $\mu_{i,j}$ inside the WS cell is defined by

$$\mu_{i,j}(r) = \mu_{i,j}^{*} + k_{\mathrm{b}}T \ln\left(\frac{c_{i,j}(r)}{c^{+}}\right) + ez_{i,j}\psi(r), \tag{6.9}$$

where $\mu_{i,j}^{*}$ is the reference potential at infinite dilution, k_{b} is the Boltzmann constant and c^{+} is a reference concentration to make the term inside the logarithm dimensionless. Inside the permeate, ψ vanishes and $\mu_{i,j}$ simplifies to

$$\mu_{\mathrm{Perm},i,j} = \mu_{i,j}^{*} + k_{\mathrm{b}}T \ln\left(\frac{c_{\mathrm{Perm},i,j}}{c^{+}}\right). \tag{6.10}$$

Using Equations 6.9 and 6.10 and the equilibrium condition $\mu_{i,j}(r) = \mu_{\mathrm{Perm},i,j}$, $c_{i,j}$ can be related to $c_{\mathrm{Perm},i,j}$ using the Boltzmann relation

$$c_{i,j}(r) = c_{\mathrm{Perm},i,j} \exp\left(-z_{i,j}\frac{e\psi(r)}{k_{\mathrm{b}}T}\right). \tag{6.11}$$

Using Equations 6.11 and 6.8, $r_{\mathrm{D},i,j}$ can be defined by

$$r_{\mathrm{D},i,j} = (1-\Theta)\frac{3}{(R_{WS}^{3} - a_{M}^{3})} \cdot \int_{\mathrm{a_M}}^{\mathrm{R_{WS}}} \exp\left(-\mathrm{z_{i,j}}\frac{\mathrm{e}\psi(\mathrm{r})}{\mathrm{k_b T}}\right)\mathrm{r}^{2}\,\mathrm{dr}. \tag{6.12}$$

Introducing the average (Donnan) potential

$$\bar{\psi} = -\frac{k_{\mathrm{b}}T}{ez_{i,j}} \ln\left(\frac{3}{(R_{WS}^{3} - a_{M}^{3})} \cdot \int_{a_{\mathrm{M}}}^{R_{\mathrm{WS}}} \exp\left(-z_{i,j}\frac{e\psi(r)}{k_{\mathrm{b}}T}\right) r^{2}\,dr\right), \tag{6.13}$$

$r_{\mathrm{D},i,j}$ can also be expressed as

$$r_{\mathrm{D},i,j} = (1-\Theta)\exp\left(-z_{i,j}\frac{e\bar{\psi}}{k_{\mathrm{b}}T}\right). \tag{6.14}$$

As $r_{\mathrm{D},i,j}$ is a function of Θ and $\bar{\psi}$, the Gibbs-Donnan coefficient in this work accounts for both volume exclusion and electrostatic interactions between a solute and the protein.

6.2.5. Basic Stern model and Donnan potential

In this section, we discuss $\bar{\psi}$ in more detail and how it can be calculated. In contrast to previous works (Ambrožič et al., 2021; Ladwig et al., 2020), we use the basic Stern model (Westall & Hohl, 1980) to describe the distribution of ψ inside the WS cell and thus $\bar{\psi}$. Within the framework of the basic Stern model, the diffuse layer is separated from the inner protein surface by a charge-free Stern layer, as schematically shown in Figure 6.2. Inside the Stern layer, ψ

drops linearly from ψ_0, i.e. the electrostatic potential at the protein surface, to ψ_D at the origin of the diffuse layer. The drop is defined by σ_M and the stern capacitance (Behrens & Borkovec, 1999; Gisler et al., 1994)

$$C_S = \frac{\sigma_M(\psi_0)}{\psi_0 - \psi_D}. \tag{6.15}$$

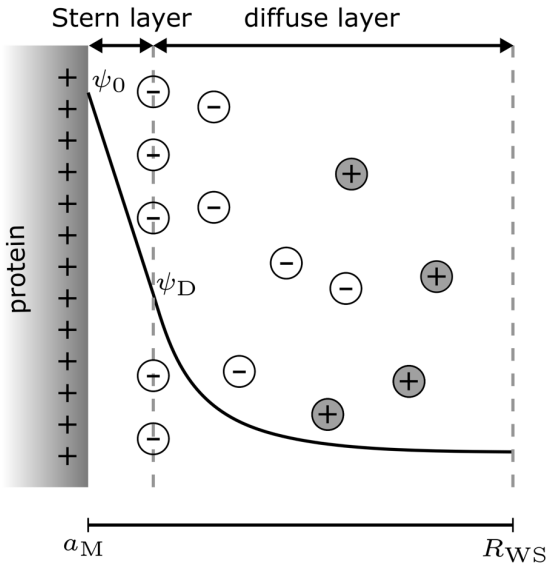

Figure 6.2. Schematic representation of the electric double layer according to the basic Stern model.

The charge density σ_M is thereby often a function of ψ_0 itself. In the limiting case $C_S \to \infty$, it follows $\psi_0 = \psi_D$ and the basic stern model simplifies to the traditional Gouy-Chapman theory used in previous works (Ambrožič et al., 2021; Ladwig et al., 2020). Inside the diffuse layer, ψ obeys the Poisson equation in spherical coordinates

$$\frac{\partial^2\psi}{\partial r^2}(r) + \frac{2}{r}\frac{\partial\psi}{\partial r}(r) = -\frac{eN_A}{\varepsilon\varepsilon_0}\sum_i\sum_j z_{i,j}\, c_{i,j}(r), \tag{6.16}$$

where ε_0 denotes the vacuum permittivity. Using $\overline{\psi}$ introduced earlier, $c_{i,j}$ on the right-hand side of the Poisson equation can be related to $\bar{c}_{i,j}$ according to

$$c_{i,j}(r) = \bar{c}_{i,j}\left(\overline{\mathrm{pH}}\right)\exp\left(-z_{i,j}\frac{e}{k_b T}\left(\psi(r) - \bar{\psi}\right)\right). \tag{6.17}$$

Combining the Boltzmann relation (Equation 6.17) with the Poisson equation leads to the PB equation. It can be solved numerically once $\overline{\mathrm{pH}}$ and $\overline{\psi}$ are known and appropriate boundary conditions at $r = a_M$ and $r = R_{WS}$ are defined. According to Gauss's law, the condition at the boundary of the WS cell is given by

$$\left.\frac{\partial \psi}{\partial r}\right|_{r=R_{\mathrm{WS}}} = 0. \tag{6.18}$$

To ensure electroneutrality within the WS cell, the boundary condition at the origin of the diffuse layer is given by

$$\left.\frac{\partial \psi}{\partial r}\right|_{r=a_{\mathrm{M}}} = -\frac{\sigma_{\mathrm{M}}(\psi_0)}{\varepsilon\varepsilon_0}. \tag{6.19}$$

The potential $\bar{\psi}$ used in the PB equation and $\overline{\mathrm{pH}}$ used to determine $\bar{c}_{i,j}$ are formed in such a way that electroneutrality is fulfilled in both the WS cell and the permeate. At the same time, $\bar{\psi}$ must comply with Equation 6.13 and thus the solution of the PB equation itself. To ensure electroneutrality in the permeate, $\bar{\psi}$ and $\overline{\mathrm{pH}}$ must fulfill

$$\begin{aligned} 0 &= \sum_i \sum_j z_{i,j}\, c_{\mathrm{Perm},i,j} \\ &= \sum_i \sum_j z_{i,j}\, \bar{c}_{i,j}\left(\overline{\mathrm{pH}}\right) \exp\left(z_{i,j}\frac{e\bar{\psi}}{k_{\mathrm{b}}T}\right). \end{aligned} \tag{6.20}$$

As electroneutrality in the WS cell is ensured by the boundary condition (Equation 6.19), the PB equation must be solved iteratively until $\bar{\psi}$ and $\overline{\mathrm{pH}}$ fulfill both Equations 6.20 and 6.13.

6.2.6. Protein charge

The surface charge density of the protein σ_{M} used in Equations 6.15 and 6.19 originates mostly from ionizable amino acid side chains located on the surface of the protein. It can in general be described by

$$\sigma_{\mathrm{M}}(\mathrm{pH}_0) = eN_{\mathrm{A}} \sum_k \Gamma_k\left((\zeta_k - 1)[1 + 10^{\mathrm{p}K_k - \mathrm{pH}_0}]^{-1} + \zeta_k[1 + 10^{\mathrm{pH}_0 - \mathrm{p}K_k}]^{-1}\right), \tag{6.21}$$

where pH_0 denotes the pH at the surface of the protein, ζ_k represents the charge of the protonated side chain, and Γ_k is the surface density of the k-th amino acid side chain characterized by $\mathrm{p}K_k$ (Briskot et al., 2020). Based on the Boltzmann relation (Equation 6.17), pH_0 is defined by

$$\mathrm{pH}_0 = \overline{\mathrm{pH}} + \frac{1}{\ln(10)}\frac{e}{k_{\mathrm{b}}T}(\psi_0 - \bar{\psi}). \tag{6.22}$$

In agreement with previous works (Ladwig et al., 2020), it is in the following assumed that all ionizable amino acids of a protein are located at the surface of the protein. Under this assumption,

$$\Gamma_k = \frac{N_k}{4\pi a_M^2 N_{\mathrm{A}}} \tag{6.23}$$

can be derived from a_M and the number of amino acids in the primary protein structure N_k.

6.3. Materials and methods

6.3.1. Chemicals and proteins

Unless stated otherwise, all chemicals were purchased from Merck KGaA (Darmstadt, Germany). All buffers and solutions were prepared with ultrapure water and filtered with 0.2 µm pore size. Two monoclonal antibodies (mAbA and mAbB) as well as one antigen-binding fragment FabC were provided by Boehringer Ingelheim Pharma GmbH & Co. KG (Biberach an der Riß, Germany).

6.3.2. UF/DF system

Filtration experiments with mAbB were performed using a KrosFlo Research KRIIi (Spectrum Labs, Rancho-Dominguez, CA, USA) equipped with a 88 cm^2, 30 kDa, C screen, Ultracel Pellicon 3 (regenerated cellulose) membrane (Merck KGaA). Experiments with mAbA and FabC were performed using a custom-made cross-flow filtration setup similar to the one used for mAbB. For mAbA, the system was equipped with a 200 cm^2, 30 kDa, Hydrosart (stabilized cellulose), Sartocon Slice ECO membrane (Sartorius Stedim Biotech GmbH, Göttingen, Germany). For FabC, a 176 cm^2, 10 kDa, A screen, Pellicon 3 cassette with Biomax (polyethersulfone) membrane (Merck KGaA) was used.

6.3.3. Protein preparation

Prior to UF/DF experiments, mAbA and mAbB were diafiltrated against a 50 mM sodium acetate buffer (pH 5.5) containing 135 mM sodium chloride. The protein concentration in the prepared feed solution was 13 g L^{-1}. In case of FabC, the protein was diafiltrated against a 50 mM sodium acetate buffer (pH 5.0) containing 70 mM sodium chloride. The protein concentration of the diafiltrated feed solution was 6.5 g L^{-1}.

6.3.4. UF/DF experiments

For all proteins, combined UF/DF experiments were performed. After concentrating the protein to an intermediate concentration of approximately 50 g L^{-1} using a first UF step (UF1), the protein was diafiltrated for 10 diafiltration volumes (DVs) at a constant retentate volume (c_M = const.) by continuously feeding DF buffer into the retentate vessel. After the DF step, the protein was concentrated beyond 100 g L^{-1} using a second UF step (UF2). Depending on the experiment, the DF buffer was based on either sodium acetate, sodium succinate, or L-histidine/hydrochloric acid. Applied DF buffers varied in buffer and sodium chloride concentrations as well as pH. For

a detailed summary of all experiments, we refer to Table 6.1. Experiments with mAbB were performed with a feed flow rate of 44 mL min^{-1} and the transmembrane pressure (TMP) was set at a target of 0.4 bar. During UF2, the feed flow rate was adjusted to keep the TMP below 1 bar. In case of mAbA and FabC, the feed flow rate was 100 mL min^{-1} and the set point TMP was 0.7 and 1.5 bar as summarized in Table 6.1. During all experiments, retentate samples were taken and analyzed offline as described in Section 6.3.5. Before taking a sample, the retentate was recirculated for at least 3 min without applied transmembrane pressure to ensure retentate homogeneity. For mAbB, additional samples were drawn directly from the permeate stream via a septum and without prior retentate recirculation.

Table 6.1. Summary of all diafiltration buffers and TMP set points used for mAbA, mAbB, and FabC.

Experiment	Protein	TMP	Buffer system	Buffer conc.	DF buffer pH	NaCl conc.
		bar		mM	-	mM
ExpA1	mAbA	1.5	Acetate	10	5.0	0
ExpA2	mAbA	1.5	Acetate	40	5.0	0
ExpA3	mAbA	1.5	Acetate	10	5.0	150
ExpA4	mAbA	1.5	Acetate	40	5.5	0
ExpA5	mAbA	1.5	Succinate	10	5.5	0
ExpA6	mAbA	1.5	Histidine	10	6.0	0
ExpA7	mAbA	1.5	Histidine	40	6.0	0
ExpB1	mAbB	0.4	Acetate	10	5.0	0
ExpB2	mAbB	0.4	Succinate	10	5.0	0
ExpB3	mAbB	0.4	Succinate	10	5.5	0
ExpB4	mAbB	0.4	Histidine	10	6.0	0
ExpB5	mAbB	0.4	Histidine	30	6.0	0
ExpC1	FabC	0.7	Acetate	20	5.5	0

Abbreviations: conc., concentration; DF, diafiltration; TMP, transmembrane pressure.

6.3.5. Analytics

Samples taken during UF/DF experiments were analyzed offline using several analytical assays described in the following.

6.3.5.1. Protein concentration

The protein concentration in a sample was determined by UV absorbance measurements at 280 nm and native conditions, using either a SoloVPE (mAbA and FabC) or a FlowVPE (mAbB) spectrophotometer (both C Technologies Inc., Bridgewater, NJ, USA). At low process volumes FlowVPE measurements were partly disturbed by air bubbles and respective samples were re-measured in dilute conditions using a NanoDrop 2000 spectrophotometer (Thermo Fisher Scientific, Waltham, MA, USA).

6.3.5.2. Excipient concentrations

Acetic, succinic acid, and L-histidine were analyzed by reversed phase high-performance liquid chromatography. Samples were pre-treated by a 3.3% (w/v) trichloroacetic acid (AppliChem GmbH, Darmstadt, Germany) precipitation. The supernatant was analyzed at 30 °C using a 5 µm 4×250 mm Acclaim OA column (Thermo Fisher Scientific) and a flowrate of 0.6 mL min^{-1}. The mobile phase was 0.1 M sodium sulfate buffer at pH 2.6, adjusted with methanesulfonic acid. For mAbB, the mobile phase consisted of 1% acetonitrile (Carl Roth GmbH & Co. KG, Karlsruhe, Germany) and 99% of the mentioned buffer at a flow rate of 1.2 mL min^{-1}. UV detection was performed at 210 nm and 233 nm. The chloride ion concentration of the abovementioned supernatants was analyzed by a LCK311 photometric assay (Hach Company, Loveland, CO, USA) according to the manufacturer's instructions.

6.3.6. Simulations

For both mAbs with a molecular weight of around 150 kDa, the protein radius was considered to be $a_{\mathrm{M}} = 4.8$ nm based on literature values for the radius of gyration of mAbs (Clark et al., 2013; Garidel et al., 2017). For FabC, $a_{\mathrm{M}} = 2.5$ nm was derived from its molecular weight. For all proteins, the number of amino acids used in Equation 6.23 was derived from the primary structure of the protein. The average pK values used in Equation 6.21 were taken from the advanced null model (Antosiewicz et al., 1996). Values for pK are summarized along ζ_k in Table 6.2. For the applied buffer systems, both ζ_i and thermodynamic ideal pK values are summarized in Table 6.3. Simulations were performed with MATLAB R2018b (The Mathworks Inc., Natick, MA, USA). The ordinary differential equations described in Section 6.2.2 were numerically solved using the solver *ode15s*. The nonlinear PB equation was solved numerically using *bvp5c* and the boundary conditions defined by Equations 6.18 and 6.19. For all proteins and process conditions, a Stern layer capacitance of $C_{\mathrm{S}} = 0.2\ \mathrm{F\,m^{-2}}$ was used based on literature data (Butt et al., 2003).

Table 6.2. Average pK values according to the advanced null model (Antosiewicz et al., 1996). The charge of the fully protonated side chain is indicated by ζ_k.

Residual	Functional group	ζ_k	pK_k
N-terminal	Amine	1	7.5
Glutamic acid	Carboxyl	0	4.4
Aspartic acid	Carboxyl	0	4.0
Tyrosine	Phenyl	0	9.6
Lysine	Amine	1	10.4
Arginine	Guanidyl	1	12.0
Histidine	Imidazol	1	6.3
C-terminal	Carboxyl	0	3.8

Table 6.3. Thermodynamic ideal pK values for all considered buffer systems. The charge of the fully protonated state is indicated by ζ_i.

Buffer	ζ_i	p$K_{i,1}$	p$K_{i,2}$	p$K_{i,3}$
Histidine	+2	1.82	5.99	9.17
Succinic acid	0	4.21	5.64	-
Acetic acid	0	4.76	-	-

6.4. Results and discussion

For UF/DF processes of proteins, qualitative changes in excipient concentrations due to the Donnan effect are well-known. However, their extent, progression, or the resulting pH relies on a complex network of interactions. The model derived in Section 6.2 enables a dynamic simulation of combined UF/DF processes. The input variables of the model include the composition of the feed material and DF buffer, as well as the radius and primary structure of the protein. If these variables are known, no further calibration of the model based on experimental data is required. Along with the pH of the retentate and permeate, the output variables of the model also include the concentrations of buffer substances and other excipients in both process streams. In the following, excipient concentrations in the retentate and permeate are always indicated as $\bar{c}_i$ and $c_{\mathrm{Perm},i}$, respectively. According to Equation 6.1, these concentrations represent the total concentration of a solute i, i.e. including all ionization states.

6.4.1. Impact of the buffer system

To verify whether the proposed model can adequately predict the Donnan effect under various conditions, Figures 6.3 to 6.5 show process results for three common DF buffer systems. These include acetate at pH 5.0 (Figure 6.3), succinate at pH 5.5 (Figure 6.4), and histidine at pH 6.0 (Figure 6.5), each with a buffer concentration of 10 mM. In all cases, data for mAbA and mAbB are shown. Supporting data for FabC can be found in Appendix D, Section S6.4. It is important to note that the scale on the y-axes may differ in Figures 6.3 to 6.5.

In general, model predictions are in good agreement with experimental data. Changes in the retentate pH and solute concentrations throughout the entire UF/DF process are predicted by the model in a quantitative manner. Deviations between measured and simulated pH values are on average less than 0.1 pH units and are thus within the range of the measurement tolerance of common pH electrodes. Only in the case of mAbA and histidine as DF buffer, larger deviations between measured and simulated pH values are observed during the second UF step. Furthermore, it is noticeable that model predictions are in general more accurate for acetate and succinate as DF buffer. In the case of histidine as DF buffer, the final buffer concentration in the retentate is underestimated for both mAbs. Possible explanations for these deviations are discussed in more detail in Section 6.4.3.

For all analyzed DF buffers, a significant Donnan effect was observed, indicated by an offset between the composition of the DF buffer and the retentate after the DF step and especially at the end of the second UF step. As already demonstrated in previous works, the extent of the Donnan effect is thereby strongly dependent on the ionic strength in the DF buffer and the charge of the protein (Baek, Singh, et al., 2019; Jabra et al., 2020). Given the positive net charge of both mAbs, a positive Donnan potential $\bar{\psi}$ is formed, as indicated by orange lines at the bottom of Figures 6.3 to 6.5. According to Equation 6.17, the positive potential causes negatively charged ions to be retained in the retentate and positively charged ions to be depleted. Consequently, the concentration of succinate and acetate in the retentate is higher than the reference value in the DF buffer, while the concentration of histidine is below the reference value. Due to the positive surface charge density of both proteins, the pH of the retentate is elevated in all cases compared to the DF buffer. As can be seen at the bottom of Figures 6.3 to 6.5, mAbA is characterized by a higher net charge in the analyzed pH range compared to mAbB. Thus, the Donnan effect was more pronounced in the case of the former. Comparing the retentate composition after the DF step with that of the DF buffer, it becomes apparent that the Donnan effect was more pronounced in the case of 10 mM acetate (pH 5.0) as DF buffer than for 10 mM

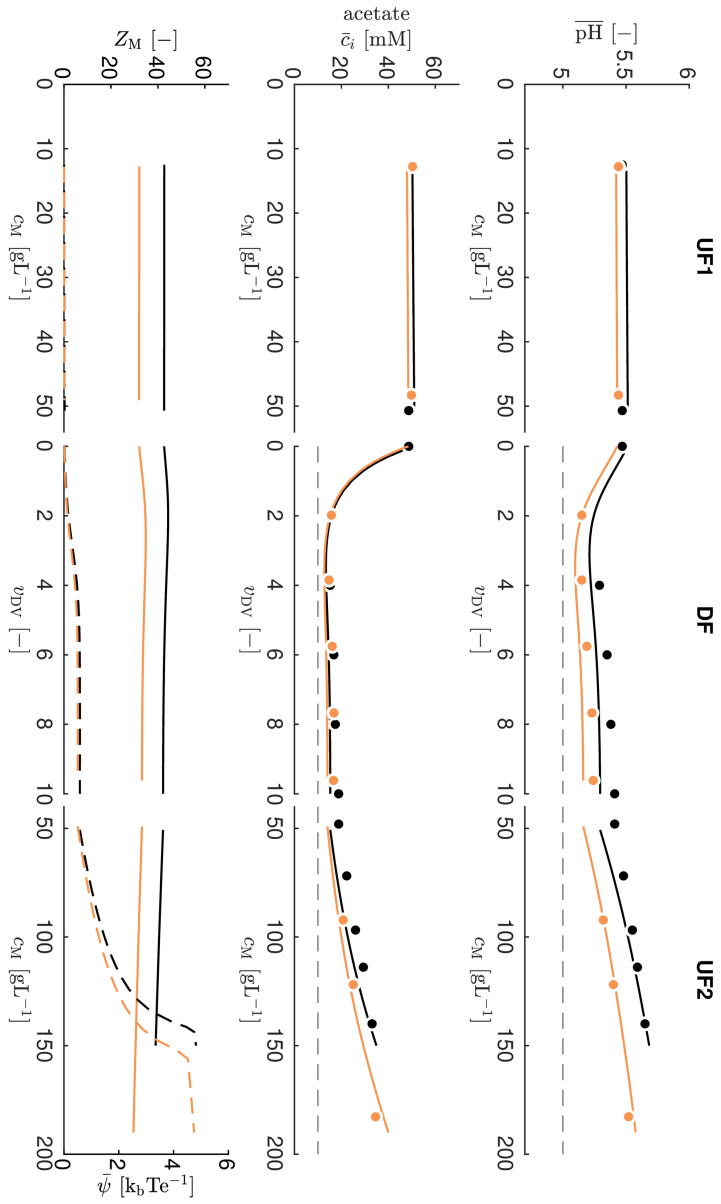

Figure 6.3. *Rotated 90° clockwise*. Illustration of model predictions and measurements according to offline analytics for a UF/DF process using 10 mM acetate (pH 5.0) as DF buffer. Model predictions and measurements are indicated by lines and markers, respectively. Data for mAbA (ExpA1) are shown in black, while data for mAbB (ExpB1) are shown in orange. Top: Comparison between predicted and measured retentate pH. For visual guidance, the pH of the DF buffer is indicated as a gray dashed line. Middle: Comparison between predicted and measured acetate concentration in the retentate. For visual guidance, the acetate concentration in the DF buffer is shown as a gray dashed line. Bottom: Protein charge and $\bar{\psi}$ shown as continuous and dashed lines, respectively.

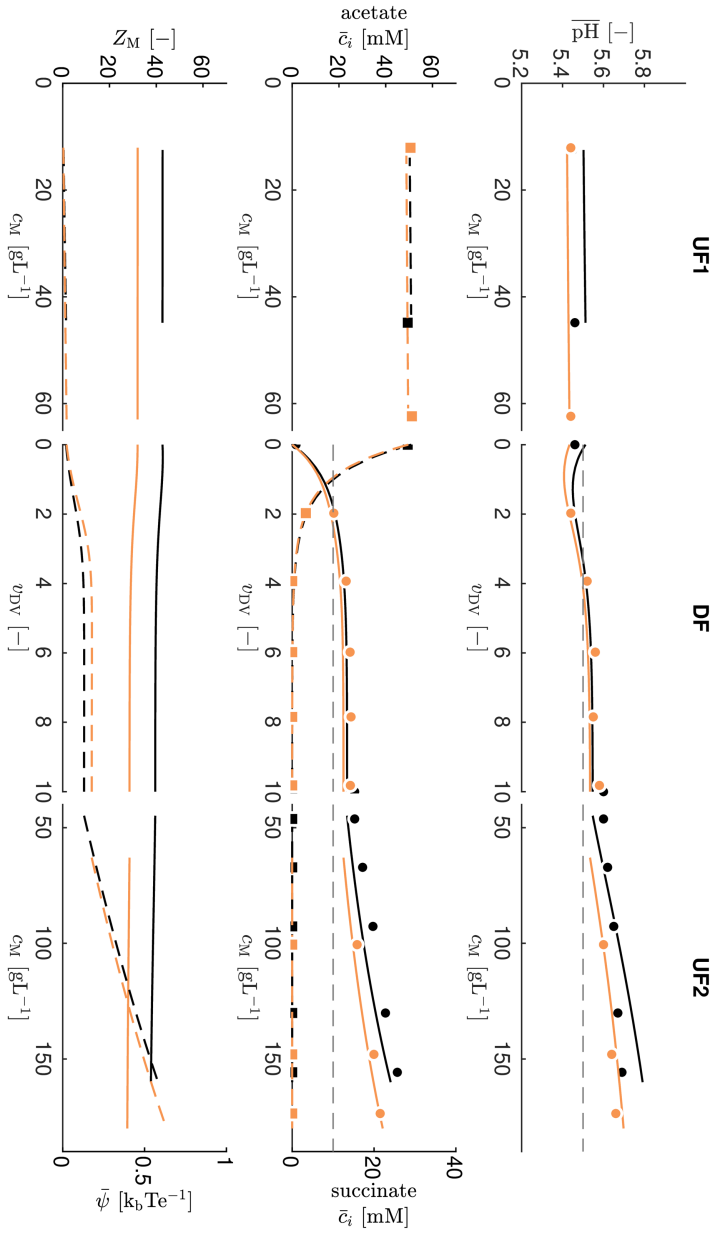

Figure 6.4. *Rotated 90° clockwise*. Illustration of model predictions and measurements according to offline analytics for a UF/DF process using 10 mM succinate (pH 5.5) as DF buffer. Model predictions and measurements are indicated by lines and markers, respectively. Data for mAbA (ExpA5) are shown in black, while data for mAbB (ExpB3) are shown in orange. Top: Comparison between predicted and measured retentate pH. For visual guidance, the pH of the DF buffer is indicated as a gray dashed line. Middle: Comparison between predicted and measured excipient concentrations in the retentate. Predicted succinate and acetate concentrations are indicated by continuous and dashed lines, respectively. Experimental succinate and acetate concentrations are shown as circles and squares, respectively. For visual guidance, the succinate concentration in the DF buffer is shown as a gray dashed line. Bottom: Protein charge and $\bar{\psi}$ shown as continuous and dashed lines, respectively.

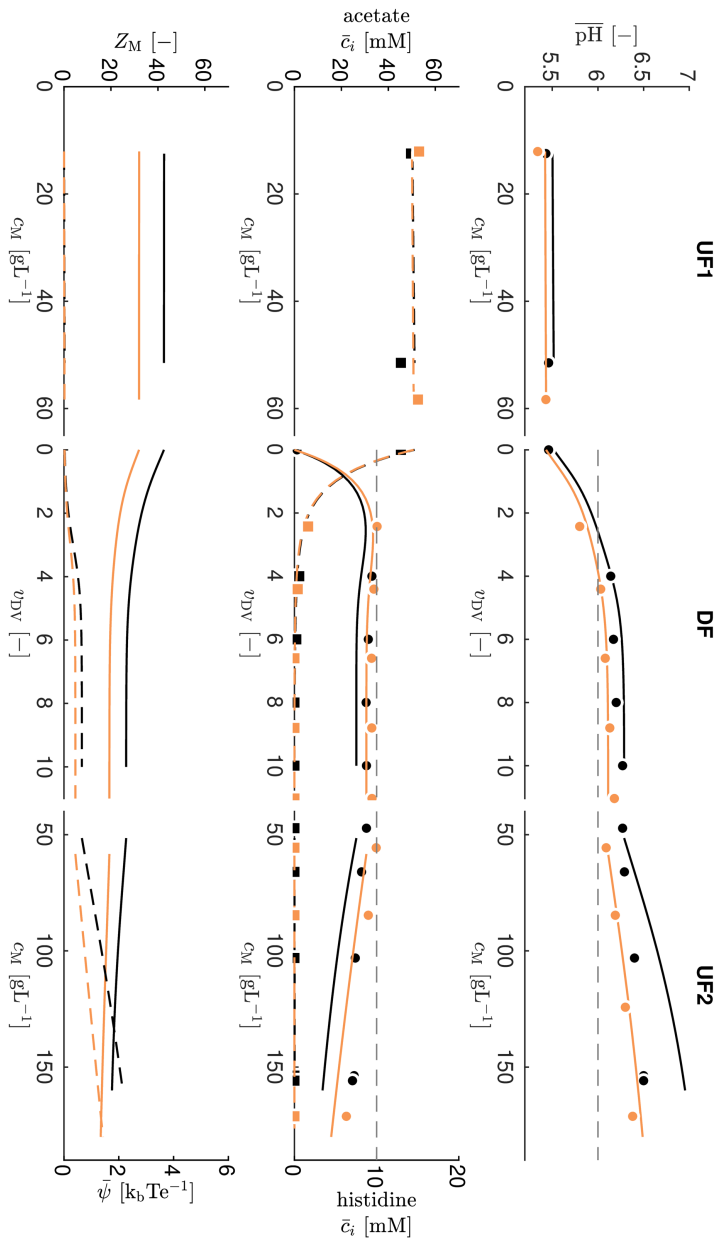

Figure 6.5. *Rotated 90° clockwise*. Illustration of model predictions and measurements according to offline analytics for a UF/DF process using 10 mM histidine (pH 6.0) as DF buffer. Model predictions and measurements are indicated by lines and markers, respectively. Data for mAbA (ExpA6) are shown in black, while data for mAbB (ExpB4) are shown in orange. Top: Comparison between predicted and measured retentate pH. For visual guidance, the pH of the DF buffer is indicated as a gray dashed line. Middle: Comparison between predicted and measured excipient concentrations in the retentate. Predicted histidine and acetate concentrations are indicated by continuous and dashed lines, respectively. Experimental histidine and acetate concentrations are shown as circles and squares, respectively. For visual guidance, the histidine concentration in the DF buffer is shown as a gray dashed line. Bottom: Protein charge and $\bar{\psi}$ shown as continuous and dashed lines, respectively.

succinate (pH 5.5). This is mainly due to the low ionic strength of the buffer system combined with the high protein charge at lower pH values. While acetate is defined by a single pK value and can be present in two ionization states, succinate possesses two dissociation sites and can therefore be present in three ionization states, depending on the solution pH. At pH 5.5, succinate is present in approximately equal proportions in its mono- ($z_{i,j} = -1$) and fully deprotonated ($z_{i,j} = -2$) forms. Thus, the 10 mM succinate buffer (pH 5.5) is characterized by a considerably higher ionic strength compared to 10 mM acetate (pH 5.0). As a consequence, $\bar{\psi}$ is considerably lower for succinate explaining the less pronounced Donnan effect despite the high net charge of the protein.

6.4.2. Impact of the ionic strength

To further analyze the effect of the ionic strength of the DF buffer on the Donnan effect, Figure 6.6 shows UF/DF data for mAbA and varying acetate buffers as DF solution, including ExpA1 as already shown in Figure 6.3. In case of ExpA2, the ionic strength of the DF buffer was increased by increasing the acetate concentration from 10 to 40 mM. In case of ExpA3, on the other hand, the ionic strength was increased by adding 150 mM sodium chloride to the buffer, keeping the acetate concentration constant at 10 mM. For the sake of comparability, the pH of the DF buffer was always 5.0. Furthermore, the same mAb feed material with a mAb concentration of approximately 13 g L^{-1} was used for all experiments. The mAb concentration after the first UF step and during the DF step varied slightly between 44 g L^{-1} (ExpA2) and 54 g L^{-1} (ExpA3).

For all DF buffers analyzed, the observed process behavior is predicted adequately by the model. As expected, the Donnan effect was most pronounced with 10 mM acetate solution as DF buffer given its low ionic strength. After the DF step, the pH and average acetate concentration in the WS cell were elevated by approximately 0.4 pH units and 10 mM, respectively, compared to the DF buffer. After the second UF, the shift between retentate composition and DF buffer increased even more to 0.6 pH units and 20 mM, respectively. Increasing the acetate concentration in the DF buffer from 10 to 40 mM (ExpA2), reduced the offset after the DF to approximately 0.05 pH units. However, as for ExpA1 with 10 mM acetate, data with 40 mM acetate also showed a considerable increase in $\overline{\mathrm{pH}}$ and $\bar{c}_i$ during the second UF step. Only by the addition of 150 mM sodium chloride (ExpA3), the Donnan effect was largely suppressed both during the DF and the second UF step. It is noticeable that the decrease in the retentate pH at the beginning of the DF step was more pronounced in the case of ExpA2 with an acetate concentration of

40 mM than in the case of ExpA1 and ExpA3 with an acetate concentration of 10 mM in the DF buffer. This can be attributed to the increased buffer capacity of the 40 mM acetate buffer. As a result, the pH reached the target after only a few DVs.

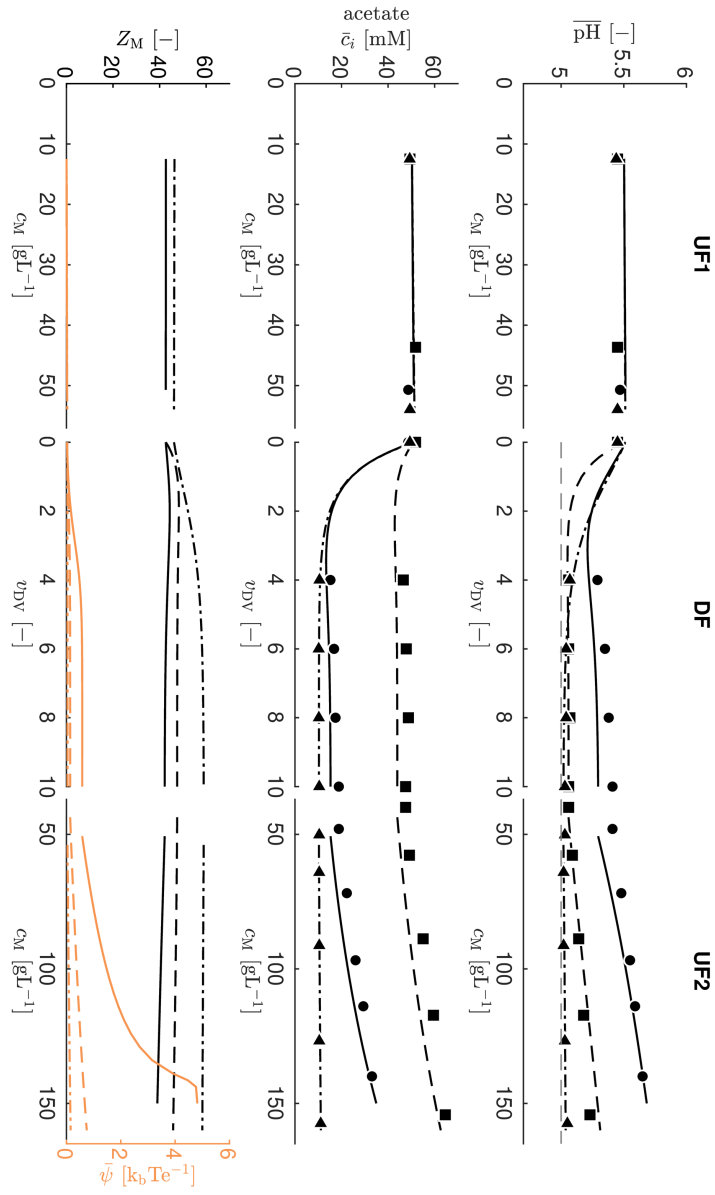

Figure 6.6. *Rotated 90° clockwise*. Illustration of model predictions and measurements according to offline analytics for a UF/DF process using mAbA. Model predictions and measurements are indicated by lines and markers, respectively. Data are shown for different acetate buffers (pH 5.0) as DF solution. These include 10 mM acetate (—, •), 40 mM acetate (---, ▪), and 10 mM acetate with 150 mM sodium chloride (-·-, ◂). Top: Comparison between predicted and measured retentate pH. For visual guidance, the pH of the DF buffers is indicated as a gray dashed line. Middle: Comparison between predicted and measured acetate concentration in the retentate. Bottom: Protein charge and $\bar{\psi}$ shown in black and orange, respectively.

As shown at the bottom of Figure 6.6, the variation of the ionic strength in the DF buffer leads to a complex regulation of Z_M and $\bar{\psi}$ during the UF/DF process, even though the pH of the DF buffer was the same as the feed pH. In contrast to previous works (Miao et al., 2009; Teeters et al., 2011), Z_M is neither considered to be constant throughput the process nor only a function of the pH in the diafiltration buffer (Jabra et al., 2020; Ladwig et al., 2020). According to Equations 6.21 and 6.22, Z_M depends on the local pH at the surface of the protein and is thus strongly affected by the electrostatic environment inside the WS cell. If the electrostatic environment is manipulated, for instance by changing the ionic strength in the WS cell, the protein regulates its charge so that the entire system is again in equilibrium and global electroneutrality is ensured. Due to this charge regulation, the predicted protein charge in the case of ExpA3 is considerably higher than in the case of ExpA1 and ExpA2, despite comparable $\overline{\text{pH}}$. However, due to the increased ionic strength, the protein charge becomes at the same time shielded more strongly by counter-ions. Despite the high value in Z_M, $\bar{\Psi}$ is therefore very low in the case of ExpA3, explaining the less pronounced Donnan effect. Results shown in Figure 6.6 again illustrate the complex interplay between the observed Donnan effect and the diafiltration buffer properties pH and ionic strength. They also show that the protein charge itself is not a direct measure for the observed degree of the Donnan effect.

6.4.3. Model assumptions

Results shown in Figures 6.3 to 6.6, along with supporting data in Appendix D, Sections S6.2 to S6.4, indicate that the proposed model is able to provide quantitative information on the Gibbs-Donnan effect for varying buffer systems, pH, and ionic strength. As the model requires no experimental calibration, model predictions can already be applied in an early stage of process development to identify a suitable DF buffer that meets specifications for the final drug substance or to analyze the robustness of the UF/DF process. However, like previous models, the proposed model is based on several assumptions and simplifications that may limit its applicability and therefore need to be critically examined. In the following, these assumptions are discussed in more detail.

6.4.3.1. Colloidal description

The mathematical description of the Gibbs-Donnan effect is based on a spherical description of proteins. In alignment with previous works, the protein is thereby approximated by a perfect sphere with constant size a_M and homogeneous surface charge density. This colloidal description has a long tradition for describing the thermodynamic and phase equilibrium properties

of protein solutions. Nevertheless, proteins have been recognized to be more complex than the typically assumed colloidal hard spheres (Sarangapani et al., 2015; Stradner & Schurtenberger, 2020). Given the ability of proteins to adjust their conformation in response to variations in pH, ionic strength, and protein concentration, representing a protein as a perfect sphere with constant a_M is a significant simplification. Despite this simplification, results shown earlier indicate that the introduced model can provide a quantitative description of the Gibbs-Donnan effect. However, a change in protein conformation with increasing concentration cannot be excluded and may explain discrepancies between model predictions and experimental data during the second UF step.

6.4.3.2. Protein charge

As described in Section 6.2.6, σ_M is derived directly from the primary structure of the protein using the number of ionizable amino acids and their respective pK values. Due to charge-charge interactions, hydrogen bonding, and burial of amino acid residues, the pK value of an ionizable side chain can deviate notably from its intrinsic value (Borkovec et al., 2001; Grimsley et al., 2009; Pace et al., 2009). To account for the deviation of pK values within proteins from their intrinsic values, pK values of the null model proposed by Antosiewicz et al. (Antosiewicz et al., 1996) were used in this study. Even though the null model has been shown to provide adequate approximations for experimental titration curves (Borkovec et al., 2001), it represents still a great simplification of reality. According to Equation 6.23 it is assumed that all amino acids are exposed to the solvent and homogeneously distributed on the surface of the protein. Since some ionizable amino acids may be buried within the protein, this represents a simplification as well. Isoelectric points of proteins predicted by the null model can therefore often deviate from experimental data (Antosiewicz et al., 1994). An erroneous estimation of the protein charge near the pI would explain why discrepancies between model predictions and experimental data are more pronounced for the histidine DF buffer. More sophisticated calculations of the protein charge using, for instance, homology models could increase the predictive accuracy of the proposed model. An experimental determination of the titration curve, as in previous works, was not considered as the goal was a purely predictive model that does not require any experimental calibration effort.

As described in Sections 6.2.6 and 6.4.2, the protein charge is influenced by the local pH at the surface of the protein and is thus regulated not only by the pH in the retentate but also its ionic strength. The influence of this charge regulation has long been neglected in previous models. The recent work of Jabra et al. (2020) highlighted the importance of charge regulation, especially in the case of buffer-free formulations where the protein of interest is

diafiltrated against pure water and thus strongly determines the buffer capacity of the solution. Despite reported benefits of buffer-free formulations, they are not yet widely used and therefore not in the focus of this work. However, simulated pH and excipient profiles during a diafiltration against pure water shown in Figure S6.7 in Appendix D, Section S6.5 are in qualitative agreement with the experimental behavior described in (Jabra et al., 2020) and indicate that the model is also applicable in case of buffer-less formulations.

6.4.3.3. Protein-solute interaction

It is assumed that interactions between the protein and other solutes are purely electrostatic in nature. Co-ions are thus in general repelled by the protein, while counter-ions are attracted. Uncharged solutes are not electrostatically affected and are therefore only subject to volume exclusion effects. However, recent work by Baek, Emami, et al. (2019) has shown that in the case of histidine, stereospecific interactions with the protein can occur as well. Such interactions are not accounted for in the model and could explain model deviations in Figure 6.5. Moreover, the theoretical description of protein-solute interactions is based on the PB theory, i.e. a mean-field approximation that, among others, neglects the finite size of ions. Therefore, for high electrostatic potentials, the PB equation is known to overestimate ion concentrations near charged surfaces (Borukhov et al., 1997, 2000). In contrast to previous works, the presented model indirectly accounts for the finite ion size by the extension of a Stern layer separating the charged protein surface from the diffuse layer that obeys the PB equation. According to Equation 6.15, the Stern layer is characterized by the Stern capacitance describing the drop of the potential from ψ_0 to ψ_D at the outer Helmholtz plane. However, it is important to note that the applied capacity value was only estimated based on literature data. Moreover, the extension of the theoretical description by the Stern layer still provides only a simplified consideration of the finite ion size and may therefore be an explanation for discrepancies between model predictions and experimental data during the second UF step, where $\overline{\psi}$ increases significantly due to the depletion of co-ions. The impact of C_S on model predictions is discussed in more detail in the following section.

6.4.3.4. Gibbs-Donnan coefficient

Consistent with previous works, the relationship between the permeate and retentate composition is described under the assumption that both process streams are in constant Donnan equilibrium, as indicated by the Boltzmann relation (Equation 6.17) and the boundary condition (Equation 6.18) at the boundary of the WS cell. Under this assumption, the composition of the permeate is determined purely by the protein concentration and the ion

composition of the retentate. The influence of other potential factors on the retentate composition, such as the permeate flux or the applied TMP, is neglected. Membrane properties, such as the hydrophobicity or the molecular weight cutoff, are also considered to have no significant impact on the permeate composition. Furthermore, it is important to note that according to Equation 6.7, the radius of the WS cell and thus the composition of the retentate is evaluated based on the average protein concentration in the bulk phase neglecting variations in the protein concentration within the membrane module, either along or orthogonal to the membrane surface, for example due to concentration polarization. As model predictions in Figures 6.3 to 6.6 show good agreement with the experimental data generated using different membranes, TMPs and feed flow rates, these assumptions are considered reasonable. An increase in model complexity by incorporating the effects of concentration gradients within the module and the permeate flux on the permeate composition was therefore not considered in this work. To further validate the equilibrium assumption and the ability of the model to correctly estimate the permeate composition, Figures 6.7 and 6.8 show measured data and model predictions for both retentate and permeate. Dashed lines correspond to simulations for the limiting case $C_S \rightarrow \infty$ and thus the neglect of the Stern layer as in previous works. Data are shown for mAbB and 10 mM acetate buffer, pH 5.0, (Figure 6.7) and 10 mM succinate, pH 5.5, (Figure 6.8). For supporting data with other DF buffers, please refer to Appendix D, Section S6.3 Comparing experimental data with model predictions, a good agreement can be observed for the DF step. As expected, the predicted permeate composition converges against the composition of the DF buffer after several DVs. While model predictions in Figure 6.8 also show good agreement for the second UF step, predicted values for the permeate shown in Figure 6.7 deviate progressively from measurements for $c_M >$ 100 g L^{-1}. It is noticeable that, according to offline measurements, the pH and excipient concentration in the permeate shown in Figure 6.7 seem to remain constant during the second UF step and to be consistent with the reference values in the DF buffer. This observation for 10 mM acetate (pH 5.0) as DF buffer is confirmed in Figure 6.8 for 10 mM succinate (pH 5.5) and further supported by results with other DF buffers shown in Appendix D, Section S6.3 In contrast to the experimental observations, the predicted pH and excipient concentration in the permeate decreases noticeably during the second UF step. The discrepancy between measurement and simulation strongly correlates with the magnitude of the predicted Donnan potential $\bar{\psi}$ shown in orange at the bottom of Figure 6.7 and 6.8. For the limiting case $\bar{\psi} \ll 1$, model predictions are in perfect alignment with experimental data for both retentate and permeate. For the case $\bar{\psi} \gg 1$, on the other hand, predicted values start to

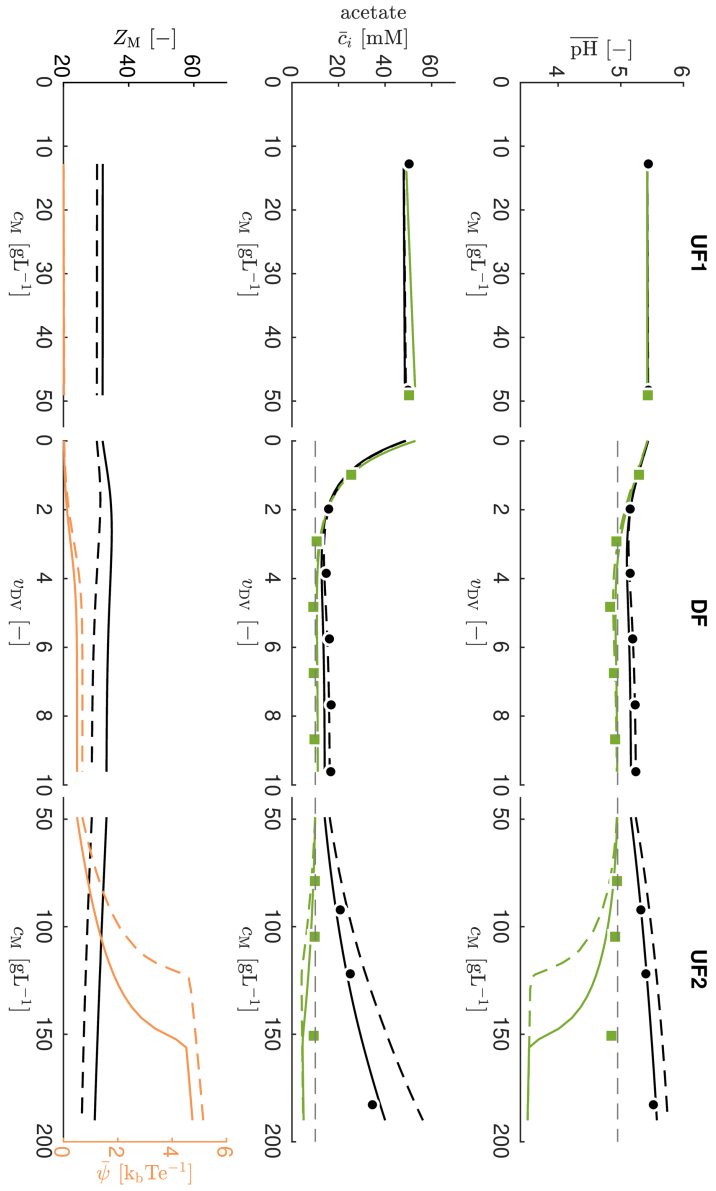

Figure 6.7. *Rotated 90° clockwise*. Comparison between retentate and permeate composition for ExpB1 using mAbB and 10 mM acetate (pH 5.0) as DF buffer. Model predictions for the retentate and permeate are indicated in black and green, respectively. Experimental data for the retentate and permeate are shown as black circles and green squares, respectively. Model predictions with a stern capacitance of $C_S = 0.2\ \mathrm{F\,m^{-2}}$ are shown as continuous lines while dashed lines represent predictions without Stern layer ($C_S \to \infty$). Top: Comparison between retentate pH and permeate pH. For visual guidance, the pH of the DF buffer is indicated as a gray dashed line. Middle: Comparison between the acetate concentration in the retentate and permeate. For visual guidance, the acetate concentration in the DF buffer is indicated as a gray dashed line. Bottom: Protein charge and $\bar{\psi}$ shown in black and orange, respectively.

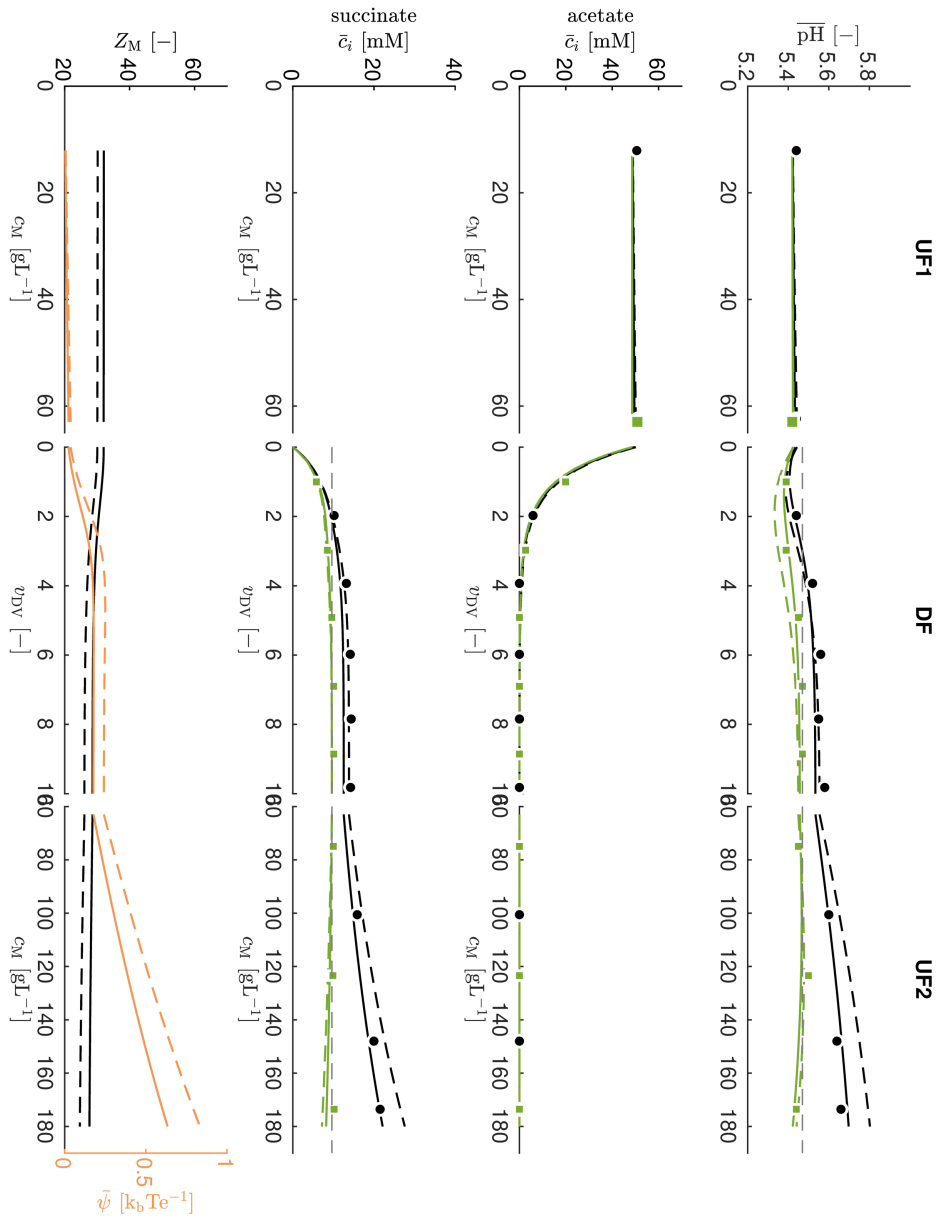

Figure 6.8. *Rotated 90° clockwise*. Comparison between retentate and permeate composition for ExpB3 using mAbB and 10 mM succinate (pH 5.5) as DF buffer. Model predictions for the retentate and permeate are indicated in black and green, respectively. Experimental data for the retentate and permeate are shown as black circles and green squares, respectively. Model predictions with a stern capacitance of $C_{\mathrm{S}} = 0.2\ \mathrm{F\,m^{-2}}$ are shown as continuous lines while dashed lines represent predictions without Stern layer ($C_{\mathrm{S}} \to \infty$). Top: Comparison between retentate pH and permeate pH. For visual guidance, the pH of the DF buffer is indicated as a gray dashed line. Second row: Comparison between the acetate concentration in the retentate and permeate. Third row: Comparison between the succinate concentration in the retentate and permeate. For visual guidance, the succinate concentration in the DF buffer is indicated as a gray dashed line. Bottom: Protein charge and $\bar{\psi}$ shown in black and orange, respectively.

deviate from measurements. As mentioned earlier, deviations for $\bar{\psi} \gg 1$ can possibly be attributed to simplifications in the PB theory, which become apparent at higher electrostatic potentials. Comparing model predictions with $C_S = 0.2\ \mathrm{F\,m^{-2}}$ with those of the limiting case $C_S \to \infty$, it becomes apparent that a description of the electrostatic potential inside the WS cell based on the basic Stern model provides more accurate predictions in the high concentration regime during the second UF step compared to the traditional PB approach used in previous models. These learnings regarding the impact of $\bar{\psi}$ and the Stern layer (C_S) on UF/DF model predictions provide a deeper understanding of the limitations of PB models and demonstrate potential for further development. Even though results shown in Figure 6.7 and 6.8 and in Appendix D, Section S6.3 limit the validity of the model to the limiting case $\bar{\psi} \ll 1$, it is noticeable that predicted retentate data show good agreement with experimental data despite deviations in the permeate composition. Since the retentate is of primary interest in practical applications, we therefore consider the model to be suitable for predicting the Donnan effect despite the observed deviations.

6.5. Conclusion

In this work, a model describing the Gibbs-Donnan coefficient in protein UF and DF steps has been presented. The model accounts for volume exclusion effects and electrostatic interactions between the protein and ions using the PB theory in combination with a basic Stern model and the cell model approximation. Combined with mass balance equations for the filtration system, the model is capable of describing differences in pH and excipient concentrations between the DF buffer and the retentate commonly observed at high protein concentrations and low ionic strength. The advantages of the proposed model have been demonstrated by predicting the retentate composition throughout combined UF/DF processes using multiple DF buffer systems and different proteins, including two mAbs and a fragment antigen binding. Shifts in retentate pH and excipient concentrations were generally accurately predicted by the model for both the DF and UF steps. The description of the electrostatic potential inside the WS cell based on the basic Stern model was found to provide more accurate predictions in the high protein concentration regime during the second UF step compared to the diffuse layer model used in previous works. Limitations of the presented model were analyzed by critically examining and experimentally validating model assumptions and simplifications. It was shown that model assumptions are remarkably accurate for low and moderate Donnan potentials. For dimensionless Donnan potentials $\bar{\psi} \gg 1$, model predictions increasingly deviate from experimental data. However, since deviations were only

observed in the permeate composition and not in the retentate composition, the applicability of the model to high Donnan potentials is still given.

Since model predictions are based purely on molecular structural information on the protein as well as buffer compositions, the model requires no experimental calibration effort. This makes the model a valuable tool at an early stage of process development to streamline development activities and reduce the experimental effort required for process design and characterization. It also increases process understanding in a scientific manner and can therefore help to develop robust and well-controlled processes for biomanufacturing within frameworks of modern regulatory initiatives like Quality by Design.

Acknowledgments

The authors would like to express their gratitude to Robin Schiemer for his contributions to the project in its early stages. Furthermore, the authors want to thank Jens Smiatek for reviewing the manuscript.

Supplementary material

Appendix D contains the supplementary material associated with this chapter:

- S6.1 Mass balances
- S6.2 UF/DF experiments – mAbA
- S6.3 UF/DF experiments – mAbB
- S6.4 UF/DF experiments – FabC
- S6.5 Buffer-less systems

7

General discussion and conclusion

Cross-flow filtration (CFF) is a ubiquitous size-selective separation technique in biopharmaceutical downstream processing (DSP) and bioprocessing in general. However, CFF process development comes with several challenges such as limited purification performance, high experimental effort and protein material requirements, and non-idealities at high protein concentrations. Emerging process development tools may help to overcome these challenges but are rarely applied to CFF when compared to chromatography, the workhorse in biopharmaceutical DSP. This thesis therefore applied process integration, high-throughput screenings (HTS), process analytical technology (PAT), and mechanistic modeling to CFF, aiming to provide solutions to current process development challenges.

Good purification performance is one of the overall goals of DSP development. However, alternative separation techniques to chromatography often lack good purification performance. Process integration is a promising approach to improve yield and purity by combining multiple separation techniques. Integration can either be performed by merging separation techniques into one unit operation or by their seamless connection. The first part of this thesis (Chapter 3) therefore demonstrates the process integration of CFF for the capture and purification of virus-like particles (VLPs). Process integration was realized by combining CFF with VLP precipitation, wash, and re-dissolution. Permeate flow rate control was implemented to achieve a low conversion rate during the intermediate wash step and avoid compaction of precipitate flocs at the membrane surface. A constant flow rate was also required for additional integration of multimodal size-exclusion chromatography (mmSEC) during re-dissolution. Implementation of monitoring and fractionation enabled data-based in-process decision-making during wash and re-dissolution, ultimately leading to a higher purity. The multi-level integration of three size-selective techniques resulted in synergistic effects with regard to process performance. The CFF-based wash step reduced precipitate compaction resulting in a higher yield and faster redissolution. Furthermore, the depletion of impurities by CFF is less limited by capacity as compared to mmSEC. On the other hand,

mmSEC reveals its full potential in the removal of low-concentrated impurities which would be inefficient when performed by CFF. Overall, the multi-level integrated approach showed superior process performance compared to process variants with a lower degree of integration and comparable processes in literature. The resulting process was scalable with high automation potential. The utilization of mainly size-selective separation techniques promises good applicability to other viral particles with the potential for a platform purification approach.

Limited time and low protein material availability are common challenges in biopharmaceutical process development. These limitations contrast with a large amount of protein material and laborious experiments required for CFF process development. The second part of this thesis (Chapter 4) therefore presents a development approach for cross-flow diafiltration (DF) processes driving a reaction of the protein through a buffer exchange. As a case study, the VLP disassembly process step as part of non-enveloped VLP DSP was investigated. VLP disassembly was initiated by increasing urea concentration and pH. In HTS, VLPs were mixed with concentrated stock solutions at a small scale to reach representative reaction conditions for the DF process. Automated analysis of the mixture over time using size-exclusion chromatography allowed for low reaction volumes. The size-exclusion chromatography method was designed to have minimal impact on the disassembly reaction, providing rapid and accurate data with high resolution. Optimal conditions resulting from the HTS were subsequently applied in a novel laboratory-scale cross-flow DF process step. DF enabled a controlled change of liquid phase conditions avoiding concentration spikes of urea or pH and thus associated protein degradation. Furthermore, DF allowed for the simultaneous depletion of impurities and undesired solutes. In the presented case of non-enveloped VLPs, an additional advantage of DF-based processing was the depletion of nucleic acids and a higher yield compared to the small-scale screening based on mixing. The disassembly process step was successfully integrated into a filtration-based DSP sequence including VLP reassembly, which considerably reduced undesired high molecular weight species. The DSP sequence based on size-selective separations has the potential to serve as a platform approach for non-enveloped VLPs as no other molecular properties are exploited for separations. Finally, decoupling the condition screening from laboratory-scale CFF enabled time- and material-efficient process development along with comprehensive characterization.

While Chapter 4 focused on time and protein material savings as well as characterization in preparation for the CFF process, these challenges remain for the actual CFF experiments, which aim for comprehensive process

knowledge. The third part of this thesis (Chapter 5) demonstrates the application of a PAT framework to thoroughly monitor and characterize CFF process steps. Compared to simple off-line analysis, this approach aims to increase the knowledge obtained per experiment and thus reduce the number of experiments required. In particular, the VLP disassembly step presented in Chapter 4 was investigated. The suitability of the PAT sensors was assessed under varying conditions representing process variations. Monitoring filtration performance in-line, product properties on-line, and VLP disassembly progress at-line provided a comprehensive picture of the process in (near) real-time. On-line monitoring by light scattering and UV absorbance spectroscopy enabled qualitative tracing of the VLP disassembly progress, associated changes in protein tertiary structure, and undesired aggregation. VLP disassembly was quantitatively traced by predicting target species concentrations from UV spectra in combination with regression models. Predicted concentrations were used for automated process endpoint detection. Furthermore, simple data-driven approaches suitable for less complex monitoring equipment were developed and successfully detected the process endpoint. In the specific case study in Chapter 5, the VLP disassembly process step was characterized in depth with an array of PAT sensors. More broadly, the study outlines a framework for the implementation of PAT for CFF characterization. The framework is especially applicable to processes in which species concentrations in a complex mixture, particle size, and tertiary structure are relevant product characteristics, for example, inclusion body dissolution/refolding. The ability to monitor and control processes on the basis of a thorough characterization follows the principles of Quality by Design (QbD). This ability makes the presented approach a valuable tool throughout the whole biopharmaceutical process life cycle from development to manufacturing.

DSP of biopharmaceutical proteins often finishes with cross-flow ultrafiltration/diafiltration (UF/DF) to change the liquid phase composition and increase the protein concentration. Here, pH and excipient concentrations are commonly expected to reach and remain at the level of the DF buffer. However, with increasing protein concentrations, the retentate composition often deviates from the DF buffer (target), posing a challenge during process development. These deviations arise from phenomena such as the electrostatic interactions between retained proteins and permeating ions (Gibbs-Donnan effect) and volume exclusion. The fourth part of this thesis (Chapter 6) therefore presents the development and validation of a mechanistic model to describe UF/DF process steps subjective to the mentioned phenomena. In the developed model, Poisson-Boltzmann theory is

used to describe the underlying electrostatic interactions between the proteins and charged excipients. Model development focused on a purely predictive model solely based on model inputs that are easily accessible theoretical information and without any experimental calibration. The model was compared to existing models and assumptions were critically reviewed to identify limitations. Combined UF/DF/UF sequences were designed and executed to validate model simulations of retentate and permeate compositions experimentally. A comprehensive validation was performed using multiple mAbs and formulations along with thorough sampling. Investigating the impact of model variables on predictions under consideration of validation data provided a deep understanding of model limitations. Consequently, Poisson-Boltzmann theory was combined with a basic Stern model to improve predictions of the retentate composition for protein concentrations above 100 gL^{-1}. Model predictions for the retentate pH and excipient concentrations were in good agreement with experimental data throughout the process. Overall, the developed model facilitates systematic process development based on *in silico* data. Processing routes and suitable buffer systems for high-concentration formulations can be identified without any physical protein material present. Furthermore, the mechanistic model can support as a QbD tool during process characterization and robustness studies to save valuable resources.

In conclusion, this thesis presents new strategies to overcome common challenges in CFF process development. The utilization of emerging process development tools for knowledge-based development approaches and their potential for QbD are presented. In addition, the benefits of CFF implementation as a size-selective purification technique are demonstrated. CFF is shown to be especially valuable during the entire DSP of non-enveloped VLPs and offers potential for a platform DSP approach. Lastly, the findings during the development of the mechanistic model for UF/DF processes provide a deeper understanding of model variables and thereby the basis for future research. Considering these conclusions, this thesis expands the toolbox and scientific knowledge of CFF process development and thus contributes to more efficient CFF development work and better processes in the future.

Bibliography

Abel, J., Kosky, A., Ball, N., Bacon, H., Kaushik, R., & Kleemann, G. R. (2018). A Small-Scale Process for Predicting Donnan and Volume Exclusion Effects During Ultrafiltration/Diafiltration Process Development. *Journal of Pharmaceutical Sciences*, *107*(5), 1296–1303. https://doi.org/10.1016/j.xphs.2018.01.010

Ahrer, K., Buchacher, A., Iberer, G., & Jungbauer, A. (2006). Effects of ultra-/diafiltration conditions on present aggregates in human immunoglobulin G preparations. *Journal of Membrane Science*, *274*(1–2), 108–115. https://doi.org/10.1016/j.memsci.2005.08.018

Aldington, S., & Bonnerjea, J. (2007). Scale-up of monoclonal antibody purification processes. *Journal of Chromatography B*, *848*(1), 64–78. https://doi.org/10.1016/j.jchromb.2006.11.032

Ambrožič, R., Arzenšek, D., & Podgornik, A. (2021). Designing scalable ultrafiltration/diafiltration process of monoclonal antibodies via mathematical modeling by coupling mass balances and Poisson–Boltzmann equation. *Biotechnology and Bioengineering*, *118*(2), 633–646. https://doi.org/10.1002/bit.27598

Andersen, C. M., & Bro, R. (2010). Variable selection in regression-a tutorial. *Journal of Chemometrics*, *24*(11–12), 728–737. https://doi.org/10.1002/cem.1360

Andersen, D. C., & Reilly, D. E. (2004). Production technologies for monoclonal antibodies and their fragments. *Current Opinion in Biotechnology*, *15*(5), 456–462. https://doi.org/10.1016/j.copbio.2004.08.002

Andris, S., Seidel, J., & Hubbuch, J. (2019). Kinetic reaction modeling for antibody-drug conjugate process development. *Journal of Biotechnology*, *306*, 71–80. https://doi.org/10.1016/j.jbiotec.2019.09.013

Antosiewicz, J., McCammon, J. A. A., & Gilson, M. K. (1994). Prediction of pH-dependent Properties of Proteins. *Journal of Molecular Biology*, *238*(3), 415–436. https://doi.org/10.1006/jmbi.1994.1301

Antosiewicz, J., McCammon, J. A., & Gilson, M. K. (1996). The determinants of pKas in proteins. *Biochemistry*, *35*(24), 7819–7833. https://doi.org/10.1021/bi9601565

Arunkumar, A., Singh, N., Schutsky, E. G., Peck, M., Swanson, R. K., Borys, M. C., & Li, Z. J. (2016). Effect of channel-induced shear on biologics during

ultrafiltration/diafiltration (UF/DF). *Journal of Membrane Science, 514*, 671–683. https://doi.org/10.1016/j.memsci.2016.05.031

Ashley, C. E., Carnes, E. C., Phillips, G. K., Durfee, P. N., Buley, M. D., Lino, C. A., Padilla, D. P., Phillips, B., Carter, M. B., Willman, C. L., Brinker, C. J., Caldeira, J. D. C., Chackerian, B., Wharton, W., & Peabody, D. S. (2011). Cell-Specific Delivery of Diverse Cargos by Bacteriophage MS2 Virus-like Particles. *ACS Nano*, *5*(7), 5729–5745. https://doi.org/10.1021/nn201397z

Ausar, S. F., Foubert, T. R., Hudson, M. H., Vedvick, T. S., & Middaugh, C. R. (2006). Conformational Stability and Disassembly of Norwalk Virus-like Particles. *Journal of Biological Chemistry*, *281*(28), 19478–19488. https://doi.org/10.1074/jbc.M603313200

Baek, Y., Emami, P., Singh, N., Ilott, A., Sahin, E., & Zydney, A. (2019). Stereospecific interactions between histidine and monoclonal antibodies. *Biotechnology and Bioengineering*, *116*(10), 2632–2639. https://doi.org/10.1002/bit.27109

Baek, Y., Singh, N., Arunkumar, A., Borwankar, A., & Zydney, A. L. (2019). Mass Balance Model with Donnan Equilibrium Accurately Describes Unusual pH and Excipient Profiles during Diafiltration of Monoclonal Antibodies. *Biotechnology Journal*, *1800517*(7), 1800517. https://doi.org/10.1002/biot.201800517

Baek, Y., Yang, D., Singh, N., Arunkumar, A., Ghose, S., Li, Z. J., & Zydney, A. L. (2017). pH variations during diafiltration due to buffer nonidealities. *Biotechnology Progress*, *33*(6), 1555–1560. https://doi.org/10.1002/btpr.2544

Bangaru, S., Ozorowski, G., Turner, H. L., Antanasijevic, A., Huang, D., Wang, X., Torres, J. L., Diedrich, J. K., Tian, J.-H., Portnoff, A. D., Patel, N., Massare, M. J., Yates, J. R., Nemazee, D., Paulson, J. C., Glenn, G., Smith, G., & Ward, A. B. (2020). Structural analysis of full-length SARS-CoV-2 spike protein from an advanced vaccine candidate. *Science*, *370*(6520), 1089–1094. https://doi.org/10.1126/science.abe1502

Bates, A., & Power, C. A. (2019). David vs. Goliath: The Structure, Function, and Clinical Prospects of Antibody Fragments. *Antibodies*, *8*(2), 28. https://doi.org/10.3390/antib8020028

Bee, J. S., Stevenson, J. L., Mehta, B., Svitel, J., Pollastrini, J., Platz, R., Freund, E., Carpenter, J. F., & Randolph, T. W. (2009). Response of a concentrated monoclonal antibody formulation to high shear. *Biotechnology and Bioengineering*, *103*(5), 936–943. https://doi.org/10.1002/bit.22336

Behrens, S. H., & Borkovec, M. (1999). Electrostatic Interaction of Colloidal Surfaces with Variable Charge. *The Journal of Physical Chemistry B*, *103*(15), 2918–2928. https://doi.org/10.1021/jp984099w

Belfort, G., Pimbley, J. M., Greiner, A., & Chung, K. Y. (1993). Diagnosis of membrane fouling using a rotating annular filter. 1. Cell culture media. *Journal of Membrane Science*, *77*(1), 1–22. https://doi.org/10.1016/0376-7388(93)85231-K

Benavides, J., Mena, J. A., Cisneros-Ruiz, M., Ramírez, O. T., Palomares, L. A., & Rito-Palomares, M. (2006). Rotavirus-like particles primary recovery from insect cells in aqueous two-phase systems. *Journal of Chromatography. B, Analytical Technologies in the Biomedical and Life Sciences*, *842*(1), 48–57. https://doi.org/10.1016/j.jchromb.2006.05.006

Berg, A., Oelmeier, S. A., Kittelmann, J., Dismer, F., & Hubbuch, J. (2012). Development and characterization of an automated high throughput screening method for optimization of protein refolding processes. *Journal of Separation Science*, *35*(22), 3149–3159. https://doi.org/10.1002/jssc.201200306

Beynon, R. J., & Easterby, J. S. (1996). *Buffer Solutions* (1st ed.). Oxford University Press Inc. https://doi.org/10.4324/9780203494691

Bhambure, R., Kumar, K., & Rathore, A. S. (2011). High-throughput process development for biopharmaceutical drug substances. *Trends in Biotechnology*, *29*(3), 127–135. https://doi.org/10.1016/j.tibtech.2010.12.001

Billaud, J.-N., Peterson, D. L., Barr, M., Chen, A., Sällberg, M., Garduno, F., Goldstein, P., McDowell, W., Hughes, J., Jones, J., & Milich, D. R. (2005). Combinatorial Approach to Hepadnavirus-Like Particle Vaccine Design. *J Virology*, *79*(21), 13656–13666. https://doi.org/10.1128/JVI.79.21.13656

Binabaji, E., Ma, J., Rao, S., & Zydney, A. L. (2015). Theoretical analysis of the ultrafiltration behavior of highly concentrated protein solutions. *Journal of Membrane Science*, *494*, 216–223. https://doi.org/10.1016/j.memsci.2015.07.068

Binabaji, E., Ma, J., Rao, S., & Zydney, A. L. (2016). Ultrafiltration of highly concentrated antibody solutions: Experiments and modeling for the effects of module and buffer conditions. *Biotechnology Progress*, *32*(3), 692–701. https://doi.org/10.1002/btpr.2252

Binabaji, E., Rao, S., & Zydney, A. L. (2014). The osmotic pressure of highly concentrated monoclonal antibody solutions: Effect of solution

conditions. *Biotechnology and Bioengineering*, *111*(3), 529–536. https://doi.org/10.1002/bit.25104

Bin Mohamed Suffian, I. F., Garcia-Maya, M., Brown, P., Bui, T., Nishimura, Y., Palermo, A. R. B. M. J., Ogino, C., Kondo, A., & Al-Jamal, K. T. (2017). Yield Optimisation of Hepatitis B Virus Core Particles in E. coli Expression System for Drug Delivery Applications. *Scientific Reports*, *7*(1), 43160. https://doi.org/10.1038/srep43160

Birrer, M. J., Moore, K. N., Betella, I., & Bates, R. C. (2019). Antibody-Drug Conjugate-Based Therapeutics: State of the Science. *JNCI: Journal of the National Cancer Institute*, *111*(6), 538–549. https://doi.org/10.1093/jnci/djz035

Bissinger, T., Wu, Y., Marichal-Gallardo, P., Riedel, D., Liu, X., Genzel, Y., Tan, W., & Reichl, U. (2021). Towards integrated production of an influenza A vaccine candidate with MDCK suspension cells. *Biotechnology and Bioengineering*, *118*(10), 3996–4013. https://doi.org/10.1002/bit.27876

Blatt, W. F., Dravid, A., Michaels, A. S., & Nelsen, L. (1970). Solute Polarization and Cake Formation in Membrane Ultrafiltration: Causes, Consequences, and Control Techniques. In *Membrane Science and Technology* (pp. 47–97). Springer US. https://doi.org/10.1007/978-1-4684-1851-4_4

Bohren, C. F., & Huffman, D. R. (2004). *Absorption and Scattering of Light by Small Particles*. Wiley-VCH Verlag GmbH & Co. KGaA. https://doi.org/10.1002/9783527618156

Bolli, E., O'Rourke, J. P., Conti, L., Lanzardo, S., Rolih, V., Christen, J. M., Barutello, G., Forni, M., Pericle, F., & Cavallo, F. (2018). A Virus-Like-Particle immunotherapy targeting Epitope-Specific anti-xCT expressed on cancer stem cell inhibits the progression of metastatic cancer in vivo. *OncoImmunology*, *7*(3), e1408746. https://doi.org/10.1080/2162402X.2017.1408746

Bolton, G. R., Boesch, A. W., Basha, J., LaCasse, D. P., Kelley, B. D., & Acharya, H. (2011). Effect of protein and solution properties on the donnan effect during the ultrafiltration of proteins. *Biotechnology Progress*, *27*(1), 140–152. https://doi.org/10.1002/btpr.523

Borisova, G., Borschukova, O., Skrastina, D., Dislers, A., Ose, V., Pumpens, P., & Grens, E. (1999). Behavior of a Short preS1 Epitope on the Surface of Hepatitis B Core Particles. *Biological Chemistry*, *380*(3), 315–324. https://doi.org/10.1515/BC.1999.043

Borkovec, M., Jönsson, B., & Koper, G. J. M. (2001). Ionization Processes and Proton Binding in Polyprotic Systems: Small Molecules, Proteins,

Interfaces, and Polyelectrolytes. In *Surface and Colloid Science* (pp. 99–339). Springer US. https://doi.org/10.1007/978-1-4615-1223-3_2

Borukhov, I., Andelman, D., & Orland, H. (1997). Steric Effects in Electrolytes: A Modified Poisson-Boltzmann Equation. *Physical Review Letters, 79*(3), 435–438. https://doi.org/10.1103/PhysRevLett.79.435

Borukhov, I., Andelman, D., & Orland, H. (2000). Adsorption of large ions from an electrolyte solution: a modified Poisson–Boltzmann equation. *Electrochimica Acta, 46*(2–3), 221–229. https://doi.org/10.1016/S0013-4686(00)00576-4

Böttcher, B., Vogel, M., Ploss, M., & Nassal, M. (2006). High Plasticity of the Hepatitis B Virus Capsid Revealed by Conformational Stress. *Journal of Molecular Biology, 356*(3), 812–822. https://doi.org/10.1016/j.jmb.2005.11.053

Böttcher, B., Wynne, S. A., & Crowther, R. A. (1997). Determination of the fold of the core protein of hepatitis B virus by electron cryomicroscopy. *Nature, 386*(6620), 88–91. https://doi.org/10.1038/386088a0

Brestich, N., Rüdt, M., Büchler, D., & Hubbuch, J. (2018). Selective protein quantification for preparative chromatography using variable pathlength UV/Vis spectroscopy and partial least squares regression. *Chemical Engineering Science, 176*, 157–164. https://doi.org/10.1016/j.ces.2017.10.030

Brestrich, N., Sanden, A., Kraft, A., McCann, K., Bertolini, J., & Hubbuch, J. (2015). Advances in inline quantification of co-eluting proteins in chromatography: Process-data-based model calibration and application towards real-life separation issues. *Biotechnology and Bioengineering, 112*(7), 1406–1416. https://doi.org/10.1002/bit.25546

Briskot, T., Hahn, T., Huuk, T., & Hubbuch, J. (2020). Adsorption of colloidal proteins in ion-exchange chromatography under consideration of charge regulation. *Journal of Chromatography A, 1611*, 460608. https://doi.org/10.1016/j.chroma.2019.460608

Bryan, J. T., Buckland, B., Hammond, J., & Jansen, K. U. (2016). Prevention of cervical cancer: journey to develop the first human papillomavirus virus-like particle vaccine and the next generation vaccine. *Current Opinion in Chemical Biology, 32*, 34–47. https://doi.org/10.1016/j.cbpa.2016.03.001

Bull, H. B., Breese, K., Ferguson, G. L., & Swenson, C. A. (1964). The pH of urea solutions. *Archives of Biochemistry and Biophysics, 104*(2), 297–304. https://doi.org/10.1016/S0003-9861(64)80017-5

Buonaguro, L., Aurisicchio, L., Buonaguro, F. M., & Ciliberto, G. (2013). New developments in cancer vaccines. *Expert Review of Vaccines*, *12*(10), 1109–1110. https://doi.org/10.1586/17476348.2013.838013

Burgstaller, D., Jungbauer, A., & Satzer, P. (2019). Continuous integrated antibody precipitation with two-stage tangential flow microfiltration enables constant mass flow. *Biotechnology and Bioengineering*, *116*(5), 1053–1065. https://doi.org/10.1002/bit.26922

Butt, H.-J., Graf, K., & Kappl, M. (2003). *Physics and Chemistry of Interfaces*. Wiley. https://doi.org/10.1002/3527602313

Callahan, D. J., Stanley, B., & Li, Y. (2014). Control of Protein Particle Formation During Ultrafiltration/Diafiltration Through Interfacial Protection. *Journal of Pharmaceutical Sciences*, *103*(3), 862–869. https://doi.org/10.1002/jps.23861

Capelle, M. A. H., Gurny, R., & Arvinte, T. (2007). High throughput screening of protein formulation stability: Practical considerations. *European Journal of Pharmaceutics and Biopharmaceutics*, *65*(2), 131–148. https://doi.org/10.1016/j.ejpb.2006.09.009

Carreira, A., Menéndez, M., Reguera, J., Almendral, J. M., & Mateu, M. G. (2004). In Vitro Disassembly of a Parvovirus Capsid and Effect on Capsid Stability of Heterologous Peptide Insertions in Surface Loops. *Journal of Biological Chemistry*, *279*(8), 6517–6525. https://doi.org/10.1074/jbc.M307662200

Carvalho, S. B., Fortuna, A. R., Wolff, M. W., Peixoto, C., M Alves, P., Reichl, U., & JT Carrondo, M. (2018). Purification of influenza virus-like particles using sulfated cellulose membrane adsorbers. *Journal of Chemical Technology & Biotechnology*, *93*(7), 1988–1996. https://doi.org/10.1002/jctb.5474

Carvalho, S. B., Silva, R. J. S., Moleirinho, M. G., Cunha, B., Moreira, A. S., Xenopoulos, A., Alves, P. M., Carrondo, M. J. T., & Peixoto, C. (2019). Membrane-Based Approach for the Downstream Processing of Influenza Virus-Like Particles. *Biotechnology Journal*, *14*(8), 1800570. https://doi.org/10.1002/biot.201800570

Castiblanco, J., & Anaya, J.-M. (2015). Genetics and vaccines in the era of personalized medicine. *Current Genomics*, *16*(1), 47–59. https://doi.org/10.2174/1389202916666141223220551

Ceres, P., & Zlotnick, A. (2002). Weak Protein−Protein Interactions Are Sufficient To Drive Assembly of Hepatitis B Virus Capsids †. *Biochemistry*, *41*(39), 11525–11531. https://doi.org/10.1021/bi0261645

Cerqueira, C., Thompson, C. D., Day, P. M., Pang, Y.-Y. S., Lowy, D. R., & Schiller, J. T. (2017). Efficient Production of Papillomavirus Gene Delivery Vectors in Defined In Vitro Reactions. *Molecular Therapy - Methods & Clinical Development*, *5*, 165–179. https://doi.org/10.1016/j.omtm.2017.04.005

Chackerian, B. (2007). Virus-like particles: flexible platforms for vaccine development. *Expert Review of Vaccines*, *6*(3), 381–390. https://doi.org/10.1586/14760584.6.3.381

Chandler, M., & Zydney, A. (2004). High throughput screening for membrane process development. *Journal of Membrane Science*, *237*(1–2), 181–188. https://doi.org/10.1016/j.memsci.2004.03.011

Chandramohan, D., Zongo, I., Sagara, I., Cairns, M., Yerbanga, R.-S., Diarra, M., Nikièma, F., Tapily, A., Sompougdou, F., Issiaka, D., Zoungrana, C., Sanogo, K., Haro, A., Kaya, M., Sienou, A.-A., Traore, S., Mahamar, A., Thera, I., Diarra, K., … Greenwood, B. (2021). Seasonal Malaria Vaccination with or without Seasonal Malaria Chemoprevention. *New England Journal of Medicine*, *385*(11), 1005–1017. https://doi.org/10.1056/NEJMoa2026330

Chaudhuri, R., Cheng, Y., Middaugh, C. R., & Volkin, D. B. (2014). High-Throughput Biophysical Analysis of Protein Therapeutics to Examine Interrelationships Between Aggregate Formation and Conformational Stability. *The AAPS Journal*, *16*(1), 48–64. https://doi.org/10.1208/s12248-013-9539-6

Chen, Q., Abdul Latiff, S. M., Toh, P., Peng, X., Hoi, A., Xian, M., Zhang, H., Nian, R., Zhang, W., & Gagnon, P. (2016). A simple and efficient purification platform for monoclonal antibody production based on chromatin-directed cell culture clarification integrated with precipitation and void-exclusion anion exchange chromatography. *Journal of Biotechnology*, *236*, 128–140. https://doi.org/10.1016/j.jbiotec.2016.08.014

Cherkasov, A. N., & Polotsky, A. E. (1996). The resolving power of ultrafiltration. *Journal of Membrane Science*, *110*(1), 79–82. https://doi.org/10.1016/0376-7388(95)00233-2

Chhatre, S., Farid, S. S., Coffman, J., Bird, P., Newcombe, A. R., & Titchener-Hooker, N. J. (2011). How implementation of Quality by Design and advances in Biochemical Engineering are enabling efficient bioprocess development and manufacture. *Journal of Chemical Technology & Biotechnology*, *86*(9), 1125–1129. https://doi.org/10.1002/jctb.2628

Chopda, V., Gyorgypal, A., Yang, O., Singh, R., Ramachandran, R., Zhang, H., Tsilomelekis, G., Chundawat, S. P. S., & Ierapetritou, M. G. (2021). Recent advances in integrated process analytical techniques, modeling, and control strategies to enable continuous biomanufacturing of monoclonal antibodies. *Journal of Chemical Technology & Biotechnology, April*. https://doi.org/10.1002/jctb.6765

Chu, K.-B., Kang, H.-J., Yoon, K.-W., Lee, H.-A., Moon, E.-K., Han, B.-K., & Quan, F.-S. (2021). Influenza Virus-like Particle (VLP) Vaccines Expressing the SARS-CoV-2 S Glycoprotein, S1, or S2 Domains. *Vaccines*, *9*(8), 920. https://doi.org/10.3390/vaccines9080920

Chung, C.-Y., Chen, C.-Y., Lin, S.-Y., Chung, Y.-C., Chiu, H.-Y., Chi, W.-K., Lin, Y.-L., Chiang, B.-L., Chen, W.-J., & Hu, Y.-C. (2010). Enterovirus 71 virus-like particle vaccine: Improved production conditions for enhanced yield. *Vaccine*, *28*(43), 6951–6957. https://doi.org/10.1016/j.vaccine.2010.08.052

Clark, N. J., Zhang, H., Krueger, S., Lee, H. J., Ketchem, R. R., Kerwin, B., Kanapuram, S. R., Treuheit, M. J., McAuley, A., & Curtis, J. E. (2013). Small-Angle Neutron Scattering Study of a Monoclonal Antibody Using Free-Energy Constraints. *The Journal of Physical Chemistry B*, *117*(45), 14029–14038. https://doi.org/10.1021/jp408710r

Clincke, M., Mölleryd, C., Zhang, Y., Lindskog, E., Walsh, K., & Chotteau, V. (2013). Very high density of CHO cells in perfusion by ATF or TFF in WAVE bioreactor™. Part I. Effect of the cell density on the process. *Biotechnology Progress*, *29*(3), 754–767. https://doi.org/10.1002/btpr.1704

Cohn, E. J. (1941). The Properties and Functions of the Plasma Proteins, with a Consideration of the Methods for their Separation and Purification. *Chemical Reviews*, *28*(2), 395–417. https://doi.org/10.1021/cr60090a007

Cohn, E. J., Strong, L. E., Hughes, W. L., Mulford, D. J., Ashworth, J. N., Melin, M., & Taylor, H. L. (1946). Preparation and Properties of Serum and Plasma Proteins. IV. A System for the Separation into Fractions of the Protein and Lipoprotein Components of Biological Tissues and Fluids 1a,b,c,d. *Journal of the American Chemical Society*, *68*(3), 459–475. https://doi.org/10.1021/ja01207a034

Cook, J. C., Joyce, J. G., George, H. A., Schultz, L. D., Hurni, W. M., Jansen, K. U., Hepler, R. W., Ip, C., Lowe, R. S., Keller, P. M., & Lehman, E. D. (1999). Purification of Virus-like Particles of Recombinant Human Papillomavirus Type 11 Major Capsid Protein L1 from Saccharomyces

cerevisiae. *Protein Expression and Purification*, *17*(3), 477–484. https://doi.org/10.1006/prep.1999.1155

Coronel, J., Behrendt, I., Bürgin, T., Anderlei, T., Sandig, V., Reichl, U., & Genzel, Y. (2019). Influenza A virus production in a single-use orbital shaken bioreactor with ATF or TFF perfusion systems. *Vaccine*, *37*(47), 7011–7018. https://doi.org/10.1016/j.vaccine.2019.06.005

Council of Europe. (2017). Cell substrates for the production of vaccines for human use. In Council of Europe (Ed.), *European Pharmacopoeia* (9th ed., Issue 1, pp. 602–606).

Crommelin, D. J. A., Storm, G., Verrijk, R., de Leede, L., Jiskoot, W., & Hennink, W. E. (2003). Shifting paradigms: biopharmaceuticals versus low molecular weight drugs. *International Journal of Pharmaceutics*, *266*(1–2), 3–16. https://doi.org/10.1016/S0378-5173(03)00376-4

Crowther, R. A., Kiselev, N. A., Böttcher, B., Berriman, J. A., Borisova, G. P., Ose, V., & Pumpens, P. (1994). Three-dimensional structure of hepatitis B virus core particles determined by electron cryomicroscopy. *Cell*, *77*(6), 943–950. https://doi.org/10.1016/0092-8674(94)90142-2

Cruz, P. E., Goncalves, D., Almeida, J., Moreira, J. L., & Carrondo, M. J. T. (2000). Modeling Retrovirus Production for Gene Therapy. 2. Integrated Optimization of Bioreaction and Downstream Processing. *Biotechnology Progress*, *16*(3), 350–357. https://doi.org/10.1021/bp000017l

Curtis, R. A., Montaser, A., Prausnitz, J. M., & Blanch, H. W. (1998). Protein-protein and protein-salt interactions in aqueous protein solutions containing concentrated electrolytes. *Biotechnology and Bioengineering*, *58*(4), 451–451. https://doi.org/10.1002/(sici)1097-0290(19980520)58:4<451::aid-bit13>3.3.co;2-e

da Costa, A. R., & Fane, A. G. (1994). Net-Type Spacers: Effect of Configuration on Fluid Flow Path and Ultrafiltration Flux. *Industrial & Engineering Chemistry Research*, *33*(7), 1845–1851. https://doi.org/10.1021/ie00031a026

da Costa, A. R., Fane, A. G., Fell, C. J. D., & Franken, A. C. M. (1991). Optimal channel spacer design for ultrafiltration. *Journal of Membrane Science*, *62*(3), 275–291. https://doi.org/10.1016/0376-7388(91)80043-6

Dai, S., Wang, H., & Deng, F. (2018). Advances and challenges in enveloped virus-like particle (VLP)-based vaccines. *Journal of Immunological Sciences*, *2*(2), 36–41. https://doi.org/10.29245/2578-3009/2018/2.1118

Daugherty, A. L., & Mrsny, R. J. (2006). Formulation and delivery issues for monoclonal antibody therapeutics. *Advanced Drug Delivery Reviews, 58*(5–6), 686–706. https://doi.org/10.1016/j.addr.2006.03.011

Davies, C. W. (1938). The extent of dissociation of salts in water. Part VIII. An equation for the mean ionic activity coefficient of an electrolyte in water, and a revision of the dissociation constants of some sulphates. *Journal of the Chemical Society (Resumed), 28*, 2093. https://doi.org/10.1039/jr9380002093

Davies, J. L., & Smith, M. P. (2010). Membrane Applications in Monoclonal Antibody Production. In Z. F. Cui & H. S. Muralidhara (Eds.), *Membrane Technology* (pp. 79–120). Butterworth-Heinemann. https://doi.org/10.1016/B978-1-85617-632-3.00006-9

Davis, R. H. (1992). Modeling of Fouling of Crossflow Microfiltration Membranes. *Separation and Purification Methods, 21*(2), 75–126. https://doi.org/10.1080/03602549208021420

Deep, K., Singh, K. P., Kansal, M. L., & Mohan, C. (2009). A real coded genetic algorithm for solving integer and mixed integer optimization problems. *Applied Mathematics and Computation, 212*(2), 505–518. https://doi.org/10.1016/j.amc.2009.02.044

de Jong, S. (1993). SIMPLS: An alternative approach to partial least squares regression. *Chemometrics and Intelligent Laboratory Systems, 18*(3), 251–263. https://doi.org/10.1016/0169-7439(93)85002-X

Denton, A. R. (2010). Poisson–Boltzmann theory of charged colloids: limits of the cell model for salty suspensions. *Journal of Physics: Condensed Matter, 22*(36), 364108. https://doi.org/10.1088/0953-8984/22/36/364108

Deserno, M., & Holm, C. (2001). Cell Model and Poisson-Boltzmann Theory: A Brief Introduction. In *Electrostatic Effects in Soft Matter and Biophysics* (pp. 27–52). Springer Netherlands. https://doi.org/10.1007/978-94-010-0577-7_2

Devereux, N., & Hoare, M. (1986). Membrane separation of protein precipitates: Studies with cross flow in hollow fibers. *Biotechnology and Bioengineering, 28*(3), 422–431. https://doi.org/10.1002/bit.260280316

Ding, F.-X., Wang, F., Lu, Y.-M., Li, K., Wang, K.-H., He, X.-W., & Sun, S.-H. (2009). Multiepitope peptide-loaded virus-like particles as a vaccine against hepatitis B virus–related hepatocellular carcinoma. *Hepatology, 49*(5), 1492–1502. https://doi.org/10.1002/hep.22816

Ding, Y., Chuan, Y. P., He, L., & Middelberg, A. P. J. (2010). Modeling the competition between aggregation and self-assembly during virus-like particle processing. *Biotechnology and Bioengineering*, *107*(3), 550–560. https://doi.org/10.1002/bit.22821

Dizon-Maspat, J., Bourret, J., D'Agostini, A., & Li, F. (2012). Single pass tangential flow filtration to debottleneck downstream processing for therapeutic antibody production. *Biotechnology and Bioengineering*, *109*(4), 962–970. https://doi.org/10.1002/bit.24377

Donnan, F. G. (1911). Theorie der Membrangleichgewichte und Membranpotentiale bei Vorhandensein von nicht dialysierenden Elektrolyten. Ein Beitrag zur physikalisch-chemischen Physiologie. *Zeitschrift Für Elektrochemie Und Angewandte Physikalische Chemie*, *17*(14), 572–581. https://doi.org/10.1002/bbpc.19110171405

Donovan, J. W. (1969). Ultraviolet Absorption. In *Physical Principles and Techniques of Protein Chemistry* (Second Edi, pp. 101–170). Elsevier. https://doi.org/10.1016/B978-0-12-440101-3.50009-6

Dormond, E., Chahal, P., Bernier, A., Tran, R., Perrier, M., & Kamen, A. (2010). An efficient process for the purification of helper-dependent adenoviral vector and removal of helper virus by iodixanol ultracentrifugation. *Journal of Virological Methods*, *165*(1), 83–89. https://doi.org/10.1016/j.jviromet.2010.01.008

Dutra, G., Komuczki, D., Jungbauer, A., & Satzer, P. (2020). Continuous capture of recombinant antibodies by ZnCl 2 precipitation without polyethylene glycol. *Engineering in Life Sciences*, *20*(7), 265–274. https://doi.org/10.1002/elsc.201900160

Eifler, N., Medaglia, G., Anderka, O., Laurin, L., & Hermans, P. (2014). Development of a novel affinity chromatography resin for platform purification of lambda fabs. *Biotechnology Progress*, *30*(6), 1311–1318. https://doi.org/10.1002/btpr.1958

European Medicines Agency. (2015). *European public assessment reports: Mosquirix*.

European Medicines Agency Committee for Advanced Therapies (CAT). (2018). Guideline on the quality, non-clinical and clinical aspects of gene therapy medicinal products. *European Medicines Agency Guidelines*, *44*(March), 1–41. https://www.ema.europa.eu/en/documents/scientific-guideline/guideline-quality-non-clinical-clinical-aspects-gene-therapy-medicinal-products_en.pdf

Evens, R. P. (2016). Pharma Success in Product Development—Does Biotechnology Change the Paradigm in Product Development and Attrition. *The AAPS Journal*, *18*(1), 281–285. https://doi.org/10.1208/s12248-015-9833-6

Fernandez-Cerezo, L., Wismer, M. K., Han, I., & Pollard, J. M. (2020). High throughput screening of ultrafiltration and diafiltration processing of monoclonal antibodies via the ambr® crossflow system. *Biotechnology Progress*, *36*(2), 1–10. https://doi.org/10.1002/btpr.2929

Frokjaer, S., & Otzen, D. E. (2005). Protein drug stability: a formulation challenge. *Nature Reviews Drug Discovery*, *4*(4), 298–306. https://doi.org/10.1038/nrd1695

Fuenmayor, J., Gòdia, F., & Cervera, L. (2017). Production of virus-like particles for vaccines. *New Biotechnology*, *39*, 174–180. https://doi.org/10.1016/j.nbt.2017.07.010

Gagnon, P. (2009). Chromatographic Purification of Virus Particles. In M. C. Flickinger (Ed.), *Encyclopedia of Industrial Biotechnology* (pp. 1–21). John Wiley & Sons, Inc. https://doi.org/10.1002/9780470054581.eib583

Garcea, R. L., & Gissmann, L. (2004). Virus-like particles as vaccines and vessels for the delivery of small molecules. *Current Opinion in Biotechnology*, *15*(6), 513–517. https://doi.org/10.1016/j.copbio.2004.10.002

Garidel, P., Kuhn, A. B., Schäfer, L. V., Karow-Zwick, A. R., & Blech, M. (2017). High-concentration protein formulations: How high is high? *European Journal of Pharmaceutics and Biopharmaceutics*, *119*, 353–360. https://doi.org/10.1016/j.ejpb.2017.06.029

Gasteiger, E., Hoogland, C., Gattiker, A., Duvaud, S., Wilkins, M. R., Appel, R. D., & Bairoch, A. (2005). Protein Identification and Analysis Tools on the ExPASy Server. In J. M. Walker (Ed.), *The Proteomics Protocols Handbook* (pp. 571–607). Humana Press. https://doi.org/10.1385/1-59259-890-0:571

Gates, T. J., Lyu, Y. F., Fang, X., & Liao, X. (2020). Clearance of solvents and small molecule impurities in antibody drug conjugates via ultrafiltration and diafiltration operation. *Biotechnology Progress*, *36*(1), 1–8. https://doi.org/10.1002/btpr.2923

Gerstweiler, L., Bi, J., & Middelberg, A. (2021). Virus-like particle preparation is improved by control over capsomere-DNA interactions during chromatographic purification. *Biotechnology and Bioengineering*, bit.27687. https://doi.org/10.1002/bit.27687

Gerstweiler, L., Billakanti, J., Bi, J., & Middelberg, A. (2021). Comparative evaluation of integrated purification pathways for bacterial modular polyomavirus major capsid protein VP1 to produce virus-like particles using high throughput process technologies. *Journal of Chromatography A*, *1639*, 461924. https://doi.org/10.1016/j.chroma.2021.461924

Ghorbani, A., Zare, F., Sazegari, S., Afsharifar, A., Eskandari, M. H., & Pormohammad, A. (2020). Development of a novel platform of virus-like particle (VLP)-based vaccine against COVID-19 by exposing epitopes: an immunoinformatics approach. *New Microbes and New Infections*, *38*, 100786. https://doi.org/10.1016/j.nmni.2020.100786

Ghosh, R. (2003). Novel cascade ultrafiltration configuration for continuous, high-resolution protein–protein fractionation: a simulation study. *Journal of Membrane Science*, *226*(1–2), 85–99. https://doi.org/10.1016/j.memsci.2003.08.012

Gisler, T., Schulz, S. F., Borkovec, M., Sticher, H., Schurtenberger, P., D'Aguanno, B., & Klein, R. (1994). Understanding colloidal charge renormalization from surface chemistry: Experiment and theory. *The Journal of Chemical Physics*, *101*(11), 9924–9936. https://doi.org/10.1063/1.467894

Godawat, R., Konstantinov, K., Rohani, M., & Warikoo, V. (2015). End-to-end integrated fully continuous production of recombinant monoclonal antibodies. *Journal of Biotechnology*, *213*, 13–19. https://doi.org/10.1016/j.jbiotec.2015.06.393

Goldinger, S. M., Dummer, R., Baumgaertner, P., Mihic-Probst, D., Schwarz, K., Hammann-Haenni, A., Willers, J., Geldhof, C., Prior, J. O., Kündig, T. M., Michielin, O., Bachmann, M. F., & Speiser, D. E. (2012). Nano-particle vaccination combined with TLR-7 and -9 ligands triggers memory and effector CD8+ T-cell responses in melanoma patients. *European Journal of Immunology*, *42*(11), 3049–3061. https://doi.org/10.1002/eji.201142361

Gomis-Fons, J., Löfgren, A., Andersson, N., Nilsson, B., Berghard, L., & Wood, S. (2019). Integration of a complete downstream process for the automated lab-scale production of a recombinant protein. *Journal of Biotechnology*, *301*(April), 45–51. https://doi.org/10.1016/j.jbiotec.2019.05.013

Gottschalk, U. (2008). Bioseparation in Antibody Manufacturing: The Good, The Bad and The Ugly. *Biotechnology Progress*, *24*(3), 496–503. https://doi.org/10.1021/bp070452g

Greenwood, B. (2014). The contribution of vaccination to global health: Past, present and future. *Philosophical Transactions of the Royal Society B: Biological Sciences, 369*(1645). https://doi.org/10.1098/rstb.2013.0433

Grgacic, E. V. L., & Anderson, D. A. (2006). Virus-like particles: Passport to immune recognition. *Methods, 40*(1), 60–65. https://doi.org/10.1016/j.ymeth.2006.07.018

Grimsley, G. R., Scholtz, J. M., & Pace, C. N. (2009). A summary of the measured pK values of the ionizable groups in folded proteins. *Protein Science, 18*(1), 247–251. https://doi.org/10.1002/pro.19

Großhans, S., Rüdt, M., Sanden, A., Brestrich, N., Morgenstern, J., Heissler, S., & Hubbuch, J. (2018). In-line Fourier-transform infrared spectroscopy as a versatile process analytical technology for preparative protein chromatography. *Journal of Chromatography A, 1547*, 37–44. https://doi.org/10.1016/j.chroma.2018.03.005

Großhans, S., Suhm, S., & Hubbuch, J. (2019). Precipitation of complex antibody solutions: influence of contaminant composition and cell culture medium on the precipitation behavior. *Bioprocess and Biosystems Engineering, 42*(6), 1039–1051. https://doi.org/10.1007/s00449-019-02103-y

Grzenia, D. L., Carlson, J. O., & Wickramasinghe, S. R. (2008). Tangential flow filtration for virus purification. *Journal of Membrane Science, 321*(2), 373–380. https://doi.org/10.1016/j.memsci.2008.05.020

Hammerschmidt, N., Hobiger, S., & Jungbauer, A. (2016). Continuous polyethylene glycol precipitation of recombinant antibodies: Sequential precipitation and resolubilization. *Process Biochemistry, 51*(2), 325–332. https://doi.org/10.1016/j.procbio.2015.11.032

Hansen, S. K., Jamali, B., & Hubbuch, J. (2013). Selective high throughput protein quantification based on UV absorption spectra. *Biotechnology and Bioengineering, 110*(2), 448–460. https://doi.org/10.1002/bit.24712

Hartzell, E. J., Lieser, R. M., Sullivan, M. O., & Chen, W. (2020). Modular Hepatitis B Virus-like Particle Platform for Biosensing and Drug Delivery. *ACS Nano, 14*(10), 12642–12651. https://doi.org/10.1021/acsnano.9b08756

Hassan, P. A., Rana, S., & Verma, G. (2015). Making sense of Brownian motion: colloid characterization by dynamic light scattering. *Langmuir : The ACS Journal of Surfaces and Colloids, 31*(1), 3–12. https://doi.org/10.1021/la501789z

Hekmat, D., Maslak, D., Freiherr von Roman, M., Breitschwerdt, P., Ströhle, C., Vogt, A., Berensmeier, S., & Weuster-Botz, D. (2015). Non-

chromatographic preparative purification of enhanced green fluorescent protein. *Journal of Biotechnology*, *194*, 84–90. https://doi.org/10.1016/j.jbiotec.2014.11.027

Hillebrandt, N., Vormittag, P., Bluthardt, N., Dietrich, A., & Hubbuch, J. (2020). Integrated Process for Capture and Purification of Virus-like Particles: Enhancing Process Performance by Cross-flow Filtration. *Frontiers in Bioengineering and Biotechnology*, *8*. https://doi.org/10.3389/fbioe.2020.00489

Hillebrandt, N., Vormittag, P., Dietrich, A., Wegner, C. H., & Hubbuch, J. (2021). Process development for cross-flow diafiltration-based VLP disassembly: A novel high-throughput screening approach. *Biotechnology and Bioengineering*, *118*(10), 3926–3940. https://doi.org/10.1002/bit.27868

Holliger, P., & Hudson, P. J. (2005). Engineered antibody fragments and the rise of single domains. *Nature Biotechnology*, *23*(9), 1126–1136. https://doi.org/10.1038/nbt1142

Holmes, K., Shepherd, D. A., Ashcroft, A. E., Whelan, M., Rowlands, D. J., & Stonehouse, N. J. (2015). Assembly pathway of hepatitis B core virus-like particles from genetically fused dimers. *Journal of Biological Chemistry*, *290*(26), 16238–16245. https://doi.org/10.1074/jbc.M114.622035

Holstein, M., Hung, J., Feroz, H., Ranjan, S., Du, C., Ghose, S., & Li, Z. J. (2020). Strategies for high-concentration drug substance manufacturing to facilitate subcutaneous administration: A review. *Biotechnology and Bioengineering*, *117*(11), 3591–3606. https://doi.org/10.1002/bit.27510

Hung, J. J., Borwankar, A. U., Dear, B. J., Truskett, T. M., & Johnston, K. P. (2016). High concentration tangential flow ultrafiltration of stable monoclonal antibody solutions with low viscosities. *Journal of Membrane Science*, *508*, 113–126. https://doi.org/10.1016/j.memsci.2016.02.031

ICH Expert Working Group. (2009). *Q8(R2) Guideline - Pharmaceutical Development*. International Conference on Harmonisation of Technical Requirements for Registration of Pharmaceuticals for Human Use. https://database.ich.org/sites/default/files/Q8%28R2%29 Guideline.pdf

ICH Expert Working Group. (2012). *Q11 Guideline - Development and Manufacture of Drug Substances*. International Conference on Harmonisation of Technical Requirements for Registration of Pharmaceuticals for Human Use. https://database.ich.org/sites/default/files/Q11 Guideline.pdf

Iverius, P. H., & Laurent, T. C. (1967). Precipitation of some plasma proteins by the addition of dextran or polyethylene glycol. *Biochimica et Biophysica*

Acta (BBA) - Protein Structure, *133*(2), 371–373. https://doi.org/10.1016/0005-2795(67)90079-7

Jabra, M. G., Tao, Y., Moomaw, J. F., Yu, Z., Hotovec, B. J., Geng, S. B., & Zydney, A. L. (2020). pH and excipient profiles during formulation of highly concentrated biotherapeutics using bufferless media. *Biotechnology and Bioengineering*, *117*(11), 3390–3399. https://doi.org/10.1002/bit.27502

Jagschies, G., & Lacki, K. (2018). Process Capability Requirements. In G. Jagschies, E. Lindskog, K. Lacki, & P. Galliher (Eds.), *Biopharmaceutical Processing* (pp. 73–94). Elsevier. https://doi.org/10.1016/B978-0-08-100623-8.00004-9

Jain, N. K., Sahni, N., Kumru, O. S., Joshi, S. B., Volkin, D. B., & Russell Middaugh, C. (2015). Formulation and stabilization of recombinant protein based virus-like particle vaccines. *Advanced Drug Delivery Reviews*, *93*, 42–55. https://doi.org/10.1016/j.addr.2014.10.023

Jegerlehner, A. (2002). A molecular assembly system that renders antigens of choice highly repetitive for induction of protective B cell responses. *Vaccine*, *20*(25–26), 3104–3112. https://doi.org/10.1016/S0264-410X(02)00266-9

Jiang, X., Wang, M., Graham, D. Y., & Estes, M. K. (1992). Expression, self-assembly, and antigenicity of the Norwalk virus capsid protein. *Journal of Virology*, *66*(11), 6527–6532. https://doi.org/10.1128%2Fjvi.66.11.6527-6532.1992

Jönsson, A.-S., & Trägårdh, G. (1990). Fundamental principles of ultrafiltration. *Chemical Engineering and Processing: Process Intensification*, *27*(2), 67–81. https://doi.org/10.1016/0255-2701(90)85011-R

Kalbfuss, B., Genzel, Y., Wolff, M., Zimmermann, A., Morenweiser, R., & Reichl, U. (2007). Harvesting and concentration of human influenza A virus produced in serum-free mammalian cell culture for the production of vaccines. *Biotechnology and Bioengineering*, *97*(1), 73–85. https://doi.org/10.1002/bit.21139

Karow, A. R., Bahrenburg, S., & Garidel, P. (2013). Buffer capacity of biologics-from buffer salts to buffering by antibodies. *Biotechnology Progress*, *29*(2), 480–492. https://doi.org/10.1002/btpr.1682

Karpenko, L. I., Ivanisenko, V. A., Pika, I. A., Chikaev, N. A., Eroshkin, A. M., Veremeiko, T. A., & Ilyichev, A. A. (2000). Insertion of foreign epitopes in HBcAg: how to make the chimeric particle assemble. *Amino Acids*, *18*(4), 329–337. https://doi.org/10.1007/s007260070072

Karst, D. J., Serra, E., Villiger, T. K., Soos, M., & Morbidelli, M. (2016). Characterization and comparison of ATF and TFF in stirred bioreactors for continuous mammalian cell culture processes. *Biochemical Engineering Journal*, *110*, 17–26. https://doi.org/10.1016/j.bej.2016.02.003

Kattur Venkatachalam, A. R., Szyporta, M., Kiener, T. K., Balraj, P., & Kwang, J. (2014). Concentration and purification of enterovirus 71 using a weak anion-exchange monolithic column. *Virology Journal*, *11*(1), 99. https://doi.org/10.1186/1743-422X-11-99

Kaufmann, A. M., Nieland, J. D., Jochmus, I., Baur, S., Friese, K., Gabelsberger, J., Gieseking, F., Gissmann, L., Glasschröder, B., Grubert, T., Hillemanns, P., Höpfl, R., Ikenberg, H., Schwarz, J., Karrasch, M., Knoll, A., Küppers, V., Lechmann, M., Lelle, R. J., … Schneider, A. (2007). Vaccination trial with HPV16 L1E7 chimeric virus-like particles in women suffering from high grade cervical intraepithelial neoplasia (CIN 2/3). *International Journal of Cancer*, *121*(12), 2794–2800. https://doi.org/10.1002/ijc.23022

Kawahara, K., & Tanford, C. (1966). Viscosity and Density of Aqueous Solutions of Urea and Guanidine Hydrochloride. *Journal of Biological Chemistry*, *241*(13), 3228–3232. https://doi.org/10.1016/S0021-9258(18)96519-1

Kawka, K., Wilton, A. N., Madadkar, P., Medina, M. F. C., Lichty, B. D., Ghosh, R., & Latulippe, D. R. (2021). Integrated development of enzymatic DNA digestion and membrane chromatography processes for the purification of therapeutic adenoviruses. *Separation and Purification Technology*, *254*(April 2020), 117503. https://doi.org/10.1016/j.seppur.2020.117503

Kazaks, A., Lu, I.-N., Farinelle, S., Ramirez, A., Crescente, V., Blaha, B., Ogonah, O., Mukhopadhyay, T., de Obanos, M. P., Krimer, A., Akopjana, I., Bogans, J., Ose, V., Kirsteina, A., Kazaka, T., Stonehouse, N. J., Rowlands, D. J., Muller, C. P., Tars, K., & Rosenberg, W. M. (2017). Production and purification of chimeric HBc virus-like particles carrying influenza virus LAH domain as vaccine candidates. *BMC Biotechnology*, *17*(1), 79. https://doi.org/10.1186/s12896-017-0396-8

Kazemi, A. S., Kawka, K., & Latulippe, D. R. (2016). Optimization of biomolecule separation by combining microscale filtration and design-of-experiment methods. *Biotechnology and Bioengineering*, *113*(10), 2131–2139. https://doi.org/10.1002/bit.25975

Kazemi, A. S., & Latulippe, D. R. (2014). Stirred well filtration (SWF) – A high-throughput technique for downstream bio-processing. *Journal of*

Membrane Science, *470*, 30–39. https://doi.org/10.1016/j.memsci.2014.07.011

Kedem, O., & Katchalsky, A. (1958). Thermodynamic analysis of the permeability of biological membranes to non-electrolytes. *Biochimica et Biophysica Acta*, *27*(C), 229–246. https://doi.org/10.1016/0006-3002(58)90330-5

Kelley, B. (2017). Downstream Processing Of Monoclonal Antibodies: Current Practices And Future Opportunities. In U. Gottschalk (Ed.), *Process Scale Purification of Antibodies* (2nd ed., pp. 1–21). John Wiley & Sons, Inc. https://doi.org/10.1002/9781119126942.ch1

Kelley, B., Kiss, R., & Laird, M. (2018). A Different Perspective: How Much Innovation Is Really Needed for Monoclonal Antibody Production Using Mammalian Cell Technology? In *Advances in Biochemical Engineering/Biotechnology* (Vol. 165, Issue May 2017, pp. 443–462). https://doi.org/10.1007/10_2018_59

Kessler, W. (2006). *Multivariate Datenanalyse*. Wiley. https://doi.org/10.1002/9783527610037

Khanal, O., & Lenhoff, A. M. (2021). Developments and opportunities in continuous biopharmaceutical manufacturing. *MAbs*, *13*(1). https://doi.org/10.1080/19420862.2021.1903664

Kim, H. J., Kim, S. Y., Lim, S. J., Kim, J. Y., Lee, S. J., & Kim, H.-J. (2010). One-step chromatographic purification of human papillomavirus type 16 L1 protein from Saccharomyces cerevisiae. *Protein Expression and Purification*, *70*(1), 68–74. https://doi.org/10.1016/j.pep.2009.08.005

Kingston, N. J., Kurtovic, L., Walsh, R., Joe, C., Lovrecz, G., Locarnini, S., Beeson, J. G., & Netter, H. J. (2019). Hepatitis B virus-like particles expressing Plasmodium falciparum epitopes induce complement-fixing antibodies against the circumsporozoite protein. *Vaccine*, *37*(12), 1674–1684. https://doi.org/10.1016/j.vaccine.2019.01.056

Kiss, B., Gottschalk, U., & Pohlscheidt, M. (Eds.). (2018). *New Bioprocessing Strategies: Development and Manufacturing of Recombinant Antibodies and Proteins* (1st ed., Vol. 165). Springer International Publishing. https://doi.org/10.1007/978-3-319-97110-0

Klamp, T., Schumacher, J., Huber, G., Kühne, C., Meissner, U., Selmi, A., Hiller, T., Kreiter, S., Markl, J., Türeci, Ö., & Sahin, U. (2011). Highly specific auto-antibodies against claudin-18 isoform 2 induced by a chimeric HBcAg virus-like particle vaccine kill tumor cells and inhibit the

growth of lung metastases. *Cancer Research*, *71*(2), 516–527. https://doi.org/10.1158/0008-5472.CAN-10-2292

Kleiner, M., Hooper, L. V, & Duerkop, B. A. (2015). Evaluation of methods to purify virus-like particles for metagenomic sequencing of intestinal viromes. *BMC Genomics*, *16*(1), 7. https://doi.org/10.1186/s12864-014-1207-4

Klijn, M. E., & Hubbuch, J. (2018). Application of Empirical Phase Diagrams for Multidimensional Data Visualization of High-Throughput Microbatch Crystallization Experiments. *Journal of Pharmaceutical Sciences*, *107*(8), 2063–2069. https://doi.org/10.1016/j.xphs.2018.04.018

Koho, T., Mäntylä, T., Laurinmäki, P., Huhti, L., Butcher, S. J., Vesikari, T., Kulomaa, M. S., & Hytönen, V. P. (2012). Purification of norovirus-like particles (VLPs) by ion exchange chromatography. *Journal of Virological Methods*, *181*(1), 6–11. https://doi.org/10.1016/j.jviromet.2012.01.003

Konstantinov, K. B., & Cooney, C. L. (2015). White Paper on Continuous Bioprocessing May 20–21 2014 Continuous Manufacturing Symposium. *Journal of Pharmaceutical Sciences*, *104*(3), 813–820. https://doi.org/10.1002/jps.24268

Koppel, D. E. (1972). Analysis of Macromolecular Polydispersity in Intensity Correlation Spectroscopy: The Method of Cumulants. *The Journal of Chemical Physics*, *57*(11), 4814–4820. https://doi.org/10.1063/1.1678153

Kramberger, P., Urbas, L., & Štrancar, A. (2015). Downstream processing and chromatography based analytical methods for production of vaccines, gene therapy vectors, and bacteriophages. *Human Vaccines & Immunotherapeutics*, *11*(4), 1010–1021. https://doi.org/10.1080/21645515.2015.1009817

Kröber, T., Wolff, M. W., Hundt, B., Seidel-Morgenstern, A., & Reichl, U. (2013). Continuous purification of influenza virus using simulated moving bed chromatography. *Journal of Chromatography A*, *1307*, 99–110. https://doi.org/10.1016/j.chroma.2013.07.081

Kruse, T., Schmidt, A., Kampmann, M., & Strube, J. (2019). Integrated Clarification and Purification of Monoclonal Antibodies by Membrane Based Separation of Aqueous Two-Phase Systems. *Antibodies*, *8*(3), 40. https://doi.org/10.3390/antib8030040

Kuczewski, M., Schirmer, E., Lain, B., & Zarbis-Papastoitsis, G. (2011). A single-use purification process for the production of a monoclonal antibody produced in a PER.C6 human cell line. *Biotechnology Journal*, *6*(1), 56–65. https://doi.org/10.1002/biot.201000292

Kumar, V., & Lenhoff, A. M. (2020). Mechanistic Modeling of Preparative Column Chromatography for Biotherapeutics. *Annual Review of Chemical and Biomolecular Engineering*, *11*(1), 235–255. https://doi.org/10.1146/annurev-chembioeng-102419-125430

Kurnik, R. T., Yu, A. W., Blank, G. S., Burton, A. R., Smith, D., Athalye, A. M., & van Reis, R. (1995). Buffer exchange using size exclusion chromatography, countercurrent dialysis, and tangential flow filtration: Models, development, and industrial application. *Biotechnology and Bioengineering*, *45*(2), 149–157. https://doi.org/10.1002/bit.260450209

Kushnir, N., Streatfield, S. J., & Yusibov, V. (2012). Virus-like particles as a highly efficient vaccine platform: Diversity of targets and production systems and advances in clinical development. *Vaccine*, *31*(1), 58–83. https://doi.org/10.1016/j.vaccine.2012.10.083

Lacki, K., & Brekkan, E. (2011). High throughput screening techniques in protein purification. In J.-C. Janson (Ed.), *Protein purification: Principles, high resolution methods, and applications.* (3rd ed., pp. 489–506). John Wiley & Sons, Inc.

Ladd Effio, C., Hahn, T., Seiler, J., Oelmeier, S. A., Asen, I., Silberer, C., Villain, L., & Hubbuch, J. (2016). Modeling and simulation of anion-exchange membrane chromatography for purification of Sf9 insect cell-derived virus-like particles. *Journal of Chromatography A*, *1429*, 142–154. https://doi.org/10.1016/j.chroma.2015.12.006

Ladd Effio, C., & Hubbuch, J. (2015). Next generation vaccines and vectors: Designing downstream processes for recombinant protein-based virus-like particles. *Biotechnology Journal*, *10*(5), 715–727. https://doi.org/10.1002/biot.201400392

Ladd Effio, C., Oelmeier, S. A., & Hubbuch, J. (2016). High-throughput characterization of virus-like particles by interlaced size-exclusion chromatography. *Vaccine*, *34*(10), 1259–1267. https://doi.org/10.1016/j.vaccine.2016.01.035

Ladd Effio, C., Wenger, L., Ötes, O., Oelmeier, S. A., Kneusel, R., & Hubbuch, J. (2015). Downstream processing of virus-like particles: Single-stage and multi-stage aqueous two-phase extraction. *Journal of Chromatography A*, *1383*, 35–46. https://doi.org/10.1016/j.chroma.2015.01.007

Ladwig, J. E., Zhu, X., Rolandi, P., Hart, R., Robinson, J., & Rydholm, A. (2020). Mechanistic model of pH and excipient concentration during ultrafiltration and diafiltration processes of therapeutic antibodies. *Biotechnology Progress*, *36*(5), e2993. https://doi.org/10.1002/btpr.2993

Lagoutte, P., Mignon, C., Donnat, S., Stadthagen, G., Mast, J., Sodoyer, R., Lugari, A., & Werle, B. (2016). Scalable chromatography-based purification of virus-like particle carrier for epitope based influenza A vaccine produced in Escherichia coli. *Journal of Virological Methods, 232*, 8–11. https://doi.org/10.1016/j.jviromet.2016.02.011

Layne, E. (1957). [73] Spectrophotometric and turbidimetric methods for measuring proteins. In *Methods in Enzymology* (Vol. 3, Issue C, pp. 447–454). Academic Press. https://doi.org/10.1016/S0076-6879(57)03413-8

Leader, B., Baca, Q. J., & Golan, D. E. (2008). Protein therapeutics: a summary and pharmacological classification. *Nature Reviews Drug Discovery, 7*(1), 21–39. https://doi.org/10.1038/nrd2399

Le, D. T., & Müller, K. M. (2021). In Vitro Assembly of Virus-Like Particles and Their Applications. *Life, 11*(4), 334. https://doi.org/10.3390/life11040334

Lee, J., Gan, H. T., Latiff, S. M. A., Chuah, C., Lee, W. Y., Yang, Y. S., Loo, B., Ng, S. K., & Gagnon, P. (2012). Principles and applications of steric exclusion chromatography. *Journal of Chromatography A, 1270*, 162–170. https://doi.org/10.1016/j.chroma.2012.10.062

Lee, K. W., & Tan, W. S. (2008). Recombinant hepatitis B virus core particles: Association, dissociation and encapsidation of green fluorescent protein. *Journal of Virological Methods, 151*(2), 172–180. https://doi.org/10.1016/j.jviromet.2008.05.025

Leszczyszyn, O. (2012). *Hydrodynamic Radius Vs Radius of Gyration.* Material Talks. http://www.materials-talks.com/blog/2012/11/15/size-matters-rh-versus-rg/

Leung, A. B., Suh, K. I., & Ansari, R. R. (2006). Particle-size and velocity measurements in flowing conditions using dynamic light scattering. *Applied Optics, 45*(10), 2186–2190. https://doi.org/10.1364/AO.45.002186

Liderfelt, J., & Royce, J. (2018). Filtration Methods for Use in Purification Processes (Concentration and Buffer Exchange). In G. Jagschies, E. Lindskog, K. Lacki, & P. M. Galliher (Eds.), *Biopharmaceutical Processing* (pp. 441–453). Elsevier. https://doi.org/10.1016/B978-0-08-100623-8.00023-2

Liew, M. W. O., Chuan, Y. P., & Middelberg, A. P. J. (2012). Reactive diafiltration for assembly and formulation of virus-like particles. *Biochemical Engineering Journal, 68*, 120–128. https://doi.org/10.1016/j.bej.2012.07.009

Lima, T. M., Souza, M. O., & Castilho, L. R. (2019). Purification of flavivirus VLPs by a two-step chomatographic process. *Vaccine*, *37*(47), 7061–7069. https://doi.org/10.1016/j.vaccine.2019.05.066

Link, A., Zabel, F., Schnetzler, Y., Titz, A., Brombacher, F., & Bachmann, M. F. (2012). Innate Immunity Mediates Follicular Transport of Particulate but Not Soluble Protein Antigen. *The Journal of Immunology*, *188*(8), 3724–3733. https://doi.org/10.4049/jimmunol.1103312

Lin, S.-Y., Chiu, H.-Y., Chiang, B.-L., & Hu, Y.-C. (2015). Development of EV71 virus-like particle purification processes. *Vaccine*, *33*(44), 5966–5973. https://doi.org/10.1016/j.vaccine.2015.04.077

Liu, H. F., Ma, J., Winter, C., & Bayer, R. (2010). Recovery and purification process development for monoclonal antibody production. *MAbs*, *2*(5), 480–499. https://doi.org/10.4161/mabs.2.5.12645

Liu, J., Nguyen, M. D. H., Andya, J. D., & Shire, S. J. (2005). Reversible Self-Association Increases the Viscosity of a Concentrated Monoclonal Antibody in Aqueous Solution. *Journal of Pharmaceutical Sciences*, *94*(9), 1928–1940. https://doi.org/10.1002/jps.20347

Liu, W., Fan, X., Wang, X., Bao, Z., Sun, Y., Rai, K., Shaliutina-Kolešová, A., Su, J., Xian, M., & Nian, R. (2019). Salt-enhanced permeabilization for monoclonal antibody precipitation and purification in a tubular reactor with a depth filtration membrane with advanced chromatin extraction. *Biochemical Engineering Journal*, *151*(May). https://doi.org/10.1016/j.bej.2019.107332

Li, Y., Zhu, M., Luo, H., & Weaver, J. R. (2017). Development Of A Platform Process For The Purification Of Therapeutic Monoclonal Antibodies. In U. Gottschalk (Ed.), *Process Scale Purification of Antibodies* (2nd ed., pp. 343–363). John Wiley & Sons, Inc. https://doi.org/10.1002/9781119126942.ch16

Li, Z., Gu, Q., Coffman, J. L., Przybycien, T., & Zydney, A. L. (2019). Continuous precipitation for monoclonal antibody capture using countercurrent washing by microfiltration. *Biotechnology Progress*, *July*, 1–8. https://doi.org/10.1002/btpr.2886

Lizotte, P. H., Wen, A. M., Sheen, M. R., Fields, J., Rojanasopondist, P., Steinmetz, N. F., & Fiering, S. (2016). In situ vaccination with cowpea mosaic virus nanoparticles suppresses metastatic cancer. *Nature Nanotechnology*, *11*(3), 295–303. https://doi.org/10.1038/nnano.2015.292

Li, Z., & Zydney, A. L. (2017). Effect of zinc chloride and PEG concentrations on the critical flux during tangential flow microfiltration of BSA

precipitates. *Biotechnology Progress*, *33*(6), 1561–1567. https://doi.org/10.1002/btpr.2545

Loewe, Häussler, Grein, Dieken, Weidner, Salzig, & Czermak. (2019). Forced Degradation Studies to Identify Critical Process Parameters for the Purification of Infectious Measles Virus. *Viruses*, *11*(8), 725. https://doi.org/10.3390/v11080725

Lohmann, L. J., & Strube, J. (2020). Accelerating biologics manufacturing by modeling: Process integration of precipitation in mAb downstream processing. *Processes*, *8*(1). https://doi.org/10.3390/pr8010058

Lothert, K., Offersgaard, A. F., Pihl, A. F., Mathiesen, C. K., Jensen, T. B., Alzua, G. P., Fahnøe, U., Bukh, J., Gottwein, J. M., & Wolff, M. W. (2020). Development of a downstream process for the production of an inactivated whole hepatitis C virus vaccine. *Scientific Reports*, *10*(1), 16261. https://doi.org/10.1038/s41598-020-72328-5

Lothert, K., Pagallies, F., Eilts, F., Sivanesapillai, A., Hardt, M., Moebus, A., Feger, T., Amann, R., & Wolff, M. W. (2020). A scalable downstream process for the purification of the cell culture-derived Orf virus for human or veterinary applications. *Journal of Biotechnology*, *323*(August), 221–230. https://doi.org/10.1016/j.jbiotec.2020.08.014

Lua, L. H. L., Connors, N. K., Sainsbury, F., Chuan, Y. P., Wibowo, N., & Middelberg, A. P. J. (2014). Bioengineering virus-like particles as vaccines. *Biotechnology and Bioengineering*, *111*(3), 425–440. https://doi.org/10.1002/bit.25159

Luechau, F., Ling, T. C., & Lyddiatt, A. (2011). Recovery of B19 virus-like particles by aqueous two-phase systems. *Food and Bioproducts Processing*, *89*(4), 322–327. https://doi.org/10.1016/j.fbp.2010.10.008

Luttmann, R., Bracewell, D. G., Cornelissen, G., Gernaey, K. v., Glassey, J., Hass, V. C., Kaiser, C., Preusse, C., Striedner, G., & Mandenius, C.-F. (2012). Soft sensors in bioprocessing: A status report and recommendations. *Biotechnology Journal*, *7*(8), 1040–1048. https://doi.org/10.1002/biot.201100506

Lutz, H., & Raghunath, B. (2006). Ultrafiltration Process Design and Implementation. In A. A. Shukla, M. R. Etzel, & S. Gadam (Eds.), *Process Scale Bioseparations for the Biopharmaceutical Industry* (1st ed., pp. 297–332). CRC Press. https://doi.org/10.1201/9781420016024

Mach, H., & Middaugh, C. R. (1994). Simultaneous monitoring of the environment of tryptophan, tyrosine, and phenylalanine residues in

proteins by near-ultraviolet second-derivative spectroscopy. *Analytical Biochemistry*, *222*(2), 323–331. https://doi.org/10.1006/abio.1994.1499

Mach, H., Volkin, D. B., Troutman, R. D., Wang, B., Luo, Z., Jansen, K. U., & Shi, L. (2006). Disassembly and reassembly of yeast-derived recombinant human papillomavirus virus-like particles (HPV VLPs). *Journal of Pharmaceutical Sciences*, *95*(10), 2195–2206. https://doi.org/10.1002/jps.20696

Marcus, R. A. (1955). Calculation of Thermodynamic Properties of Polyelectrolytes. *The Journal of Chemical Physics*, *23*(6), 1057–1068. https://doi.org/10.1063/1.1742191

Marichal-Gallardo, P., Börner, K., Pieler, M. M., Sonntag-Buck, V., Obr, M., Bejarano, D., Wolff, M. W., Kräusslich, H.-G., Reichl, U., & Grimm, Di. (2021). Single-Use Capture Purification of Adeno-Associated Viral Gene Transfer Vectors by Membrane-Based Steric Exclusion Chromatography. *Human Gene Therapy*, *32*(17–18), 959–974. https://doi.org/10.1089/hum.2019.284

Marichal-Gallardo, P., Pieler, M. M., Wolff, M. W., & Reichl, U. (2017). Steric exclusion chromatography for purification of cell culture-derived influenza A virus using regenerated cellulose membranes and polyethylene glycol. *Journal of Chromatography A*, *1483*, 110–119. https://doi.org/10.1016/j.chroma.2016.12.076

Marshall, A. D., Munro, P. A., & Trägårdh, G. (1993). The effect of protein fouling in microfiltration and ultrafiltration on permeate flux, protein retention and selectivity: A literature review. *Desalination*, *91*(1), 65–108. https://doi.org/10.1016/0011-9164(93)80047-Q

Martinez, M., Spitali, M., Norrant, E. L., & Bracewell, D. G. (2019). Precipitation as an Enabling Technology for the Intensification of Biopharmaceutical Manufacture. *Trends in Biotechnology*, *37*(3), 237–241. https://doi.org/10.1016/j.tibtech.2018.09.001

Mason, H. S., Ball, J. M., Shi, J. J., Jiang, X., Estes, M. K., & Arntzen, C. J. (1996). Expression of Norwalk virus capsid protein in transgenic tobacco and potato and its oral immunogenicity in mice. *Proceedings of the National Academy of Sciences of the United States of America*, *93*(11), 5335–5340. https://doi.org/10.1073/pnas.93.11.5335

Mayani, M., Filipe, C. D. M., & Ghosh, R. (2010). Cascade ultrafiltration systems—Integrated processes for purification and concentration of lysozyme. *Journal of Membrane Science*, *347*(1–2), 150–158. https://doi.org/10.1016/j.memsci.2009.10.016

McAleer, W. J., Buynak, E. B., Maigetter, R. Z., Wampler, D. E., Miller, W. J., & Hilleman, M. R. (1984). Human hepatitis B vaccine from recombinant yeast. *Nature*, *307*(5947), 178–180. https://doi.org/10.1038/307178a0

McCarthy, M. P., White, W. I., Palmer-Hill, F., Koenig, S., & Suzich, J. A. (1998). Quantitative Disassembly and Reassembly of Human Papillomavirus Type 11 Viruslike Particles In Vitro. *Journal of Virology*, *72*(1), 32–41. https://doi.org/10.1128/JVI.72.1.32-41.1998

Mehta, A., & Zydney, A. L. (2005). Permeability and selectivity analysis for ultrafiltration membranes. *Journal of Membrane Science*, *249*(1–2), 245–249. https://doi.org/10.1016/j.memsci.2004.09.040

Meireles, M., Aimar, P., & Sanchez, V. (1991). Effects of protein fouling on the apparent pore size distribution of sieving membranes. *Journal of Membrane Science*, *56*(1), 13–28. https://doi.org/10.1016/0376-7388(91)85013-U

Mellado, M. C. M., Mena, J. A., Lopes, A., Ramírez, O. T., Carrondo, M. J. T., Palomares, L. A., & Alves, P. M. (2009). Impact of physicochemical parameters on in vitro assembly and disassembly kinetics of recombinant triple-layered rotavirus-like particles. *Biotechnology and Bioengineering*, *104*(4), n/a-n/a. https://doi.org/10.1002/bit.22430

Merten, O.-W., Charrier, S., Laroudie, N., Fauchille, S., Dugué, C., Jenny, C., Audit, M., Zanta-Boussif, M.-A., Chautard, H., Radrizzani, M., Vallanti, G., Naldini, L., Noguiez-Hellin, P., & Galy, A. (2011). Large-Scale Manufacture and Characterization of a Lentiviral Vector Produced for Clinical Ex Vivo Gene Therapy Application. *Human Gene Therapy*, *22*(3), 343–356. https://doi.org/10.1089/hum.2010.060

Miao, F., Velayudhan, A., DiBella, E., Shervin, J., Felo, M., Teeters, M., & Alred, P. (2009). Theoretical analysis of excipient concentrations during the final ultrafiltration/diafiltration step of therapeutic antibody. *Biotechnology Progress*, *25*(4), 964–972. https://doi.org/10.1002/btpr.168

Michalsky, R., Pfromm, P. H., Czermak, P., Sorensen, C. M., & Passarelli, A. L. (2008). Effects of temperature and shear force on infectivity of the baculovirus Autographa californica M nucleopolyhedrovirus. *Journal of Virological Methods*, *153*(2), 90–96. https://doi.org/10.1016/j.jviromet.2008.07.030

Middelberg, A. P. J., Rivera-Hernandez, T., Wibowo, N., Lua, L. H. L., Fan, Y., Magor, G., Chang, C., Chuan, Y. P., Good, M. F., & Batzloff, M. R. (2011). A microbial platform for rapid and low-cost virus-like particle and

capsomere vaccines. *Vaccine*, *29*(41), 7154–7162. https://doi.org/10.1016/j.vaccine.2011.05.075

Mohr, J., Chuan, Y. P., Wu, Y., Lua, L. H. L., & Middelberg, A. P. J. (2013). Virus-like particle formulation optimization by miniaturized high-throughput screening. *Methods*, *60*(3), 248–256. https://doi.org/10.1016/j.ymeth.2013.04.019

Mohsen, M. O., Gomes, A., Vogel, M., & Bachmann, M. (2018). Interaction of Viral Capsid-Derived Virus-Like Particles (VLPs) with the Innate Immune System. *Vaccines*, *6*(3), 37. https://doi.org/10.3390/vaccines6030037

Mohsen, M. O., Heath, M. D., Cabral-Miranda, G., Lipp, C., Zeltins, A., Sande, M., Stein, J. V, Riether, C., Roesti, E., Zha, L., Engeroff, P., El-Turabi, A., Kundig, T. M., Vogel, M., Skinner, M. A., Speiser, D. E., Knuth, A., Kramer, M. F., & Bachmann, M. F. (2019). Vaccination with nanoparticles combined with micro-adjuvants protects against cancer. *Journal for ImmunoTherapy of Cancer*, *7*(1), 114. https://doi.org/10.1186/s40425-019-0587-z

Mohsen, M. O., Speiser, D. E., Knuth, A., & Bachmann, M. F. (2020). Virus-like particles for vaccination against cancer. *Wiley Interdisciplinary Reviews: Nanomedicine and Nanobiotechnology*, *12*(1), 1–17. https://doi.org/10.1002/wnan.1579

Mohsen, M. O., Vogel, M., Riether, C., Muller, J., Salatino, S., Ternette, N., Gomes, A. C., Cabral-Miranda, G., El-Turabi, A., Ruedl, C., Kundig, T. M., Dermime, S., Knuth, A., Speiser, D. E., & Bachmann, M. F. (2019). Targeting Mutated Plus Germline Epitopes Confers Pre-clinical Efficacy of an Instantly Formulated Cancer Nano-Vaccine. *Frontiers in Immunology*, *10*, 1015. https://doi.org/10.3389/fimmu.2019.01015

Moleirinho, M. G., Rosa, S., Carrondo, M. J. T., Silva, R. J. S., Hagner-McWhirter, Å., Ahlén, G., Lundgren, M., Alves, P. M., & Peixoto, C. (2018). Clinical-Grade Oncolytic Adenovirus Purification Using Polysorbate 20 as an Alternative for Cell Lysis. *Current Gene Therapy*, *18*(6), 366–374. https://doi.org/10.2174/1566523218666181109141257

Moleirinho, M. G., Silva, R. J. S., Alves, P. M., Carrondo, M. J. T., & Peixoto, C. (2020). Current challenges in biotherapeutic particles manufacturing. *Expert Opinion on Biological Therapy*, *20*(5), 451–465. https://doi.org/10.1080/14712598.2020.1693541

Molek, J. R., & Zydney, A. L. (2007). Separation of PEGylated α-Lactalbumin from Unreacted Precursors and Byproducts Using Ultrafiltration.

Biotechnology Progress, *23*(6), 1417–1424. https://doi.org/10.1021/bp070243w

Molin, S., Givskov, M., & Riise, E. (1992). *Production in Escherichia coli of extracellular Serratia spp. hydrolases* (Patent No. U.S. Patent No. 5,173,418). Washington DC: U.S. Patent and Trademark Office.

Moreira, A. S., Faria, T. Q., Oliveira, J. G., Kavara, A., Schofield, M., Sanderson, T., Collins, M., Gantier, R., Alves, P. M., Carrondo, M. J. T., & Peixoto, C. (2021). Enhancing the purification of Lentiviral vectors for clinical applications. *Separation and Purification Technology*, *274*(March), 118598. https://doi.org/10.1016/j.seppur.2021.118598

Morenweiser, R. (2005). Downstream processing of viral vectors and vaccines. *Gene Therapy*, *12*(S1), S103–S110. https://doi.org/10.1038/sj.gt.3302624

Morgan, B. A., Manser, M., Jeyanathan, M., Xing, Z., Cranston, E. D., & Thompson, M. R. (2020). Effect of Shear Stresses on Adenovirus Activity and Aggregation during Atomization To Produce Thermally Stable Vaccines by Spray Drying. *ACS Biomaterials Science & Engineering*, *6*(7), 4304–4313. https://doi.org/10.1021/acsbiomaterials.0c00317

Nahler, G. (2017). Dictionary of Pharmaceutical Medicine. In G. Nahler (Ed.), *Reference Reviews* (4th ed., Vol. 31, Issue 8). Springer International Publishing. https://doi.org/10.1007/978-3-319-50669-2

Nambiar, A. M. K., Li, Y., & Zydney, A. L. (2018). Countercurrent staged diafiltration for formulation of high value proteins. *Biotechnology and Bioengineering*, *115*(1), 139–144. https://doi.org/10.1002/bit.26441

Narayanan, H., Luna, M. F., Stosch, M., Cruz Bournazou, M. N., Polotti, G., Morbidelli, M., Butté, A., & Sokolov, M. (2020). Bioprocessing in the Digital Age: The Role of Process Models. *Biotechnology Journal*, *15*(1), 1900172. https://doi.org/10.1002/biot.201900172

Nassal, M., Skamel, C., Kratz, P. A., Wallich, R., Stehle, T., & Simon, M. (2005). A fusion product of the complete Borrelia burgdorferi outer surface protein A (OspA) and the hepatitis B virus capsid protein is highly immunogenic and induces protective immunity similar to that seen with an effective lipidated OspA vaccine formula. *European Journal of Immunology*, *35*(2), 655–665. https://doi.org/10.1002/eji.200425449

Negrete, A., Pai, A., & Shiloach, J. (2014). Use of hollow fiber tangential flow filtration for the recovery and concentration of HIV virus-like particles produced in insect cells. *Journal of Virological Methods*, *195*, 240–246. https://doi.org/10.1016/j.jviromet.2013.10.017

Neirynck, S., Deroo, T., Saelens, X., Vanlandschoot, P., Jou, W. M., & Fiers, W. (1999). A universal influenza A vaccine based on the extracellular domain of the M2 protein. *Nature Medicine*, *5*(10), 1157–1163. https://doi.org/10.1038/13484

Nejatishahidein, N., & Zydney, A. L. (2021). Depth filtration in bioprocessing — new opportunities for an old technology. *Current Opinion in Chemical Engineering*, *34*, 100746. https://doi.org/10.1016/j.coche.2021.100746

Nestola, P., Peixoto, C., Silva, R. R. J. S., Alves, P. M., Mota, J. P. B., & Carrondo, M. J. T. (2015). Improved virus purification processes for vaccines and gene therapy. *Biotechnology and Bioengineering*, *112*(5), 843–857. https://doi.org/10.1002/bit.25545

Newman, M., Chua, P. K., Tang, F.-M., Su, P.-Y., & Shih, C. (2009). Testing an Electrostatic Interaction Hypothesis of Hepatitis B Virus Capsid Stability by Using an In Vitro Capsid Disassembly/Reassembly System. *Journal of Virology*, *83*(20), 10616–10626. https://doi.org/10.1128/JVI.00749-09

Newman, M., Suk, F.-M., Cajimat, M., Chua, P. K., & Shih, C. (2003). Stability and Morphology Comparisons of Self-Assembled Virus-Like Particles from Wild-Type and Mutant Human Hepatitis B Virus Capsid Proteins. *Journal of Virology*, *77*(24), 12950–12960. https://doi.org/10.1128/JVI.77.24.12950-12960.2003

Nfor, B. K., Ahamed, T., van Dedem, G. W., van der Wielen, L. A., van de Sandt, E. J., Eppink, M. H., & Ottens, M. (2008). Design strategies for integrated protein purification processes: challenges, progress and outlook. *Journal of Chemical Technology & Biotechnology*, *83*(2), 124–132. https://doi.org/10.1002/jctb.1815

Ng, M. Y. T., Tan, W. S., Abdullah, N., Ling, T. C., & Tey, B. T. (2008). Effect of different operating modes and biomass concentrations on the recovery of recombinant hepatitis B core antigen from thermal-treated unclarified Escherichia coli feedstock. *Journal of Biotechnology*, *138*(3–4), 74–79. https://doi.org/10.1016/j.jbiotec.2008.08.004

Nilsson, J., de Jong, S., & Smilde, A. K. (1997). Multiway calibration in 3D QSAR. *Journal of Chemometrics*, *11*(6), 511–524. https://doi.org/10.1002/(SICI)1099-128X(199711/12)11:6<511::AID-CEM488>3.0.CO;2-W

Nooraei, S., Bahrulolum, H., Hoseini, Z. S., Katalani, C., Hajizade, A., Easton, A. J., & Ahmadian, G. (2021). Virus-like particles: preparation, immunogenicity and their roles as nanovaccines and drug nanocarriers.

Journal of Nanobiotechnology, *19*(1), 59. https://doi.org/10.1186/s12951-021-00806-7

Opitz, L., Lehmann, S., Reichl, U., & Wolff, M. W. (2009). Sulfated membrane adsorbers for economic pseudo-affinity capture of influenza virus particles. *Biotechnology and Bioengineering*, *103*(6), 1144–1154. https://doi.org/10.1002/bit.22345

Opitz, L., Lehmann, S., Zimmermann, A., Reichl, U., & Wolff, M. W. (2007). Impact of adsorbents selection on capture efficiency of cell culture derived human influenza viruses. *Journal of Biotechnology*, *131*(3), 309–317. https://doi.org/10.1016/j.jbiotec.2007.07.723

Pace, C. N., Grimsley, G. R., & Scholtz, J. M. (2009). Protein Ionizable Groups: pK Values and Their Contribution to Protein Stability and Solubility. *Journal of Biological Chemistry*, *284*(20), 13285–13289. https://doi.org/10.1074/jbc.R800080200

Pace, C. N., Vajdos, F., Fee, L., Grimsley, G., & Gray, T. (1995). How to measure and predict the molar absorption coefficient of a protein. *Protein Science*, *4*(11), 2411–2423. https://doi.org/10.1002/pro.5560041120

Palladini, A., Thrane, S., Janitzek, C. M., Pihl, J., Clemmensen, S. B., de Jongh, W. A., Clausen, T. M., Nicoletti, G., Landuzzi, L., Penichet, M. L., Balboni, T., Ianzano, M. L., Giusti, V., Theander, T. G., Nielsen, M. A., Salanti, A., Lollini, P.-L., Nanni, P., & Sander, A. F. (2018). Virus-like particle display of HER2 induces potent anti-cancer responses. *OncoImmunology*, *7*(3), e1408749. https://doi.org/10.1080/2162402X.2017.1408749

Pattenden, L. K., Middelberg, A. P. J., Niebert, M., & Lipin, D. I. (2005). Towards the preparative and large-scale precision manufacture of virus-like particles. *Trends in Biotechnology*, *23*(10), 523–529. https://doi.org/10.1016/j.tibtech.2005.07.011

Paulen, R., Fikar, M., Foley, G., Kovács, Z., & Czermak, P. (2012). Optimal feeding strategy of diafiltration buffer in batch membrane processes. *Journal of Membrane Science*, *411–412*, 160–172. https://doi.org/10.1016/j.memsci.2012.04.028

Peixoto, C., Ferreira, T. B., Sousa, M. F. Q., Carrondo, M. J. T., & Alves, P. M. (2008). Towards purification of adenoviral vectors based on membrane technology. *Biotechnology Progress*, *24*(6), 1290–1296. https://doi.org/10.1002/btpr.25

Peixoto, C., Sousa, M. F. Q., Silva, A. C., Carrondo, M. J. T., & Alves, P. M. (2007). Downstream processing of triple layered rotavirus like particles.

Journal of Biotechnology, *127*(3), 452–461. https://doi.org/10.1016/j.jbiotec.2006.08.002

Petrovskis, I., Lieknina, I., Dislers, A., Jansons, J., Bogans, J., Akopjana, I., Zakova, J., & Sominskaya, I. (2021). Production of the HBc Protein from Different HBV Genotypes in E. coli. Use of Reassociated HBc VLPs for Packaging of ss- and dsRNA. *Microorganisms*, *9*(2), 283. https://doi.org/10.3390/microorganisms9020283

Pfister, D., Nicoud, L., & Morbidelli, M. (2018). Introduction to Biopharmaceutical Processes. In *Continuous Biopharmaceutical Processes* (pp. 1–26). Cambridge University Press. https://doi.org/10.1017/9781108332897.002

Phillips, A. T., & Signs, M. W. (2004). Desalting, Concentration, and Buffer Exchange by Dialysis and Ultrafiltration. *Current Protocols in Protein Science*, *38*(1), 1–15. https://doi.org/10.1002/0471140864.ps0404s38

Plisko, T. V, Bildyukevich, A. V, Usosky, V. V, & Volkov, V. V. (2016). Influence of the concentration and molecular weight of polyethylene glycol on the structure and permeability of polysulfone hollow fiber membranes. *Petroleum Chemistry*, *56*(4), 321–329. https://doi.org/10.1134/S096554411604006X

Porterfield, J. Z., Dhason, M. S., Loeb, D. D., Nassal, M., Stray, S. J., & Zlotnick, A. (2010). Full-Length Hepatitis B Virus Core Protein Packages Viral and Heterologous RNA with Similarly High Levels of Cooperativity. *Journal of Virology*, *84*(14), 7174–7184. https://doi.org/10.1128/JVI.00586-10

Porterfield, J. Z., & Zlotnick, A. (2010). A simple and general method for determining the protein and nucleic acid content of viruses by UV absorbance. *Virology*, *407*(2), 281–288. https://doi.org/10.1016/j.virol.2010.08.015

Przybycien, T. M. (1998). Protein-protein interactions as a means of purification. *Current Opinion in Biotechnology*, *9*(2), 164–170. https://doi.org/10.1016/S0958-1669(98)80110-9

Pumpens, P., & Grens, E. (2001). HBV core particles as a carrier for B cell/T cell epitopes. *Intervirology*, *44*(2–3), 98–114. https://doi.org/10.1159/000050037

Quezada, C., Estay, H., Cassano, A., Troncoso, E., & Ruby-Figueroa, R. (2021). Prediction of Permeate Flux in Ultrafiltration Processes: A Review of Modeling Approaches. *Membranes*, *11*(5). https://doi.org/10.3390/membranes11050368

Rader, R. A. (2008). (Re)defining biopharmaceutical. *Nature Biotechnology*, *26*(7), 743–751. https://doi.org/10.1038/nbt0708-743

Ragone, R., Colonna, G., Balestrieri, C., Servillo, L., & Irace, G. (1984). Determination of tyrosine exposure in proteins by second-derivative spectroscopy. *Biochemistry*, *23*(8), 1871–1875. https://doi.org/10.1021/bi00303a044

Ramasubramanyan, N., Malmberg, L.-H., & Sternman, M. (2011). *Raman Spectroscopy for Bioprocess Operations* (Patent No. WO2012037430A1).

Rammensee, H.-G., & Singh-Jasuja, H. (2013). HLA ligandome tumor antigen discovery for personalized vaccine approach. *Expert Review of Vaccines*, *12*(10), 1211–1217. https://doi.org/10.1586/14760584.2013.836911

Rathore, A. S., Agarwal, H., Sharma, A. K., Pathak, M., & Muthukumar, S. (2015). Continuous Processing for Production of Biopharmaceuticals. *Preparative Biochemistry and Biotechnology*, *45*(8), 836–849. https://doi.org/10.1080/10826068.2014.985834

Rathore, A. S., Bhambure, R., & Ghare, V. (2010). Process analytical technology (PAT) for biopharmaceutical products. *Analytical and Bioanalytical Chemistry*, *398*(1), 137–154. https://doi.org/10.1016/j.apnum.2011.05.004

Rathore, A. S., & Kapoor, G. (2015). Application of process analytical technology for downstream purification of biotherapeutics. *Journal of Chemical Technology and Biotechnology*, *90*(2), 228–236. https://doi.org/10.1002/jctb.4447

Rathore, A. S., Kateja, N., & Kumar, D. (2018). Process integration and control in continuous bioprocessing. *Current Opinion in Chemical Engineering*, *22*, 18–25. https://doi.org/10.1016/j.coche.2018.08.005

Rathore, A. S., Kumar, V., Arora, A., Lute, S., Brorson, K., & Shukla, A. (2014). Mechanistic modeling of viral filtration. *Journal of Membrane Science*, *458*, 96–103. https://doi.org/10.1016/j.memsci.2014.01.037

Rathore, A. S., & Shirke, A. (2011). Recent developments in membrane-based separations in biotechnology processes: Review. *Preparative Biochemistry and Biotechnology*, *41*(4), 398–421. https://doi.org/10.1080/10826068.2011.613976

Reiser, J. (2000). Production and concentration of pseudotyped HIV-1-based gene transfer vectors. *Gene Therapy*, *7*(11), 910–913. https://doi.org/10.1038/sj.gt.3301188

Reiter, K., Aguilar, P. P., Wetter, V., Steppert, P., Tover, A., & Jungbauer, A. (2019). Separation of virus-like particles and extracellular vesicles by flow-through and heparin affinity chromatography. *Journal of Chromatography A*, *1588*, 77–84. https://doi.org/10.1016/j.chroma.2018.12.035

Ren, Y., Wong, S.-M., & Lim, L.-Y. (2006). In vitro-reassembled plant virus-like particles for loading of polyacids. *Journal of General Virology*, *87*(9), 2749–2754. https://doi.org/10.1099/vir.0.81944-0

Rodgers, K. R., & Chou, R. C. (2016). Therapeutic monoclonal antibodies and derivatives: Historical perspectives and future directions. *Biotechnology Advances*, *34*(6), 1149–1158. https://doi.org/10.1016/j.biotechadv.2016.07.004

Rodrigues, G. A., Shalaev, E., Karami, T. K., Cunningham, J., Slater, N. K. H., & Rivers, H. M. (2019). Pharmaceutical Development of AAV-Based Gene Therapy Products for the Eye. *Pharmaceutical Research*, *36*(2), 29. https://doi.org/10.1007/s11095-018-2554-7

Rodrigues, T., Carvalho, A., Carmo, M., Carrondo, M. J. T., Alves, P. M., & Cruz, P. E. (2007). Scaleable purification process for gene therapy retroviral vectors. *The Journal of Gene Medicine*, *9*(4), 233–243. https://doi.org/10.1002/jgm.1021

Roldão, A., Mellado, M. C. M., Castilho, L. R., Carrondo, M. J. T., & Alves, P. M. (2010). Virus-like particles in vaccine development. *Expert Review of Vaccines*, *9*(10), 1149–1176. https://doi.org/10.1586/erv.10.115

Roldão, A., Mellado, M. C. M., Lima, J. C., Carrondo, M. J. T., Alves, P. M., & Oliveira, R. (2012). On the Effect of Thermodynamic Equilibrium on the Assembly Efficiency of Complex Multi-Layered Virus-Like Particles (VLP): the Case of Rotavirus VLP. *PLoS Computational Biology*, *8*(2), e1002367. https://doi.org/10.1371/journal.pcbi.1002367

Rolinger, L., Rüdt, M., Diehm, J., Chow-Hubbertz, J., Heitmann, M., Schleper, S., & Hubbuch, J. (2020). Multi-attribute PAT for UF/DF of Proteins—Monitoring Concentration, particle sizes, and Buffer Exchange. *Analytical and Bioanalytical Chemistry*, *412*(9), 2123–2136. https://doi.org/10.1007/s00216-019-02318-8

Rolinger, L., Rüdt, M., & Hubbuch, J. (2020a). A critical review of recent trends, and a future perspective of optical spectroscopy as PAT in biopharmaceutical downstream processing. *Analytical and Bioanalytical Chemistry*, *412*(9), 2047–2064. https://doi.org/10.1007/s00216-020-02407-z

Rolinger, L., Rüdt, M., & Hubbuch, J. (2020b). A multisensor approach for improved protein A load phase monitoring by conductivity-based background subtraction of UV spectra. *Biotechnology and Bioengineering*, *October*. https://doi.org/10.1002/bit.27616

Rosenberg, E., Hepbildikler, S., Kuhne, W., & Winter, G. (2009). Ultrafiltration concentration of monoclonal antibody solutions: Development of an optimized method minimizing aggregation. *Journal of Membrane Science*, *342*(1–2), 50–59. https://doi.org/10.1016/j.memsci.2009.06.028

Rothstein, F. (1994). Differential Precipitation of Proteins. In R. G. Harrison (Ed.), *Protein Purification Process Engineering* (Vol. 18, pp. 115–208). Marcel Dekker.

Roy, P., & Noad, R. (2009). *Virus-Like Particles as a Vaccine Delivery System: Myths and Facts* (pp. 145–158). https://doi.org/10.1007/978-1-4419-1132-2_11

Rucker-Pezzini, J., Arnold, L., Hill-Byrne, K., Sharp, T., Avazhanskiy, M., & Forespring, C. (2018). Single pass diafiltration integrated into a fully continuous mAb purification process. *Biotechnology and Bioengineering*, *115*(8), 1949–1957. https://doi.org/10.1002/bit.26708

Rüdt, M., Brestrich, N., Rolinger, L., & Hubbuch, J. (2017). Real-time monitoring and control of the load phase of a protein A capture step. *Biotechnology and Bioengineering*, *114*(2), 368–373. https://doi.org/10.1002/bit.26078

Rüdt, M., Briskot, T., & Hubbuch, J. (2017). Advances in downstream processing of biologics – Spectroscopy: An emerging process analytical technology. *Journal of Chromatography A*, *1490*, 2–9. https://doi.org/10.1016/j.chroma.2016.11.010

Rüdt, M., Vormittag, P., Hillebrandt, N., & Hubbuch, J. (2019). Process monitoring of virus-like particle reassembly by diafiltration with UV/Vis spectroscopy and light scattering. *Biotechnology and Bioengineering*, *116*(6), 1366–1379. https://doi.org/10.1002/bit.26935

Rutgers, T., Gordon, D., Gathoye, A. M., Hollingdale, M., Hockmeyer, W., Rosenberg, M., & Wilde, M. de. (1988). Hepatitis B Surface Antigen as Carrier Matrix for the Repetitive Epitope of the Circumsporozoite Protein of Plasmodium Falciparum. *Nature Biotechnology*, *6*(9), 1065–1070. https://doi.org/10.1038/nbt0988-1065

Rybka, J. D., Mieloch, A. A., Plis, A., Pyrski, M., Pniewski, T., & Giersig, M. (2019). Assembly and characterization of HBc derived virus-like particles

with magnetic core. *Nanomaterials*, *9*(2). https://doi.org/10.3390/nano9020155

Ryś, S., Muca, R., Kołodziej, M., Piątkowski, W., Dürauer, A., Jungbauer, A., & Antos, D. (2015). Design and optimization of protein refolding with crossflow ultrafiltration. *Chemical Engineering Science*, *130*, 290–300. https://doi.org/10.1016/j.ces.2015.03.035

Samandoulgou, I., Hammami, R., Morales Rayas, R., Fliss, I., & Jean, J. (2015). Stability of Secondary and Tertiary Structures of Virus-Like Particles Representing Noroviruses: Effects of pH, Ionic Strength, and Temperature and Implications for Adhesion to Surfaces. *Applied and Environmental Microbiology*, *81*(22), 7680–7686. https://doi.org/10.1128/AEM.01278-15

Sarangapani, P. S., Hudson, S. D., Jones, R. L., Douglas, J. F., & Pathak, J. A. (2015). Critical examination of the colloidal particle model of globular proteins. *Biophysical Journal*, *108*(3), 724–737. https://doi.org/10.1016/j.bpj.2014.11.3483

Schagen, F. H. E., Rademaker, H. J., Rabelink, M. J. W. E., van Ormondt, H., Fallaux, F. J., van der Eb, A. J., & Hoeben, R. C. (2000). Ammonium sulphate precipitation of recombinant adenovirus from culture medium: An easy method to increase the total virus yield. *Gene Therapy*, *7*(18), 1570–1574. https://doi.org/10.1038/sj.gt.3301285

Schärtl, W. (2007). *Light Scattering from Polymer Solutions and Nanoparticle Dispersions*. Springer Berlin Heidelberg. https://doi.org/10.1007/978-3-540-71951-9

Schellekens, H. (2002). Bioequivalence and the immunogenicity of biopharmaceuticals. *Nature Reviews Drug Discovery*, *1*(6), 457–462. https://doi.org/10.1038/nrd818

Schlaeppi, J.-M., Henke, M., Mahnke, M., Hartmann, S., Schmitz, R., Pouliquen, Y., Kerins, B., Weber, E., Kolbinger, F., & Kocher, H. P. (2006). A semi-automated large-scale process for the production of recombinant tagged proteins in the Baculovirus expression system. *Protein Expression and Purification*, *50*(2), 185–195. https://doi.org/10.1016/j.pep.2006.06.021

Schügerl, K., & Hubbuch, J. (2005). Integrated bioprocesses. *Current Opinion in Microbiology*, *8*(3), 294–300. https://doi.org/10.1016/j.mib.2005.01.002

Schumacher, J., Bacic, T., Staritzbichler, R., Daneschdar, M., Klamp, T., Arnold, P., Jägle, S., Türeci, Ö., Markl, J., & Sahin, U. (2018). Enhanced stability of a chimeric hepatitis B core antigen virus-like-particle (HBcAg-

VLP) by a C-terminal linker-hexahistidine-peptide. *Journal of Nanobiotechnology*, *16*(1), 39. https://doi.org/10.1186/s12951-018-0363-0

Sedlik, C., Saron, M. F., Sarraseca, J., Casal, I., & Leclerc, C. (1997). Recombinant parvovirus-like particles as an antigen carrier: A novel nonreplicative exogenous antigen to elicit protective antiviral cytotoxic T cells. *Proceedings of the National Academy of Sciences*, *94*(14), 7503–7508. https://doi.org/10.1073/pnas.94.14.7503

Selzer, L., & Zlotnick, A. (2017). *Assembly and Release of Hepatitis B Virus*. 1–18. https://doi.org/10.1101/cshperspect.a021394

Shan, W., Zhang, D., Wu, Y., Lv, X., Hu, B., Zhou, X., Ye, S., Bi, S., Ren, L., & Zhang, X. (2018). Modularized peptides modified HBc virus-like particles for encapsulation and tumor-targeted delivery of doxorubicin. *Nanomedicine: Nanotechnology, Biology and Medicine*, *14*(3), 725–734. https://doi.org/10.1016/j.nano.2017.12.002

Shi, L., Sanyal, G., Ni, A., Luo, Z., Doshna, S., Wang, B., Graham, T. L., Wang, N., & Volkin, D. B. (2005). Stabilization of human papillomavirus virus-like particles by non-ionic surfactants. *Journal of Pharmaceutical Sciences*, *94*(7), 1538–1551. https://doi.org/10.1002/jps.20377

Shire, S. J. (2009). Formulation and manufacturability of biologics. *Current Opinion in Biotechnology*, *20*(6), 708–714. https://doi.org/10.1016/j.copbio.2009.10.006

Shire, S. J., Shahrokh, Z., & Liu, J. (2004). Challenges in the development of high protein concentration formulations. *Journal of Pharmaceutical Sciences*, *93*(6), 1390–1402. https://doi.org/10.1002/jps.20079

Shukla, A. A., Rameez, S., Wolfe, L. S., & Oien, N. (2018). High-Throughput Process Development for Biopharmaceuticals. In B. Kiss, U. Gottschalk, & M. Pohlscheidt (Eds.), *New Bioprocessing Strategies: Development and Manufacturing of Recombinant Antibodies and Proteins* (pp. 401–441). Springer International Publishing. https://doi.org/10.1007/10_2017_20

Shukla, A. A., Wolfe, L. S., Mostafa, S. S., & Norman, C. (2017). Evolving trends in mAb production processes. *Bioengineering & Translational Medicine*, *2*(1), 58–69. https://doi.org/10.1002/btm2.10061

Sim, S. L., He, T., Tscheliessnig, A., Mueller, M., Tan, R. B. H., & Jungbauer, A. (2012). Protein precipitation by polyethylene glycol: A generalized model based on hydrodynamic radius. *Journal of Biotechnology*, *157*(2), 315–319. https://doi.org/10.1016/j.jbiotec.2011.09.028

Singh, S., & Zlotnick, A. (2003). Observed Hysteresis of Virus Capsid Disassembly Is Implicit in Kinetic Models of Assembly. *Journal of Biological Chemistry*, *278*(20), 18249–18255. https://doi.org/10.1074/jbc.M211408200

Smiatek, J., Jung, A., & Bluhmki, E. (2020). Towards a Digital Bioprocess Replica: Computational Approaches in Biopharmaceutical Development and Manufacturing. *Trends in Biotechnology*, *38*(10), 1141–1153. https://doi.org/10.1016/j.tibtech.2020.05.008

Somasundaram, B., Chang, C., Fan, Y. Y., Lim, P.-Y., Cardosa, J., & Lua, L. (2016). Characterizing Enterovirus 71 and Coxsackievirus A16 virus-like particles production in insect cells. *Methods*, *95*, 38–45. https://doi.org/10.1016/j.ymeth.2015.09.023

Staby, A., Ahuja, S., & Rathore, A. S. (2017). Model-Based Preparative Chromatography Process Development in the QbD Paradigm. In A. Staby, S. Ahuja, & A. S. Rathore (Eds.), *Preparative Chromatography for Separation of Proteins* (pp. 1–10). John Wiley & Sons, Inc. https://doi.org/10.1002/9781119031116.ch1

Steppert, P., Mosor, M., Stanek, L., Burgstaller, D., Palmberger, D., Preinsperger, S., Pereira Aguilar, P., Müllner, M., Csar, P., & Jungbauer, A. (2022). A scalable, integrated downstream process for production of a recombinant measles virus-vectored vaccine. *Vaccine*, *40*(9), 1323–1333. https://doi.org/10.1016/j.vaccine.2022.01.004

Stetefeld, J., McKenna, S. A., & Patel, T. R. (2016). Dynamic light scattering: a practical guide and applications in biomedical sciences. *Biophysical Reviews*, *8*(4), 409–427. https://doi.org/10.1007/s12551-016-0218-6

Stoner, M. R., Fischer, N., Nixon, L., Buckel, S., Benke, M., Austin, F., Randolph, T. W., & Kendrick, B. S. (2004). Protein-solute interactions affect the outcome of ultrafiltration/ diafiltration operations. *Journal of Pharmaceutical Sciences*, *93*(9), 2332–2342. https://doi.org/10.1002/jps.20145

Stradner, A., & Schurtenberger, P. (2020). Potential and limits of a colloid approach to protein solutions. *Soft Matter*, *16*(2), 307–323. https://doi.org/10.1039/c9sm01953g

Strods, A., Ose, V., Bogans, J., Cielens, I., Kalnins, G., Radovica, I., Kazaks, A., Pumpens, P., & Renhofa, R. (2015). Preparation by alkaline treatment and detailed characterisation of empty hepatitis B virus core particles for vaccine and gene therapy applications. *Scientific Reports*, *5*(1), 11639. https://doi.org/10.1038/srep11639

Subramani, A., Kim, S., & Hoek, E. (2006). Pressure, flow, and concentration profiles in open and spacer-filled membrane channels. *Journal of Membrane Science*, *277*(1–2), 7–17. https://doi.org/10.1016/j.memsci.2005.10.021

Suffian, I. F. B. M., & Al-Jamal, K. T. (2022). Bioengineering of virus-like particles as dynamic nanocarriers for in vivo delivery and targeting to solid tumours. *Advanced Drug Delivery Reviews*, *180*. https://doi.org/10.1016/j.addr.2021.114030

Sundaram, S., Auriemma, M., Howard, G., Brandwein, H., & Leo, F. (1999). Application of membrane filtration for removal of diminutive bioburden organisms in pharmaceutical products and processes. *PDA Journal of Pharmaceutical Science and Technology*, *53*(4), 186–201. http://www.ncbi.nlm.nih.gov/pubmed/10754712

Sviben, D., Forčić, D., Kurtović, T., Halassy, B., & Brgles, M. (2016). Stability, biophysical properties and effect of ultracentrifugation and diafiltration on measles virus and mumps virus. *Archives of Virology*, *161*(6), 1455–1467. https://doi.org/10.1007/s00705-016-2801-3

Swinehart, D. F. (1962). The Beer-Lambert Law. *Journal of Chemical Education*, *39*(7), 333. https://doi.org/10.1021/ed039p333

Tan, T. K., Rijal, P., Rahikainen, R., Keeble, A. H., Schimanski, L., Hussain, S., Harvey, R., Hayes, J. W. P., Edwards, J. C., McLean, R. K., Martini, V., Pedrera, M., Thakur, N., Conceicao, C., Dietrich, I., Shelton, H., Ludi, A., Wilsden, G., Browning, C., … Townsend, A. R. (2021). A COVID-19 vaccine candidate using SpyCatcher multimerization of the SARS-CoV-2 spike protein receptor-binding domain induces potent neutralising antibody responses. *Nature Communications*, *12*(1), 542. https://doi.org/10.1038/s41467-020-20654-7

Teeters, M., Bezila, D., Benner, T., Alfonso, P., & Alred, P. (2011). Predicting diafiltration solution compositions for final ultrafiltration/diafiltration steps of monoclonal antibodies. *Biotechnology and Bioengineering*, *108*(6), 1338–1346. https://doi.org/10.1002/bit.23067

Thomas, J. C. (1987). The determination of log normal particle size distributions by dynamic light scattering. *Journal of Colloid and Interface Science*, *117*(1), 187–192. https://doi.org/10.1016/0021-9797(87)90182-2

Timasheff, S. N., & Arakawa, T. (1988). Mechanism of protein precipitation and stabilization by co-solvents. *Journal of Crystal Growth*, *90*(1–3), 39–46. https://doi.org/10.1016/0022-0248(88)90296-5

Titchener-Hooker, N. J., Dunnill, P., & Hoare, M. (2008). Micro biochemical engineering to accelerate the design of industrial-scale downstream processes for biopharmaceutical proteins. *Biotechnology and Bioengineering*, *100*(3), 473–487. https://doi.org/10.1002/bit.21788

Tomono, T., Hirai, Y., Okada, H., Adachi, K., Ishii, A., Shimada, T., Onodera, M., Tamaoka, A., & Okada, T. (2016). Ultracentrifugation-free chromatography-mediated large-scale purification of recombinant adeno-associated virus serotype 1 (rAAV1). *Molecular Therapy - Methods & Clinical Development*, *3*(December 2015), 15058. https://doi.org/10.1038/mtm.2015.58

Tomono, T., Hirai, Y., Okada, H., Miyagawa, Y., Adachi, K., Sakamoto, S., Kawano, Y., Chono, H., Mineno, J., Ishii, A., Shimada, T., Onodera, M., Tamaoka, A., & Okada, T. (2018). Highly Efficient Ultracentrifugation-free Chromatographic Purification of Recombinant AAV Serotype 9. *Molecular Therapy - Methods & Clinical Development*, *11*(December), 180–190. https://doi.org/10.1016/j.omtm.2018.10.015

Tsoka, S., Ciniawskyj, O. C., Thomas, O. R. T., Titchener-Hooker, N. J., & Hoare, M. (2000). Selective Flocculation and Precipitation for the Improvement of Virus-Like Particle Recovery from Yeast Homogenate. *Biotechnology Progress*, *16*(4), 661–667. https://doi.org/10.1021/bp0000407

U.S. Food and Drug Administration. (2004). *PAT - A Framework for Innovative Pharmaceutical Development, Manufacuring, and Quality Assurance*. Guidance for Industry. https://www.fda.gov/media/71012/download

Valkama, A. J., Oruetxebarria, I., Lipponen, E. M., Leinonen, H. M., Käyhty, P., Hynynen, H., Turkki, V., Malinen, J., Miinalainen, T., Heikura, T., Parker, N. R., Ylä-Herttuala, S., & Lesch, H. P. (2020). Development of Large-Scale Downstream Processing for Lentiviral Vectors. *Molecular Therapy - Methods & Clinical Development*, *17*(June), 717–730. https://doi.org/10.1016/j.omtm.2020.03.025

van Reis, R., Gadam, S., Frautschy, L. N., Orlando, S., Goodrich, E. M., Saksena, S., Kuriyel, R., Simpson, C. M., Pearl, S., & Zydney, A. L. (1997). High performance tangential flow filtration. *Biotechnology and Bioengineering*, *56*(1), 71–82. https://doi.org/10.1002/(SICI)1097-0290(19971005)56:1<71::AID-BIT8>3.0.CO;2-S

van Reis, R., Goodrich, E. M., Yson, C. L., Frautschy, L. N., Dzengeleski, S., & Lutz, H. (1997). Linear scale ultrafiltration. *Biotechnology and Bioengineering*, *55*(5), 737–746. https://doi.org/10.1002/(SICI)1097-0290(19970905)55:5<737::AID-BIT4>3.0.CO;2-C

van Reis, R., Goodrich, E. M., Yson, C. L., Frautschy, L. N., Whiteley, R., & Zydney, A. L. (1997). Constant Cwall ultrafiltration process control. *Journal of Membrane Science*, *130*(1–2), 123–140. https://doi.org/10.1016/S0376-7388(97)00012-4

van Reis, R., Leonard, L. C., Hsu, C. C., & Builder, S. E. (1991). Industrial scale harvest of proteins from mammalian cell culture by tangential flow filtration. *Biotechnology and Bioengineering*, *38*(4), 413–422. https://doi.org/10.1002/bit.260380411

van Reis, R., & Saksena, S. (1997). Optimization diagram for membrane separations. *Journal of Membrane Science*, *129*(1), 19–29. https://doi.org/10.1016/S0376-7388(96)00319-5

van Reis, R., & Zydney, A. (2001). Membrane separations in biotechnology. *Current Opinion in Biotechnology*, *12*(2), 208–211. https://doi.org/10.1016/S0958-1669(00)00201-9

van Reis, R., & Zydney, A. (2007). Bioprocess membrane technology. *Journal of Membrane Science*, *297*(1–2), 16–50. https://doi.org/10.1016/j.memsci.2007.02.045

van Reis, R., & Zydney, A. L. (2010). Protein Ultrafiltration. In M. C. Flickinger (Ed.), *Encyclopedia of Industrial Biotechnology* (pp. 1–20). John Wiley & Sons, Inc. https://doi.org/10.1002/9780470054581.eib515

van Rosmalen, M. G. M., Li, C., Zlotnick, A., Wuite, G. J. L., & Roos, W. H. (2018). Effect of dsDNA on the Assembly Pathway and Mechanical Strength of SV40 VP1 Virus-like Particles. *Biophysical Journal*, *115*(9), 1656–1665. https://doi.org/10.1016/j.bpj.2018.07.044

Venkiteshwaran, A., Heider, P., Teysseyre, L., & Belfort, G. (2008). Selective precipitation-assisted recovery of immunoglobulins from bovine serum using controlled-fouling crossflow membrane microfiltration. *Biotechnology and Bioengineering*, *101*(5), 957–966. https://doi.org/10.1002/bit.21964

Vicente, T., Mota, J. P. B., Peixoto, C., Alves, P. M., & Carrondo, M. J. T. (2011). Rational design and optimization of downstream processes of virus particles for biopharmaceutical applications: Current advances. *Biotechnology Advances*, *29*(6), 869–878. https://doi.org/10.1016/j.biotechadv.2011.07.004

Vicente, T., Roldão, A., Peixoto, C., Carrondo, M. J. T., & Alves, P. M. (2011). Large-scale production and purification of VLP-based vaccines. *Journal of Invertebrate Pathology*, *107*(SUPPL.), S42–S48. https://doi.org/10.1016/j.jip.2011.05.004

Vincentelli, R., Canaan, S., Campanacci, V., Valencia, C., Maurin, D., Frassinetti, F., Scappucini-Calvo, L., Bourne, Y., Cambillau, C., & Bignon, C. (2009). High-throughput automated refolding screening of inclusion bodies. *Protein Science*, *13*(10), 2782–2792. https://doi.org/10.1110/ps.04806004

Vogel, J. H., Anspach, B., Kroner, K. H., Piret, J. M., & Haynes, C. A. (2002). Controlled shear affinity filtration (CSAF): A new technology for integration of cell separation and protein isolation from mammalian cell cultures. *Biotechnology and Bioengineering*, *78*(7), 806–814. https://doi.org/10.1002/bit.10262

von Stosch, M., Oliveira, R., Peres, J., & Feyo de Azevedo, S. (2014). Hybrid semi-parametric modeling in process systems engineering: Past, present and future. *Computers & Chemical Engineering*, *60*, 86–101. https://doi.org/10.1016/j.compchemeng.2013.08.008

Vormittag, P., Klamp, T., & Hubbuch, J. (2020a). Ensembles of Hydrophobicity Scales as Potent Classifiers for Chimeric Virus-Like Particle Solubility – An Amino Acid Sequence-Based Machine Learning Approach. *Frontiers in Bioengineering and Biotechnology*, *8*, 395:1-15. https://doi.org/10.3389/fbioe.2020.00395

Vormittag, P., Klamp, T., & Hubbuch, J. (2020b). Optimization of a Soft Ensemble Vote Classifier for the Prediction of Chimeric Virus-Like Particle Solubility and Other Biophysical Properties. *Frontiers in Bioengineering and Biotechnology*, *8*(July), 1–17. https://doi.org/10.3389/fbioe.2020.00881

Wagner, J. M., Pajerowski, J. D., Daniels, C. L., McHugh, P. M., Flynn, J. A., Balliet, J. W., Casimiro, D. R., & Subramanian, S. (2014). Enhanced Production of Chikungunya Virus-Like Particles Using a High-pH Adapted Spodoptera frugiperda Insect Cell Line. *PLoS ONE*, *9*(4), e94401. https://doi.org/10.1371/journal.pone.0094401

Walsh, G. (1999). Biopharmaceuticals, an overview. In G. Walsh & B. Murphy (Eds.), *Biopharmaceuticals, an Industrial Perspective* (pp. 1–34). Springer Netherlands. https://doi.org/10.1007/978-94-017-0926-2_1

Walsh, G. (2002). Biopharmaceuticals and biotechnology medicines: an issue of nomenclature. *European Journal of Pharmaceutical Sciences*, *15*(2), 135–138. https://doi.org/10.1016/S0928-0987(01)00222-6

Walsh, G. (2010). Biopharmaceutical benchmarks 2010. *Nature Biotechnology*, *28*(9), 917–924. https://doi.org/10.1038/nbt0910-917

Walsh, G. (2013). Pharmaceuticals, biologics and biopharmaceuticals. In G. Walsh (Ed.), *Biopharmaceuticals: Biochemistry and Biotechnology* (2nd ed.). John Wiley & Sons, Ltd.

Walsh, G. (2018). Biopharmaceutical benchmarks 2018. *Nature Biotechnology*, *36*(12), 1136–1145. https://doi.org/10.1038/nbt.4305

Wang, W., Singh, S., Zeng, D. L., King, K., & Nema, S. (2007). Antibody Structure, Instability, and Formulation. *Journal of Pharmaceutical Sciences*, *96*(1), 1–26. https://doi.org/10.1002/jps.20727

Warikoo, V., Godawat, R., Brower, K., Jain, S., Cummings, D., Simons, E., Johnson, T., Walther, J., Yu, M., Wright, B., Mclarty, J., Karey, K. P., Hwang, C., Zhou, W., Riske, F., & Konstantinov, K. (2012). Integrated continuous production of recombinant therapeutic proteins. *Biotechnology and Bioengineering*, *109*(12), 3018–3029. https://doi.org/10.1002/bit.24584

Wasalathanthri, D. P., Feroz, H., Puri, N., Hung, J., Lane, G., Holstein, M., Chemmalil, L., Both, D., Ghose, S., Ding, J., & Li, Z. J. (2020). Real-time monitoring of quality attributes by in-line Fourier transform infrared spectroscopic sensors at ultrafiltration and diafiltration of bioprocess. *Biotechnology and Bioengineering*, *117*(12), 3766–3774. https://doi.org/10.1002/bit.27532

Weigel, T., Solomaier, T., Peuker, A., Pathapati, T., Wolff, M. W., & Reichl, U. (2014). A flow-through chromatography process for influenza A and B virus purification. *Journal of Virological Methods*, *207*, 45–53. https://doi.org/10.1016/j.jviromet.2014.06.019

Weigel, T., Solomaier, T., Wehmeyer, S., Peuker, A., Wolff, M. W., & Reichl, U. (2016). A membrane-based purification process for cell culture-derived influenza A virus. *Journal of Biotechnology*, *220*, 12–20. https://doi.org/10.1016/j.jbiotec.2015.12.022

Wenger, M. D., DePhillips, P., Price, C. E., & Bracewell, D. G. (2007). An automated microscale chromatographic purification of virus-like particles as a strategy for process development. *Biotechnology and Applied Biochemistry*, *47*(2), 131. https://doi.org/10.1042/BA20060240

Wennerström, H., Jönsson, B., & Linse, P. (1982). The cell model for polyelectrolyte systems. Exact statistical mechanical relations, Monte Carlo simulations, and the Poisson–Boltzmann approximation. *The Journal of Chemical Physics*, *76*(9), 4665–4670. https://doi.org/10.1063/1.443547

Westall, J., & Hohl, H. (1980). A comparison of electrostatic models for the oxide/solution interface. *Advances in Colloid and Interface Science*, *12*(4), 265–294. https://doi.org/10.1016/0001-8686(80)80012-1

West, J. M., Feroz, H., Xu, X., Puri, N., Holstein, M., Ghose, S., Ding, J., & Li, Z. J. (2021). Process analytical technology for on-line monitoring of quality attributes during single-use ultrafiltration/diafiltration. *Biotechnology and Bioengineering*, *118*(6), 2293–2300. https://doi.org/10.1002/bit.27741

Wetzel, D., Rolf, T., Suckow, M., Kranz, A., Barbian, A., Chan, J.-A., Leitsch, J., Weniger, M., Jenzelewski, V., Kouskousis, B., Palmer, C., Beeson, J. G., Schembecker, G., Merz, J., & Piontek, M. (2018). Establishment of a yeast-based VLP platform for antigen presentation. *Microbial Cell Factories*, *17*(1), 17. https://doi.org/10.1186/s12934-018-0868-0

Whitacre, D. C., Lee, B. O., & Milich, D. R. (2009). Use of hepadnavirus core proteins as vaccine platforms. *Expert Review of Vaccines*, *8*(11), 1565–1573. https://doi.org/10.1586/erv.09.121

Wickramasinghe, S. R., Kalbfuß, B., Zimmermann, A., Thom, V., & Reichl, U. (2005). Tangential flow microfiltration and ultrafiltration for human influenza A virus concentration and purification. *Biotechnology and Bioengineering*, *92*(2), 199–208. https://doi.org/10.1002/bit.20599

Wijmans, J. G., Nakao, S., & Smolders, C. A. (1984). Flux limitation in ultrafiltration: Osmotic pressure model and gel layer model. *Journal of Membrane Science*, *20*(2), 115–124. https://doi.org/10.1016/S0376-7388(00)81327-7

Wilfinger, W. W., Mackey, K., & Chomczynski, P. (1997). Effect of pH and Ionic Strength on the Spectrophotometric Assessment of Nucleic Acid Purity. *BioTechniques*, *22*(3), 474–481. https://doi.org/10.2144/97223st01

Wingfield, P. T. (1998). Protein Precipitation Using Ammonium Sulfate. In *Current Protocols in Protein Science* (Vol. 3, p. A.3F.1-A.3F.8). John Wiley & Sons, Inc. https://doi.org/10.1002/0471140864.psa03fs13

Wingfield, P. T., Stahl, S. J., Williams, R. W., & Steven, A. C. (1995). Hepatitis Core Antigen Produced in Escherichia coli: Subunit Composition, Conformation Analysis, and in Vitro Capsid Assembly. *Biochemistry*, *34*(15), 4919–4932. https://doi.org/10.1021/bi00015a003

Wise, J. (2022). Covid-19: UK approves Novavax's protein based vaccine. *BMJ*, *376*, o309. https://doi.org/10.1136/bmj.o309

Wold, S., Sjöström, M., & Eriksson, L. (2001). PLS-regression: a basic tool of chemometrics. *Chemometrics and Intelligent Laboratory Systems*, *58*(2), 109–130. https://doi.org/10.1016/S0169-7439(01)00155-1

Wold, S., Trygg, J., Berglund, A., & Antti, H. (2001). Some recent developments in PLS modeling. *Chemometrics and Intelligent Laboratory Systems*, *58*(2), 131–150. https://doi.org/10.1016/S0169-7439(01)00156-3

Wolff, M. W., & Reichl, U. (2011). Downstream processing of cell culture-derived virus particles. *Expert Review of Vaccines*, *10*(10), 1451–1475. https://doi.org/10.1586/erv.11.111

World Health Organization. (2021). *Full Evidence Report on the RTS,S/AS01 Malaria Vaccine*.

Wright, A., & Morrison, S. L. (1997). Effect of glycosylation on antibody function: implications for genetic engineering. *Trends in Biotechnology*, *15*(1), 26–32. https://doi.org/10.1016/S0167-7799(96)10062-7

Wyatt, P. J. (1993). Mean square radius of molecules and secondary instrumental broadening. *Journal of Chromatography A*, *648*(1), 27–32. https://doi.org/10.1016/0021-9673(93)83285-Z

Wynne, S. A., Crowther, R. A., & Leslie, A. G. W. (1999). The Crystal Structure of the Human Hepatitis B Virus Capsid. *Molecular Cell*, *3*(6), 771–780. https://doi.org/10.1016/S1097-2765(01)80009-5

Yang, Y., Shi, W., Abiona, O. M., Nazzari, A., Olia, A. S., Ou, L., Phung, E., Stephens, T., Tsybovsky, Y., Verardi, R., Wang, S., Werner, A., Yap, C., Ambrozak, D., Bylund, T., Liu, T., Nguyen, R., Wang, L., Zhang, B., … Kwong, P. D. (2021). Newcastle Disease Virus-Like Particles Displaying Prefusion-Stabilized SARS-CoV-2 Spikes Elicit Potent Neutralizing Responses. *Vaccines*, *9*(2), 73. https://doi.org/10.3390/vaccines9020073

Yap, W. B., Tey, B. T., Alitheen, N. B. M., & Tan, W. S. (2010). Purification of His-tagged hepatitis B core antigen from unclarified bacterial homogenate using immobilized metal affinity-expanded bed adsorption chromatography. *Journal of Chromatography A*, *1217*(21), 3473–3480. https://doi.org/10.1016/j.chroma.2010.03.012

Ying, W., Levons, J. K., Carney, A., Gandhi, R., Vydra, V., & Rubin, A. E. (2016). Semiautomated Sample Preparation for Protein Stability and Formulation Screening via Buffer Exchange. *SLAS Technology*, *21*(3), 378–386. https://doi.org/10.1177/2211068215585484

Yuan, W., & Parrish, C. R. (2001). Canine Parvovirus Capsid Assembly and Differences in Mammalian and Insect Cells. *Virology*, *279*(2), 546–557. https://doi.org/10.1006/viro.2000.0734

Zahavi, D., & Weiner, L. (2020). Monoclonal Antibodies in Cancer Therapy. *Antibodies*, *9*(3), 34. https://doi.org/10.3390/antib9030034

Zahin, M., Joh, J., Khanal, S., Husk, A., Mason, H., Warzecha, H., Ghim, S. J., Miller, D. M., Matoba, N., & Jenson, A. B. (2016). Scalable production of HPV16 L1 protein and VLPs from tobacco leaves. *PLoS ONE*, *11*(8), 1–16. https://doi.org/10.1371/journal.pone.0160995

Zeltins, A. (2013). Construction and characterization of virus-like particles: A review. *Molecular Biotechnology*, *53*(1), 92–107. https://doi.org/10.1007/s12033-012-9598-4

Zha, L., Chang, X., Zhao, H., Mohsen, M. O., Hong, L., Zhou, Y., Chen, H., Liu, X., Zhang, J., Li, D., Wu, K., Martina, B., Wang, J., Vogel, M., & Bachmann, M. F. (2021). Development of a Vaccine against SARS-CoV-2 Based on the Receptor-Binding Domain Displayed on Virus-Like Particles. *Vaccines*, *9*(4), 395. https://doi.org/10.3390/vaccines9040395

Zhang, J., Conley, L., Pieracci, J., & Ghose, S. (2017). Pool-less processing to streamline downstream purification of monoclonal antibodies. *Engineering in Life Sciences*, *17*(2), 117–124. https://doi.org/10.1002/elsc.201600104

Zhang, Y., Liu, Y., Zhang, B., Yin, S., Li, X., Zhao, D., Wang, W., Bi, J., & Su, Z. (2021). In vitro preparation of uniform and nucleic acid free hepatitis B core particles through an optimized disassembly-purification-reassembly process. *Protein Expression and Purification*, *178*, 105747. https://doi.org/10.1016/j.pep.2020.105747

Zhang, Y., Song, S., Liu, C., Wang, Y., Xian, X., He, Y., Wang, J., Liu, F., & Sun, S. (2007). Generation of chimeric HBc proteins with epitopes in E.coli: Formation of virus-like particles and a potent inducer of antigen-specific cytotoxic immune response and anti-tumor effect in vivo. *Cellular Immunology*, *247*(1), 18–27. https://doi.org/10.1016/j.cellimm.2007.07.003

Zhao, D., Liu, Y., Wang, Y., Li, X., Wang, Q., & Su, Z. (2014). Membrane combined with hydrophilic macromolecules enhances protein refolding at high concentration. *Process Biochemistry*, *49*(7), 1129–1134. https://doi.org/10.1016/j.procbio.2014.03.010

Zhao, D., Sun, B., Jiang, H., Sun, S., Kong, F. T., Ma, Y., Jiang, L., Bai, L., Chen, X., Yang, P., Liu, C., Xu, Y., Su, W., Kong, W., Xu, F., & Jiang, C. (2015). Enterovirus71 virus-like particles produced from insect cells and purified

by multistep chromatography elicit strong humoral immune responses in mice. *Journal of Applied Microbiology*, *119*(4), 1196–1205. https://doi.org/10.1111/jam.12922

Zhao, Q., Allen, M. J., Wang, Y., Wang, B., Wang, N., Shi, L., & Sitrin, R. D. (2012). Disassembly and reassembly improves morphology and thermal stability of human papillomavirus type 16 virus-like particles. *Nanomedicine: Nanotechnology, Biology, and Medicine*, *8*(7), 1182–1189. https://doi.org/10.1016/j.nano.2012.01.007

Zhao, Q., Modis, Y., High, K., Towne, V., Meng, Y., Wang, Y., Alexandroff, J., Brown, M., Carragher, B., Potter, C. S., Abraham, D., Wohlpart, D., Kosinski, M., Washabaugh, M. W., & Sitrin, R. D. (2012). Disassembly and reassembly of human papillomavirus virus-like particles produces more virion-like antibody reactivity. *Virology Journal*, *9*(1), 52. https://doi.org/10.1186/1743-422X-9-52

Zlotnick, A., Ceres, P., Singh, S., & Johnson, J. M. (2002). A Small Molecule Inhibits and Misdirects Assembly of Hepatitis B Virus Capsids. *Journal of Virology*, *76*(10), 4848–4854. https://doi.org/10.1128/JVI.76.10.4848-4854.2002

Zlotnick, A., Cheng, N., Conway, J. F., Booy, F. P., Steven, A. C., Stahl, S. J., & Wingfield, P. T. (1996). Dimorphism of Hepatitis B Virus Capsids Is Strongly Influenced by the C-Terminus of the Capsid Protein. *Biochemistry*, *35*(23), 7412–7421. https://doi.org/10.1021/bi9604800

Zlotnick, A., Cheng, N., Stahl, S. J., Conway, J. F., Steven, A. C., & Wingfield, P. T. (1997). Localization of the C terminus of the assembly domain of hepatitis B virus capsid protein: Implications for morphogenesis and organization of encapsidated RNA. *Proceedings of the National Academy of Sciences*, *94*(18), 9556–9561. https://doi.org/10.1073/pnas.94.18.9556

Zobel-Roos, S., Mouellef, M., Siemers, C., & Strube, J. (2017). Process Analytical Approach towards Quality Controlled Process Automation for the Downstream of Protein Mixtures by Inline Concentration Measurements Based on Ultraviolet/Visible Light (UV/VIS) Spectral Analysis. *Antibodies*, *6*(4), 24. https://doi.org/10.3390/antib6040024

Zydney, A. L. (1997). Stagnant film model for concentration polarization in membrane systems. *Journal of Membrane Science*, *130*(1–2), 275–281. https://doi.org/10.1016/S0376-7388(97)00006-9

Zydney, A. L. (2020). New developments in membranes for bioprocessing – A review. *Journal of Membrane Science*, 118804. https://doi.org/10.1016/j.memsci.2020.118804

Abbreviations

A260/A280	absorbance ratio 260 nm to 280 nm
AEX	anion exchange chromatography
API	active pharmaceutical ingredient
CFF	cross-flow filtration
CGE	capillary gel electrophoresis
CV	cross validation
DAD	diode array detector
DF	diafiltration
DisA-oC	disassembly on column
DisA-TS	disassembly time series
DLS	dynamic light scattering
DNA	deoxyribonucleic acid
DSP	downstream processing
DTT	dithiothreitol
DV	diafiltration volumes
E. coli	*Escherichia coli*
Fab	fragment antigen binding
HBcAg	hepatitis B core antigen
HCP	host cell protein
HMWS	high-molecular-weight species
HPLC	high-performance liquid chromatography
HPV	human papillomavirus
HT	high-throughput
HTS	high-throughput screenings
LMWS	low-molecular-weight species
mAb	monoclonal antibody
MALS	multi angle light scattering
mmSEC	multimodal size-exclusion chromatography
MWCO	molecular weight cut-off
nLV	number of latent variables
OLS	ordinary least squares
P&ID	piping and instrumentation diagram
PAT	process analytical technology
PB	Poisson-Boltzmann
PEG	polyethylene glycol
PLS	partial least squares
PRESS	predictive residual sum of squares
QbD	quality by design
QELS	quasi-elastic light scattering

RMSE	root mean square error
RMSECV	root mean square error of cross validation
RMSEP	root mean square error of prediction
RT	room temperature
SEC	size-exclusion chromatography
SLS	static light scattering
SXC	steric exclusion chromatography
TEM	transmission electron microscopy
TFF	tangential flow filtration
TMP	transmembrane pressure
UF	ultrafiltration
UV	ultraviolet light
UV/Vis	ultraviolet and visible light
VLP	virus-like particle
VP	virus particle
WS	Wigner-Seitz
z-average	z-average hydrodynamic particle diameter (or radius)

Appendix A: Supplementary material of Chapter 3

S3.1 Chimeric HBcAg expression and cell lysis

The chimeric HBcAg construct was modified with a foreign epitope in the major immunodominant region and C-terminally truncated as previously described (Klamp et al., 2011; Schumacher et al., 2018). HBcAg protein was recombinantly overexpressed in *E. coli* BL21 DE3 (New England Biolabs, Ipswitch, US-MA). Expression was induced using a TB-based auto-induction medium developed by BioNTech Protein Therapeutics GmbH. Cells were cultured at 180 rpm and 37 °C for 7 h in a MaxQ 6000 Shaker (Thermo Scientific, Marietta, US-OH) with 250 mL medium in 1 L baffled glass shake flasks (Schott AG, Mainz, DE) up to an OD_{600} of 6. Cells were harvested by centrifugation at 4 °C at 3220 rcf for 30 min in an Eppendorf Centrifuge 5810 R (Eppendorf, Hamburg, DE), washing the pellet with phosphate-buffered saline at pH 7.4, and centrifugation at 4 °C at 17387 rcf for 20 min. Pellets were generated from 500 mL of culture volume and frozen at -30 °C for storage. For lysis, the pellet was thawed and resuspended in 20 mL of lysis buffer. Ultrasonic disruption was performed with a Digital Sonifier 450 (Branson Ultrasonic Corporation, Danbury, US-CT) at 80% amplitude for 2×40 s with a 3 min break. During this procedure, the sample was cooled in a stirred ice bath. Cell debris were separated from the supernatant by centrifugation at 4 °C and 17387 rcf for 20 min and filtration through a glass fiber and 0.45 µm cellulose acetate syringe filter (both Sartorius Stedim Biotech GmbH, Göttingen, DE). The lysate was stored at -30 °C. Prior to precipitation and re-dissolution experiments and processes, lysate was thawed and filtered again through a 0.45 µm syringe filter.

S3.2 CFF set-up and temporal alignment

In pre-experiments, flow rates for the CFF-DF steps were tested. Constraints were the linear range of permeate flowrate over TMP and the maximum tolerable flow rate of the mmSEC column. Resulting flowrates were 30 and 2 mL/min for feed and permeate flow rate, respectively. The pump of the ÄKTA Start chromatography system was bypassed and the flow generated and controlled by the CFF unit's backpressure valve. Setting the set-point as surrogate flow rate in the chromatography system settings was necessary to enable data collection and fractionation. Flow meter, chromatography fraction, and UV absorbance data were temporally aligned and processed volumes as well as fraction volumes were retrospectively corrected by integration of flow rate over time. Before integration, flow rate data were

smoothed using a moving mean with a window of 50 data points, corresponding to 3 s. Delay volumes of the chromatography system were automatically corrected. For the *mmSEC* process, the column was inserted after the fractionation valve to ensure UV absorbance monitoring during the wash procedure avoiding flow over the column. Contrary to the other processes, the wash step permeate had to be collected from the wash valve before the column. Fractions were collected manually based on the flow meter cumulative volume readings. During re-dissolution, a volume of 1.96 mL was needed for VLPs to pass the mmSEC column and was therefore manually added to the delay volume during alignment. Manual and automatic flow rate control in all processes resulted in maximum 3% deviation of the mean flow rate from the set-point and a coefficient of variation smaller than 9%. Flow rate data of the first three minutes showed transient oscillation and were omitted in the calculations.

S3.3 SEC analysis

Samples were separated by size using analytical SEC. Three detectors were coupled to the UHPLC system, which were a DAD, MALS detector, and QELS detector. The DAD recorded spectra as well as single wavelengths, of which 260 nm and 280 nm were used for SEC purity and A260/A280 calculation. A typical UV chromatogram is shown in Figure S3.1.

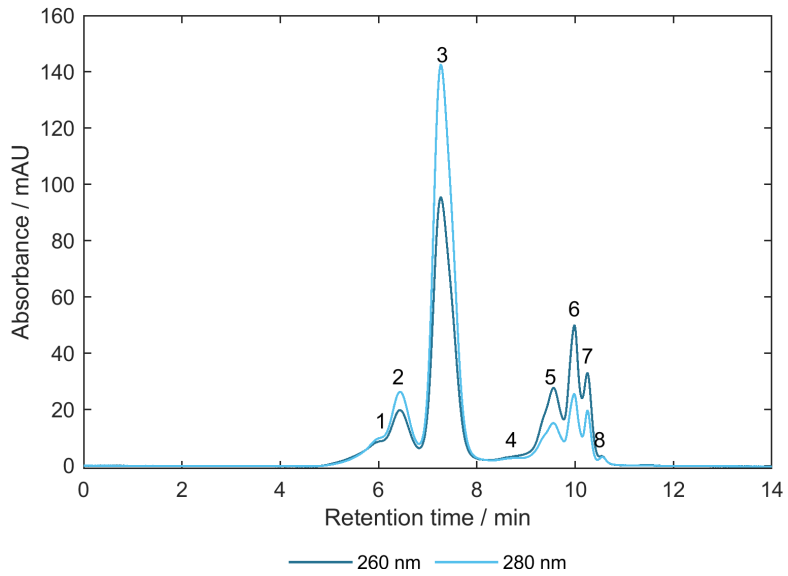

Figure S3.1. Size-exclusion chromatography chromatogram of the *Basic* process fraction F4 showing absorbance at 280 and 260 nm over retention time. Detected peaks are marked with numbers. Peaks 1-3 represent hepatitis B virus core antigen species; peaks 4-8 represent impurities.

Eight peaks were detected, whereby peaks 1-3, showing protein-typical A260/280 values of mostly <0.75, were attributed to HBcAg. This assumption was confirmed by HT-CGE analysis of samples that showed almost only peaks 1-3 (average 98% SEC purity, main text Table 3.1), such as samples of strategic pooling for process *mmSEC*. These samples exhibited one dominant peak in the HT-CGE electropherogram corresponding to monomeric HBcAg (average 96% HT-CGE purity, main text Table 3.1). During sample preparation for the protein HT-CGE assay, all proteins are denatured and reduced and therefore disassembled to monomers. It is therefore reasonable to assume that peaks 1-3 only differ in their quaternary structure while being based on HBcAg molecules. Peaks 4-8 showed higher absorbance at 260 nm and are therefore probably mainly nucleic acid species (Wilfinger et al., 1997). This scheme was observed for all CFF re-dissolution samples. For re-dissolution samples in the *Reference* process, peak 5 was dominated by protein contaminants, according to the UV spectral data (A260/A280 < 1.0, data not shown), not seen in the CFF processes. This is in accordance with lower protein purities seen for the *Reference* process samples (main text Table 3.1).

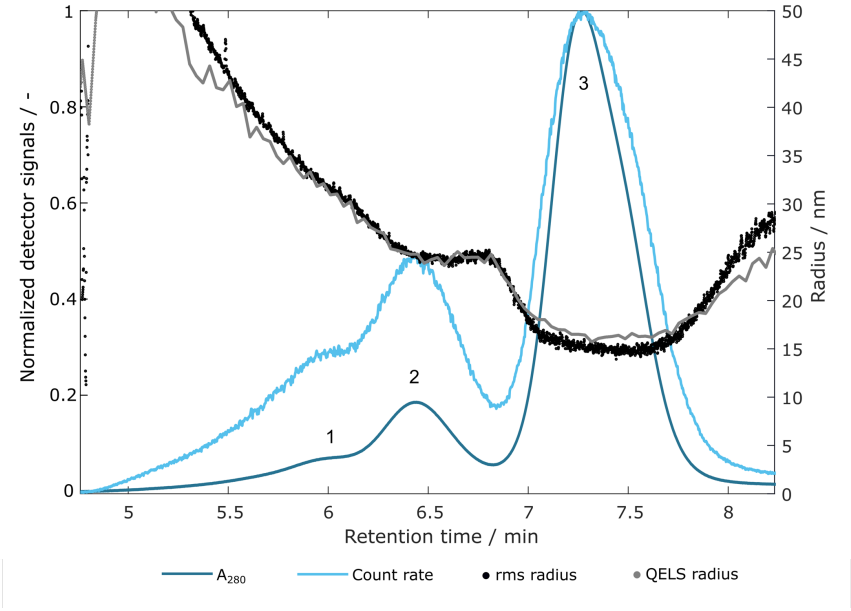

Figure S3.2. Absorbance at 280 nm and light scattering signals of a size-exclusion chromatography analysis of fraction F4 of the *Basic* process. Absorbance at 280 nm (A_{280}, —) and light scattering count rate (—) are normalized by their maximum value. Peaks 1, 2, and 3 are marked with numbers 1-3. Root mean square (rms, •) and quasi-elastic light scattering radius (QELS, •) are shown as absolute values.

Figure S3.2 shows an excerpt of the above shown SEC chromatogram with normalized signals of absorbance at 280 nm and count rate derived from the light scattering device focusing on peaks of HBcAg species. Root mean square

(rms) radius and quasi-elastic light scattering (QELS) radius are shown which were calculated by a 1st degree Zimm model and by the manufacturers' QELS model, respectively. The size measurements were in good agreement and resulted in radii of 31-32 nm, 25 nm, and 15-16 nm for peaks 1, 2, and 3, respectively. Only peak 2 and 3 represent typical peak shapes and therefore likely represent a distinct species each, while peak 1 probably represents a broad range of aggregates of various sizes. The largest peak, peak 3, showed a radius typical for HBcAg VLPs (15-17 nm (Selzer & Zlotnick, 2017)). Other chromatograms were almost identical, but tended to diverge more at very low sample concentrations due to a disadvantageous signal-to-noise ratio (data not shown).

Figure S3.3 shows size and mass of species behind peak 1-3 as indicated in Figure S3.2 for processes *Basic*, *mmSEC*, and *Nuclease* (Figure S3.3A-C). The difference between the processes was small but most notably between *Nuclease* and the other two processes. This is probably due to lower sample concentrations and therefore lower signal-to-noise ratio. As discussed above, peaks represent HBcAg species, which was concluded due to a low A260/280 ratio (~0.7), and high HT-CGE purity (≥96%), and typical protein UV spectra (not shown). QELS and rms radii are in good agreement. Only for peak 3 representing VLPs, QELS radius was slightly larger than rms radius, which is expected for spherical particles (Leszczyszyn, 2012). In the following, peak radii are discussed indifferent of measurement type (rms or QELS) and processes. Peak 1 showed largest radius and weight with 30.4-32.0 nm and 11.2-12.7 MDa, respectively, and probably represents a broad size range of aggregates. The small range of the measured sizes for peak 1 is derived from the calculation method of peak data, which is based on a window of 0.15 min around the peak maximum as determined by SEC. Peak 2 was smaller with 24.4-25.2 nm and 7.5-8.0 MDa. Peak 3 was the smallest with 15.3-17.7 nm and 3.8-4.1 MDa. Its radius is consistent with HBcAg capsid size reported in literature.

Based on manual graphical size evaluation of TEM micrographs (main text Figure 3.7), it was not possible to identify distinct particle size species as seen with SEC (MALS/QELS), illustrating the limitation of this quantification method. The difference between the even distribution of VLPs in the *Reference* and *mmSEC* process and the observed VLP clusters in *Basic* and *Nuclease* process can most probably be caused by TEM grid preparation, sample adsorption, negative staining, and washing steps, rather than by differences in the samples. Existence of such clusters were not reflected by the results of SEC. SEC, as opposed to TEM measurements, reflects solution conditions and is therefore the preferred size analytical method.

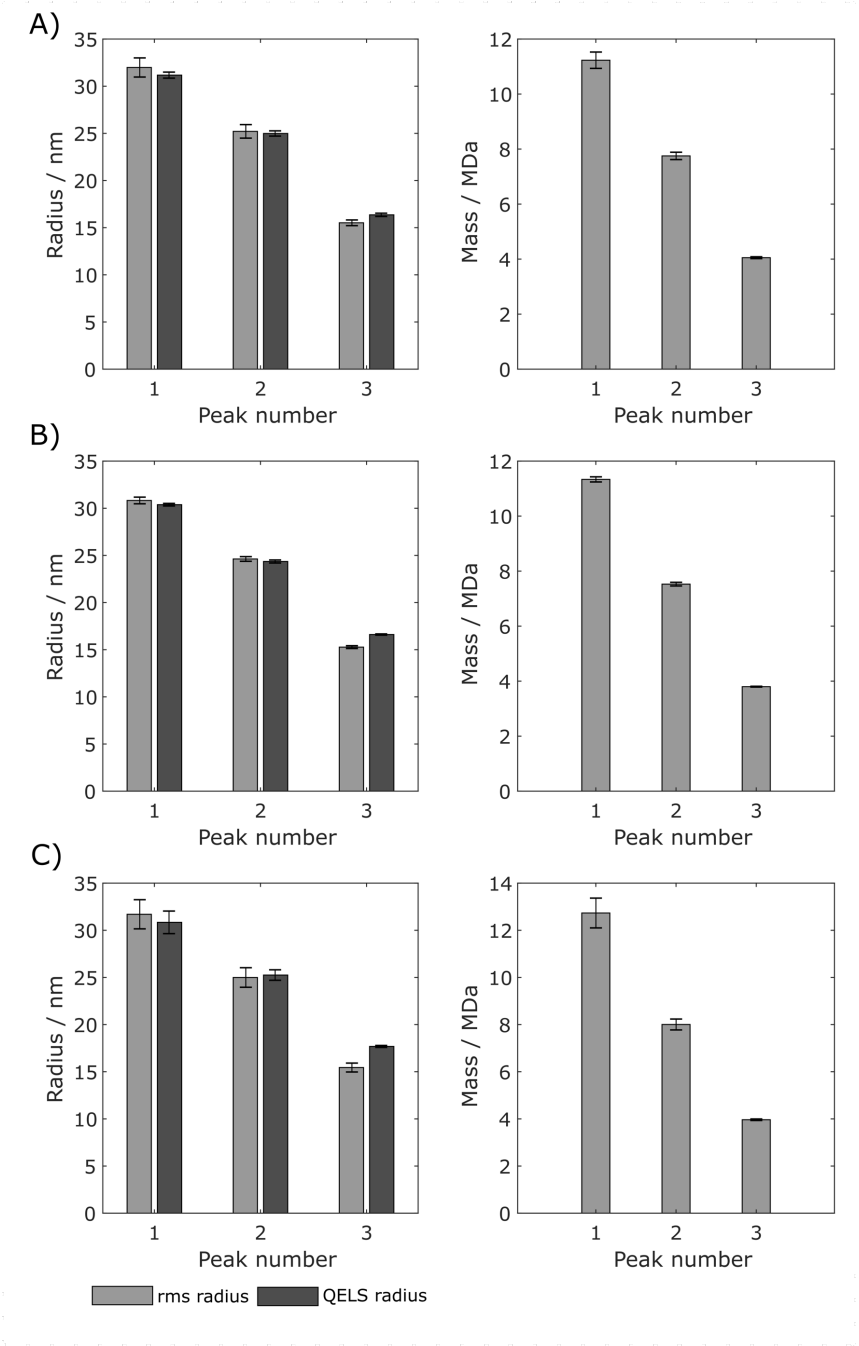

Figure S3.3. Size measurements of fractions with highest hepatitis B virus core antigen concentrations of the processes (A) *Basic*, (B) *mmSEC*, and (C) *Nuclease*. The left column shows root mean square radius (rms) and quasi-elastic light scattering (QELS) radius of peaks 1, 2, and 3, as indicated in Figure S3.2. The right column shows calculated mass of peak species 1-3. Error bars indicate standard deviations of cumulated measurement values within 0.15 min left and right of the SEC peak maximum from duplicate measurements.

S3.4 CFF wash and re-dissolution process data

Figure S3.4 depicts on-line concentrations for the processes *Basic*, *mmSEC*, and *Nuclease* showing both wash and re-dissolution process steps as a

complement to Figure 3.6 in the main text. Initially, the signal was in saturation for processes *Basic* as well as *mmSEC* and decreased exponentially afterwards. The on-line concentration of the *Nuclease* process started below 1 g/L and also decreased exponentially. During wash, UV active impurities, such as proteins and nucleic acids, are depleted, leading to an elevated absorbance of the permeate at 280 nm which decreases over time. During the *Nuclease* process, the enzymatic digestion of nucleic acids and wash prior to precipitation leads to a lower initial contaminant level in the following wash step.

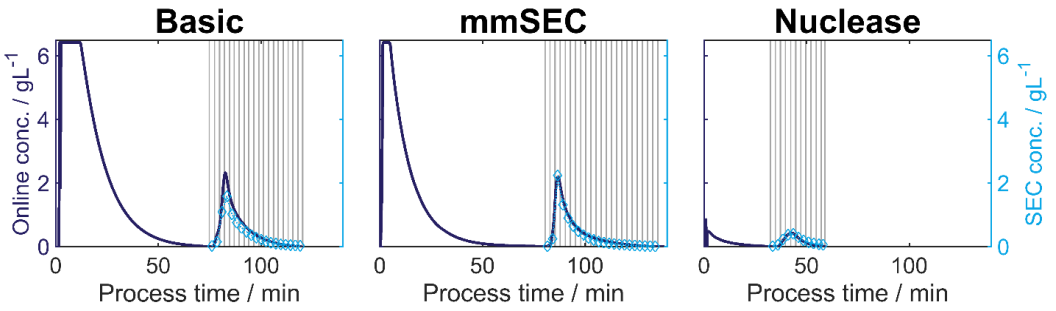

Figure S3.4. On-line monitoring of the permeate protein concentration (conc.) of wash and re-dissolution and off-line protein concentration of the re-dissolution fractions (indicated by vertical lines). Each column represents a process variant: Basic, mmSEC and Nuclease. Protein concentrations (—) are based on the absorbance at 280 nm, assuming the chimeric hepatitis B virus core antigen (HBcAg) extinction coefficient. Off-line concentrations (◊) were derived from size-exclusion chromatography (SEC) peak areas of HBcAg species (Figure S3.1).

S3.5 Analytical considerations

Analysis of turbid samples

Turbidity prohibits analysis of the samples with SEC due to presence of precipitate that would block the column. During the *mmSEC* process, turbidity was observed in fractions F2 and F3, probably due to an erroneous priming of the mmSEC column with wash buffer, containing 150 mM $(NH_4)_2SO_4$. The $(NH_4)_2SO_4$ permeates slower through the column than VLPs, as it can penetrate the pores. VLP solution therefore leaves the column in a buffer with higher $(NH_4)_2SO_4$ concentration than before entering the column, thus leading to precipitation. This effect can be circumvented by priming the column in a non-$(NH_4)_2SO_4$-containing buffer. Upon dilution, the samples became clear and could be measured by SEC. Wash samples were measured by HT-CGE as, in particular for early samples, heavy precipitation was observed.

Comparability of yields

Yields are calculated from re-dissolution and lysate HBcAg concentrations. Two separate methods have been employed to assess HBcAg concentration in the lysate and the re-dissolution samples, i.e. HT-CGE and SEC, respectively. SEC measurements exhibit much better reproducibility but could not be applied for lysate concentration measurements due to high impurity levels. Concentration determination by HT-CGE has a reproducibility of only 30% according to the manufacturer's manual. Reasons for that include low-volume liquid handling of sample and buffers, interfering particles, and baseline determination. Yields relative to each other are well comparable due to highly reproducible SEC HBcAg concentration measurements of the re-dissolution samples. Additionally, HT-CGE assessed lysate HBcAg concentrations were consistent between processes, which is owed to identical lysate preparation. However, absolute yield values are subject to variability related to HT-CGE reproducibility.

Appendix B: Supplementary material of Chapter 4

S4.1 Purification of virus-like particles

For purification, the re-dissolved and sterile-filtered virus-like particle (VLP) solution was diafiltered against a 50 mM Tris buffer at pH 7.2 using a 100 kDa molecular weight cut-off (MWCO) Hydrosart Sartocon Slice 200 membrane (Sartorius Stedim Biotech GmbH, Göttingen, DE) with 200 cm^2 membrane area. The process was conducted for 6 diafiltration volumes (DV) on a KrosFlo Research KRIIi system (Spectrum Labs, Rancho-Dominguez, US-CA) or a Cogent µScale TFF System (Merck KGaA, Darmstadt, DE), both with a feed flow rate of 30 mL min^{-1} and a transmembrane pressure of 0.03 bar. VLP solutions were stored at -20 °C. Prior to disassembly experiments, the VLP solutions were polished by flow-through multimodal size-exclusion chromatography (SEC) using a CaptoCore 400 HiScreen column (GE Healthcare, Uppsala, SE) with a nominal volume of 4.7 mL on a ÄKTA Pure with fraction collector F9-C, controlled by Unicorn (Version 6.4.1 SP2, all GE Healthcare), at 2 mL min^{-1} flow rate. The column was equilibrated with 50 mM Tris buffer at pH 7.2, 15 to 20 column volumes were loaded on the column, and the flow-through peak was fractionated into 12 mL fractions. Fractions were analyzed for VLP content by high-performance liquid chromatography (HPLC)-SEC with a Bio SEC-5 1000 Å, 4.6 × 300 mm, 5 µm column (Agilent, Santa Clara, US-CA) and pooled according to the analysis results. Aliquots of 1 mL and 7 mL were stored at -20 °C until usage in screening and filtration-based experiments, respectively.

S4.2 Implications of diafiltration-based depletion of solution components on disassembly time series

In this study, disassembly was initiated solely by addition of urea and titrant (first case), not by removal of solution components, such as commonly used stability-enhancing salts from previous process steps (second case). In the first case, the disassembly time series (DisA-TS) represents the solution conditions of the diafiltration (DF)-based disassembly. In the second case, the mixing approach for disassembly, i.e. the DisA-TS, does not account for the depletion of substances during DF. This results in different solution conditions between screening and DF-based processing, hampering comparability between both. A possible approach to solving this problem is the realization of the DisA-TS with pre-disassembly VLP stock solutions omitting components not contained in the DF disassembly buffer, e.g. stability-enhancing salts. While, at the beginning of the DF, the time series

would not accurately represent the retentate (buffer) composition, after several DV it does. Since the DF-based disassembly can include a hold step, this approach is appropriate.

S4.3 Extended discussion of the filtration-based process for VLP A

Compared to Cp149, the VLP A feed contained a larger amount of HMWS with 10.65 mg but less dimers with 0.08 mg supporting the assumption of a higher VLP stability and higher aggregation tendency of VLP A. Its total dimer yield decreased from 0.77 to 0.73 during the overnight hold, suggesting that, compared to the DisA-TS, aggregation was reduced but not completely avoided. A similar yield decrease was observed in the DisA-TS and is expected to be enhanced by the temperature-related pH increase (Figure 4.4B). An immediate continuation of the process without the hold step could circumvent the observed yield decrease. Incomplete VLP A disassembly, indicated by a HMWS mass of 0.20 mg and a VLP mass of 1.06 mg, and the depletion of impurities associated with HMWS or VLPs also contribute to a yield reduction. The implementation of pump-driven filtration instead of centrifugal filters could improve the dimer separation yield as the extended exposure of proteins to air-liquid interfaces is known to provoke the formation of HMWS and aggregates (Callahan et al., 2014). Apart from yield optimization, the separation performance of the dimer separation step could be further increased by a smaller membrane MWCO, e.g. 50 kDa or 30 kDa. The VLP A reassembly yield of 0.57 was markedly lower than for Cp149. Filtration of the reassembly product with 0.2 µm pore size required pre-filtration to prevent clogging while it did not for Cp149 again indicating the formation of larger aggregates. The reassembly buffer, especially the NaCl concentration, was not optimized for VLP A and an optimization could improve the yield by reducing aggregation.

S4.4 Derivation of the evaporation correction factors (Equation 4.2)

The calculation of the evaporation correction factor requires a prior determination of the volumetric solvent evaporation rate

$$r_{\mathrm{v}} = \frac{V(t_{\mathrm{v}}) - V(t_0)}{t_{\mathrm{v}} - t_0} \tag{S4.1}$$

where V is the solution volume, t_0 the starting time, and t_{v} the end of the observed interval. Note that r_{v} is negative in this case and assumed to be constant over time. Proteins, such as HBcAg, do not evaporate and therefore mass conservation holds

$$V(t_0)\,\bar{c}_{\mathrm{HBcAg}}(t_0) = V(t_{\mathrm{v}})\,\bar{c}_{\mathrm{HBcAg}}(t_{\mathrm{v}}) \tag{S4.2}$$

where $\bar{c}_{\mathrm{HBcAg}}$ is the average HBcAg concentration of multiple observations and disassembly conditions. Substituting $V(t_\mathrm{v})$ in Equation S4.1 with Equation S4.2 leads to a mean evaporation rate

$$r_\mathrm{v} = \frac{V(t_0)\left(\frac{\bar{c}_{\mathrm{HBcAg}}(t_0)}{\bar{c}_{\mathrm{HBcAg}}(t_\mathrm{v})} - 1\right)}{t_\mathrm{v} - t_0}. \tag{S4.3}$$

For the DisA-TS, this previously determined mean evaporation rate is then used to compare the evaporation-corrected sample volume $V_\mathrm{c}(t)$ at a time t with a theoretical sample volume $V_\mathrm{th}(t)$. The latter is solely based on volume reduction by sampling (drawn injections) from the initial volume. The reduced volumes $V_\mathrm{c}(t)$ and their relation to the theoretical volumes $V_\mathrm{th}(t)$ is expressed by evaporation correction factors

$$f_\mathrm{v}(t) = \frac{V_\mathrm{th}(t)}{V_\mathrm{c}(t)} = \frac{V_\mathrm{th}(t)}{V_\mathrm{th}(t) + r_\mathrm{v}(t - t_0)} \tag{S4.4}$$

where $(t - t_0)$ is the current experiment duration. For example, considering an initial volume of 500 µL and a second sample after 60 min (one 20 µL sampling already passed), a theoretical volume of $V_\mathrm{th} = 500\,\mu\mathrm{L} - 20\,\mu\mathrm{L} = 480\,\mu\mathrm{L}$ is expected when neglecting evaporation. Including an evaporation rate would lead to a smaller corrected volume of $V_\mathrm{c} = 480\,\mu\mathrm{L} + r_\mathrm{v}(t - t_0)$, where $(t - t_0) = 60$ min. While in this case, the influence of evaporation is small, it increases for later samples.

Due to volume reduction, the measured dimer concentration $\tilde{c}_{\mathrm{dimer,tot}}$ is increased due to mass conservation. The corrected concentration is

$$c_{\mathrm{dimer,tot}}(t) = \tilde{c}_{\mathrm{dimer,tot}}(t)\frac{\left(V_\mathrm{th}(t) + r_\mathrm{v}(t - t_0)\right)}{V_\mathrm{th}(t)}. \tag{S4.5}$$

Substituting Equation S4.4 into S4.5 leads to Equation 4.2. A potential error of this evaporation correction approach is the neglected influence of differing urea concentrations and pH on evaporation. Further, an increase in urea or buffer species concentration due to evaporation during the DisA-TS was neglected. The maximum urea concentration increase is expected for conditions with $c_\mathrm{urea} =$ 4 M at 24 h, which amounts to 0.3 M.

S4.5 Supplementary figures

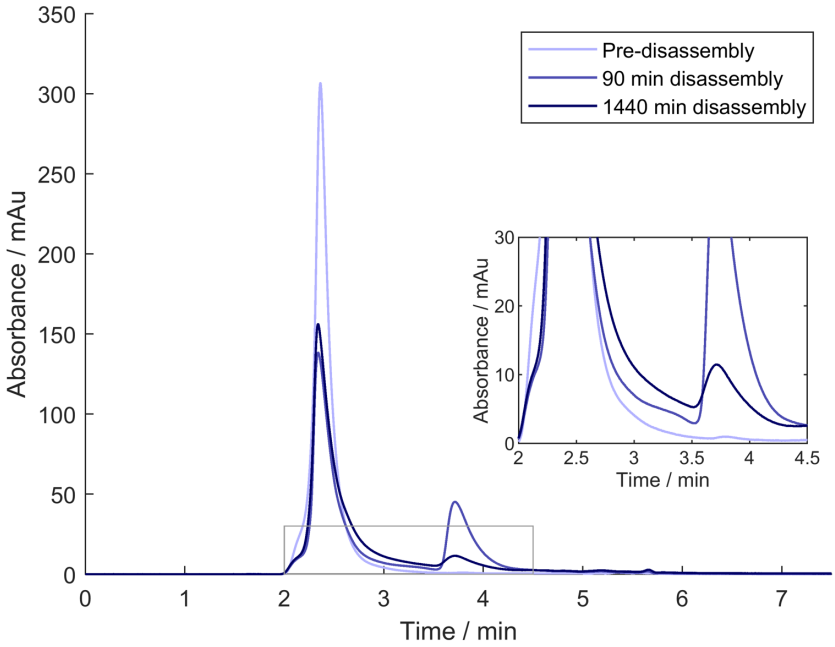

Figure S4.1. Evaporation-corrected SEC-HPLC chromatogram of Cp149 in the DisA-TS at pH 7.2 and $c_{\mathrm{urea}} = 4\ \mathrm{M}$ after 90 min and 1440 min compared to a pre-disassembly sample. Evaporation correction accounts for sample volume changes due to evaporation during the screening as described in the main article. An enlarged view highlights the interval between 2 min and 4.5 min, which is indicated by the gray box. During the disassembly reaction, the increasing absorbance between the VLP peak (~2.5 min) and the dimer peak (~3.7 min) is assumed to be caused an intermediate species.

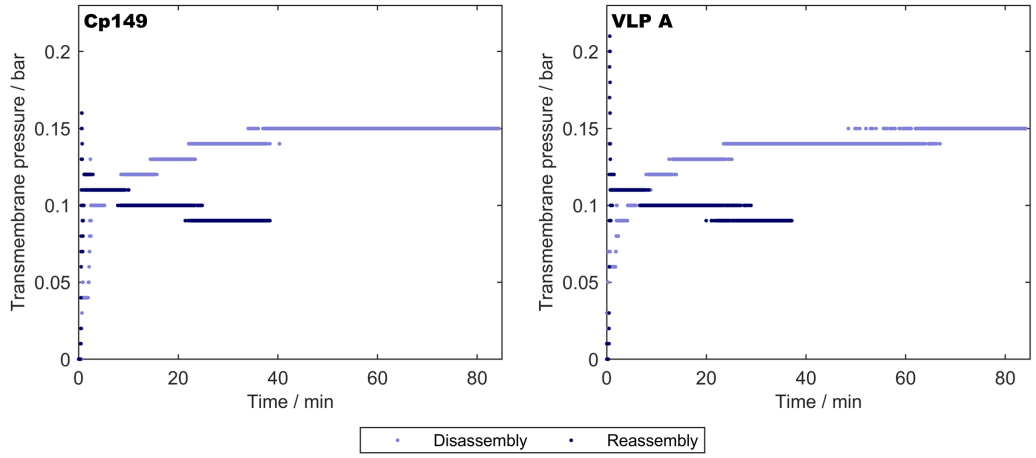

Figure S4.2. Recorded transmembrane pressures from the filtration-based process sequence. The two process steps, VLP dis- and reassembly, were conducted with different membrane areas and permeate fluxes (main text, Section 4.2.4). Cp149 and VLP A show a similar progression over time. The resolution of the pressure sensors was 0.01 bar.

Appendix C: Supplementary material of Chapter 5

S5.1 Supplementary process data

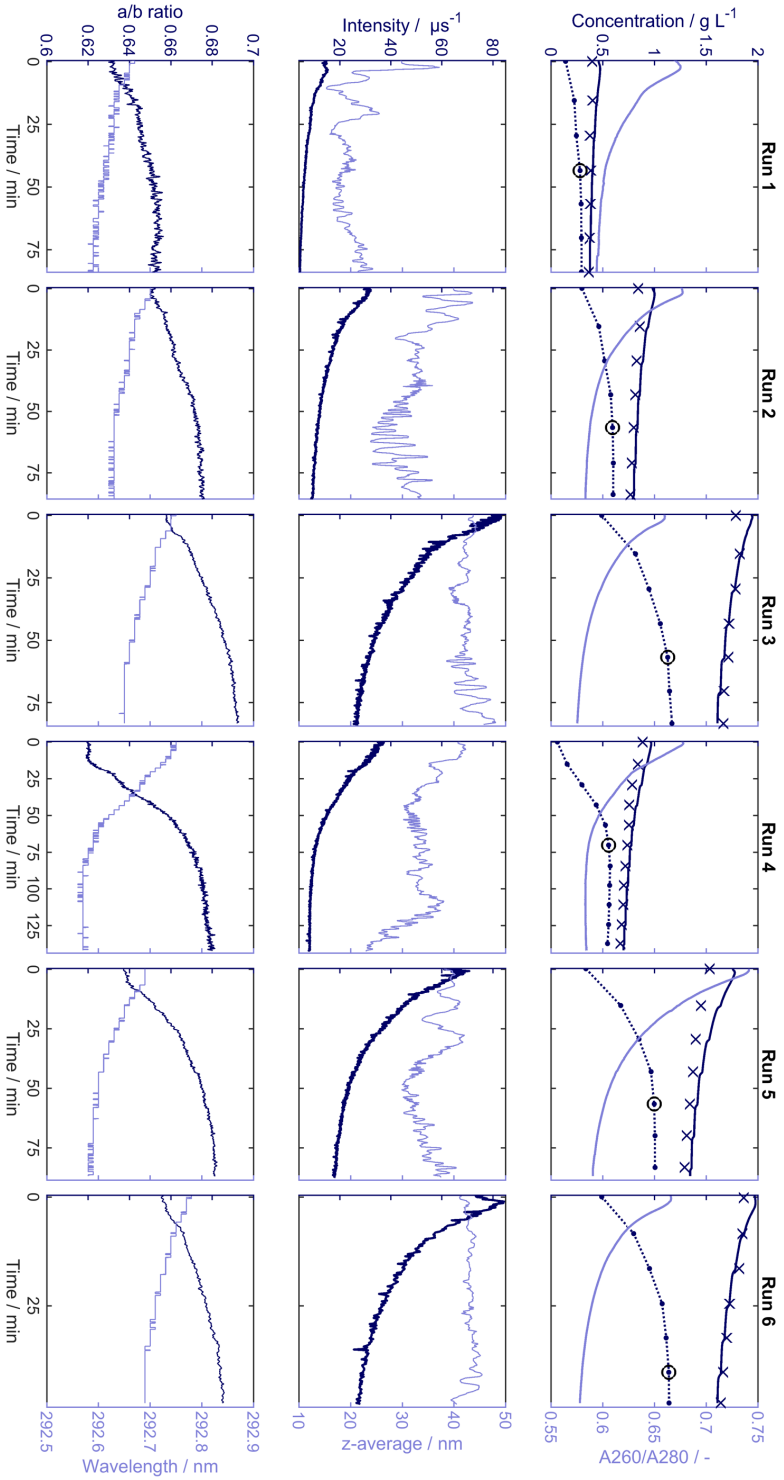

Figure S5.1. *Rotated 90° clockwise*. Process data from on-line monitoring (showing the full data set of run 4). For details, see Figure 5.2 (main text).

S5.2 Extended discussion of in-line monitoring

Figure S5.2 shows the in-line monitoring results. The transmembrane pressure (TMP) und the delta pressure increased initially and reached a plateau toward the end. The increase most probably results from the higher viscosity of the urea-containing diafiltration buffer. A higher permeate flux (run 6) led to a higher TMP level while the delta pressure was between 0.33 and 0.46 bar for all runs. The pressure monitoring could be beneficial for monitoring the filtration performance. For example, a decrease in filtration performance due to pore blockage can be identified by an increasing TMP as the permeate flux is kept constant by a controller.

The initial pH of all runs was between 7.0 and 7.1 and increases over time to final values ranging from 8.3 to 8.4. The deviations compared to the target pH of feed and diafiltration buffer are expected to originate from an off-set of the in-line electrode and might be minimized by an optimized calibration under process conditions (e.g. in flow). Nevertheless, the signal represents the progression and steady state of the pH and thereby the state of buffer exchange. For all runs, the conductivity decreased over time to 2 mS cm^{-1} after 6 DV. The initial conductivity was highest for run 4 which contained 300 mM NaCl and slightly higher for run 5 which was spiked with impurities. While NaCl is known to increase the conductivity, the negatively charged nucleic acids are expected to be the reason for the increased feed conductivity of run 5. Therefore, the conductivity could be used to monitor the nucleic acid level, however, only in a non-specific manner. The main advantage of a conductivity monitoring is the possibility to identify the necessity of additional DV due to changes of the feed composition, for example a higher NaCl concentration. In combination, pH and conductivity signals reveal the state of buffer exchange and the point in time when the target conditions are reached.

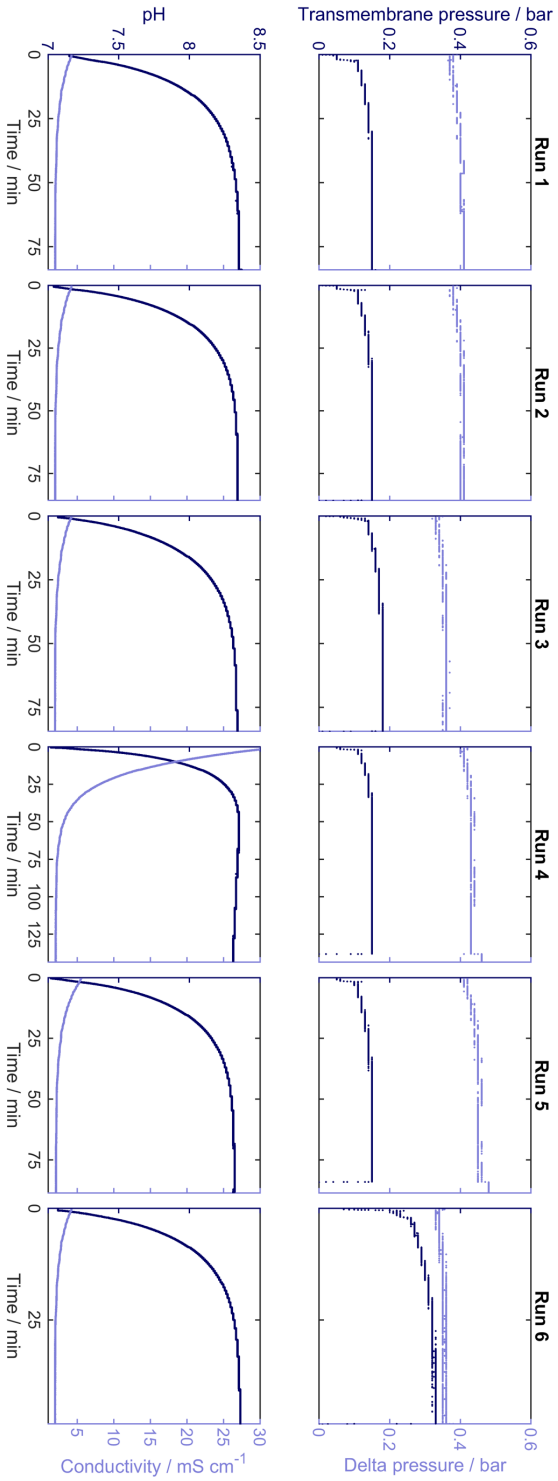

Figure S5.2. *Rotated 90° clockwise*. Process data from in-line monitoring. Each column represents the data of one experiment (compare Table 5.1, main text). Top row: transmembrane pressure (dark blue) and delta pressure (light blue) which is defined as the difference of feed and retentate pressure at the membrane module. The resolution of pressures was 0.01 bar. Bottom row: in-line pH (dark blue) and in-line conductivity (light blue).

S5.3 Supplementary regression modeling data

Table S5.1. Root mean square errors of prediction (RMSEP) for each regression model and run. The classification into calibration set and external validation set is specified in the last column. Abbreviations: cal., calibration; val., validation.

Experiment	**RMSEP** $g\ L^{-1}$			**Set**
	Model A	Model B	Model C	
Run 1	0.018	0.012	0.037	Cal.
Run 2	0.055	0.060	0.066	Val.
Run 3	0.064	0.048	0.064	Val.
Run 4	0.044	0.041	0.050	Cal.
Run 5	0.043	0.025	0.051	Cal.
Run 6	0.055	0.049	0.053	Cal.

Appendix D: Supplementary material of Chapter 6

S6.1 Mass balances

Considering that the membrane is not permeable to the protein, the temporal change of the protein concentration in the retentate c_{M} can be defined by the global mass balance

$$\frac{\mathrm{d}c_{\mathrm{M}}}{\mathrm{d}t} = -\frac{c_{\mathrm{M}}}{V_{\mathrm{Ret}}}(Q_{\mathrm{DF}} - Q_{\mathrm{Perm}}), \tag{S6.1}$$

where t represents the process time, V_{Ret} is the total retentate volume within the UF/DF system, Q_{DF} is the flow rate of the diafiltration buffer added to the system, and Q_{Perm} is the flow rate of the permeate. Given Q_{DF} and Q_{Perm}, the temporal change in V_{Ret} is given by the balance

$$\frac{\mathrm{d}V_{\mathrm{Ret}}}{\mathrm{d}t} = Q_{\mathrm{DF}} - Q_{\mathrm{Perm}}. \tag{S6.2}$$

During UF, no DF buffer is added to the system ($Q_{\mathrm{DF}} = 0$) and the protein is concentrated. During constant volume DF, the condition $Q_{\mathrm{DF}} = Q_{\mathrm{Perm}}$ holds, so that V_{Ret} and c_{M} remain constant. Smaller solutes like ions and excipients can usually pass the membrane. Due to the Gibbs-Donnan effect the solute concentration in the retentate $c_{\mathrm{Ret},i}$ and permeate $c_{\mathrm{Perm},i}$ often deviate from each other. Introducing the Gibbs-Donnan coefficient as

$$r_{\mathrm{D},i,j} = \frac{c_{\mathrm{Ret},i,j}}{c_{\mathrm{Perm},i,j}}, \tag{S6.3}$$

the mass balance for a solute i with ionization state j is given by

$$\frac{\mathrm{d}c_{\mathrm{Ret},i}}{\mathrm{d}t} = \frac{Q_{\mathrm{DF}}}{V_{\mathrm{Ret}}}\sum_j\left(c_{\mathrm{DF},i,j} - c_{\mathrm{Ret},i,j}\right) - \frac{Q_{\mathrm{Perm}}}{V_{\mathrm{Ret}}}\sum_j c_{\mathrm{Ret},i,j}\left(r_{\mathrm{D},i,j}^{-1} - 1\right) \tag{S6.4}$$

During UF, it is often more convenient to express the process duration in terms of c_{M} rather than t. During DF, on the other hand, the diafiltration volume v_{DV} is a common measure of the process duration. Using Equations S6.1 and S6.2, Equation S6.4 can also be expressed as

$$\frac{\mathrm{d}c_{\mathrm{Ret},i}}{\mathrm{d}c_{\mathrm{M}}} = \sum_j \frac{c_{\mathrm{Ret},i,j}}{c_{\mathrm{M}}}\left(1 - r_{\mathrm{D},i,j}^{-1}\right) \tag{S6.5}$$

for the UF step and

$$\frac{\mathrm{d}c_{\mathrm{Ret},i}}{\mathrm{d}v_{\mathrm{DV}}} = \sum_j\left(c_{\mathrm{DF},i,j} - r_{\mathrm{D},i,j}^{-1}c_{\mathrm{Ret},i,j}\right) \tag{S6.6}$$

for the DF step. The concentration $c_{\mathrm{DF},i,j}$ is commonly known. Thus, having an expression for $r_{\mathrm{D},i,j}$ and starting conditions for $c_{\mathrm{Ret},i}$, Equations S6.5 and S6.6 can be used to describe the temporal change in $c_{\mathrm{Ret},i}$.

S6.2 UF/DF experiments – mAbA

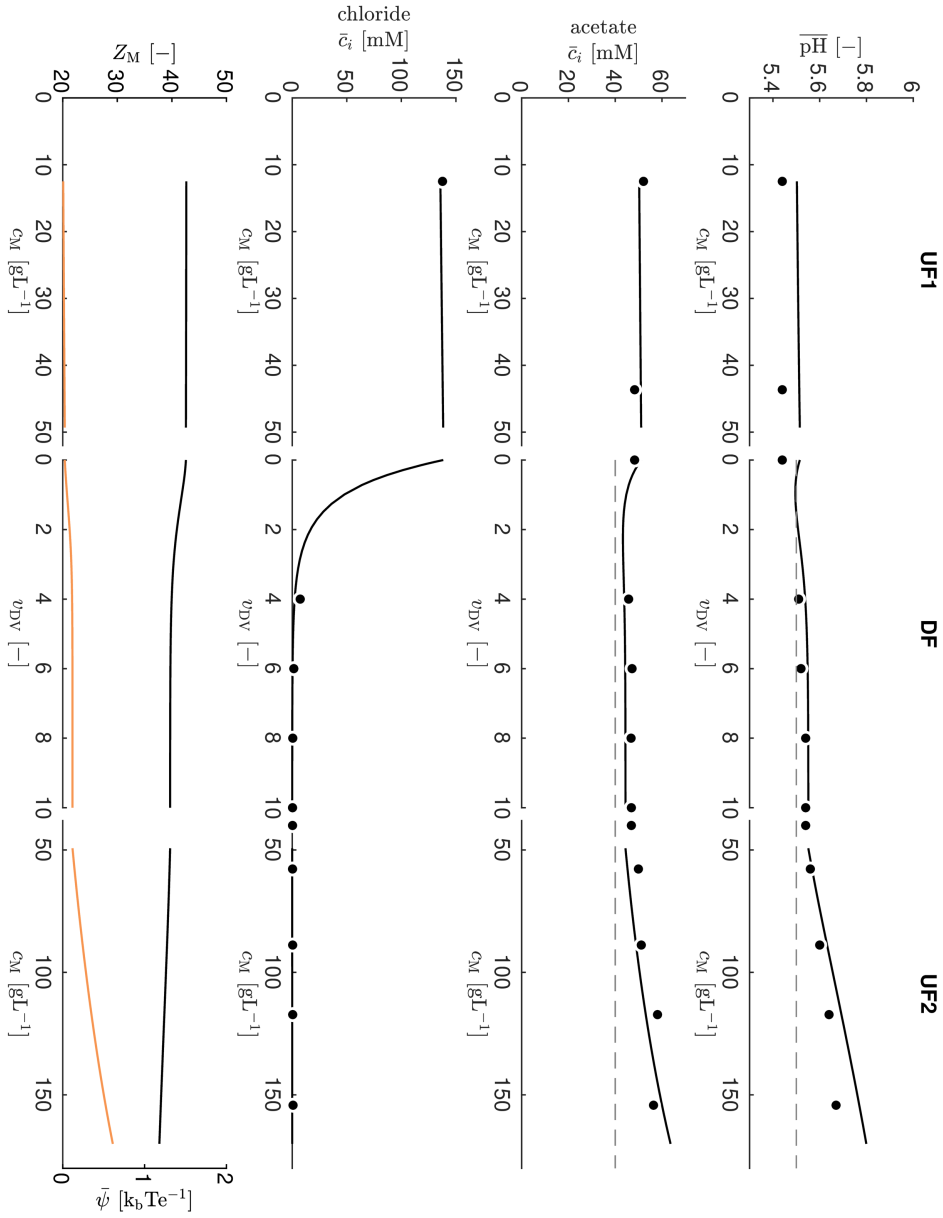

Figure S6.1. *Rotated 90° clockwise*. Illustration of model predictions and measurements according to offline analytics for ExpA4 using mAbA and 40 mM acetate (pH 5.5) as DF buffer. Model predictions and measurements are indicated by lines and markers, respectively. Top: Comparison between predicted and measured retentate pH. For visual guidance, the pH of the DF buffer is indicated as a gray dashed line. Second row: Comparison between predicted and measured acetate concentration in the retentate. For visual guidance, the acetate concentration in the DF buffer is shown as a gray dashed line. Third row: Comparison between predicted

and measured chloride concentration in the retentate. Bottom: Protein charge and $\bar{\psi}$ shown in black and orange, respectively.

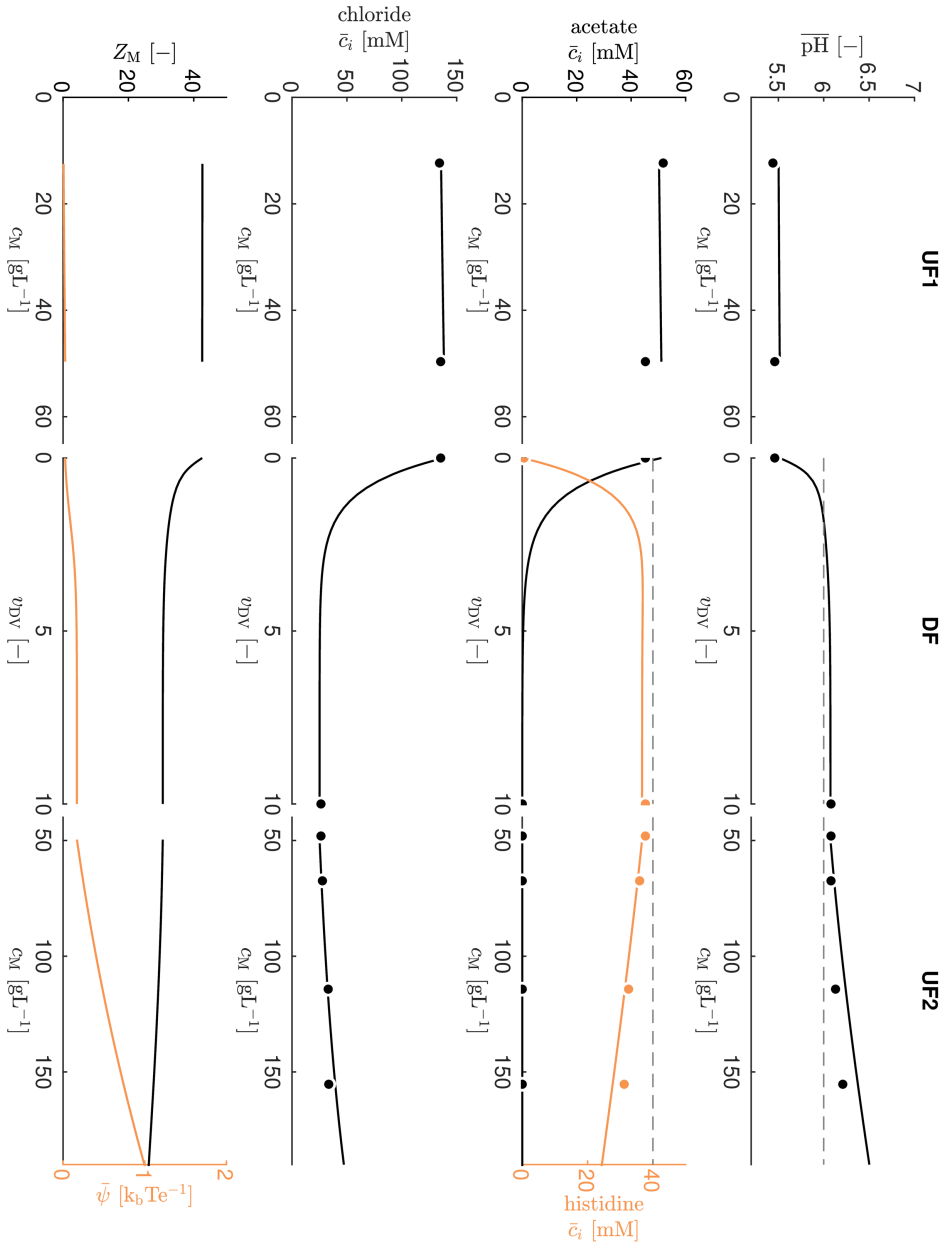

Figure S6.2. *Rotated 90° clockwise*. Illustration of model predictions and measurements according to offline analytics for ExpA7 using mAbA and 40 mM histidine (pH 6.0) as DF buffer. Model predictions and measurements are indicated by lines and markers, respectively. Top: Comparison between predicted and measured retentate pH. For visual guidance, the pH of the DF buffer is indicated as a gray dashed line. Second row: Comparison between predicted and measured excipient concentrations in the retentate. The concentration of acetate and histidine are shown in black and orange, respectively. For visual guidance, the histidine concentration in the DF buffer is shown as a gray dashed line. Third row: Comparison between predicted and measured chloride concentration in the retentate. Bottom: Protein charge and $\bar{\psi}$ shown in black and orange, respectively.

S6.3 UF/DF experiments – mAbB

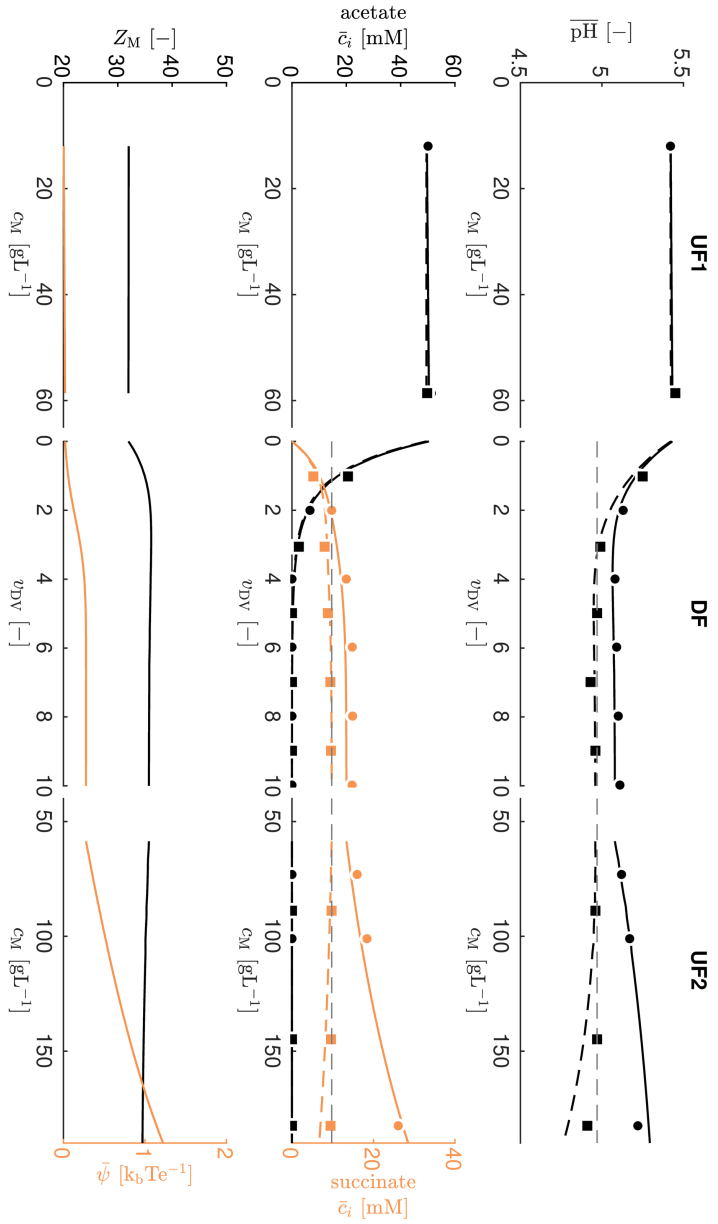

Figure S6.3. *Rotated 90° clockwise*. Comparison between retentate and permeate composition for ExpB2 using mAbB and 10 mM succinate (pH 5.0) as DF buffer. Model predictions for the retentate and permeate are indicated by continuous and dashed lines, respectively. Experimental data for the retentate and permeate are shown as circles and squares, respectively. Top: Comparison between retentate pH and permeate pH. For visual guidance, the pH of the DF buffer is indicated as a gray dashed line. Middle: Comparison between excipient concentrations in the retentate and permeate. For visual guidance, the succinate concentration in the DF buffer is indicated as a gray dashed line. Bottom: Protein charge and $\bar{\psi}$ shown in black and orange, respectively.

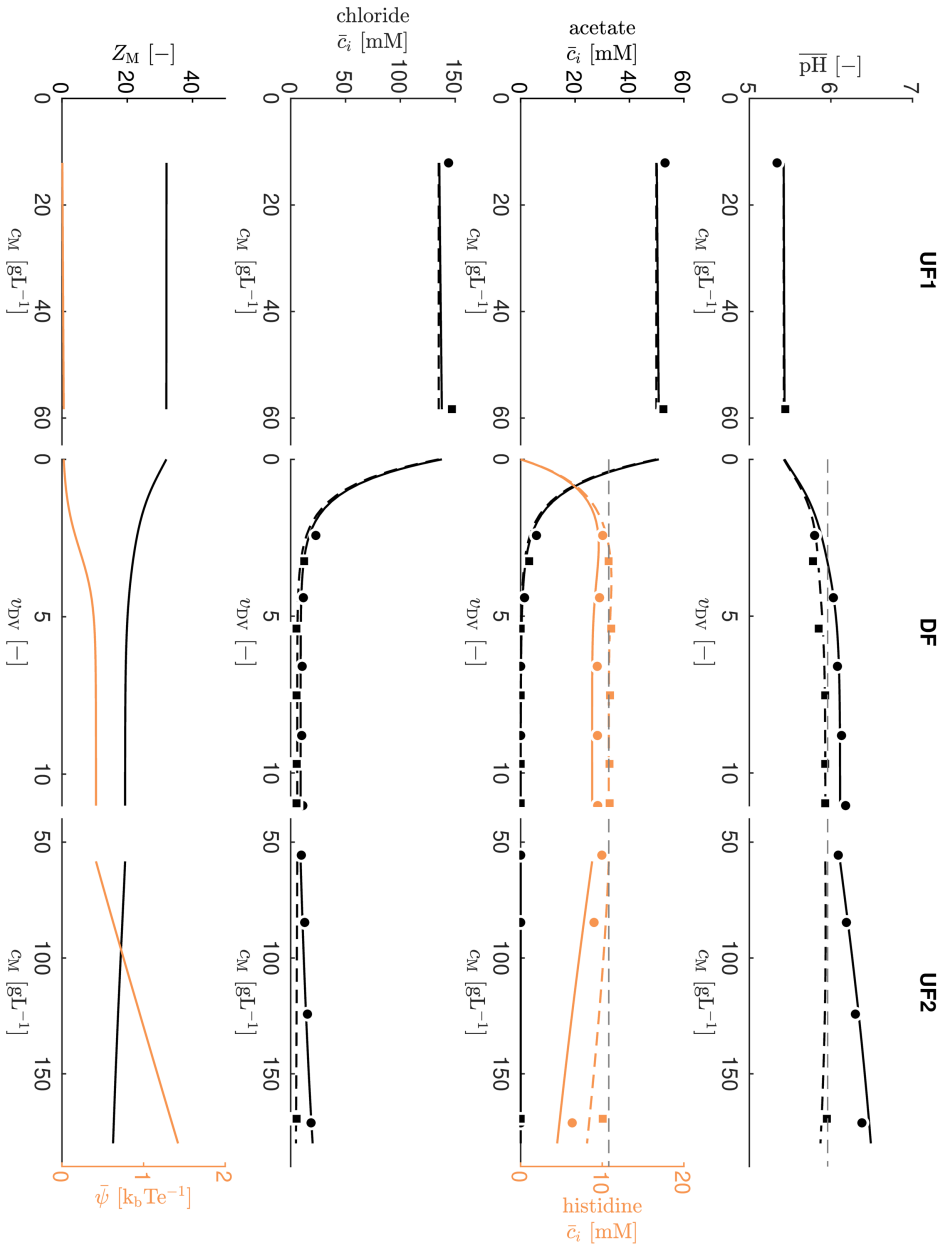

Figure S6.4. *Rotated 90° clockwise*. Comparison between retentate and permeate composition for ExpB4 using mAbB and 10 mM histidine (pH 6.0) as DF buffer. Model predictions for the retentate and permeate are indicated by continuous and dashed lines, respectively. Experimental data for the retentate and permeate are shown as circles and squares, respectively. Top: Comparison between retentate pH and permeate pH. For visual guidance, the pH of the DF buffer is indicated as a gray dashed line. Second row: Comparison between excipient concentrations in the retentate and permeate. The acetate and histidine concentration are indicated in black and orange, respectively. For visual guidance, the histidine concentration in the DF buffer is indicated as a gray dashed line. Third row: Comparison between the chloride concentration in the retentate and permeate. Bottom: Protein charge and $\bar{\psi}$ shown in black and orange, respectively.

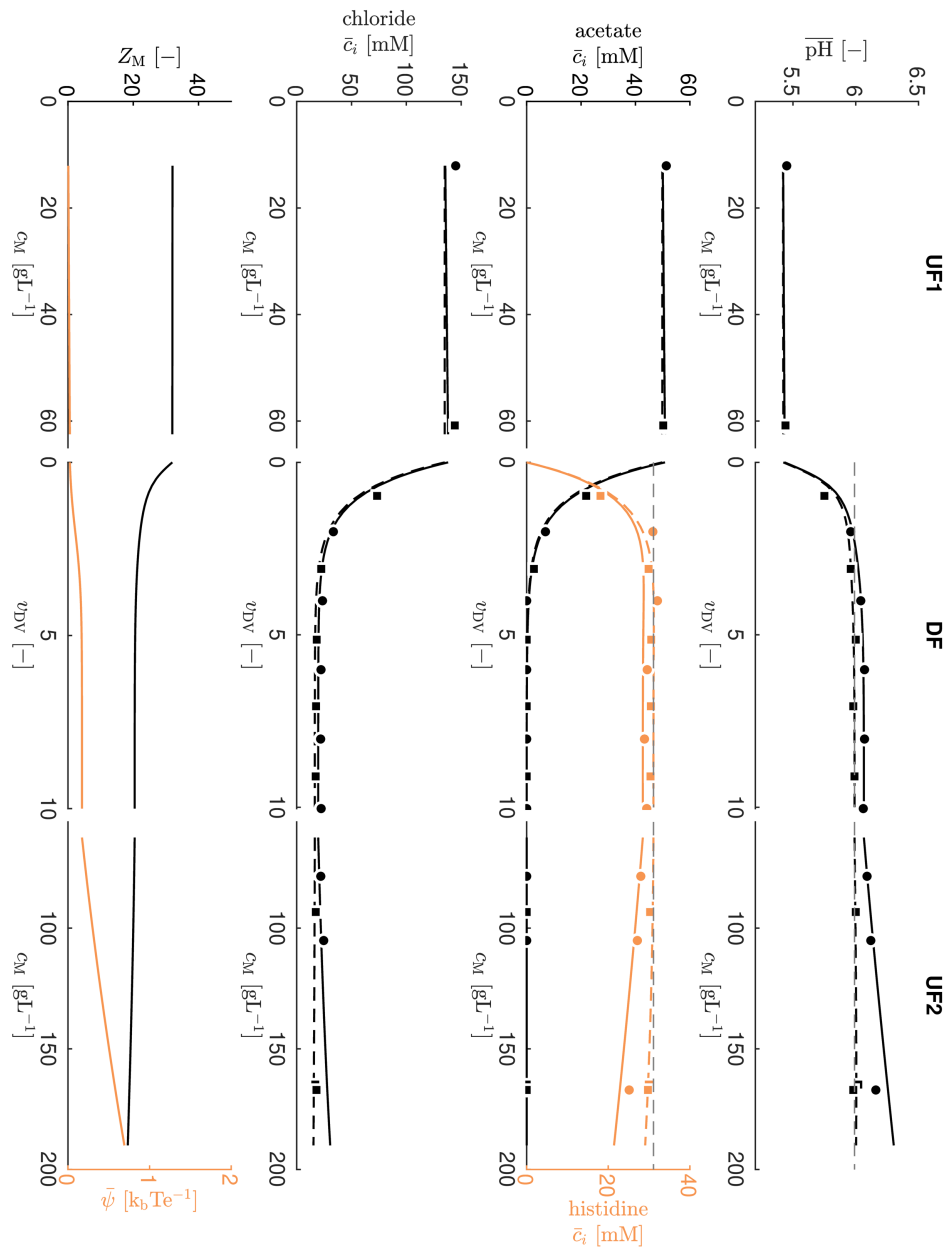

Figure S6.5. *Rotated 90° clockwise*. Comparison between retentate and permeate composition for ExpB5 using mAbB and 30 mM histidine (pH 6.0) as DF buffer. Model predictions for the retentate and permeate are indicated by continuous and dashed lines, respectively. Experimental data for the retentate and permeate are shown as circles and squares, respectively. Top: Comparison between retentate pH and permeate pH. For visual guidance, the pH of the DF buffer is indicated as a gray dashed line. Second row: Comparison between excipient concentrations in the retentate and permeate. The acetate and histidine concentration are indicated in black and orange, respectively. For visual guidance, the histidine concentration in the DF buffer is indicated as a gray dashed line. Third row: Comparison between the chloride concentration in the retentate and permeate. Bottom: Protein charge and $\bar{\psi}$ shown in black and orange, respectively.

S6.4 UF/DF experiments – FabC

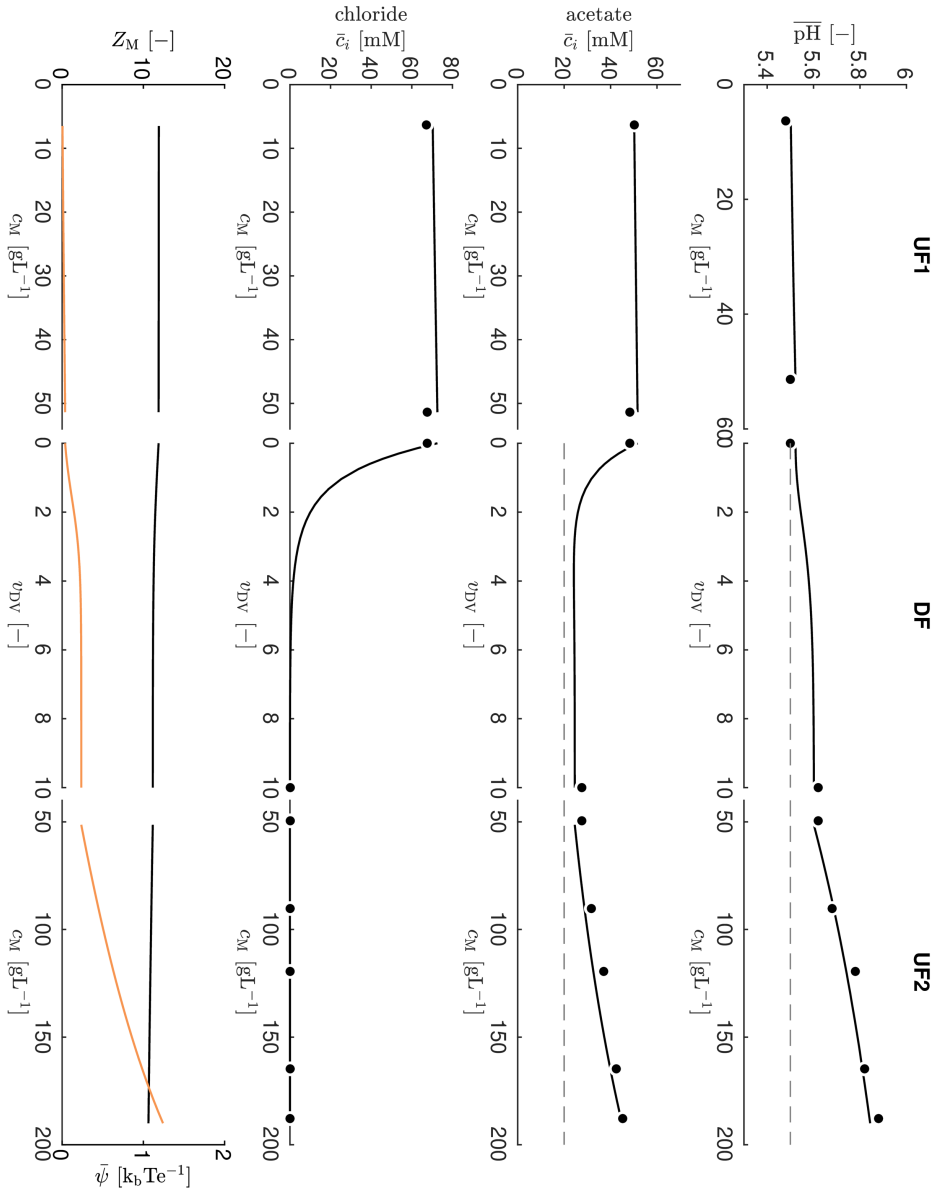

Figure S6.6. *Rotated 90° clockwise*. Illustration of model predictions and measurements according to offline analytics for ExpC1 using FabC and 20 mM acetate (pH 5.5) as DF buffer. Model predictions and measurements are indicated by lines and markers, respectively. Top: Comparison between predicted and measured retentate pH. For visual guidance, the pH of the DF buffer is indicated as a gray dashed line. Second row: Comparison between predicted and measured acetate concentration in the retentate. For visual guidance, the acetate concentration in the DF buffer is shown as a gray dashed line. Third row: Comparison between predicted and measured chloride concentration in the retentate. Bottom: Protein charge and $\bar{\psi}$ shown in black and orange, respectively.

S6.5 Buffer-less systems

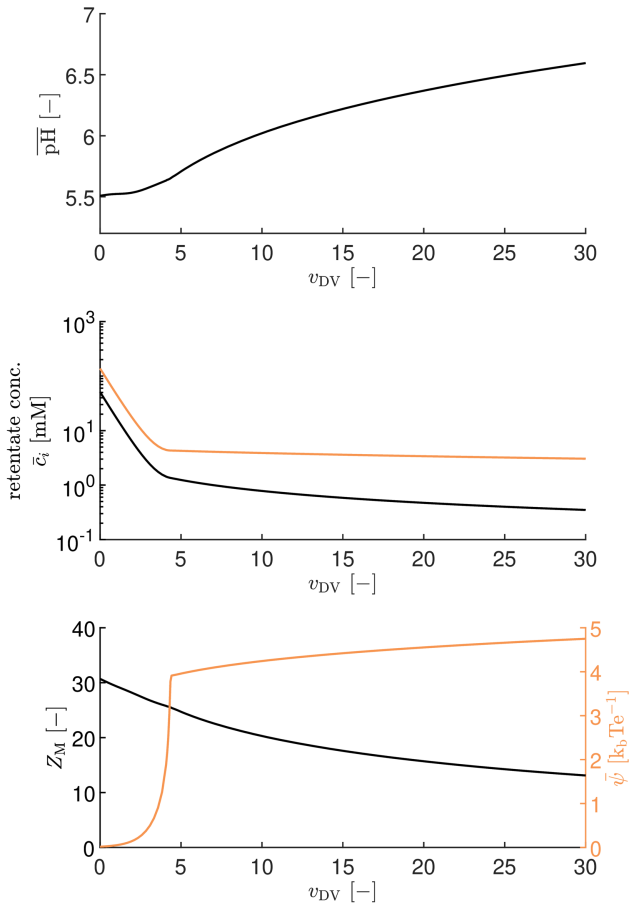

Figure S6.7. Illustration of model predictions for a diafiltration of a 50 g L^{-1} mAbB solution initially in a 50 mM acetate buffer with 135 mM sodium chloride against pure water (pH 7.0) over 30 diafiltration volumes. Top: retentate pH. Middle: Predicted acetate (black) and chloride (orange) concentration in the retentate. Bottom: Protein charge and $\bar{\psi}$ shown in black and orange, respectively.